Topochemical Reduction and Doping of Some Complex Iridium Oxides

Jacob Page

St Cross College
July 2018



A thesis submitted to the Board of the Faculty of Physical Sciences in partial fulfilment of the requirements for the degree of Doctor of Philosophy

Topochemical Reduction and Doping of Some Complex Iridium Oxides

The main body of the work is focussed on the topochemical reduction of iridium containing oxides which adopt the perovskite or the *n = 1* Ruddlesden-Popper structures. The second part of this work is focussed on the doping of Sr_2FeIrO_6.

The topochemical reduction chemistry of some 3*d*/Ir containing oxides was investigated using the group I/II hydrides as reducing agents. These reactions were successful however the by-products of reaction could not be removed without decomposing the reduced phases. To overcome these issues new reduction methods were developed.

Reduction of the double perovskite Sr_2FeIrO_6 with 5%/95% H_2/N_2 resulted in the formation of Sr_2FeIrO_4. At temperatures above 115 K Sr_2FeIrO_4 adopts a highly symmetric infinite-layer structure that consists of a rigorously ordered array of vertex sharing $Ir^{II}O_4$ and $Fe^{II}O_4$ units. The structure distorts with the onset of magnetic order. At above 115 K the spins in Sr_2FeIrO_4 are strongly interacting but frustrated. At 115 K the spins in Sr_2FeIrO_4 order resulting in a canted-antiferromagnetic state that is highly unusual and is dominated by Ir-Ir and Fe-Fe exchange interactions.

To extend this work we synthesised and reduced $Sr_2Fe_{0.5}Ir_{0.5}O_4$. $Sr_2Fe_{0.5}Ir_{0.5}O_4$ adopts the archetypal *n=1* Ruddlesden-Popper structure. Magnetisation data suggest $Sr_2Fe_{0.5}Ir_{0.5}O_4$ may have two magnetic transitions however the structure is paracrystalline so the magnetic structures cannot be determined. Reduction of $Sr_2Fe_{0.5}Ir_{0.5}O_4$ using a zirconium getter resulted in the formation of $Sr_2Fe_{0.5}Ir_{0.5}O_3$. The structure of $Sr_2Fe_{0.5}Ir_{0.5}O_3$ is the layered analogue of the infinite-layer structure.

The reduction of the solid-solution $CaMn_{0.5}Ir_{0.5}O_3$ was achieved using a NaH getter reaction and resulted in the formation of $CaMn_{0.5}Ir_{0.5}O_{2.5}$. The B-site disorder present in $CaMn_{0.5}Ir_{0.5}O_3$ is retained in $CaMn_{0.5}Ir_{0.5}O_{2.5}$ and the oxide vacancies introduced are also disordered. $CaMn_{0.5}Ir_{0.5}O_{2.5}$ is the first example of Ir^{III} in a topochemically reduced phase and the first example of square pyramidal Ir^{III}.

The final set of phases that were synthesised and reduced were $La_xSr_{2-x}Co_{0.5}Ir_{0.5}O_4$ (x = 0, 0.5). These *n=1* Ruddlesden-Popper phases were reduced using a zirconium getter reaction to form $La_xSr_{2-x}Co_{0.5}Ir_{0.5}O_3$ (x = 0, 0.5). Similarly other Ruddlesden-Popper phases and reduced analogues, $La_xSr_{2-x}Co_{0.5}Ir_{0.5}O_3$ (x = 0, 0.5) are paracrystalline so accurate structural determination is difficult however refinements suggest these phases could have a distorted anion structure.

The doping chemistry of Sr_2FeIrO_6 was investigated by doping the double perovskite with low levels of Ca, Ba, Ga and La. Structural analysis showed that the doped samples undergo phase separation and consist of an $I\bar{1}$ phase and a $P2_1/n$ phase. Magnetisation data suggest that the doped samples have two magnetic transitions. The second transition is to a type-II antiferromagnetically ordered state similar to that of Sr_2FeIrO_6. It is not clear what causes the first transition but Fe Mössbauer data show it is not due to Fe-based spins, indicating a $j_{eff} \neq 0$state for Ir^V.

Declaration

The work described in this thesis was carried out at the Inorganic Chemistry Laboratory at the University of Oxford between October 2015 and July 2018 under the supervision of Professor Michael A. Hayward. All the work presented in this thesis is my own except where I have either acknowledged help from a named person of given reference to a published source. None of the work has been submitted by the author for any degree at any other university.

Jacob Page

July 2018

Acknowledgements

I would like to start by thanking my supervisor Professor Michael Hayward for offering me the opportunity to stay on after my Part II to complete this Dphil. Thank you for your guidance, patience and knowledge without which we would not have been able to complete this work.

Thank you to the Leverhume Society for providing the funding for this work. Thank you to the neutron beam scientists and technicians at the ILL and ISIS. Specifically, I would like to thank Dr E Suard and Dr M Pascal, for the help collecting neutron diffraction data. Thank you to the Clarke, Battle and Goodwin groups and the I11 beam scientists at diamond for helping to the synchrotron diffraction data presented in this thesis. Thank you to Dr P. A. Bingham for collecting Fe Mössbauer data.

I would also like to thank my research group and the various people I have worked with over the past 4 years. Specifically thank you to Dr Midori Amano Patino and Dr Ronghuan Zhang for teaching me all the practical skills I ever needed and for welcoming me to the group all those years ago.

Thank you to my parents, Tracy and Kevin Page, for all the love, help and support they have given me over the years, everything I have achieved is a testament to you. Thank you to James Blythe for your love and for providing a refuge away from all the science whenever I needed it. Thank you to Larissa Butler, oh Commodore, for the many years of friendship and for being the perfect person to moan to when stuff went wrong.

Finally, thank you Tina Fey, Amy Poehler and Mindy Kaling.

Table of Contents

Topochemical reduction and doping of some complex iridium oxides.....i
Declaration.....ii
Acknowledgements.....iii
Table of Contents.....iv
Chapter 1 – Introduction.....1
1.1 Complex metal oxides.....1
1.2 The electronic structure of metal oxides.....2
1.2.1 Band theory.....2
1.2.2 The Hubbard model.....3
1.3 Spin-Orbit coupling.....5
1.3.1 The origin of spin-orbit coupling.....5
1.3.2 Spin-orbit coupling and iridium.....6
1.4 The Perovskite and related structures.....8
1.4.1 The Perovskite structure.....8
1.4.2 The double Perovskite structure.....10
1.4.3 The Ruddlesden-Popper structure.....11
1.5 Topochemical Reactions.....12
1.5.2 Traditional synthesis of crystalline solids.....12
1.5.2 Topochemical reduction.....13
1.5.2.1 Oxyhydride phases.....17
1.5.2.2 Electronic properties of reduced oxides.....18
Chapter 2 - Experimental Methods and Techniques.....22
2.1 Synthesis methods.....22
2.1.1 Ceramic method.....22
2.1.2 Citrate Method.....22
2.2 Handling Air Sensitive Compounds and Reactions.....23
2.2.1 Glove Box.....24
2.2.2 Air Sensitive Powder X-ray Diffraction.....24
2.3 Hydride Reductions.....24
2.3.1 Sealed Glass Ampules.....25
2.3.2 “Venting System”.....25
2.4 Washing reaction mixtures.....26

2.5 Reactions under flowing H_2.....26
2.6 Getter reactions.....28
2.7 Powder diffraction.....29
2.7.1 X-ray Powder diffraction.....30
2.7.1.1 Panalytical Empyrean and Panalytical X'Pert diffractometers.....30
2.7.1.2 Synchrotron powder X-ray diffraction.....31
2.7.2 Neutron powder diffraction.....32
2.7.2.1 WISH.....33
2.7.2.2 D2B.....34
2.8 Rietveld refinement.....35
2.9 Thermogravimetric analysis (TGA).....36
2.10 SQUID magnetometry.....37
2.10.1 Ferrosubtraction measurements.....37
2.11 Magnetism.....39
2.11.1 The Curie-Weiss law.....39
2.11.2 Correlated magnetic behaviour and magnetic ordering.....40
2.12 Superexchange and the Goodenough-Kanamori rules.....40
2.13 ^{57}Fe Mössbauer spectroscopy.....42
Chapter 3 - The Synthetic Methods and Chemical Challenges of Reducing Iridium-containing Oxides.....45
3.1 Introduction.....45
3.2 Synthesis and results.....45
3.2.1 Synthesis of parent oxides.....45
3.2.2 Reduction of Sr_2FeIrO_6.....47
3.2.2.1 Reaction with CaH_2 and LiH.....47
3.2.2.2 Reaction with 95%/5% N_2/H_2 gas.....49
3.2.3 Reactions of Sr_2CoIrO_6 and $LaSrMIrO_6$ (M = Co, Ni).....50
3.2.3.1 Reaction with CaH_2.....50
3.2.4 Reductions of $Sr_2Fe_{0.5}Ir_{0.5}O_4$.....51
3.2.4.1 Reaction with CaH_2.....51
3.2.4.2 Reaction with 95%/5% N_2/H_2 gas.....52
3.2.4.3 Reaction with zirconium.....53
3.2.5 Reduction of $La_xSr_{2-x}Co_{0.5}Ir_{0.5}O_4$ (x = 0, 0.5).....54
3.2.5.1 Reaction with CaH_2.....54

3.2.5.2 Reaction with 95%/5% N_2/H_2 gas.....55
3.2.5.3 Reaction with zirconium.....55
3.2.6 Reduction of $CaMn_{0.5}Ir_{0.5}O_3$.....57
3.2.6.1 Reaction with CaH_2.....57
3.2.6.2 Reaction of $CaMn_{0.5}Ir_{0.5}O_3$ with NaH.....58
3.3 Discussion.....60
3.3.1 Stability of iridium-containing perovskites and reduced phases.....60
3.3.2 Reduction methods used to reduce iridium-containing oxides.....63
3.3.2.1 Failure of metal hydrides.....63
3.3.2.2 Solid-gas reduction using hydrogen.....64
3.3.2.3 Success of the zirconium getter.....66
3.3.2.4 Summary of reduction methods.....67
3.3.3 Perovskite vs Ruddlesden-Popper parent phases.....67
3.4 Conclusions.....69
Chapter 4 – Topochemical Reduction of Sr_2FeIrO_6.....71
4.1 Introduction.....71
4.2 Synthesis.....72
4.2.1 Synthesis of Sr_2FeIrO_6.....72
4.2.2 Synthesis of Sr_2FeIrO_{6-x}.....73
4.3 Results.....73
4.3.1 Thermogravimetric analysis.....73
4.3.3. Structural characterisation of Sr_2FeIrO_4.....74
4.3.3.1 Room temperature Synchrotron X-ray powder diffraction.....74
4.3.3.2 Neutron Powder Diffraction.....76
4.3.3.2.1 High temperature neutron powder diffraction data.....76
4.3.3.2.2 Low temperature neutron powder diffraction data.....81
4.3.4 Magnetic Characterisation of Sr_2FeIrO_4.....84
4.3.4.1 SQUID Magnetometry.....84
4.3.4.2 Neutron powder diffraction data.....87
4.3.4.3 Variable temperature neutron powder diffraction data.....89
4.4 Discussion.....90
4.4.1 Stability of Sr_2FeIrO_4.....90
4.4.2 High temperature structure and magnetism.....93
4.4.3 Low temperature structure and magnetism.....94

4.4.3.1 Low temperature magnetic frustration.....100
4.5 Conclusion.....101
Chapter 5 – Synthesis and Characterisation of Doped Sr_2FeIrO_6.....103
5.1 Introduction.....103
5.2 Synthesis.....104
5.2.1 Synthesis of $Sr_{2-x}A_xFeIrO_6$ (A = Ca, Ba, La) and $Sr_2Fe_{0.95}Ga_{0.05}IrO_6$.....104
5.3 Results.....105
5.3.1 Structural Characterisation of Sr_2FeIrO_6 and $La_{0.05}Sr_{1.95}FeIrO_6$.....105
5.3.1.1 Sr_2FeIrO_6 Synchrotron X-ray Powder Diffraction Data.....105
5.3.1.2 $La_{0.05}Sr_{1.95}FeIrO_6$ synchrotron X-ray powder diffraction data.....109
5.3.1.3 $La_{0.05}Sr_{1.95}FeIrO_6$ variable temperature synchrotron X-ray powder diffraction data.. 113
5.3.1.4 $La_{0.05}Sr_{1.95}FeIrO_6$ Neutron Powder Diffraction Data.....114
5.3.2 Magnetic characterisation of $La_{0.05}Sr_{1.95}FeIrO_6$ and Sr_2FeIrO_6.....118
5.3.2.1 SQUID Magnetometry of $La_{0.05}Sr_{1.95}FeIrO_6$ and Sr_2FeIrO_6.....118
5.3.2.2 Neutron powder diffraction data.....120
5.3.2.3 Variable temperature neutron powder diffraction data.....122
5.3.3 ^{57}Fe Mössbauer Spectroscopy of $La_{0.05}Sr_{1.95}FeIrO_6$.....123
5.3.4 Structural characterisation of $Sr_{2-x}A_xFeIrO_6$ (A= La, Ca, Ba) and $Sr_2Ga_{0.05}FeIrO_6$.....125
5.3.4.1 $Sr_{2-x}A_xFeIrO_6$ (A= La, Ca, Ba) synchrotron X-ray powder diffraction data.....125
5.3.5 Magnetic characterisation of $Sr_{2-x}A_xFeIrO_6$ (A= La, Ca, Ba) and $Sr_2Ga_{0.05}FeIrO_6$.....136
5.3.5.1 SQUID magnetisation data.....136
5.4 Discussion.....138
5.4.1 The structure of Sr_2FeIrO_6.....138
5.4.2 Structure of doped Sr_2FeIrO_6.....140
5.4.3 Magnetism of Doped Sr_2FeIrO_6.....145
5.4.3.1 Magnetic properties of Sr_2FeIrO_6.....145
5.4.3.2 Magnetic properties of $La_{0.05}Sr_{1.95}FeIrO_6$.....146
5.4.3.3 Magnetisation of doped Sr_2FeIrO_6.....149
5.4.3.4 The electronic state and magnetism of Ir^v.....150
5.5 Conclusions.....153
Chapter 6 – Synthesis and Topochemical reduction of $Sr_2Fe_{0.5}Ir_{0.5}O_4$.....155

6.1 Introduction.....155
6.2 Synthesis.....156
6.2.1 Synthesis of $Sr_2Fe_{0.5}Ir_{0.5}O_4$.....156
6.2.2 Synthesis of $Sr_2Fe_{0.5}Ir_{0.5}O_{4-x}$.....156
6.3 Results.....157
6.3.1 Structural characterisation of $Sr_2Fe_{0.5}Ir_{0.5}O_4$.....157
6.3.1.1 Synchrotron powder X-ray diffraction data.....157
6.3.1.2 Neutron powder diffraction data.....158
6.3.2 Magnetic characterisation of $Sr_2Fe_{0.5}Ir_{0.5}O_4$.....160
6.3.2.1 SQUID magnetometry.....160
6.3.2.2 Neutron diffraction data.....162
6.3.3 Structural characterisation of $Sr_2Fe_{0.5}Ir_{0.5}O_{4-x}$.....163
6.3.3.1 Thermogravimetric analysis of $Sr_2Fe_{0.5}Ir_{0.5}O_{4-x}$.....163
6.3.3.2 Synchrotron powder X-ray diffraction data.....164
6.3.3.3 Neutron powder diffraction data.....166
6.3.4 Magnetic characterisation of $Sr_2Fe_{0.5}Ir_{0.5}O_3$.....167
6.3.4.1 SQUID magnetometry.....167
6.3.4.2 Neutron diffraction data.....169
6.4 Discussion.....170
6.4.1 Structure and magnetism of $Sr_2Fe_{0.5}Ir_{0.5}O_4$.....170
6.4.1.1 Structure $Sr_2Fe_{0.5}Ir_{0.5}O_4$.....170
6.4.1.2 Magnetic properties of $Sr_2Fe_{0.5}Ir_{0.5}O_4$.....173
6.4.1.3 Paracrystaillinity of $Sr_2Fe_{0.5}Ir_{0.5}O_3$.....174
6.4.1.3 $Sr_2Fe_{0.5}Ir_{0.5}O_4$ and doped Sr_2FeIrO_6.....175
6.4.2 Structure and magnetism of $Sr_2Fe_{0.5}Ir_{0.5}O_3$.....179
6.4.2.1 Structure of $Sr_2Fe_{0.5}Ir_{0.5}O_3$.....179
6.4.2.2 Magnetism of $Sr_2Fe_{0.5}Ir_{0.5}O_3$.....182
6.5 Conclusions.....187
Chapter 7 – Topochemical Reduction of $CaMn_{0.5}Ir_{0.5}O_3$.....189
7.1 Introduction.....189
7.2 Synthesis.....190
7.2.1 Synthesis of $CaMn_{0.5}Ir_{0.5}O_3$.....190
7.2.2 Synthesis of $CaMn_{0.5}Ir_{0.5}O_{3-x}$.....191
7.3 Results.....191

7.3.1 Thermogravimetric analysis of $CaMn_{0.5}Ir_{0.5}O_{3-x}$.....191
7.3.2 Structural characterisation of $CaMn_{0.5}Ir_{0.5}O_{2.5}$.....192
7.3.2.1 Synchrotron powder X-ray diffraction data.....192
7.3.2.2 Neutron powder diffraction data.....195
7.3.3 Magnetic characterisation of $CaMn_{0.5}Ir_{0.5}O_{2.5}$.....198
7.3.3.1 SQUID magnetometry.....198
7.3.3.2 Neutron powder diffraction data.....200
7.4 Discussion.....201
7.4.1 Oxidation states of $CaMn_{0.5}Ir_{0.5}O_3$.....201
7.4.2 Structure of $CaMn_{0.5}Ir_{0.5}O_{2.5}$.....203
7.4.2.1 Local structure of $CaMn_{0.5}Ir_{0.5}O_{2.5}$.....208
7.4.2.2 The prevalence of Ir^{III}.....210
7.4.3 Magnetic behaviour of $CaMn_{0.5}Ir_{0.5}O_{2.5}$.....211
7.5 Conclusions.....213
Chapter 8 – Synthesis and Characterisation of $La_xSr_{2-x}Co_{0.5}Ir_{0.5}O_4$ (x = 0, 0.5).....214
8.1 Introduction.....214
8.2 Synthesis.....214
8.2.1 Synthesis of $La_xSr_{2-x}Co_{0.5}Ir_{0.5}O_4$ (x = 0, 0.5).....214
8.3 Results.....216
8.3.1 Structural characterisation of $La_xSr_{2-x}Co_{0.5}Ir_{0.5}O_4$ (x = 0, 0.5).....216
8.3.1.1 Synchrotron powder X-ray diffraction data 216
8.3.1.2 Neutron powder diffraction data.....218
8.3.2 Magnetic characterisation of $La_xSr_{2-x}Co_{0.5}Ir_{0.5}O_4$ (x = 0, 0.5).....220
8.3.2.1 SQUID Magnetometry.....220
8.3.2.2 Low temperature neutron diffraction data.....222
8.4 Discussion.....224
8.4.1 Structure of $La_xSr_{2-x}Co_{0.5}Ir_{0.5}O_4$ (x = 0, 0.5).....224
8.4.2 B-site structure of $La_xSr_{2-x}Co_{0.5}Ir_{0.5}O_4$ (x = 0, 0.5).....225
8.4.3 Magnetic properties of $La_xSr_{2-x}Co_{0.5}Ir_{0.5}O_4$ (x = 0, 0.5).....226
8.4.3.1 Magnitude of magnetic moments.....226
8.4.3.2 Magnetic order vs spin-glass.....228
8.5 Conclusions.....229
Chapter 9 – Topochemical Reduction of $La_xSr_{2-x}Co_{0.5}Ir_{0.5}O_4$ (x = 0, 0.5).....230
9.1 Introduction.....230

9.2 Synthesis.....231
9.2.1 Synthesis of $La_xSr_{2-x}Co_{0.5}Ir_{0.5}O_{4-y}$ (x = 0, 0.5).....231
9.3 Results.....231
9.3.1 Structural characterisation of $La_xSr_{2-x}Co_{0.5}Ir_{0.5}O_{4-y}$ (x = 0, 0.5).....231
9.3.1.1 Thermogravimetric analysis.....231
9.3.1.2 Synchrotron X-ray powder diffraction data.....232
9.3.1.3 Neutron diffraction data.....234
9.3.1.3.1 Distorted structure of $La_xSr_{2-x}Co_{0.5}Ir_{0.5}O_3$ (x = 0, 0.5).....237
9.3.2 Magnetic characterisation of $La_xSr_{2-x}Co_{0.5}Ir_{0.5}O_3$ (x = 0, 0.5).....245
9.3.2.1 Magnetisation data.....245
9.3.2.2 Neutron diffraction data.....247
9.4 Discussion.....250
9.4.1 The structural distortion of $La_xSr_{2-x}Co_{0.5}Ir_{0.5}O_3$ (x = 0, 0.5).....250
9.4.2 Magnetism of $La_xSr_{2-x}Co_{0.5}Ir_{0.5}O_3$ (x = 0, 0.5).....252
9.5 Conclusions.....253
Chapter 10 – Conclusions.....255
Appendix 1 – Index of Figures.....259
Bibliography.....268

Chapter 1 – Introduction

1.1 Complex metal oxides

Research into complex metal oxides that contain transition metals has remained vibrant for many years. This enduring interest is due to the variety and importance of the properties they exhibit. This class of solid state material encompasses compounds that have a wide variety of electronic and magnetic properties[3-4] that include, but are not limited to, superconductivity[5-6], spin-polarised conduction[7-8], multiferrocity[9-10] and long range magnetic order[11]. The diversity of properties complex transition metal oxides can display mean that they are exceeding important calls of materials for technology, finding applications in catalysis[12], information processing[13] and energy storage[14].

The much-lauded properties of transition metal complex oxides arise from the co-operative behaviour of the transition metal centres. One feature of the transition metals is that they are each able to adopt a variety of oxidation states, often leading to partially filled *d*-orbitals. In complex oxides these partially filled *d*-orbitals can interact with the 2*p* orbitals of the oxide ions that bridge the metal centres. These interactions propagate through the material and lead to electronic states that lead to bulk behaviours and, in turn, macroscopic properties. As these electronic states arise from the collective behaviour of the transition metals they are directly affected by the oxidation state, coordination geometry and identity of the transition metals that are present in the material.

1.2 The electronic structure of metal oxides

1.2.1 Band theory

In extended solids the orbitals of individual ions overlap such that they can be regarded as forming crystal orbitals that permeate the entire solid. If enough orbitals are formed the differences in energy between them can be approximated to be negligible and these orbitals can be viewed as forming a continuous distribution of energy states. These distributions are called bands and a pictorial representation of this rationale is shown in Figure 1.1.

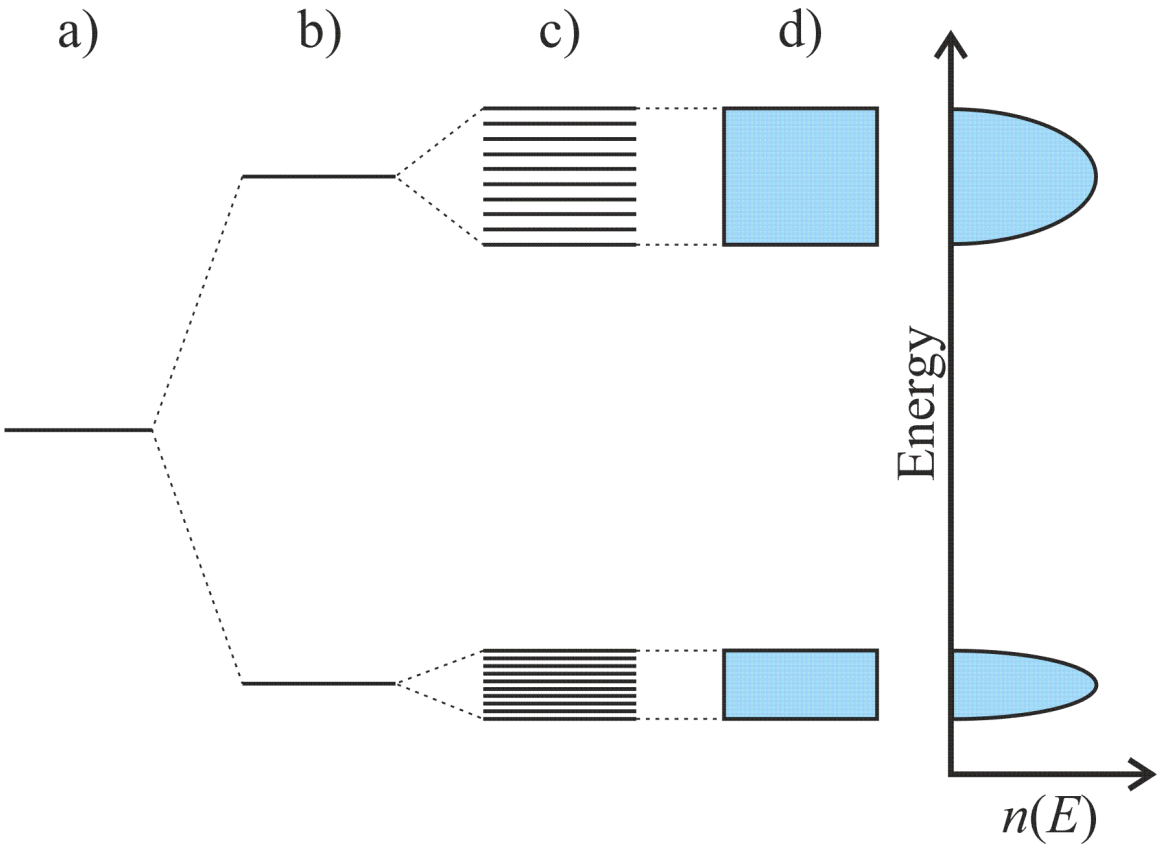

Figure 1.1: The orbital energies of a) an atom, b) a small molecule c) a large molecule d) a solid

The electron occupancy of the atomic orbitals that constitute a band determine its occupancy, i.e. filled atomic orbitals will form a filled band, and the extent of the atomic orbital overlap determines the bandwidth, i.e. small atomic overlap results in narrow

bands and visa-versa. Electrons in partially occupied bands can be excited into states that are just above the highest occupied level, known as the Fermi level. The electrons in these states delocalise and are able to move freely which leads to metallic conduction. However band theory does not take into account the interactions experienced by electrons and as such does not provide a full explanation of the behaviour of materials. This is exemplified by the simple oxides NiO and CoO which are antiferromagnetic insulators[15] despite the expectation that they should be metallic.

1.2.2 The Hubbard model

The Hubbard model[15-16] takes into account the interaction between electrons and nuclei, and mutual electron-electron repulsions present in solids. Thus the Hubbard model can be used to rationalise the conduction observed in materials, or indeed the lack thereof. The orbitals of a uniform array of atoms will overlap to form a band, in accordance with band theory (Section 1.2.1). However, the energy of electrons in the band will not be uniform throughout the band. The positively charged nuclei create energy minima, or "potential wells", due to the electrostatic attraction between the nuclei and the electrons. Consequently, electrons are not free to dissociate and move freely. In order to move, and thus be conducting, electrons must hop between nuclei. To do this an electron must have enough energy to escape the potential well i.e. the atom must be ionised, which in most solids is an exothermic process. A portion of the energy gained when the first atom is ionised will be lost when the atom moves to the second atom and reduces it. The energy of this hopping process is the difference between the ionisation energy of atom 1 and the electron affinity of atom 2. This is defined as the Hubbard "*U*". If *U* of a compound is greater than the thermal excitation energy electrons have sufficient energy to hop between centres and the system is metallic. However if the *U* of a compound is less than thermal excitation energy the electrons will remain localised and the system will be insulating.

Reducing the "depth" of the potential wells will results in a reduction in the value of U as the electron affinity will be less. This can be achieved by increasing the overlap of the orbitals that form the band. This increases the bandwidth (W). There is therefore a direct relationship between U and W. When $U > W$ the system will be a metallic conductor however when $U < W$ the system will be an insulator. Metallic conductivity is induced at the point where $U \approx W$. A graphic representation of the relationship between U and W is shown in Figure 1.2.

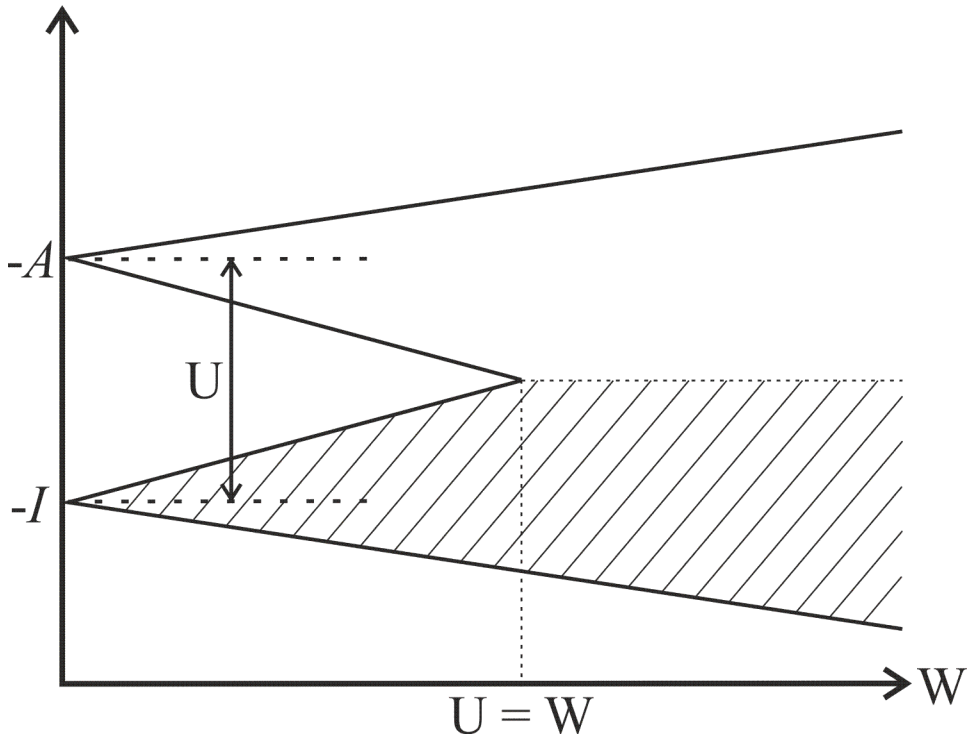

Figure 1.2: Hubbard sub-bands as a function of bandwidth, *W*.

Materials in which $U \approx W$ are of certain interest to the solid state research community. At this point the factors that favour localisation and those that favour delocalisation are finely balanced yet still conflicting. Consequently materials in this regime settle the energy requirements of these situations by adopting atypical properties. Key examples include the ferromagnetism observed in iron, cobalt and nickel[17] and the high temperature superconductivity of the cuprate superconductors[5-6]. Exerting control over these

properties is an important goal for the functional materials community, therefore there have significant efforts being put into modifying materials that lie close to this critical energy point.

1.3 Spin-Orbit coupling

1.3.1 The origin of spin-orbit coupling

For so called "light" elements electronic structure can be understood by making use of the Russell-Saunders coupling scheme, in which the orbital angular momentum (*l*) and spin (*s*) of electrons orbiting a nucleus are assumed effectively to not interact. However, this assumption is not true.

From the perspective of an electron in an atom, the nucleus is orbiting the electron with the same angular moment (*l*) with which it is orbiting the nucleus. The orbit of the positively charged nucleus about the electron creates a charge loop which in turn induces a magnetic field perpendicular to its plane. The spin (*s*) within the electron interacts with this magnetic field resulting in coupling of orbital angular momentum (*l*) and electron spin (*s*).

Solving the Hamiltonian for spin-orbit coupling (Equation 1.1) proves that the energy of the spit-orbit interaction is directly proportional to Z^4, where Z is the atomic number of an atom (Equation 1.2)[18-19]. The consequence of this is that spin-orbit coupling has a very small, often negligible, effect on the energy levels of 3*d* and 4*d* elements however it has as a significant effect on the energy levels of 5*d* elements.

$$\hat{\mathbf{H}} = \zeta_{nl}\, \boldsymbol{l}.\boldsymbol{s} \qquad 1.1$$

$$\zeta_{nl} = \frac{2\alpha^2 R_\infty Z^4}{n^3(l+1)(2l+1)hc} \qquad 1.2$$

In the regime where spin-orbit coupling is strong Russell-Saunders coupling is no long applicable, thus we must use the *j-j* coupling regime instead. In the *j-j* coupling regime the total angular momentum (*J*) is the sum of the momentum of each spin-orbit interaction (*l* + *s*) (Equation 1.4). This is different to Russell-Saunders coupling in which the total angular momentum (*J*) is the sum of the total orbital angular momentum (*l*) and the total spin (*s*) (Equation 1.3).

$$J = \sum_i l_i + \sum_i s_i \qquad 1.3$$

$$J = \sum_i (l + s)_i \qquad 1.4$$

1.3.2 Spin-orbit coupling and iridium

The atomic number of iridium is 77 and as such has very strong spin-orbit coupling. Consequently *j-j coupling* is dominant and results in electronic structures that Russell-Saunders coupling would not predict. These structures are atypical in the context of the more common and better understood electronic structures of the 3*d* and 4*d* elements. In the case of octahedrally coordinated iridium the 5*d* orbitals are split into an e_g set and a t_{2g} set, as expected. However, the strong spin-orbit coupling further splits the t_{2g} orbital set to form a low energy triplet state and a slightly higher energy singlet state. These splittings are shown in Figure 1.3.

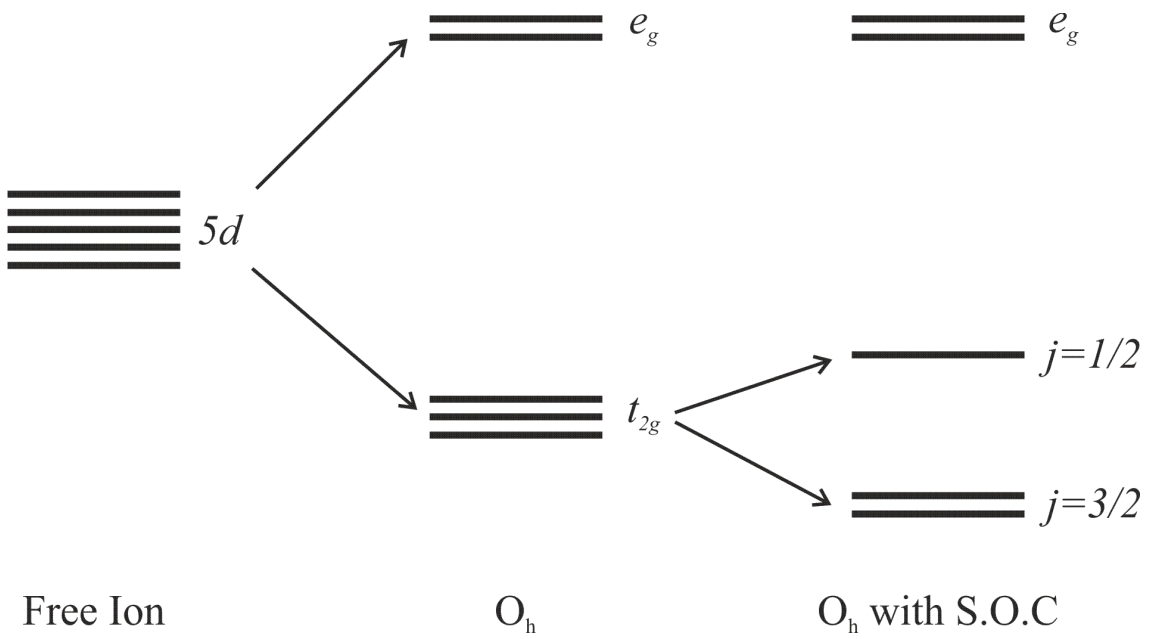

Figure 1.3: The orbital arrangements of a) an iridium free ion, b) iridium in octahedral co-ordination c) Ir^{IV} d^5 low spin in octahedral co-ordination with spin-orbit coupling

Given that atomic orbitals inform the bands that are formed in crystalline phases (Section 1.2.1) this unusual orbital regime results in a number of properties. For example, Sr_2IrO_4 is expected to have broad bands and low on-site electron repulsion and as such is predicted to be an electrical conductor by the Hubbard model (Section 1.2.2). However, Sr_2IrO_4 is an insulator[20]. This is because the spin-orbit coupling of Ir^{IV} results in the formation of two narrow bands: the j = 3/2 which is filled and the j = 1/2 which is half filled. The partially filled j = 1/2 is very narrow with high on-site electron repulsions and if we reapply the Hubbard model to this band regime it can clearly be seen why Sr_2IrO_4 is an electrical insulator. Spin-orbit coupling in iridium also leads to unusual magnetic properties. The two dominant oxidation states of iridium in solid state oxides are Ir^{IV} and Ir^{V} both of which exhibit atypical magnetic behaviours. The most studied of these two states is Ir^{IV}. As outlined above Ir^{IV} has a singly occupied singlet orbital resulting in a j = 1/2 state. This state is of particular interest to physicists as it is predicted to have desirable properties such as topological insulators and those that fulfil the conditions required for a material that satisfies the Kitaev model[21].

The magnetic properties of materials containing Ir^V have received comparatively little attention. The electronic state of Ir^V is expected to be a $j_{eff} = 0$ cation as it is a d^4 cation. The best examples in which the $j_{eff} = 0$ state can be observed are the 3*d*/Ir double Perovskites. The magnetic structures of Sr_2FeIrO_6[22] and $BaLaCoIrO_6$[23] are both type-II antiferromagnetic structures in which the 3*d* cations couple antiferromagnetically via the vacant orbitals of Ir. The $j_{eff} = 0$ state of Ir^V is well established in the literature however further investigation into published data cast some doubt on the certainty of this state. Compounds in which Ir^V is the sole B-site cation or those in which Ir^V is paired with a diamagnetic group I/II or rare earth cation should be diamagnetic however published magnetisation data show this is not always the case. $NaIrO_3$[24], $LaSrMgIrO_6$[25], $LaSrZnIrO_6$[25], La_2LiIrO_6[26], La_2NaIrO_6[27], Sr_2YIrO_6[28-29], Ba_2YSrO_6[29-30], Ba_2ScIrO_6[31], Sr_2ScIrO_6[31] are examples of Ir^V containing compounds that should be diamagnetic but exhibit paramagnetic behaviour. This flies in the face of conventional wisdom regarding the electron structure and magnetic properties of Ir^V. These seemingly anomalous behaviours and lack of understanding pertaining to their source highlights the need to expand research into iridium-containing oxides.

1.4 The Perovskite and related structures

1.4.1 The Perovskite structure

The perovskite structure is adopted by oxides with the chemical composition ABO_3 and is common among ternary metal oxides[32]. The structure can be regarded as an array of corner-sharing BO_6 octahedra in which the A cation sits in the twelve-co-ordinate site. The BO_6 octahedra in the structure are free to twist, expand and distort resulting in a highly flexible structure that can accommodate a large variety of cations on both the A and B sites. The archetypal Perovskite structure is cubic, perfectly symmetric octahedra that do not rotate (Figure 1.4). This “perfect” cubic structure is rare as the A and B

cations often vary in size resulting in co-operative twisting distortions propagating through the structure to compensate for mismatches in radii. The "size" of such a distortion can be quantified using the Goldschmidt tolerance factor[33]:

$$t = \frac{<A-O>}{\sqrt{2}<B-O>} = \frac{r_a + r_O}{\sqrt{2}\,(r_B + r_o)} \qquad 1.5$$

where *t* is the tolerance factor, *A-O* is the A-O bond length, *B-O* is the B-O bond length, r_A is the radius of cation A, r_B is the radius of cation B and r_O is the radius of O.

In transition metal oxides superexchange and overlap interactions couple the partially occupied *d* orbitals giving rise to a variety of correlated electronic and magnetic properties (Section 1.2). Superexchange and orbital overlap are optimal when the M-O-M bond angle is 180 ^{o} as this results in the strongest interaction. The flexibility of the perovskite structure means that by manipulating the tolerance factor the properties of materials can be altered or controlled, meaning that research into perovskite materials remains a rich and engaging field owing to its rich chemistry, flexibility and amenity to manipulation.

The simple perovskite structure described above has only one species of cation on each of the cation sites; however both the A-site and the B-site can be occupied by different cations. Multiple occupation of either site often results in a perturbation of a compound's properties. Changing the occupation of the A-site is the primary method used to alter the co-operative twisting regime of a structure and the formal oxidation states of the B-site cations, both of which change orbital overlap which in turn affects magnetic and transport properties. Multiple occupancy of the B-site has similar effects on a compound's physical properties as altering the A-site occupancy but to a much greater extent. Non-identical cations have different orbital energies, spin states and electron configurations to each other, a situation not encountered with identical cations. Consequently the bulk properties

that arise from interaction via orbital overlap or superexchange can vary greatly compared to those that arise from interaction of identical cations.

1.4.2 The double Perovskite structure

The situation in which there is a 1:1 ratio of two cations occupying the B-site is of interest as it results in one of two arrangements of cations, each of which can result in different structures. If the cations are similar in size and/or have a small charge difference (0-2 units of charge[34]) the cations are statistically distributed across the B-site resulting in a disordered structure with a chemical formula $AB_{0.5}B'_{0.5}O_3$. These disordered Perovskites are solid-solutions. If the cations differ significantly in size and/or have a large charge difference (2 < units of charge) the cations adopt an ordered array to minimise strain arising from localised clusters of structural strain or high coulombic repulsion. The consequential B-site results in a double perovskite structure which has the chemical formula $A_2BB'O_6$, $AA'B_2O_6$ or $AA'BB'O_6$ (Figure 1.4)[139]. The ordered arrangement can vary and the resulting structures have been identified by Woodward et al[35]. The rigidity and structural uniformity of double perovskites restricts number and "type" of interactions possible, having a profound effect on the physical properties of compounds adopting these structures. For example, double perovskites cannot become spin glasses since spin glass ordering requires disorder. This means that magnetic frustration must be relieved via alternative mechanisms. One such mechanism is the movement of magnetic from the position at the centre of the octahedron, which in turn can lead to the formation of a type-II multiferroic state. This is observed in Y_2CoMnO_6[36] and Lu_2MnCoO_6[37] clearly illustrating the novel states that can arise from the rigidity imposed by cation order. Further examples include combination of ferromagnetic order and insulating behaviour observed in A_2MnNiO_6[38-39] and A_2MnCoO_6 (A = La, Bi)[40], properties not observed together in the simple ABO_3 perovskite structures.

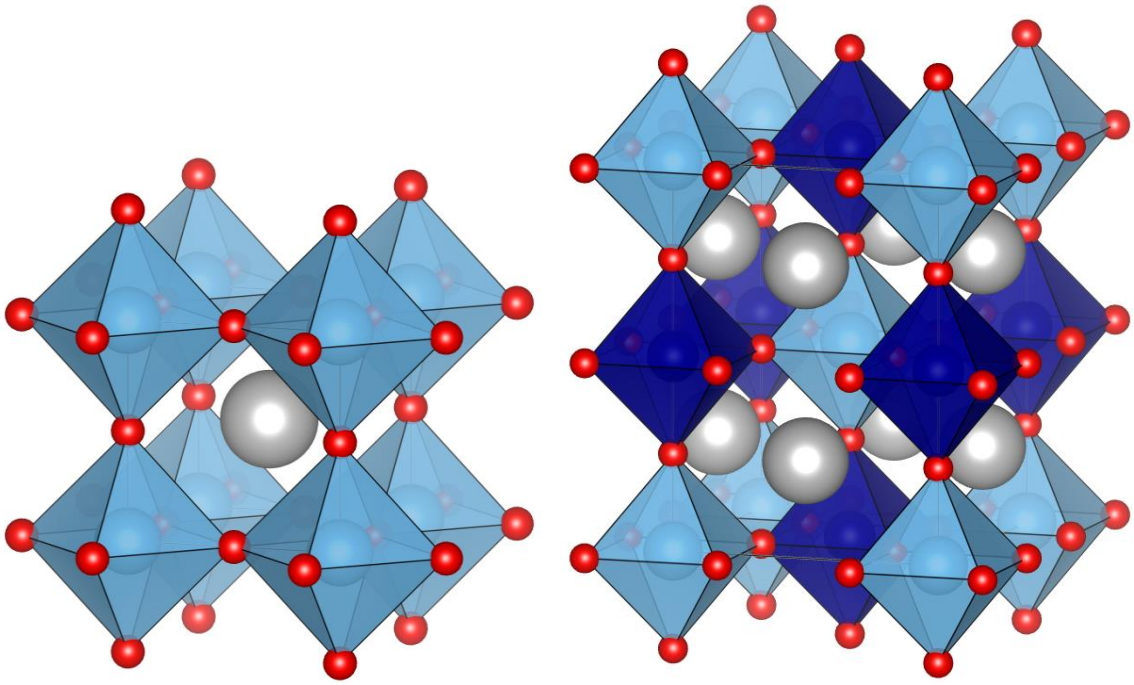

Figure 1.4: The simple cubic Perovskite structure (left), the double Perovskite structure (right)

1.4.3 The Ruddlesden-Popper structure

Related to the perovskite structure are the Ruddlesden-Popper structures[32]. The Ruddlesden-Popper structures are a layered structures that can be regarded as a regular stacked intergrowths of perovskite blocks and cations that form an AO rock salt layer. Such structures (Figure 1.5) can be described by the formula $AO(ABO_3)_n$, where n is an integer. The limiting case when $n= \infty$ is the three-dimensional perovskite structure. The addition of the rock salt layer into the structure increases the lattice energy of the structure but also breaks connectivity along the c-axis reducing the dimensionality to two-dimensional. The breaking of connectivity has two significant consequences. Firstly orbital overlap and superexchange interactions are weakened along the c-axis and as such properties are largely defined by intraplane interactions. Secondly in the case analogous to the double perovskites the cation order cannot be easily observed as the planes can stack in a disordered arrangement masking any order from conventional diffraction techniques. These structures are known as paracrystalline[41].

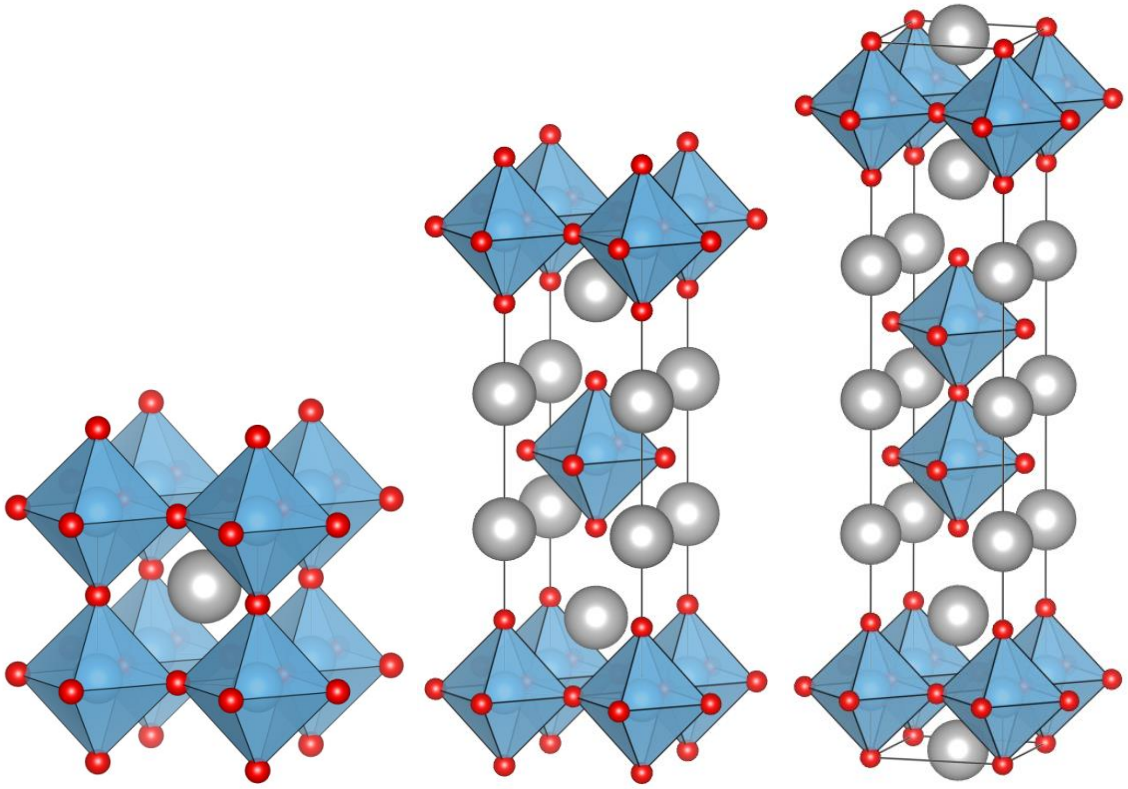

Figure 1.5: The simple Perovskite structure (left), the n=1 Ruddlesden-Popper structure (centre), the n=2 Ruddlesden-Popper structure (right)

1.5 Topochemical Reactions

1.5.1 Traditional synthesis of crystalline solids

The mobility of ions in solids is usually very low and barriers to diffusion of ions between solid grains are high. Consequently, to make crystalline sample of complex transition metal oxides samples need to be heated at high temperatures. This always leads to the formation of thermodynamic products and limits the oxidation states and coordination geometries of cation to those that minimise the free energy of the system. This severely limits the ability of researchers to probe the relation between the structure and properties of materials as it limits both to a narrow, predefined range of cases. In response to this limitation as series of low temperature techniques have been developed that allow for the synthesis of metastable, kinetic phases that are inaccessible using traditional high

temperature synthesis methods. These techniques are "topochemical" methods that take advantage of the different mobility of ions in a solid to alter the ion framework of "parent" phases while maintaining the structure of the cation sub-lattice. These methods have led to the preparation of a variety of metastable phases that have otherwise unheard-of oxidation states and coordination geometries[42-45].

1.5.2 Topochemical reduction

One topochemical reaction that has been used to make novel oxide phases is topochemical reductive deintercalation of anions from a material while leaving the cation sub-lattice unchanged. To maintain charge neutrality the cations are reduced, often leading to otherwise unheard-of oxidation states. These reactions are carried out at relatively low temperatures ($180 \leq T / {}^{o}C \leq 630$) and result in the formation of anion-deficient metastable phases[42, 46]. The majority of topochemical reductions that have been reported use group I/II metal hydrides as reducing agents. The formative example of this example of reaction is the reduction of $LaNiO_3$ to $LaNiO_2$[42] (Figure 1.6).

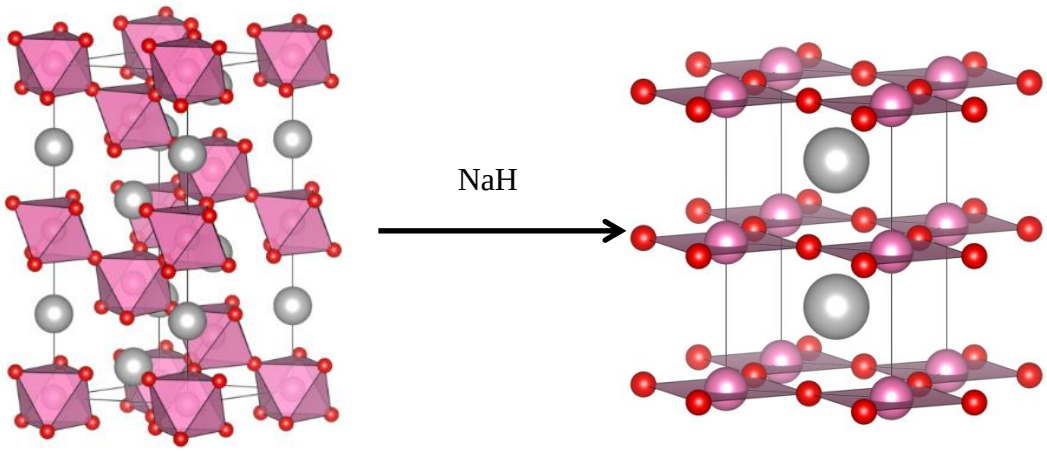

$LaNiO_3$ **$LaNiO_2$**

Figure 1.6: The topochemical reduction of $LaNiO_3$ to $LaNiO_2$

Topochemical reduction methods have been successfully applied to a variety of different perovskite and perovskite-related structures (Section 1.4). Application of these techniques have successfully resulted in the preparation of reduced phases with unusual cation oxidation states, such as square-planar $Fe^{II}/Co^{I}/Ni^{I}$ [42, 47-49] and octahedral Mn^{I} [50]. In recent years this work has been extended to include the reduction of complex transition metal oxides that contain 4*d* transition metals. This was first achieved by reduction of $SrFe_{0.5}Ru_{0.5}O_3$ to $SrFe_{0.5}Ru_{0.5}O_2$[44] (Figure 1.7). In this case it was demonstrated that $SrRuO_3$ could not be reduced to form a metastable phase and a stabilising 3*d* lattice was needed. The 3*d* provides stability by acting as a barrier to total decomposition of the 4*d* lattice. This result is of particular interest as we look to expand the scope of this method by moving into the reduction of iridium-containing complex oxides.

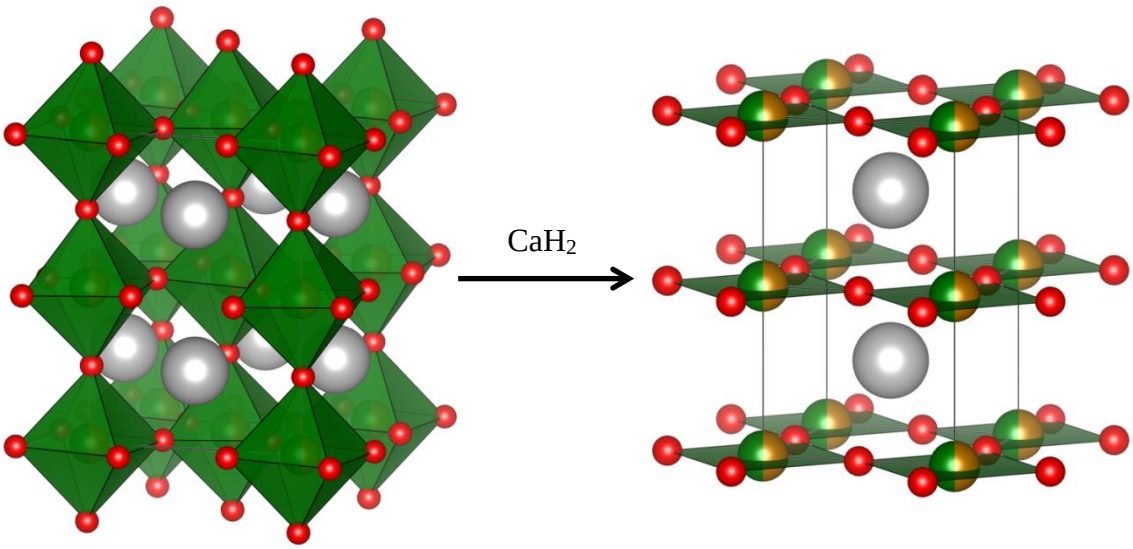

$SrFe_{0.5}Ru_{0.5}O_3$ **$SrFe_{0.5}Ru_{0.5}O_2$**

Figure 1.7: The topochemical reduction of $SrFe_{0.5}Ru_{0.5}O_3$ to $SrFe_{0.5}Ru_{0.5}O_2$

To make the most of the opportunities presented by topochemical reduction it is important to understand how the cation and anion lattices interact. Specifically, it has been shown when the anion and cation lattices interact strongly the cation lattice cam exert control over the reduction behaviour of a parent oxide. For example, the

isostructural and isoelectronic phases $LaBaCo_2O_5$ and $YBaCo_2O_5$ can both be reduced by reaction with NaH but the products of these reductions are quite different and are shown below in Figure 1.8[48]. The markedly different products that arise from these reductions highlight that the A-cation lattice is able to influence the structure of a reduced metastable phase by preferentially directing the removal of certain anions.

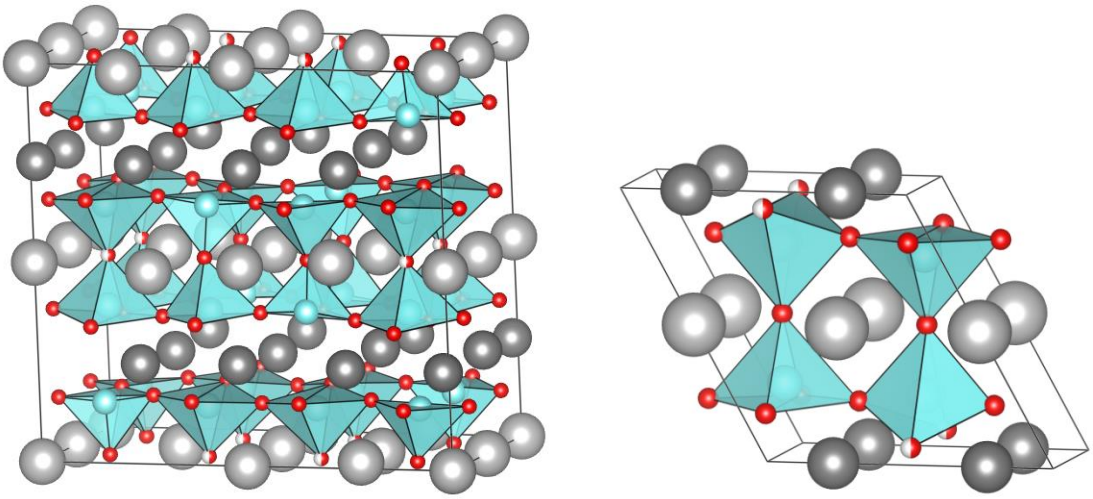

$LaBaCo_2O_{4.25}$ **$YBaCo_2O_{4.5}$**

Figure 1.8: The structures of the topochemically reduced phases $LaBaCo_2O_{4.25}$ and $YBaCo_2O_{4.5}$

Similarly, the B-cation lattice can exert control over the anion selectivity of reduction reactions. This is most clearly demonstrated by the reductions of the n = 2 Ruddlesden-Popper phases $Sr_3Mn_2O_{7-\delta}$ and $Sr_3Fe_2O_{7-\delta}$. The reactions of these compounds are shown in Figure 1.9. During the reduction of $Sr_3Fe_2O_{7-\delta}$ to $Sr_3Fe_2O_{6+\delta}$ the bridging, apical oxides ions are removed[51]. In contrast the reduction of $Sr_3Mn_2O_{7-\delta}$ to $Sr_3Mn_2O_{6+\delta}$[52] results in the removal of oxide ions from the equatorial plane.

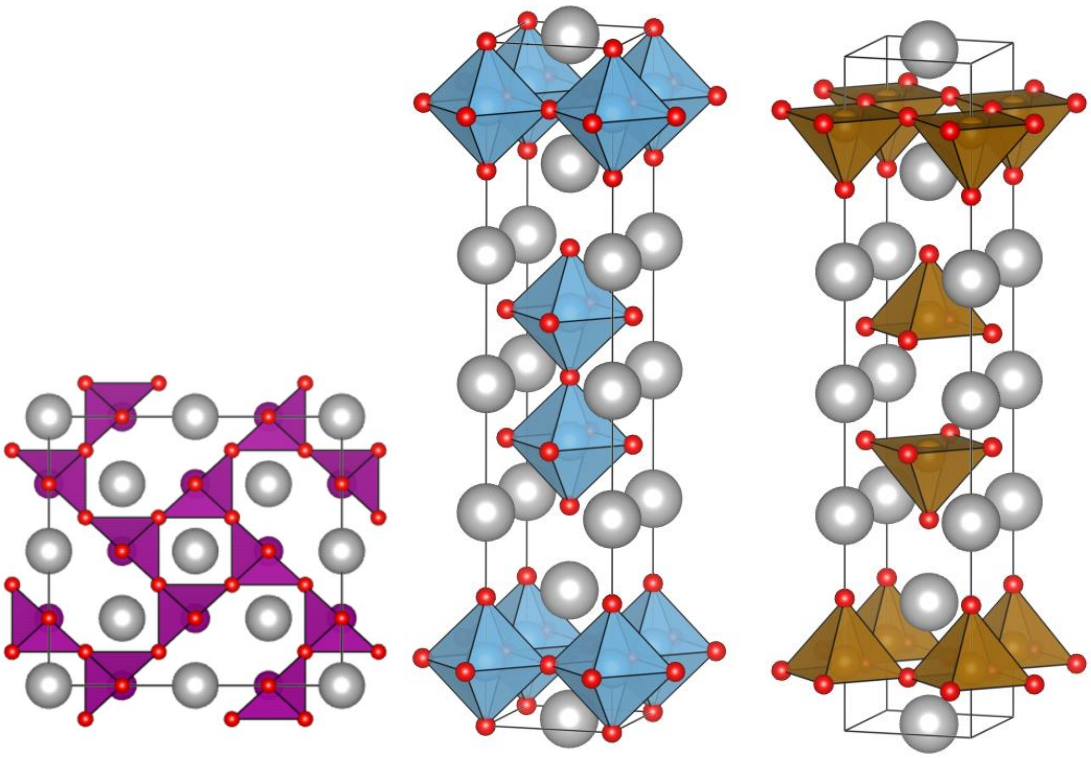

Figure 1.9: The structures of $Sr_3M_2O_7$ (M = Mn, Fe) and their topochemically reduced analogues.

Finally it is possible to take a more direct approach. The presence of heteroanions can be used to direct the removal of certain oxide ions by exploiting differences in ion mobility. This technique is exemplified by comparison of the reductions of $Sr_3FeO_{7-\delta}$ and $Sr_3FeO_5Cl_2$. $Sr_3FeO_{7-\delta}$ can be reduced to Sr_3FeO_5 (via $Sr_3FeO_{6+\delta}$) which has a structure that can be regarded as layers of double chains of square-planar FeO_4 units[53]. In contrast reduction of the oxychloride $Sr_3Fe_2O_5Cl_2$ results in the formation of $Sr_3Fe_2O_4Cl_2$ which is a phase that contains double infinite layers of square-planar FeO_4 units[54] (Figure 1.10).

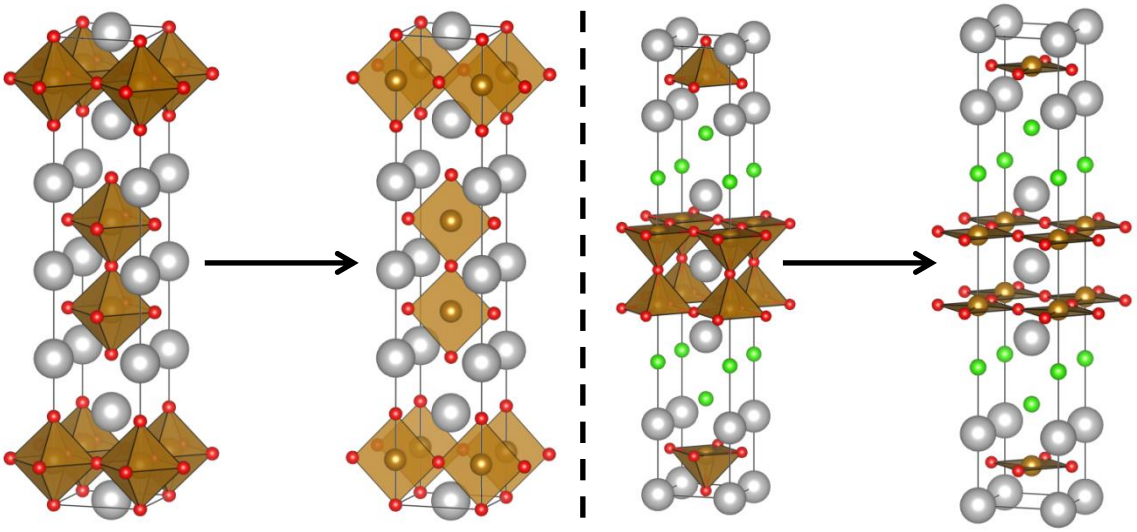

Figure 1.10: The structure of iron-based *n*=2 Ruddlesden-Popper phases and their topochemically reduced analogues

1.5.2.1 Oxyhydride phases

The examples of topochemically reduced oxides discussed in Section 1.5.2 all have oxide anion vacancy ordered structures. This is not always the result of topochemical reduction. Topochemical reduction using group I/II hydrides can result in the formation of oxyhydride phases via anion exchange. Oxyhydride phases are rare and of great interest to the condensed matter research community. In molecular compounds hydride ligands have been observed to be a strong sigma donor and the exchange interactions with transition metal cations lead to unconventional magnetic and electronic behaviours[55]. Notable examples of oxyhydride phases include $ATiO_{3-x}H_x$ (A= Ca, Sr, Ba)[56], $SrCrO_2H$[57], $LaSrCoO_3H_{0.7}$[58], $SrVO_2H$[55] and $LaSr_3NiRuO_4H_4$[59] (Figure 1.11). Oxyhydride phases are a diverse group of compounds that have been shown to exhibit both stoichiometric and non-stoichiometric anion exchange, and both anion order and disorder.

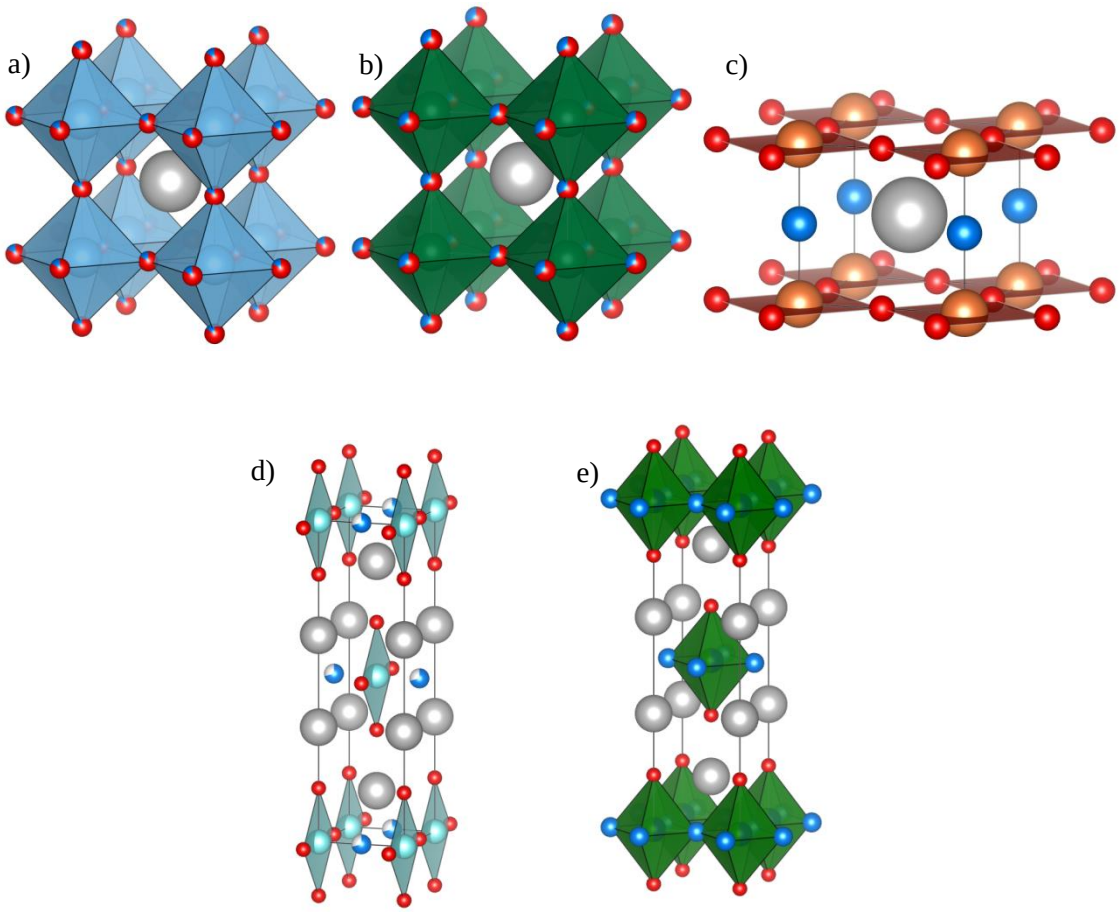

Figure 1.11: The structures of some oxyhydride phases: a) $BaTiO_{2.51}H_{0.49}$ b) $SrCrO_2H$ c) $SrVO_2H$ d) $LaSrCoO_3H_{0.7}$ and e) $LaSr_3NiRuO_4H_4$

1.5.2.2 Electronic properties of reduced oxides

The reduced phases that have been produced by reduction are electronic insulators. This is for two reasons that are consistent with the Hubbard Model discussed in Section 1.2.2. Firstly, upon reduction the ionic radii of the reduced cations increase. To accommodate these changes, and since the cations cannot move, the structure distorts by twisting M-O bonds, lowering the tolerance factor (Section 1.4.1). This reduces orbital overlap and acts to decrease the bandwidth, *W*. Secondly, as electrons are added, the on-site repulsion, *U*, increases. This is due to greater electron-electron repulsion. The combination of these two factors tends to lead to separated bands and insulating behaviour as illustrated by Figure 1.2 in Section 1.2.2. Beyond the considerations of the Hubbard Model, anion vacancies

can pin charge by two mechanisms. The partial positive charge that resides in the compound as result of the extraction of an anion can trap electrons, and the existence of different co-ordination environments can split the charge in the system due to the structural preferences of cations with certain oxidation states. These factors can be seen to be at play in $CaMnO_3$ and its related-perovskites. The reduced phases $CaMnO_{3-x}$ ($0 \leq x \leq 0.5$) are electronic insulators[2, 60] however their isoelectronic analogues with the general formula $Ca_{1-y}La_yMnO_3$ ($0.17 \leq y \leq 0.25$) are metallic[61].

As discussed in Section 1.2.2, materials with the most interesting electronic properties tend to sit in the $U \approx W$ region. The reduced complex oxides that solely contain 3*d* cations clearly do not sit in this energy regime. One way to move closer to the $U \approx W$ region is to investigate complex oxides that contain 4*d* or 5*d* cations. The higher energy, more radially extended 4*d* and 5*d* orbitals will have lower values of *U* and wider bands i.e. higher *W*. These differences are clearly manifest in the electronic properties of $SrFeO_3$, Sr_2CoO_4, $SrRuO_3$ and Sr_2RhO_4. $SrFeO_3$[62] and Sr_2CoO_4[63] are strong electrical insulators whereas their 4*d* counterparts, $SrRuO_3$[64] and Sr_2RhO_4[65], are conductors. Structure plays an important role in determining electronic and magnetic properties, as previously discussed, and it has been shown deviations from "ideal" structure has a significant effect on the electronic properties of 4*d* and 5*d* containing oxides (Figure 1.12). Sr_2RuO_4 is the only reported *p*-type superconductor and has a highly symmetric tetragonal structure in which the Ru-O-Ru bond angle is 180 ^{o} [66-67]. However, Ca_2RuO_4 is an insulator despite being isoelectronic with Sr_2RuO_4. This difference in conduction behaviour arises because the Ca_2RuO_4 structure is distorted due to tilting of the RuO_6 octahedra[68]. This means the Ru-O-Ru bonds are not 180 ^{o} and orbital overlap is worse. Similarly Sr_2IrO_4 has a distorted structure and is an insulator however in this case spin-orbit coupling plays a significant role in determining the electronic properties of Sr_2IrO_4[20, 66, 69] (See Section

1.3). Addition of ruthenium changes this regime and $Sr_2Ru_xIr_{1-x}O_4$ undergoes a metal insulator transition at x = 0.7[70].

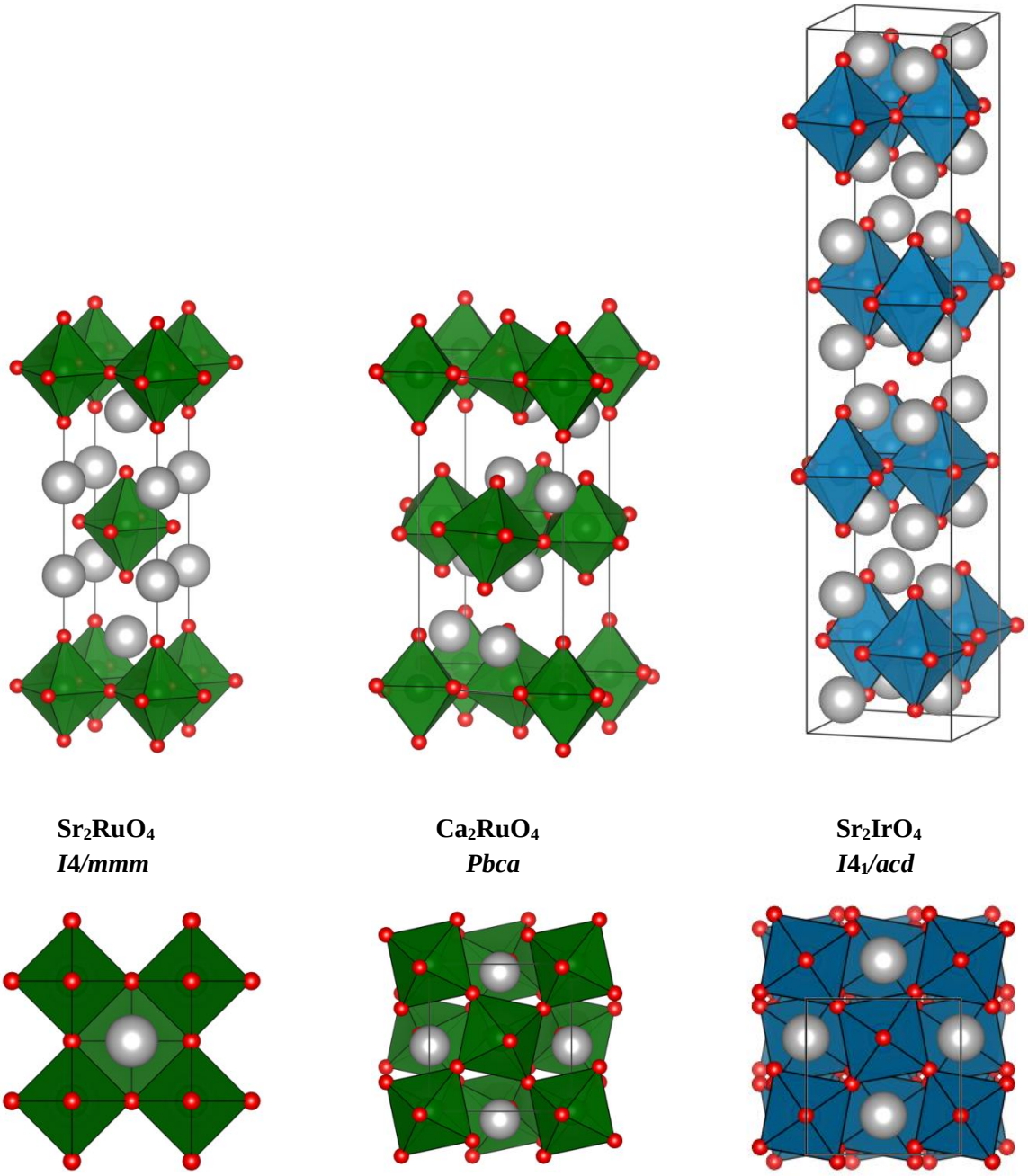

Figure 1.12: The structures of Sr_2RuO_4, Ca_2RuO_4, Sr_2IrO_4 and their structures as observed down the crystallographic *c*-axis

The variety of electronic properties exhibited by parent oxides that contain 4*d* and 5*d* cations make their potential topochemical reduction an intriguing prospect, raising the possibility of isolating compounds with highly unusual properties.

Chapter 2 - Experimental Methods and Techniques

2.1 Synthesis methods

2.1.1 Ceramic method

Conventionally crystalline solid materials are synthesised by grinding together precursor reagents, pressing them into a dense pellet and heating the pellet at the desired temperature. This is an effective method that has been used to make countless crystalline solids however it is very slow. The homogeneity of the reaction mixture is defined by the size of the grains in the mixture which are usually multiple microns in diameter. This means ions have to move over relatively large distances to reach a boundary at which reaction can occur. Furthermore, diffusion of ions in the solid state is very difficult due to low mobility. Consequently very high reaction temperatures are required to overcome the high energy barriers to diffusion and even then ions move slowly. The combination of these factors means that in order for reaction to take place at reactive grain boundaries ions must move slowly over relatively large distances. To overcome these limitations and improve the speed of reaction multiple grinding and heating cycles are required to mix the reagents and expose new boundaries where reaction can take place. Even after this additional processing reactions often take weeks to reach completion when this method is used.

2.1.2 Citrate Method

The citrate method is an alternative to ceramic synthesis. In solution, cations are co-ordinated by the tridentate citric acid ligand which, on addition of ethylene glycol and heating, undergoes an esterification reaction to form an extended organic polymer framework. The citrate method was used to make parent oxides as it has many advantages

over the traditional ceramic method described above. The polymer formed in the citrate method results in metal centres being separated by distances comparable to those of the product's unit cell. This high homogeneity means that reaction time required to form pure phases is drastically reduced. Powders that do not dissolve in nitric acid are well dispersed throughout the mixture and thus the homogeneity of the reaction mixture remains high.

Starting materials were dried as necessary and accurately weighed out to give the desired metal stoichiometry. They were then dissolved in a 1:1 mixture of deionised water and concentrated HNO_3. An amount of citric acid sufficient to balance the metal charges was then added. This solution was heated to 250 ^oC whilst being stirred and an excess of ethylene glycol was added drop wise. Continued heating resulted in the decomposition of the nitric acid, releasing NO_x and water vapour, and the formation a solid organic polymer framework. This solid was heated until combustion of the polymer occurred. The resulting powder was dried at 400 ^oC for 1 hour, then ground in an agate pestle and mortar, before being slowly heated at 1000 ^oC (1 ^oC min^{-1}) for 12 hours to remove any remaining organic compounds. The product was ground, pressed into a 13 mm pellet using a force of 5 tonnes and heated to the required reaction temperature. The heating grinding process was repeated until the reaction reached completion.

2.2 Handling Air Sensitive Compounds and Reactions

Oxygen deficient phases slowly react with oxygen resulting in the reoxidation of metastable phases to their parent oxide. Furthermore, the group I/II hydrides and zirconium metal readily react with oxygen and water in the air to produce their respective oxides or hydroxides. Therefore, reactions using these compounds must be carried out and analysed using techniques that exclude air and water.

2.2.1 Glove Box

Reduction reactions were prepared under an inert atmosphere in an argon filled glove box. The partial pressures of oxygen and water are typically kept below 5 ppm within the box by constantly circulating the internal atmosphere over a copper catalyst.

2.2.2 Air Sensitive Powder X-ray Diffraction

Powder X-ray diffraction patterns of reactions were collected by using air sensitive X-ray holders (Figure 2.1). A glass slide was covered in a thin layer of Dow-Corning high vacuum grease and, under an inert atmosphere, a small amount of powder was evenly distributed onto the slide. The slide was then sealed in the air sensitive X-ray holder by screwing on a brass cap which compresses a rubber O-ring to form an air tight seal.

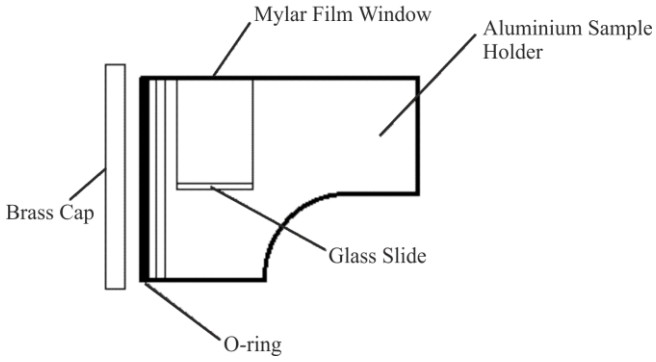

Figure 2.1: Air sensitive X-Ray Holder

2.3 Hydride Reductions

The topochemical reduction of the iridium oxides to form metastable phases was attempted by reaction with CaH_2 or NaH. The reaction schemes are as follows:

$$\mathbf{A_2BIrO_6 + xCaH_2 \rightarrow A_2BIrO_{6-x} + xCaO + xH_2}$$

$$\mathbf{A_2BIrO_6 + xNaH \rightarrow A_2BIrO_{6-x} + xNaOH}$$

All reactions were prepared and analysed as described in Section 2.2. Reactions were carried out in either sealed glass ampules or in a “venting system”.

2.3.1 Sealed Glass Ampules

Sealed glass ampules were used for reactions with NaH, as no hydrogen is produced during this reaction. The hygroscopic iridium oxides were dried at 400 ^{o}C for a minimum of 2 hours. Under an inert atmosphere, the oxide was mixed with the appropriate quantity of hydride and ground in an agate pestle and mortar. The reaction mixture was then transferred into a 9 mm Pyrex tube and sealed with a Young's tap. The tube was then evacuated and sealed under vacuum using a blow torch to form an ampule. The ampule was placed in a low temperature furnace and heated using a slow ramp rate (rr $\leq$ 2 ^{o}C min^{-1}) to exert maximum control over the temperature profile. After heating for 2 days the ampule was removed, scored with a glass cutting knife and pumped into a glove box where it was opened for analysis of the contents.

2.3.2 "Venting System"

"Venting systems" (Figure 2.2) were set up such that a steady stream of argon flowed over the reaction. This allows large volumes of hydrogen evolved during reactions to be safely removed. This system was employed for reactions using LiH and CaH_2 to ensure that hydrogen pressure did not exceed safe levels. Samples were prepared as described in Section 2.4.1 and placed in a 9 mm, 12 mm or 19 mm Pyrex tube (depending upon sample size). However instead of sealing the tube the Young's tap was then connected to an argon flow. After purging, the system was heated in a low temperature furnace using a slow ramp rate (rr $\leq$ 2 ^{o}C min^{-1}).

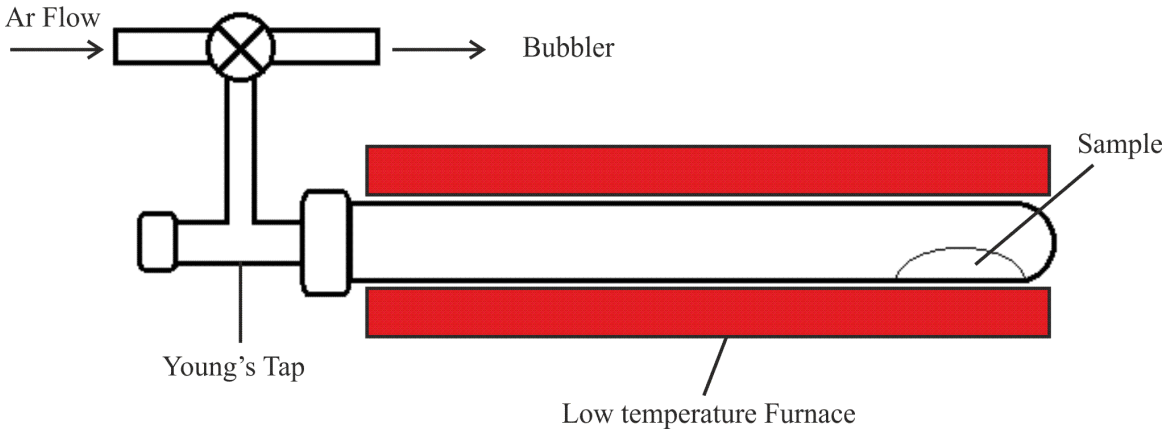

Figure 2.2: Venting System Set Up

2.4 Washing reaction mixtures

Upon completion it was necessary to remove any leftover hydride and by-products from the reaction mixtures. This was done by washing the sample under nitrogen using standard Schlenk techniques. These phases were removed by washing the reactions with an acidic methanol. The standard solution used was 0.1 M NH_4H however concentrations as high as 0.5 M were used for some experiments. Other experiments used solutions of HCl, acetic acid, citric acid, glycerol or ethylene glycol. They were then washed again with pure methanol. The removal of all by-product phases was confirmed by powder X-ray diffraction.

2.5 Reactions under flowing H_2

In addition to solid-solid reactions, reductions of iridium-containing oxide phases were attempted by heating samples under flowing 5%/95% H_2/N_2. Two reaction set-ups were used to conduct these reactions: a "horizontal" set-up and a "vertical" set-up both of which are shown in Figure 2.3.

In the "horizontal" set-up samples were prepared in an alumina boat crucible and sealed in a quartz tube with end caps attached to T-junction taps. This tube was placed in a

clamshell furnace and the gas flow apparatus attached to the T-junction taps. The gas was allowed to flow over the sample while it was heated to the desired temperature at a ramp rate that did not exceed 3 ^{o}C min^{-1}. Once the heating cycle was completed the tube was sealed, removed from the furnace, evacuated and placed in an argon filled glove box.

In the "vertical" set-up samples were loaded into a quartz tube that was fitted with a fritted disk. This tube was placed in a vertical low temperature furnace such that the sample was on top of the disk. The tube was sealed with T-junction taps which were connected to the gas flow apparatus. The gas was allowed to flow through the sample while it was heated to the desired temperature at a ramp rate that did not exceed 1 ^{o}C min^{-1}. Once the heating cycle was completed the tube was sealed, removed from the furnace, evacuated and placed in an argon filled glove box.

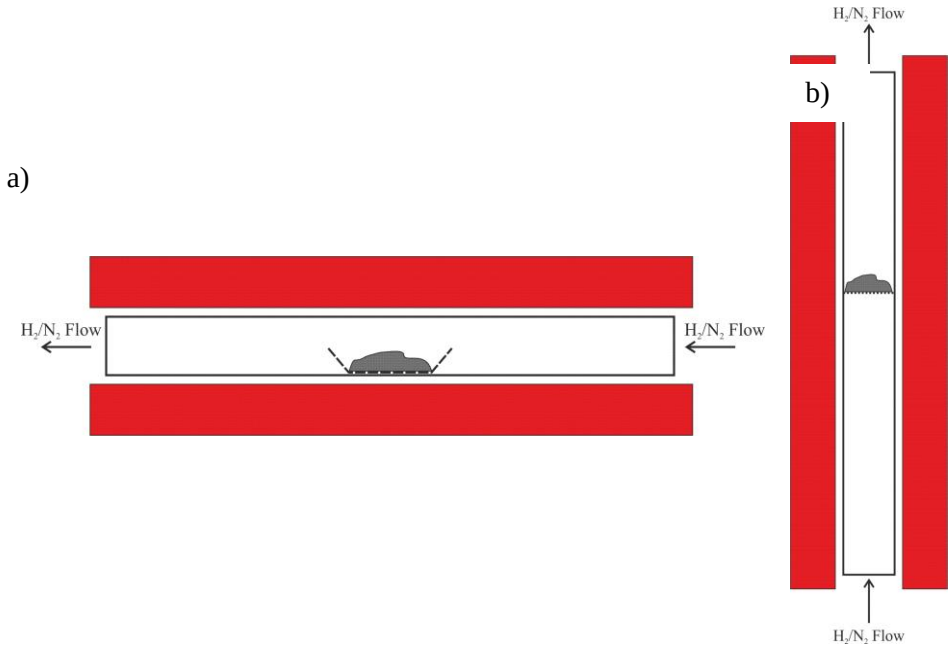

Figure 2.3: a) "Horizontal" set-up for the hydrogen gas reduction reaction b) "Vertical set-up for the hydrogen gas reduction reaction

2.6 Getter reactions

The final reaction method used to reduce iridium-containing oxides was the getter method. The getter method works by using a reactive getter reagent that siphons off and reacts with the oxygen partial pressure that forms at the surface of an oxide when it is heated. In this work we used zirconium metal and sodium hydride as getter reagents. Inside an argon filled glove box the getter reagent was weighed and placed in the bottom of a Pyrex or quartz tube that had a small indent between 0.5 – 1 cm from the base of the tube. The sample was placed in a quartz thimble which was in turn loaded into the indented glass tube. This ensured the sample and getter reagent never came into contact. The glass tube was sealed with a Young's tap and the removed from the argon filled glovebox. The tube was then evacuated and sealed under vacuum to form an ampule (Figure 2.4). The reaction vessels were placed in low temperature furnaces and heated to the desired temperature at a ramp rate no greater than 3 ^{o}C min^{-1}. After heating for 7 days the ampule was removed, scored with a glass cutting knife and pumped into a glove box for analysis of the contents.

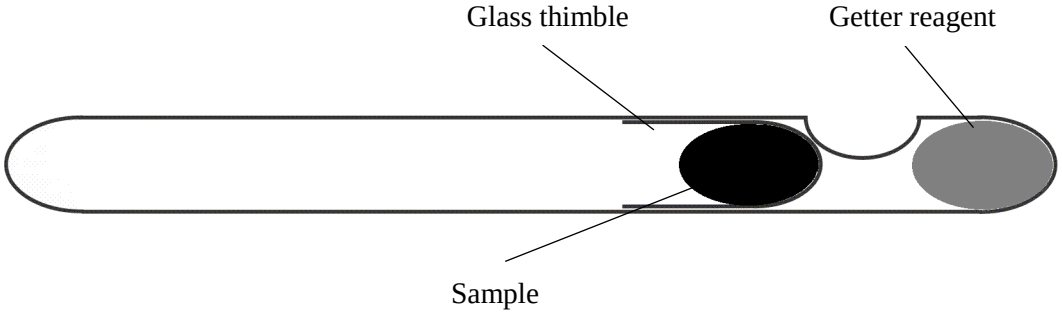

Figure 2.4: Getter reaction vessel

For some reactions it was necessary to heat the getter reagent and parent oxide at different temperatures. In this case the reaction vessel was set up in a similar way except the ampule was around 40 cm in length and the indent was around 35 cm away from the getter reagent. This meant that the parent oxide and getter reagent could be heated in separate low temperature furnaces.

2.7 Powder diffraction

Powder diffraction techniques are ubiquitous in the field of solid state chemistry. Both X-ray and neutron powder diffraction methods were essential for the structural characterisation of materials.

Diffraction of X-ray and neutron radiation in crystalline solids occurs due to the periodic arrangement of atoms within a crystal. This periodic arrangement results in a regular array of lattice planes. These planes act as a diffraction grating and can diffract radiation when the incident radiation has a wavelength comparable to the plane separation, for example X-ray or neutron radiation. This is Bragg's model of diffraction (Figure 2.5) and is described by Braggs' Law:

$$n\lambda = 2d_{hkl}\sin\theta \qquad 2.1$$

where n is an integer, λ is the wavelength of the incident radiation, d_{hkl} is the interplanar distance, and θ is the angle of incidence.

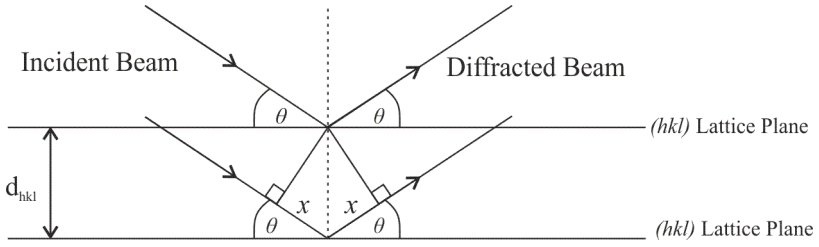

Figure 2.5 Cartoon depiction of Braggs's Model of diffraction

The *d*-spacing (d_{hkl}) of a reflection is defined by the unit cell dimensions. The intensity of the reflection (I_{hkl}) is given by the following relationship:

$$I_{hkl} \propto LmA|F_{hkl}| \qquad 2.2$$

where L is the sample-independent Lorentz-polarisation factor, m is the multiplicity, A is the absorption factor and F_{hkl} is the structure factor.

The structure factor is an expression that governs how the arrangement of atoms in the unit cell affects the intensity of a reflection.

2.7.1 X-ray Powder diffraction

Monochromatic X-ray radiation sources are readily available, thus powder X-ray diffraction is frequently used in solid state synthesis. It a valuable and versatile technique as it can be used to determine the structure of materials and monitor the progress of reactions. X-ray radiation interacts with and is diffracted by the electron density of the atoms in the material, thus the intensity of peaks observed in X-ray powder diffraction patterns is proportional to the atomic number of the atoms in the sample.

$$\boldsymbol{F_{hkl} = \sum_n f_n \exp[2\pi i(hx_n + ky_n + lz_n)] \exp\left[\frac{-8\pi^2 U_{iso_n} \sin^2 \theta_{hkl}}{\lambda^2}\right]} \qquad \mathbf{2.3}$$

where f_n is the scattering factor, x_n, y_n and z_n are the fraction co-ordinates of the nth atom in the unit cell and U_{iso} is the isotropic thermal factor

The exponential term determines the reduction in the intensity as a function of scattering angle

2.7.1.1 Panalytical Empyrean and Panalytical X'Pert diffractometers

The Panalytical Empyrean and the Panalytical X'Pert diffractometers generate monochromatic Cu K $_{\alpha 1}$ radiation and use a Bragg-Brentano focusing geometry. The Panalytical Empyrean instrument was used to track the progress of reactions and program parameters were varied to fit differing scan times. The Panalytical X'Pert diffractometer was used to collect high quality diffraction patterns. The Panalytical X'Pert diffractometer is fitted with an angle sensitive detector which works at a range $\pm$ 1.5 ^{o} from θ. This gives it an improved signal to noise ratio compared to the Empyrean diffractometer and thus gives high quality diffraction patterns which can be used for Rietveld Refinement (Section 2.9). For both instruments' samples were prepared as

follows. Air sensitive samples were assembled as described in Section 2.3.2. Non-air sensitive samples were sprinkled on a silicon wafer which was covered in a thin layer of Dow-Corning high vacuum grease. The silicon wafer is cleaved along the (110) plane which is a systematically absent diffraction peak and consequently does not appear in the diffraction pattern. The wafer was mounted onto a spinning stage which rotates whilst the measurement is being taken to minimise the effects of uneven sample distribution.

2.7.1.2 Synchrotron powder X-ray diffraction

The acceleration of electrons close to the speed of light results in the generation of electromagnetic radiation. This is called synchrotron radiation and the X-rays extracted from this radiation have a range of frequencies which can be used to collect high quality powder diffraction data.

The synchrotron X-ray powder diffraction data presented in this thesis were collected on the I11 beamline at the Diamond Light Source Facility in Didcot, Oxfordshire. I11 is a high resolution powder diffraction beamline equipped with a source that produces X-rays with energies from 5 to 30 keV[71]. The energy of the incident diffraction beam is selected using a double-crystal-monochromator (DCM) which is made up of two liquid nitrogen cooled Si(111) crystals. Samples are loaded and sealed in glass capillaries that are secured in brass holders with a magnetic base. These holders are mounted onto a magnetic spinner that is pre-aligned with the diffractometer's centre. Data were collected using the Position Sensitive Detector (PSD). This detector uses MYTHEN-II silicon microchip technology. This provides for the collection of wide-angle powder diffraction data that has a very high resolution. The X-ray powder diffraction data collected form I11 was analysed using Rietveld refinement techniques (Section 2.9)

2.7.2 Neutron powder diffraction

Neutron radiation interacts with the nuclei of atoms and magnetic moments resulting in a diffraction pattern which can be used to determine the structure of a crystalline material. Neutron diffraction has several features that allow more information pertaining to the properties of a material to be extracted compared to X-ray diffraction. Firstly, the neutron scattering lengths of elements do not follow a linear relationship with atomic number. Therefore light elements can be located while in the presence of heavier elements. Secondly, the neutron scattering form factor is independent of the scattering angle, unlike the X-ray scattering form factor. This means the diffraction peaks at high angle collected using neutron diffraction do not lose intensity and can be more reliably used to extract structural information. Finally, neutrons are half-integer spin particles and as such they are scattered by a lattice of ordered unpaired electrons. This scattering allows for the determination of the magnetic structure of materials that exhibit magnetic order.

The magnetic scattering factor of an unpolarised neutron source can be described as follows:

$$\mathbf{F}_{hkl,mag} = \sum_j q_j p_j e^{2\pi i h x_j} \qquad \textbf{2.4}$$

Where q_j is the magnetic interaction vector, p_j is the magnetic scattering length, h is the magnetic scattering vector and x_j is the position vector of the magnetic atom in the unit cell.

The observed intensity of a magnetic reflection is proportional to the square of the projection of the magnetic structure factor onto the scattering vector and can be expressed as follows:

$$I_{hkl,mag} = \left|F_{hkl,mag}\right|^2 cos^2\alpha \qquad \textbf{2.5}$$

Where α is the angle between the lattice plane and the magnetic spin vector

For each measurement samples were loaded into vanadium cans which were sealed with indium washers and screws. Vanadium has a very low coherent scattering length of -0.3828 fm[72] thus using it to contain samples minimises scattering contributions from the holder.

The neutron diffraction data presented in this thesis were collected from two instruments: the WISH beamline at the ISIS Neutron and Muon Source in Didcot, Oxfordshire, and the D2B instrument at the Institut Laue-Laugevin (ILL) in Grenoble, France.

2.7.2.1 WISH

The ISIS Neutron and Muon source uses a neutron spallation source to generate neutron radiation[73]. Pulses of protons are accelerated in a synchrotron until they reach 800 MeV after which they are fired at a tantalum target. This triggers an intranuclear cascade that produces a pulse of neutrons. The neutrons in these pulses have very high thermal energies and are slowed using a hydrogenous moderator before they reach the instrument so that the neutrons have a suitable wavelength for diffraction. The hydrogenous moderator used in the WISH instrument is solid methane. This neutron production method generates radiation pulses that are suitable for time-of-flight diffraction measurements.

The detector banks used in time-of-flight diffractometers are fixed-angle detectors to measure diffraction patterns as a function of wavelength. The wavelength is related to the velocity of the neutrons by using the de Broglie relationship:

$$\boldsymbol{\lambda = \frac{h}{m} \times \frac{t}{L}} \qquad \textbf{2.6}$$

Where h is Planck's constant, m is the neutron mass and t is the time taken to travel distance L from the moderator to the detector via the sample

WISH is a very high-intensity, high flux, low resolution powder diffractometer that has four banks of detectors that have a combined *d*-spacing range of 0.7 - 50 Å.

2.7.2.2 D2B

The neutron beam at the ILL is generated from a ^{235}U fission reactor. This reactor produces neutrons that have very high energies. In order to sustain the fission process a D_2O moderator is used to lower the energy of the neutrons produced. After moderation the neutrons are suitable to be used in diffraction experiments. At each instrument crystal monochromators are used to further discriminate for neutrons with the required wavelength.

The D2B instrument is a high-resolution, two-axis diffractometer with a monochromator that has a high take-off angle (135 ^{o})[1]. The wavelength on the incident neutron beam can be altered by rotation within the *hhl* plane of a germanium crystal monochromator. For each diffraction experiment multiple scans, performed over the range $5 \leq 2\theta / ^{o} \leq 160$, were summed to give a diffraction pattern with a good signal-to-noise ratio. This was done to ensure refinement of the data resulted in a good fit with statistically significant results. The instrument set-up of D2B is shown in Figure 2.6.

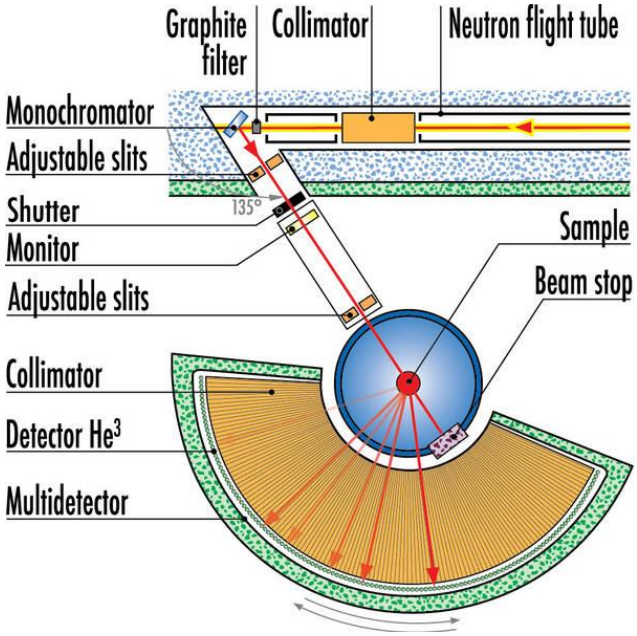

Figure 2.6: D2B instrument at the Insitut Laue-Laugevin[1]

2.8 Rietveld refinement

Miller planes which have the same or similar d-spacing but different (hkl) values will have reflections observed at the same angle of 2θ, all of which contribute intensity to a single peak. This is a consequence of powder X-ray diffraction only giving us a one-dimensional view of a three-dimensional structure and results in the loss of some information. Rietveld refinement[74] overcomes this by using the intensity of peaks at a given point and compares it to an intensity calculated from a proposed structural model. This method of refinement also enables overlapping peaks to be separated. The difference between the experimental data and the model is minimised using a least squares process:

$$\mathbf{S = \sum w_i\{y_i(obs) - y_i(calc)\}^2} \qquad \mathbf{2.7}$$

Where S is the difference between the experimental and calculated intensities, w_i is the weighting factor, y_i(obs) is the observed intensity of step i and y_i(calc) is the calculated intensity of step i.

Rietveld refinement was conducted using the General Structure Analysis System (GSAS) program. The fit of the model was assessed using the following parameters: the profile factor, $\mathbf{R_P}$, the weighted profiles factor, $\mathbf{wR_p}$, and the goodness of fit, χ^2. These parameters are defined by the following equations:

$$\mathbf{R_p} = \frac{\sum|\mathbf{y_i(obs)} - \mathbf{y_i(calc)}|}{\sum \mathbf{y_i(obs)}} \qquad \mathbf{2.8}$$

$$\mathbf{wR_P} = \left\{\frac{\sum \mathbf{w_i(y_i(obs) - y_i(calc))^2}}{\sum \mathbf{w_i(y_i(obs))^2}}\right\}^{\frac{1}{2}} = \left\{\frac{\mathbf{S}}{\sum \mathbf{w_i(y_i(obs))^2}}\right\}^{\frac{1}{2}} \qquad \mathbf{2.9}$$

$$\boldsymbol{\chi^2} = \frac{\sum \mathbf{w_i(y_i(obs) - y_i(calc))^2}}{\mathbf{N - V + C}} = \frac{\mathbf{S}}{\mathbf{N - V + C}} \qquad \mathbf{2.10}$$

From these refinements we obtained structural information including lattice parameters, atomic positions, site occupancy and peak profiles

2.9 Thermogravimetric analysis (TGA)

Thermogravimetric analysis was used to confirm the composition of parent oxides and reduced phases. A Mettler Toledo TGA/DSC 1 STARe system was used to perform the measurements. A small mass of sample (10 – 50 mg) was accurately weighed into an alumina crucible and loaded onto the instrument. The sample was then heated under a flow of either 5%/95% H_2/N_2 or O_2 and the mass change measured as a function of temperature. After the measurement was complete a powder X-ray diffraction pattern of the product was taken to confirm the reaction had reached completion. 5%/95% H_2/N_2 was used for reductive TGA measurements which confirmed the composition of starting materials. An O_2 flow was employed for oxidative TGA measurements which were used to determine the oxygen content of reduced phases.

2.10 SQUID magnetometry

The magnetic properties of samples were measured using a Quantum Design MPMS XL Superconducting Quantum Interference Device (SQUID) magnetometer. SQUIDs are able to measure the magnetisation of samples as they can detect very small changes in magnetic field by making use of the Josephson Effect[75]. In the SQUID there are superconducting rings which are separated by a thin layer of insulating material, these are called Josephson Junctions. Cooper pairs are able to tunnel through these junctions and in the absence of a magnetic field their phase coherence is maintained. When a magnetic field is applied inside the ring a current is induced in the coil in order to produce a magnetic field which opposes the applied field. The Josephson Junctions have a critical field, $\mathbf{I_c}$, over which cooper pairs can no longer tunnel through the junctions and superconductivity in the coil is lost. The voltage which arises from the induced current is proportional to the magnetic moment of the sample placed in the coil and can be measured by the SQUID.

To conduct the measurement a small mass of sample (15 – 50 mg) was loaded into a gelatine capsule. This was placed in a plastic straw with 4 more capsules above and below the sample. The end capsules and the bottom of the straw were wrapped in diamagnetic tape to ensure the container didn't fall apart. The straw was pierced with a needle multiple times so it could be evacuated. This was then taped to the end of a long rod and loaded into the SQUID. Zero-field-cooled (ZFC) and field-cooled (FC) measurements were collected using a magnetic field of 100 Oe over a temperature range of $5 \leq T / K \leq 300$. Experiments to measure magnetisation as a function of field were also conducted at various temperatures over the field range $-5 \leq H / T \leq 5$.

2.10.1 Ferrosubtraction measurements

Samples that contained ferromagnetic impurities could not be measured using the ZFC-FC method as the ferromagnetic response concealed the sample bulk response.

Application of a large magnetic field will saturate the ferromagnetic susceptibility allowing the paramagnetic susceptibility to be measured. Field-cooled isotherms were collected every 5 K over the range $10 \leq T/K \leq 300$ and at each temperature the magnetisation was measured every 0.5 T over the range $3 \leq H/T \leq 5$. For each temperature the magnetisation was plotted as a function of the field. The resultant plot gives a straight line for which the gradient is the paramagnetic susceptibility and the intercept is the saturated ferromagnetic magnetic moment of the sample. Comparison of the paramagnetic values allowed us to obtain a field-cooled plot which shows the temperature dependence of the samples magnetisation. A graphic representation of the principles of ferrosubtraction measurements is shown in Figure 2.7.

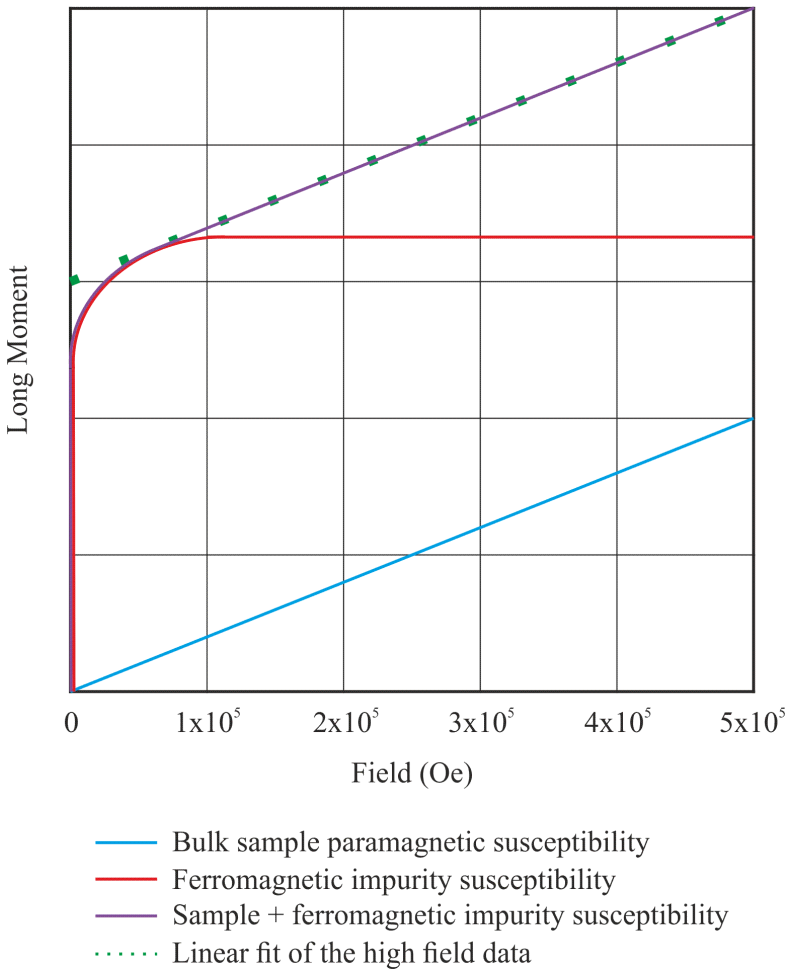

Figure 2.7: A magnetisation-field isotherm indicating the susceptibility of a bulk paramagnetic phase and a ferromagnetic impurity phase.

2.11 Magnetism

2.11.1 The Curie-Weiss law

In the presence of a magnetic field the electrons in a paramagnetic material align with the field. The extent to which the spin electrons align is related to the paramagnetic susceptibility. The relationship between the temperature of the material and the paramagnetic susceptibility is described by the Curie Law:

$$\chi = \frac{C}{T} \qquad 2.11$$

where χ is the paramagnetic susceptibility, C is the Curie constant and T is the temperature.

The Curie law assumes materials are magnetically dilute and electron spins do not interact. This is not the case in materials which exhibit correlated magnetic behaviour Section 2.13.2). The magnetic behaviour of such materials is more accurately described by a corrected version of the Curie law called the Curie-Weiss law:

$$\chi = \frac{C}{T-\theta} \qquad 2.12$$

where θ is the Weiss constant, K is a constant to account for any temperature independent magnetic behaviour and all other symbols are the same as in the Curie law. This can be extended to include a temperature independent term, K

The Curie constant is related to the spin-only magnetic moment of the sample:

$$C = \frac{N_A \mu_B{}^2 \mu^2}{3k_B} \cong \frac{\mu^2}{8} \qquad 2.13$$

$$\mu = g\sqrt{S\,(S+1)} \qquad 2.14$$

where N_A is Avogadro's constant, μ_B is the Bohr magneton, k_B is the Boltzmann constant, μ is the magnetic moment, g is the gyromagnetic ratio and s is the sum of the spin quantum numbers of the electrons in the system.

Using the Curie constant and the spin only formula we can to estimate the number of electrons of the transition metal centres in the sample, and in turn the possible oxidation states.

2.11.2 Correlated magnetic behaviour and magnetic ordering

Some materials show behaviours in which there are strong interactions between electron spins. This is called correlated magnetic behaviour and leads to different types of magnetic ordering.

Ferromagnetism arises when the localised magnetic moments align parallel to each other and results in a net magnetic moment being observed. Antiferromagnetism occurs when localised magnetic moments align antiparallel to each other. This alignment results in no net magnetisation as all spins cancel. If the angle between spin states is not 180° there is a small spontaneous moment, this is known as canted-antiferromagnetism. Ferrimagnetism is where localised magnetic moments of unequal magnitude align antiparallel to each other, this results in a magnet moment, but it is much smaller than in ferromagnetically ordered materials.

2.12 Superexchange and the Goodenough-Kanamori rules

In transition metal oxides the distance between metal centres is too far for direct orbital interaction. However, the oxide ions act as bridges to mediate the magnetic coupling of spins by superexchange. The strength of the superexchange interaction is dependent on the bond angle, principal quantum number of the metal d-orbital and length of the metal oxygen bond.

The Goodenough-Kanamori rules are a semi-empirical set of rules that can be used to predict the magnetic coupling that arises from superexchange. These rules can, and have

been, used to predict and rationalise the magnetic order observed in a variety of materials. Figure 2.8 shows a 180 º superexchange interaction a 90 º superexchange interaction.

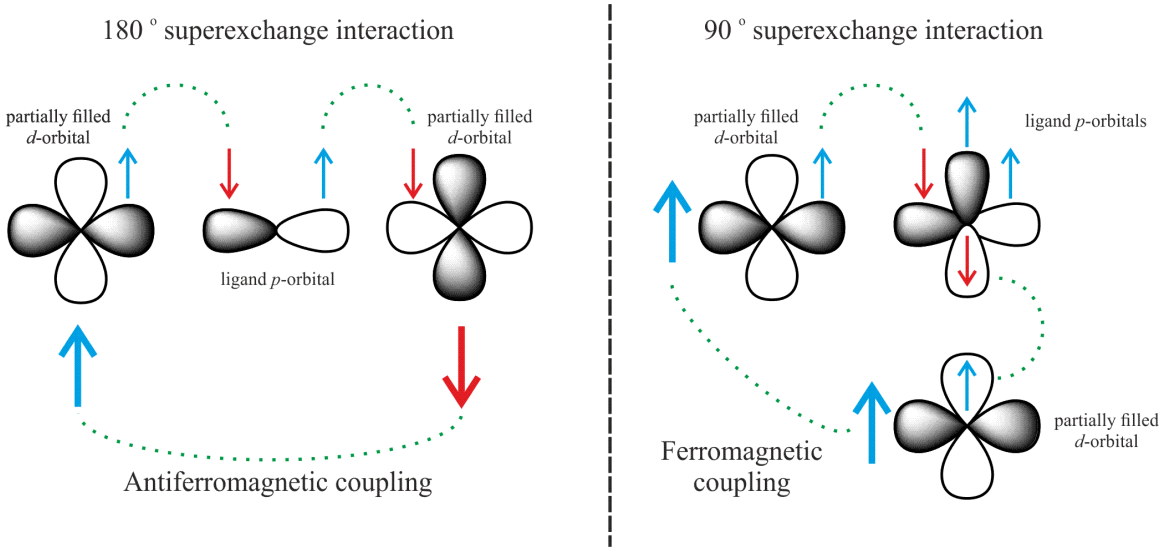

Figure 2.8: A schematic of M-O-M 180 º and 90 º superexchange interactions

The 180 º interaction is the most important with regards to the work presented in this thesis and leads to the following predictions:

- Ferromagnetic coupling arises when a half filled orbital exchanges with a filled or empty orbital.
- Antiferromagnetic coupling arises by the interaction of two half-filled orbitals or the interaction between a filled and an empty orbital.

As previously mentioned the strength of a superexchange interaction is dependent on the angle of the bond and bond length as these factors influence the orbital overlap. Thus changes to a structure have a direct impact on the superexchange, and by extension magnetic behaviours, of a material. Consequently by selecting certain structural features materials can be designed to target specific coupling regimes.

2.13 ^{57}Fe Mössbauer spectroscopy

^{57}Fe Mössbauer spectroscopy is a technique that uses the absorption and emission of gamma radiation to probe the local environment of iron centres. In the gas phase the energy of a photon that is emitted as a result of decay has a smaller energy than the energy of the nuclear transition. This is because the atom recoils upon emission as a result of Newton's third law of motion. Consequently the resonance of this process is unobservable because there is no significant overlap between the absorption and emission spectra. This is not the case in the solid state. In a solid crystal the nuclei are held in place and thus are unable to recoil. Instead a small portion of the energy of the absorbed photon can be lost as a result of quantised lattice vibrations, known as phonons. During the emission process any number of phonons can be triggered, including zero. When no phonon is triggered a "recoil free" event is said to have occurred. It has been found that a significant proportion of the absorption-emission events are "recoil free" thus a sample can absorb and emit a gamma ray emitted from a nucleus of the same isotope, i.e. resonate. The resonance that occurs as a result of this process can be measured.

^{57}Fe Mössbauer spectroscopy uses a ^{57}Co source that decays to an excited ^{57}Fe state via electron capture. This excited ^{57}Fe state decays to a ground state by emitting a gamma ray that is then absorbed and emitted by the ^{57}Fe in the sample. The energy of the gamma rays is modified via the Doppler Effect. The transmission of gamma rays through the sample can be tracked as a function of velocity. Where resonance occurs sharp peaks are observed.

The local environment of the ^{57}Fe cations modifies the energies at which the transitions occur and the structure of the peaks observed. The resonance energy of the nucleus is affected by the transition of electrons within the *s* orbital. The change that results from the *s* orbital transitions is known as the chemical shift as the spectra is "shifted" depending on

the electron charge density. The relation to the electron charge density means the chemical shift can be used to determine the oxidation state of iron in a sample. For example weaker screening by the *d* electrons in Fe^{3+} compared to Fe^{2+} results in a relative increase in the *s* electron density and a lower chemical shift[76-77]. Nuclei in states with non-spherical charge distributions (I > 1/2) result in spectra with quadrupole splitting. This occurs because these nuclei produce an asymmetrical electric field which splits the nuclear energy levels, producing a quadrupole moment. ^{57}Fe has an I = 3/2 excited state, therefore the 1/2 to 3/2 transition has two sub-states and appears as a doublet in the spectra (Figure 2.9).

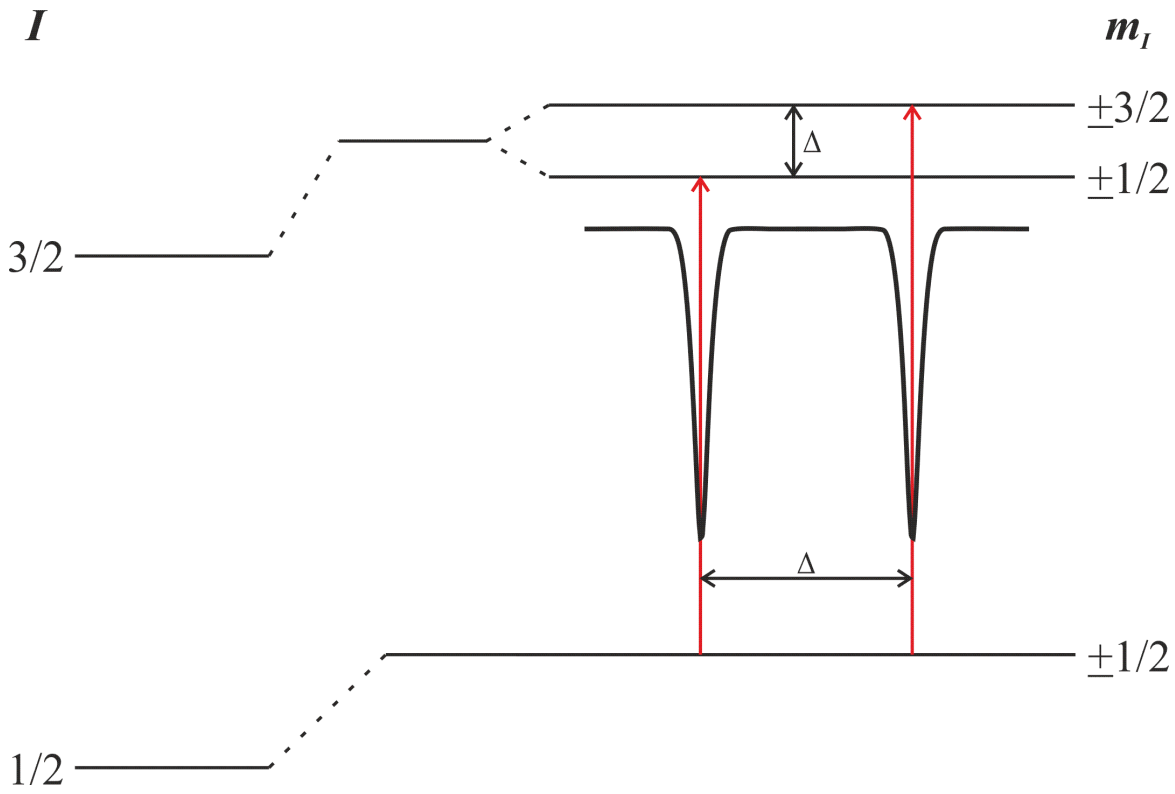

Figure 2.9: Quadrupole splitting from a 1/2 to 3/2 transition. The magnitude of the quadrupole splitting is Δ.

Finally, the structure of a Mössbauer spectrum is modified as a result of magnetic order. The interaction between a nucleus with spin *I* and a magnetic field will split the energy states into $2I + 1$ sub-energy levels. This increases the number of permitted transitions

and results in additional peaks (Figure 2.10). The transitions are limited to those where the change to m_I is 0 or $\pm$ 1.

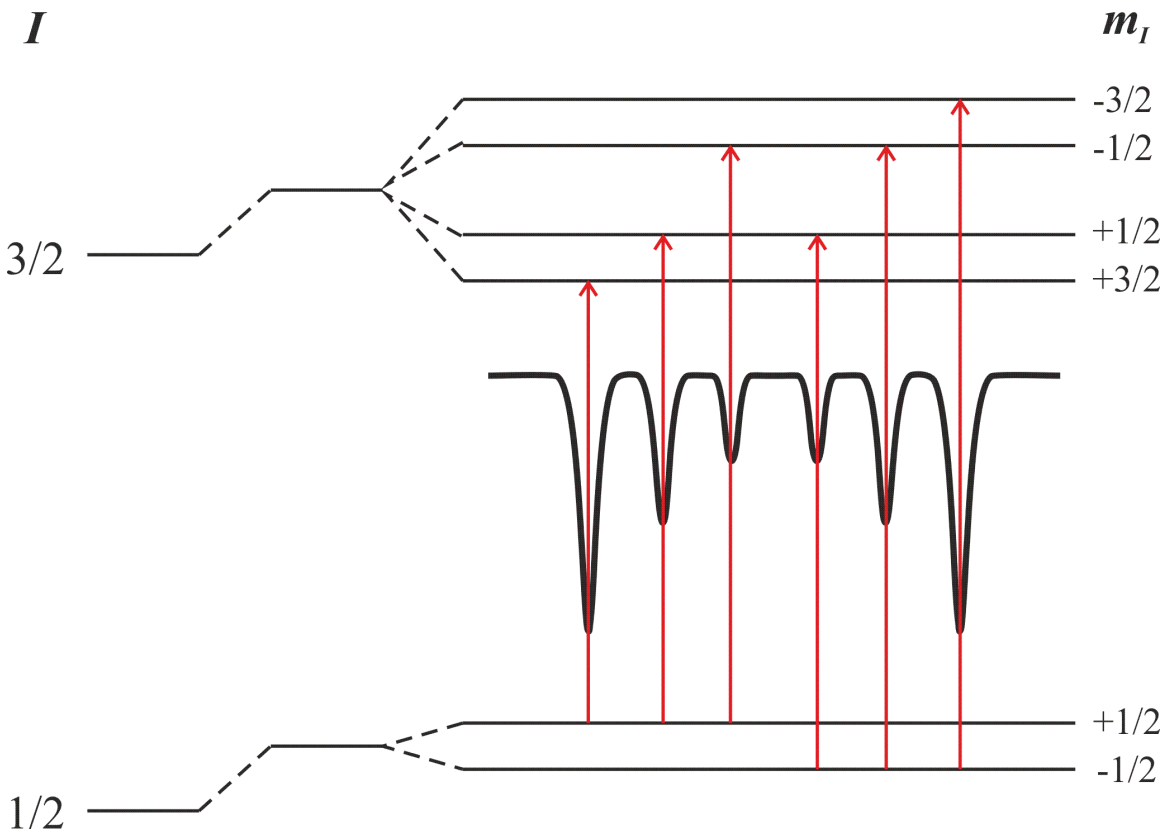

Figure 2.10: Magnetic splitting of nuclear energy levels.

Samples were ground with graphite and sealed in acrylic absorber discs. ^{57}Fe Mössbauer spectra were collected relative to an α-Fe standard using a 36 mCi ^{57}Co in Rh source. The spectra were recorded over a velocity range of $\pm$ 12 mm/s. Sub-ambient temperatures were maintained using a Janis 10 K CCR cytostatic spectrometer (Model CCS-800/204N) and a Lakeshore 335 temperature controller. All spectra were collected and fitted by Dr Paul A. Bingham at Sheffield Hallam University.

Chapter 3 - The Synthetic Methods and Chemical Challenges of Reducing Iridium-containing Oxides

3.1 Introduction

The group I/II metal hydrides have proven to be highly effective reducing agents of complex transition metal oxides. NaH and CaH_2 have both been used to synthesise a variety of metastable phases containing 3*d* and 4*d* cations; the most notable being $LaNiO_2$[42], $SrFeO_{2+\delta}$[47], $SrFe_{0.5}Ru_{0.5}O_2$[44] and $SrVO_2H$[44]. The success of these reduction processes are predicated on two criteria. Firstly, the parent oxide must be able to produce a metastable phase via reduction. Secondly, the metastable phase must be stable with respect to the reduction and the processing required to remove the by-products of reaction.

The reduction chemistry of complex metal oxides that contain 5*d* cations has remained unexplored until this study. To address this gap, we have synthesised and investigated the reduction chemistry of a series of iridium-containing complex oxides. This research has highlighted the limitations of reduction using the group I/II metal hydrides, thus it was necessary to develop alternative methods of reduction in order to successfully isolate and characterise unique metastable phases.

3.2 Synthesis and results

3.2.1 Synthesis of parent oxides

Samples of Sr_2FeIrO_6, Sr_2CoIrO_6, $LaSrMIrO_6$ (M= Co, Ni), $CaMn_{0.5}Ir_{0.5}O_3$, $Sr_2Fe_{0.5}Ir_{0.5}O_4$ and $La_xSr_{2-x}Co_{0.5}Ir_{0.5}O_4$ (x = 0, 0.5) were prepared using the citrate gel method (Chapter 2, Section 2.1.2). Appropriate quantities of $SrCO_3$ (99.994%), La_2O_3 (99.999%), $CaCO_3$

(99.999%), Fe (99.99%), MnO_2 (99.997%), Co (99.996%) and Ni (99.996%) were dissolved in a 1:1 mixture of conc. nitric acid and distilled water. After dissolution was complete the required amount of IrO_2 (99.99%, dried at 700 ^oC for 2 hours) was added. Citric acid and analar ethylene glycol were added and the solutions were heated whilst being stirred. The gel thus formed was dried and then allowed to combust in air. The subsequent products were ground into fine powders, placed in alumina crucibles and heated at 1000 ^oC in air at a rate of 1 $^oC\ min^{-1}$ to remove the organic components of the sample. The resulting powders were pressed into a 13 mm diameter pellets and heated in air at the following temperatures for two cycles of 2 days with intermediate grinding. $CaMn_{0.5}Ir_{0.5}O_3$, Sr_2FeIrO_6 and $Sr_2Co_{0.5}Ir_{0.5}O_4$ were heated at 1100 ^oC, Sr_2FeIrO_6, $LaSrCoIrO_6$ and $Sr_2Fe_{0.5}Ir_{0.5}O_4$ were heated at 1000 ^oC, and $LaSrNiIrO_6$ and $La_{0.5}Sr_{1.5}Co_{0.5}Ir_{0.5}O_4$ were heated at 1300 ^oC.

The resulting powders were observed to be phase-pure by laboratory X-ray powder diffraction. The lattice parameters of these phases were initially measured using CMPR[78] and are detailed in Table 3.1. $CaMn_{0.5}Ir_{0.5}O_3$[79], Sr_2FeIrO_6[22], Sr_2CoIrO_6[80], $LaSrCoIrO_6$[81], $Sr_2Co_{0.5}Ir_{0.5}O_4$[82] and $LaSrNiIrO_6$[25] are known compounds and the lattice parameters extracted from CMPR[78] are consistent with those reported in the literature. $Sr_2Fe_{0.5}Ir_{0.5}O_4$ and $La_{0.5}Sr_{1.5}Co_{0.5}Ir_{0.5}O_4$ are not reported in the literature but the lattice parameters extracted from CMPR[78] are consistent with those reported in Chapters 6 and 8 of this thesis.

Compound	a (Å)	b (Å)	c (Å)
$CaMn_{0.5}Ir_{0.5}O_3$	5.44	7.60	5.34
Sr_2FeIrO_6	5.55	5.57	7.84
$Sr_2Fe_{0.5}Ir_{0.5}O_4$	3.90	3.90	15.58
Sr_2CoIrO_6	5.53	5.56	7.83
$LaSrCoIrO_6$	5.57	5.57	7.86
$Sr_2Co_{0.5}Ir_{0.5}O_4$	3.86	3.86	12.32
$La_{0.5}Sr_{1.5}Co_{0.5}Ir_{0.5}O_4$	3.89	3.89	12.62
$LaSrNiIrO_6$	5.59	5.57	7.88

Table 3.1: Lattice parameters of iridium containing oxides extracted from CMPR

3.2.2 Reduction of Sr_2FeIrO_6

3.2.2.1 Reaction with CaH_2 and LiH

In order to assess the reactivity of Sr_2FeIrO_6 small samples (≈ 200-500 mg) were ground together with a double molar excess of CaH_2 in an argon filled glovebox with an agate pestle and mortar. These mixtures were placed in a "venting system" (Chapter 2, Section 2.3.2) and heated at a series of temperatures in the range $350 \leq T / {}^oC \leq 410$ for cycles of 2 days. The reaction of Sr_2FeIrO_6 with CaH_2 resulted in the formation of Sr_2FeIrO_4 (for full characterisation of this phase see Chapter 4). This reaction also results in the formation of CaO as a by-product. This CaO and any excess CaH_2 needed to be removed in order to fully characterise the reduced product. To do this the sample was washed with 0.1 M ammonium chloride in methanol and neat methanol (Chapter 2, Section 2.4). X-ray powder diffraction data collected from the washed product of the reduction of Sr_2FeIrO_6 had an additional, very broad feature at around 41 ^{o} (Figure 3.1). This broad peak is consistent with the production of iridium nanoparticles and indicates that the product of reduction is not stable with respect to the washing process. To this end two experiments to modify the washing process were conducted: increasing the acidity of the solution and changing the solvent mixture.

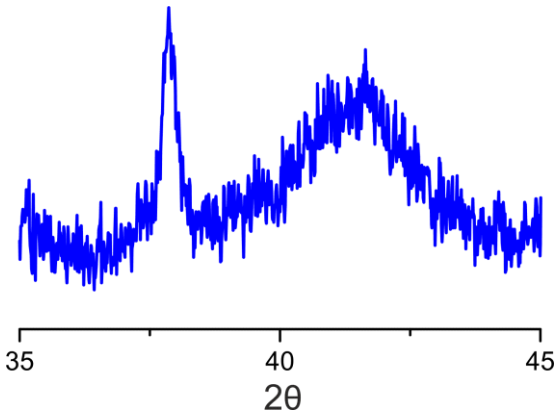

Figure 3.1: Additional broad diffraction feature attributed to elemental iridium nanoparticles

Initial experiments focused on increasing the acidity of the solution used to wash the reaction mixture by increasing the concentration of NH_4Cl. This tactic has previously been deployed to successfully isolate a pure sample of $Sr_3Co_2O_4Cl_2$[83]. The highest concentration of NH_4Cl in methanol achieved was 0.5 M, however this solution was not acidic enough and gave similar results to washing with the 0.1 M solution. It is worth noting the degree of decomposition did decrease when the more acidic solution was used, suggesting the decomposition is base catalysed. A second series of solutions were produced containing citric acid, acetic acid, hydrochloric acid or ethylene glycol. Washing with the citric acid and ethylene glycol solutions did not dissolve either the CaO or CaH_2 and washing with the acetic or hydrochloric acid solutions produced water and resulted in reoxidation of Sr_2FeIrO_4 to Sr_2FeIrO_6.

CaO has been found to react with glycerol to form a series of co-ordination complexes known as calcium glyceroxides[84-85]. A sample of the product of reduction containing CaO and CaH_2 was mixed with pure glycerol and then washed with pure methanol in an attempt to remove all calcium containing phases. The calcium oxide was successfully removed, as was the CaH_2, however once again the reduced phase had undergone decomposition, most probably due to hydride being released into solution during the final

washing with methanol. A 1:1 solution of glycerol to methanol was produced to trigger the dissolution of both calcium containing phases at the same time. Unfortunately this failed, once again resulting in decomposition of the reduced phase. It is clear that whilst CaH_2 is effective at reducing Sr_2FeIrO_6 there is no way to remove the calcium containing by-products and obtain a pure sample of the reduced phase for full characterisation.

An alternative reducing agent to CaH_2 is LiH. CaH_2 is favoured over LiH because LiH can result in the lithiation of samples as well as or instead of reduction. However the potential advantage of LiH in this case is that LiH and Li_2O dissolve in neat methanol. This means that all lithium-containing products can be removed from the reaction mixture with an acid solution more quickly than those produced by reaction with CaH_2. To assess the reactivity of Sr_2FeIrO_6 to LiH, small samples of Sr_2FeIrO_6 (≈ 200-500 mg) were ground together with double molar excesses of LiH in an argon filled glovebox with an agate pestle and mortar. These mixtures were placed in a "venting system" (Chapter 2, Section 2.3.2) and heated at temperatures in the range $300 \leq T / {}^{o}C \leq 410$ for periods of 2 days. The reaction progress was followed using X-ray powder diffraction. These reaction mixtures were washed with the same acidic solutions used to wash the CaH_2 reaction mixtures to remove the lithium-containing by-products. This reaction resulted in the formation of Sr_2FeIrO_4. Unfortunately each of these washing processes resulted in the same decomposition that was observed in the reactions of Sr_2FeIrO_6 with CaH_2.

3.2.2.2 Reaction with 95%/5% N_2/H_2 gas

Small samples of Sr_2FeIrO_6, were heated under a steady flow of 95%/5% N_2/to find an alternative to the solid-solid calcium hydride reduction method outlined in Section 3.2.2 (Chapter 2, Section 2.5). Samples were heated at temperatures in the range $390 \leq T / K \leq 410$ for cycles of 12 hours. Reaction of Sr_2FeIrO_6 with flowing 95%/5% N_2/N_2 resulted in

its conversion to Sr_2FeIrO_4. The full refinements of diffraction data collected from this sample are given in Chapter 4, Section 4.3.3.1. Figure 3.2 shows a pictorial representation of the reaction that took place. The diffraction data collected from the product of this reaction will be discussed in Chapter 4, but it shows that the reaction has been far more successful than the metal hydride reactions. However the data also highlights that the synthesis isn't perfect. The refinement of neutron powder diffraction data collected from the sample of Sr_2FeIrO_4 was fit best when models of Sr_2FeO_5, SrO and Ir were added to the refinement indicating that during the reaction some decomposition of the Sr_2FeIrO_4 phase had taken place.

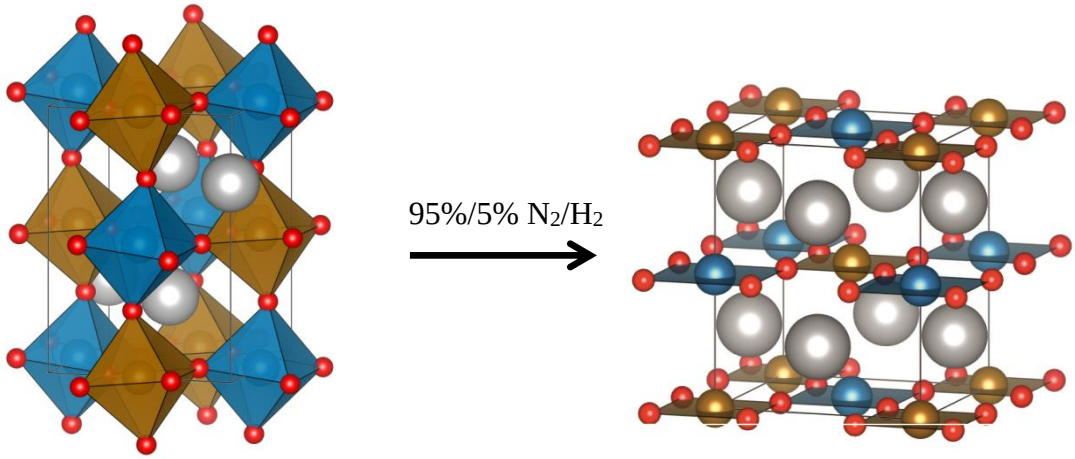

Figure 3.2: Schematic of the topochemical reduction of Sr_2FeIrO_6

3.2.3 Reactions of Sr_2CoIrO_6 and $LaSrMIrO_6$ (M = Co, Ni)

3.2.3.1 Reaction with CaH_2

To determine the reactivity of Sr_2CoIrO_6 and $LaSrMIrO_6$ (M = Co, Ni) small samples (≈ 200-500 mg) were ground together with a double molar excess of CaH_2 in an argon filled glovebox with an agate pestle and mortar. These mixtures were placed in a "venting system" (Chapter 2, Section 2.3.2) and heated for cycles of 2 days over the temperature ranges given in Table 3.2. Once a reaction was deemed to have reached completion the

products were washed with a mildly acidic methanol solution, followed by clean methanol in order to removed calcium-containing by-products and excess CaH_2 (Chapter 2, Section 2.4). The samples were then dried under vacuum and returned to the glovebox. These reactions initially proved promising and suggested that metastable phases based on these parent compounds existed. However, further heating resulted in decomposition of these parent oxides into SrO, Co/Ni, and La_2O_3.

Compound	Temperature Range (^{o} C)
Sr_2CoIrO_6	300 – 350
$LaSrCoIrO_6$	350 – 375
$LaSrNiIrO_6$	275 – 335

Table 3.2: Temperature ranges in which iridium-containing oxides were reacted with CaH_2

3.2.4 Reductions of $Sr_2Fe_{0.5}Ir_{0.5}O_4$

3.2.4.1 Reaction with CaH_2

To assess the reactivity of $Sr_2Fe_{0.5}Ir_{0.5}O_4$, small samples (≈ 200-500 mg) were ground together with a double molar excess of CaH_2 in an argon filled glovebox with an agate pestle and mortar. These mixtures were placed in a "venting system" (Chapter 2, Section 2.3.2) and heated at temperature in the range $350 \leq T / {}^oC \leq 400$ for cycles of 2 days. Once a reaction was deemed to have reached completion the products were washed with a mildly acidic methanol solution, followed by clean methanol in order to remove calcium-containing by-products and excess CaH_2 (Chapter 2, Section 2.4). The samples were then dried under vacuum and returned to the glovebox.

The reaction of $Sr_2Fe_{0.5}Ir_{0.5}O_4$ with CaH_2 resulted in the formation of $Sr_2Fe_{0.5}Ir_{0.5}O_3$, the full characterisation of which is discussed in Chapter 6 of this thesis. However similarly to the reaction of Sr_2FeIrO_6 with CaH_2 (Section 3.2.2.1), the removal of calcium oxide, calcium hydride and other calcium containing by-products from the reaction mixture

resulted in significant decomposition of $Sr_2Fe_{0.5}Ir_{0.5}O_3$. This clearly suggested that $Sr_2Fe_{0.5}Ir_{0.5}O_3$ is chemically incompatible with the washing process and an alternative method was needed to isolate a purer sample of $Sr_2Fe_{0.5}Ir_{0.5}O_3$.

3.2.4.2 Reaction with 95%/5% N_2/H_2 gas

Following on from the success of reducing Sr_2FeIrO_6 using flowing 95%/5% N_2/H_2 gas (Section 3.2.2.2), small samples of $Sr_2Fe_{0.5}Ir_{0.5}O_4$ were reacted with 95%/5% N_2/H_2 gas. The samples were heated at temperatures in the range $350 \leq T / {}^oC \leq 400$ for cycles of 12 hours. Reaction of small quantities of $Sr_2Fe_{0.5}Ir_{0.5}O_4$ with flowing 95%/5% N_2/H_2 were highly successfully and resulted in conversion to a phase pure sample of $Sr_2Fe_{0.5}Ir_{0.5}O_3$ as demonstrated by the diffraction pattern shown in Figure 3.3. However with larger samples this was not the case. Instead we observed that parts of the sample reacted and decomposed while other portions remained unreacted. Figure 3.3 shows the X-ray diffraction data collected from the reaction of approximately 1.5 g of $Sr_2Fe_{0.5}Ir_{0.5}O_4$ with flowing 95%/5% N_2/H_2 compared to that of a much smaller sample. It can clearly be seen that the larger sample contains a large proportion of impurities whereas the smaller sample does not.

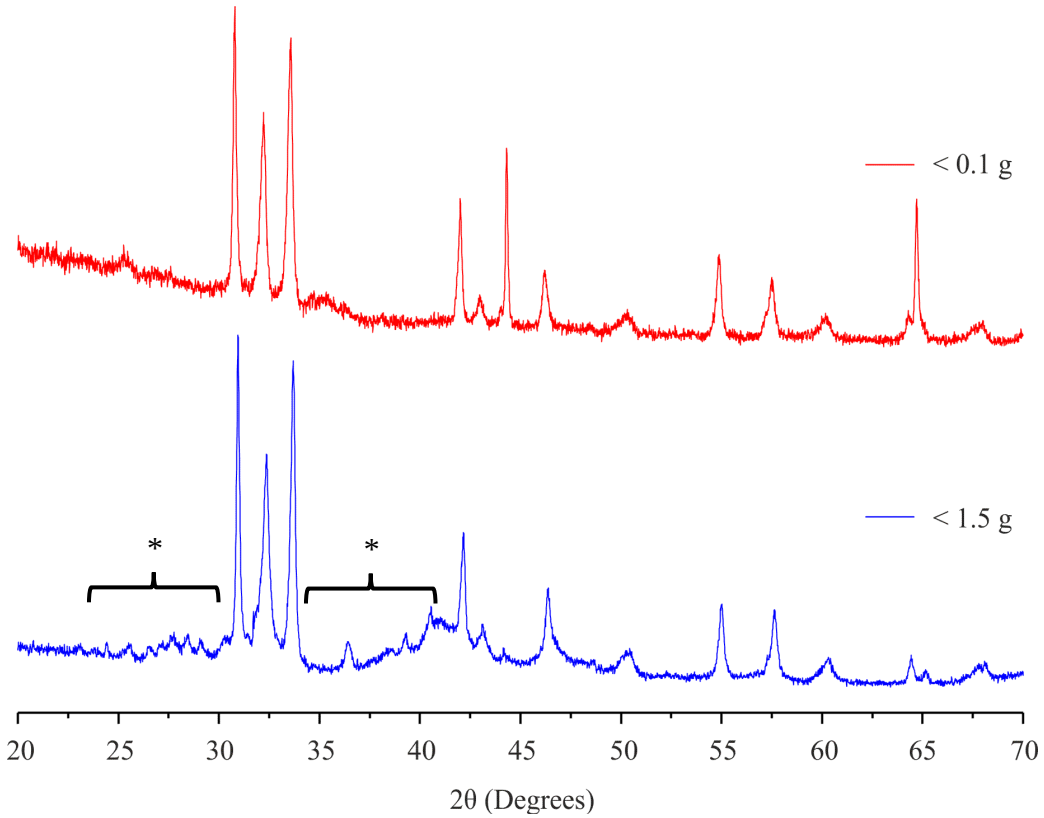

Figure 3.3: Powder X-ray diffraction data collected from the reactions of $Sr_2Fe_{0.5}Ir_{0.5}O_4$ with 95%/5% N_2/H_2. * = Impurity peaks

The failure to produce a large sample of pure $Sr_2Fe_{0.5}Ir_{0.5}O_3$ meant it was necessary to devise another reaction method that could be used to make a sample that could be characterised fully.

3.2.4.3 Reaction with zirconium

Small samples of $Sr_2Fe_{0.5}Ir_{0.5}O_4$were placed in small glass thimbles which in turn were placed in glass tubes that contained zirconium. These tubes were sealed under vacuum and the ampule thus formed was heated at 400 ^oC for 2 cycles of 7 days and 410 ^oC for one cycle of 7 days (Chapter 2, section 2.6). X-ray powder diffraction data collected from these reactions clearly indicated that pure samples of $Sr_2Fe_{0.5}Ir_{0.5}O_3$ had been synthesised, thus the reaction as scaled up to make a sample large enough to be fully characterised.

A full discussion of the data collected from $Sr_2Fe_{0.5}Ir_{0.5}O_3$ is given in Chapter 6, however diffraction data suggest that the reaction depicted below in Figure 2.4 took place with only a small amount of impurity phases being produced. This is in stark contrast to the reaction with flowing 95%/5% N_2/H_2 (Section 3.2.4.2).

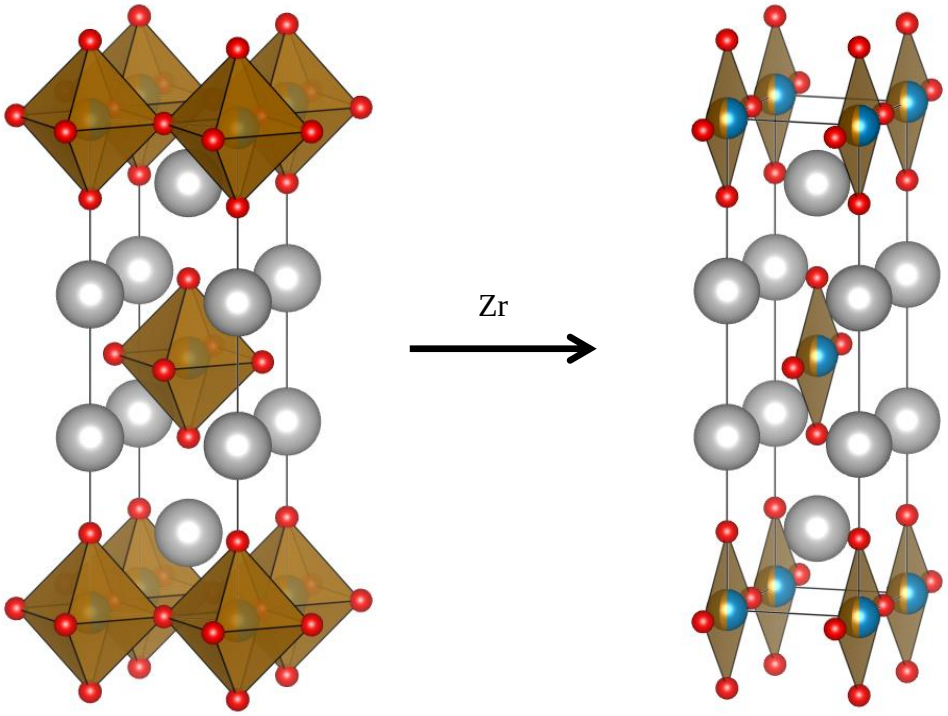

Figure 3.4: Schematic of the topochemical reduction of $Sr_2Fe_{0.5}Ir_{0.5}O_4$

3.2.5 Reduction of $La_xSr_{2-x}Co_{0.5}Ir_{0.5}O_4$ (x = 0, 0.5)

3.2.5.1 Reaction with CaH_2

To assess the reactivity of $La_xSr_{2-x}Co_{0.5}Ir_{0.5}O_4$ (x = 0, 0.5) small samples were ground together with a double molar excess of CaH_2 in an argon filled glovebox with an agate pestle and mortar. These mixtures were placed in a "venting system" (Chapter 2, Section 2.3.2) and heated for cycles of 2 days at temperatures in the ranges given in Table 3.3. Once a reaction was deemed to have reached completion the products were washed with a mildly acidic methanol solution, followed by clean methanol in order to removed

calcium-containing by-products and excess CaH_2 (Chapter 2, Section 2.4). The samples were then dried under vacuum and returned to the glovebox.

Compound	Temperature Range (^{o} C)
$Sr_2Co_{0.5}Ir_{0.5}O_4$	300 – 350
$La_{0.5}Sr_{1.5}Co_{0.5}Ir_{0.5}O_4$	300 – 450

Table 3.3: Temperature ranges at which $La_xSr_{2-x}Co_{0.5}Ir_{0.5}O_4$ were reacted with CaH_2

These reactions were successful and resulted in the synthesis of $La_xSr_{2-x}Co_{0.5}Ir_{0.5}O_3$ (x = 0, 0.5). These phases are fully characterised and discussed in Chapter 8. Similarly to the reactions of Sr_2FeIrO_6 and $Sr_2Fe_{0.5}Ir0_{0.5}O_4$ with CaH_2 (Sections 3.2.2.1 and 3.2.4.1), the removal of calcium oxide and calcium hydride from the reaction mixture resulted in significant decomposition of $La_xSr_{2-x}Co_{0.5}Ir_{0.5}O_3$ (x = 0, 0.5).

3.2.5.2 Reaction with 95%/5% N_2/H_2 gas

Small samples of $La_xSr_{2-x}Co_{0.5}Ir_{0.5}O_4$ (x = 0, 0.5) were reacted with 95%/5% N_2/H_2 gas. The samples were heated for cycles of 12 hours at temperatures in the ranges given in Table 3.4. Analogously to the reaction with $Sr_2Fe_{0.5}Ir_{0.5}O_4$, reactions of small samples of $La_xSr_{2-x}Co_{0.5}Ir_{0.5}O_4$ (x = 0, 0.5) were successful and resulted in the formation of $La_xSr_{2-x}Co_{0.5}Ir_{0.5}O_3$ (x = 0, 0.5). However, reaction of larger samples of $La_xSr_{2-x}Co_{0.5}Ir_{0.5}O_4$ (x = 0, 0.5) resulted in significant decomposition alongside reaction.

Compound	Temperature Range (^{o} C)
$Sr_2Co_{0.5}Ir_{0.5}O_4$	300 – 350
$La_{0.5}Sr_{1.5}Co_{0.5}Ir_{0.5}O_4$	300 – 550

Table 3.4: Temperature ranges at which $La_xSr_{2-x}Co_{0.5}Ir_{0.5}O_4$ were reacted with 95%/5% N_2/H_2 gas

3.2.5.3 Reaction with zirconium

Small samples of $La_xSr_{2-x}Co_{0.5}Ir_{0.5}O_4$ (x= 0, 0.5) were placed in glass thimbles which in turn were placed in glass tubes that contained zirconium. These tubes were sealed under

vacuum and the ampules thus formed were heated at various temperatures for 2 cycles of 7 days (Chapter 2, section 2.6). The temperature ranges at which each sample was heated are outlined in Table 3.5. The reactions were monitored using X-ray powder diffraction data.

X-ray powder diffraction data showed that $Sr_2Co_{0.5}Ir_{0.5}O_4$ decomposed at 400 ^oC. This is the lowest temperature at which zirconium is reactive. A second vessel was constructed in which the zirconium and $Sr_2Co_{0.5}Ir_{0.5}O_4$ could be heated at separate temperatures (Chapter 2, Section 2.6). This vessel was heated so the zirconium was heated at 550 ^oC and the $Sr_2Co_{0.5}Ir_{0.5}O_4$ was heated at various temperatures between $300 \leq T / ^oC \leq 320$. The progress of the reaction was monitored with X-ray powder diffraction data. Each of these reactions resulted in the synthesis of $La_xSr_{2-x}Co_{0.5}Ir_{0.5}O_3$ (x= 0, 0.5).

Compound	Temperature Range (^{o} C)
$Sr_2Co_{0.5}Ir_{0.5}O_4$	300 – 350
$La_{0.5}Sr_{1.5}Co_{0.5}Ir_{0.5}O_4$	400 – 550

Table 3.5: Temperature ranges at $La_xSr_{2-x}Co_{0.5}Ir_{0.5}O_4$ (x = 0, 0.5) were reacted with zirconium

The diffraction data collected from $La_{0.5}Sr_{1.5}Co_{0.5}Ir_{0.5}O_3$ and $Sr_2Co_{0.5}Ir_{0.5}O_3$ are refined and discussed in Chapter 8 of this thesis but it they clearly show that the reaction depicted in Figure 3.5 had taken place.

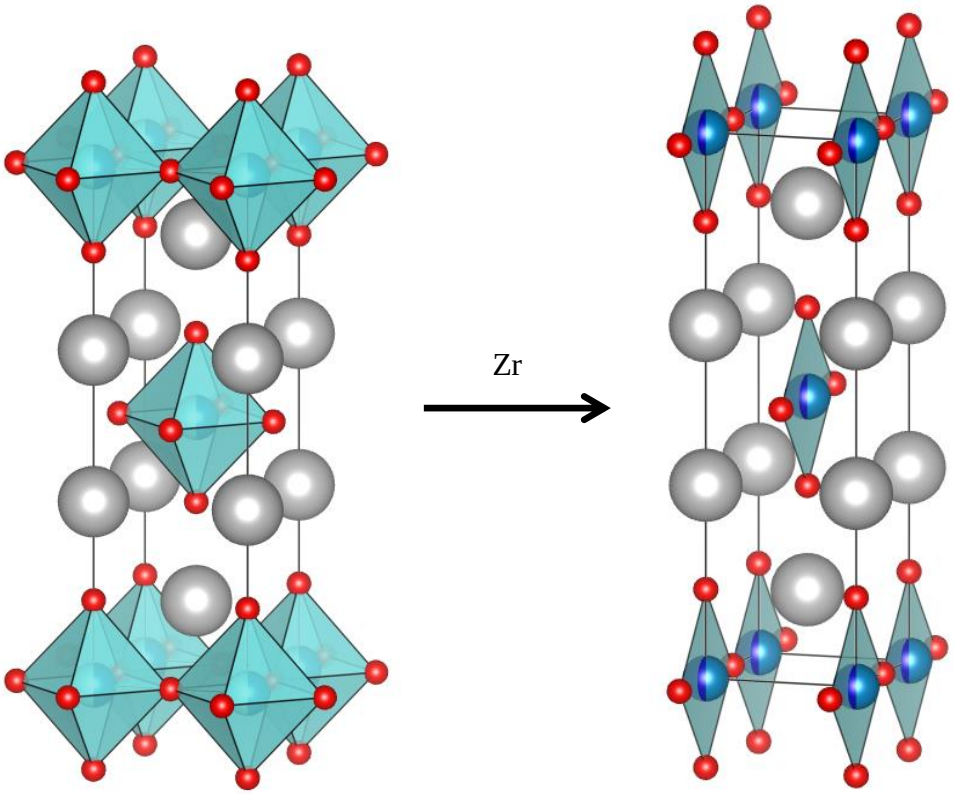

Figure 3.5: Schematic of the topochemical reduction of $La_xSr_{2-x}Co_{0.5}Ir_{0.5}O_4$ (x = 0, 0.5)

3.2.6 Reduction of $CaMn_{0.5}Ir_{0.5}O_3$

3.2.6.1 Reaction with CaH_2

Small samples of $CaMn_{0.5}Ir_{0.5}O_3$ (≈ 200-500 mg) were ground together with a double molar excess of CaH_2 in an argon filled glovebox with an agate pestle and mortar. These mixtures were placed in glass ampules (Chapter 2, Section 2.3.1) and heated at 300 ^oC for cycles of 2 days.

X-ray powder diffraction data collected from this reaction showed total decomposition of $CaMn_{0.5}IrO_3$ into CaO, MnO_2 and Ir had occurred. 300 ^oC is the lower reactivity limit of CaH_2. This is an indication that the ion mobility in $CaMn_{0.5}Ir_{0.5}O_3$ is high and to successfully reduce it we needed to try alternative reactions.

3.2.6.2 Reaction of $CaMn_{0.5}Ir_{0.5}O_3$ with NaH

Small samples of $CaMn_{0.5}Ir_{0.5}O_3$ (≈ 200-500 mg) were ground with a two molar excess of NaH in an argon filled glovebox with an agate pestle and mortar. The mixtures were placed in Pyrex tubes, sealed under vacuum and then heated at various temperatures in the range $150 \leq T / {}^{o}C \leq 210$ (Chapter 2, Section 2.3.1). The progress of the reaction was followed using X-ray powder diffraction.

Once a reaction was deemed to have reached completion the products were washed with 4 x 100 ml of clean methanol in order to removed sodium-containing by-products and excess NaH. The samples were then dried under vacuum and returned to the glovebox (Chapter 2, Section 2.4). X-ray diffraction measurements revealed that that the product of this reaction partially decomposed during the washing process. Reaction of small samples of $CaMn_{0.5}Ir_{0.5}O_3$ with NaH resulted in the formation of an orthorhombic phase with a lattice parameters a = 5.41 Å, b = 7.62 Å, c = 5.39 Å. Compositional analysis shows that this orthorhombic phase is $CaMn_{0.5}Ir_{0.5}O_{2.5}$ and the full characterisation of this phase is covered in Chapter 7. The washing of these small samples resulted in partial decomposition of the sample as indicated by the presence of a broad peak associated with iridium nanoparticles similar to that shown in Figure 3.1.

To synthesise a large sample of the product for characterisation by neutron diffraction samples of $CaMn_{0.5}Ir_{0.5}O_3$ (≈ 1.5 g) were ground with a two-fold molar excess of NaH in an argon filled glovebox with an agate pestle and mortar. The mixtures were placed in a Pyrex tube, sealed under vacuum, and then heated at various temperatures in the range $180 \leq T / {}^{o}C \leq 210$. The progress of the reaction was followed using X-ray powder diffraction. Analysis of X-ray diffraction data showed that each of these samples totally decomposed as indicated by the presence of peaks corresponding to CaO, MnO_2 and Ir.

This suggests direct reaction of $CaMn_{0.5}Ir_{0.5}O_3$ with NaH in larger quantities is not possible.

In an attempt to find another way to synthesis the reduced phase a large sample of $CaMn_{0.5}Ir_{0.5}O_3$ was placed in glass thimble which were sealed in Pyrex tubes with a molar equivalent of NaH and sealed under vacuum to make a getter-style reaction vessel (Chapter 2, Section 2.6). These reaction vessels were heated at various temperatures in the range $180 \leq T / {}^{o}C \leq 200$ for periods of 7 days and the progress of reaction was monitored using X-ray powder diffraction data. This reaction was deemed successful by analysis of X-ray powder diffraction data after a final heating at 200 ^{o}C. This reaction proved to be highly successful and resulted in the formation of a pure sample of $CaMn_{0.5}Ir_{0.5}O_{2.5}$ that is comprehensively characterised in Chapter 7. A depiction of the reduction of $CaMn_{0.5}Ir_{0.5}O_3$ to form $CaMn_{0.5}Ir_{0.5}O_{2.5}$ is given in Figure 3.6.

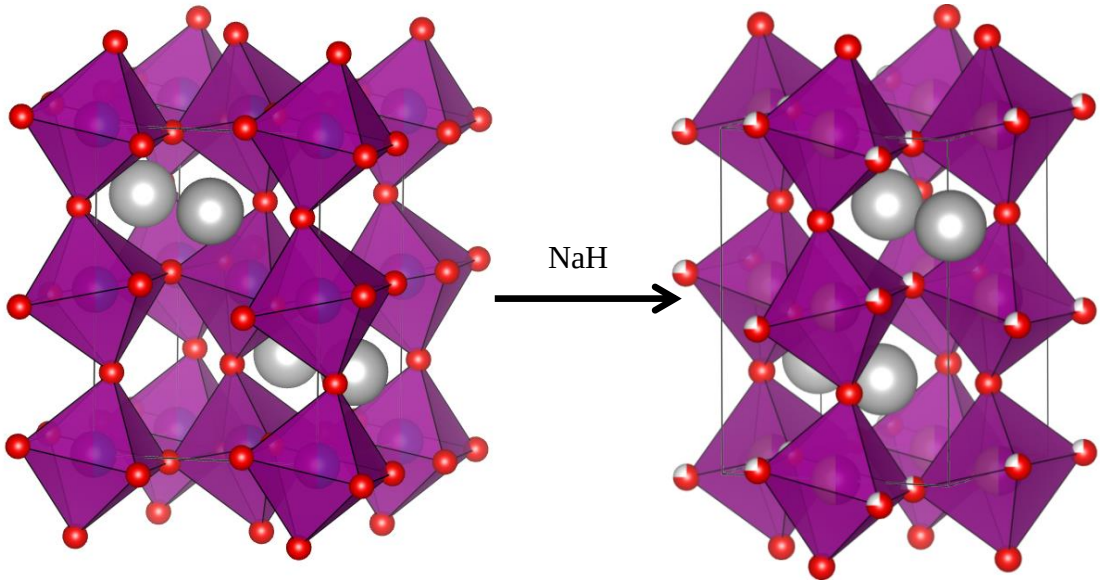

Figure 3.6: Schematic of the topochemical reduction of $CaMn_{0.5}Ir_{0.5}O_3$

3.3 Discussion

3.3.1 Stability of iridium-containing perovskites and reduced phases

In this chapter we have shown that $CaMn_{0.5}Ir_{0.5}O_3$ and Sr_2FeIrO_6 can be reduced to form metastable phases but Sr_2CoIrO_6 and $LaSrMIrO_6$ (M = Co, Ni) cannot. The obvious difference between these compounds is the 3*d* metal cation lattice. The central premise of this research is that a robust 3*d* cation lattice is needed to stabilise the iridium lattice to stop it from fully reducing to iridium metal. From the outset of this work we expected cobalt and nickel lattices would be robust enough to stabilise an iridium lattice based on their ability to stabilise the reduced ruthenium lattices in $LaSrCoRuO_4$[86], $LaSrCoRuO_4H_2$[86], $LaSrNiIrO_4$[87] and $LaSr_3NiRuO_4H_4$[59]. This assertion is not just based on the precedent set by these compounds. The electronegativities of ruthenium and iridium (Table 3.6) are the same thus we would expect ruthenium and iridium to have similar reduction chemistries[88].

Element	χ (Pauling units)
Mn	1.55
Fe	1.83
Co	1.88
Ni	1.91
Ru	2.20
Ir	2.20

Table 3.6: Pauling electronegativities of relevant 3*d*, 4*d* and 5*d* elements.

The experimental evidence clearly shows this is not the case as we have been unable to isolate a reduced perovskite phase that contains an iridium lattice coupled with a cobalt or nickel lattice. Our original assertion that ruthenium and iridium would have similar stabilities was evidently wrong and we must look beyond electronegativity to explain

why. The most significant difference between ruthenium and iridium are their frontier orbitals; that is ruthenium chemistry is defined by 4*d* orbitals whereas iridium chemistry is defined by 5*d* orbitals. It is therefore important to consider the respective bond strengths of Ru-O and Ir-O bonds when considering why iridium-containing parent phases are less stable. Calculating the strength of relevant bonds by analysis of lattice energies would provide the most accurate picture of the thermodynamics of our systems. However these calculations would be very complex and would not provide that are much more applicable than already published thermodynamic data. Thus examining the bond dissociation energies presented in the literature[89] can give us a quick and accurate insight into the stabilities of the complex oxides we are studying. Table 3.7 details a number of relevant M-O bond strengths. The bond dissociation is defined as the standard enthalpy change of the following fission:

M-O → M + O

It can clearly be seen from the table that the Ru-O bond is much stronger than the Ir-O bond. This difference is attributed to the closer energy match and better overlap of the Ru 4*d* and O 2*p* orbitals compared to that of the higher energy and more radially extended Ir 5*d* orbital. It is therefore not surprising that iridium-containing oxides are far less stable to reduction than their ruthenium-containing counterparts. We can also see that the Mn-O, Fe-O, Co-O and Ni-O bond strengths have a smaller variation, further supporting the affirmation that it is the 4*d*/5*d* lattice that defines the difference in stabilities between the ruthenium and iridium containing metastable compounds, as we would expect.

M-O Bond	M-O Bond Dissociation Energy (kJ mol^{-1})
Ti	666.5
Cr	461
V	637
Mn	362
Fe	407.0
Co	397.4
Ni	366
Ru	528
Ir	414

Table 3.7: Bond dissociation energies of relevant M-O bonds

One of the important aspects of these reductions where the weakness of the iridium lattice manifests is in the washing process discussed in Sections 3.2.2.1 and 3.2.6.2. The results discussed show that when washed Sr_2FeIrO_4 and $CaMn_{0.5}Ir_{0.5}O_{2.5}$ decompose, producing iridium metal nanoparticles. This decomposition is caused by the release of H^- into solution which mediates further reduction. There is little to no electrochemical data pertaining to the lower oxidation states of iridium and ruthenium in basic solution thus we cannot rationalise the differences by considering the behaviour of the cations in solution. However, we can look to the electronic states of Ru^{II} and Ir^{II} to rationalise the stability of $SrFe_{0.5}Ru_{0.5}O_2$ vs Sr_2FeIrO_4.

Figure 3.7 shows that Ru^{II} has a low spin d^6 electronic state. From a purely electronic point of view this is a very stable state as it has fully occupied orbitals that maximise ligand field stabilisation energy. In contrast Ir^{II} adopts a low spin d^7 electronic state. This configuration is far less stable due to the singly occupied d_{xy} orbital. From a purely electronic point of view we would expect Ir^{I} and Ir^{III} to be more stable owing to their electronic states having fully occupied orbitals. It is therefore reasonable to suggest the iridium lattice in Sr_2FeIrO_4 is base labile because there are other lower energy states that

can be accessed by disproportionation. These cations may in turn react to form iridium metal and iridium cations of higher oxidation states. This doesn't occur in $SrFe_{0.5}Ru_{0.5}O_2$ because Ru^{II} has a stable electronic state with no lower energy states that are easily accessible by disproportionation or reaction with base.

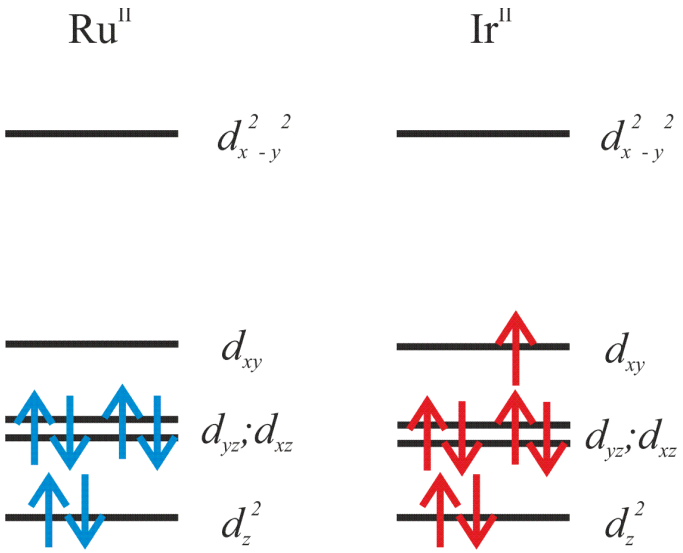

Figure 3.7: The electronic configurations of Ru^{II} and Ir^{II} in a square-planar co-ordination geometry

3.3.2 Reduction methods used to reduce iridium-containing oxides

3.3.2.1 Failure of metal hydrides

Reduction of complex metal oxides using group I/II metal hydrides has been highly successful, allowing for the synthesis of $LaNiO_2$[42], $SrFeO_{2+\delta}$[47], $SrFe_{0.5}Ru_{0.5}O_2$[46], $LaSrRuNiO_4$[87], $YBaCo_2O_{4.5}$[48] and $LaBaCo_2O_{4.25}$[48] to name but a few examples. This technique has become the cornerstone of this field in part due to the versatility of metal hydrides as reducing agents. Each hydride is "active" within a different temperature range which means oxides with varying anion mobility can be reduced by selecting a metal hydride that compliments the temperature at which the anions become mobile.

The disadvantage of this technique, as highlighted by this work, is the processing it requires. Successful reduction results in the production of group I/II oxides and leaves

some hydride unreacted both of which need to be removed. In the synthesis of the compounds mentioned above this washing was carried out with ease and did not cause any problems. Unfortunately this was not the case for the iridium-containing metastable phases we have synthesised. Attempts to modify the washing process to prevent decomposition failed. It is clear from these results that the iridium-containing metastable phases we have synthesised and the processes required to remove the by-products of reaction are chemically incompatible. This has not been observed in the reduction of the non-iridium-containing metastable phases previously discussed and highlights the fragility of iridium-containing metastable phases.

The decomposition of iridium-containing metastable phases presented a significant barrier with regards to full characterisation of these phases. The dominant isotope of iridium (^{193}Ir) has a large neutron absorption cross section. Consequently the presence of a significant proportion of iridium metal in these samples would have made the collection and analysis of neutron diffraction data very difficult. To circumvent this issue we elected to develop alternative methods of reduction using two reducing agents: hydrogen gas and zirconium metal.

3.3.2.2 Solid-gas reduction using hydrogen

One of the alternative reducing agents we used was flowing hydrogen gas. The clear advantage of a solid-gas reduction is that there are no solid by-products produced that need to be removed from the reaction mixture. As such reduction using dilute hydrogen was seen as a promising route via which we could produce large samples of metastable phases for full characterisation. Test reductions with small samples of Sr_2FeIrO_6, $Sr_2Fe_{0.5}Ir_{0.5}O_4$ and $La_xSr_{2-x}Co_{0.5}Ir_{0.5}O_4$ (x= 0, 0.5) were very successful.

Unfortunately scaling up this process did not result in seamless conversion of the parent oxides into metastable phases. Reaction of large samples of Sr_2FeIrO_6, $Sr_2Fe_{0.5}Ir_{0.5}O_4$ and $La_xSr_{2-x}Co_{0.5}Ir_{0.5}O_4$ (x = 0, 0.5) with dilute hydrogen all showed some degree of decomposition (Sections 3.2.4.2 and 3.2.5.2). If we examine the reaction set up this isn't entirely surprising. In Figure 3.8 it can be seen that in the "Horizontal" set up the hydrogen gas mostly flows over the sample. For larger sample sizes this means the core remains unexposed to the gas and remains unreduced. Consequently more grinding and heating cycles are required for the entirety of a larger sample to react than a smaller sample. During this extended reaction timeframe portions of the sample that reacted earlier to form a metastable phase slowly decompose under the reducing conditions. To combat this, an alternative, "vertical" set up was tried and is shown in Figure 3.8. This vertical set up allowed a greater proportion of the sample to be exposed to the flowing hydrogen and was thus expected to reduce both reaction time and decomposition. However the samples of $La_xSr_{2-x}Co_{0.5}Ir_{0.5}O_4$ (x= 0, 0.5) that were reacted using this set up decomposed after one heating cycle of 12 hours and as such it was deemed unsuitable from the preparation of large samples.

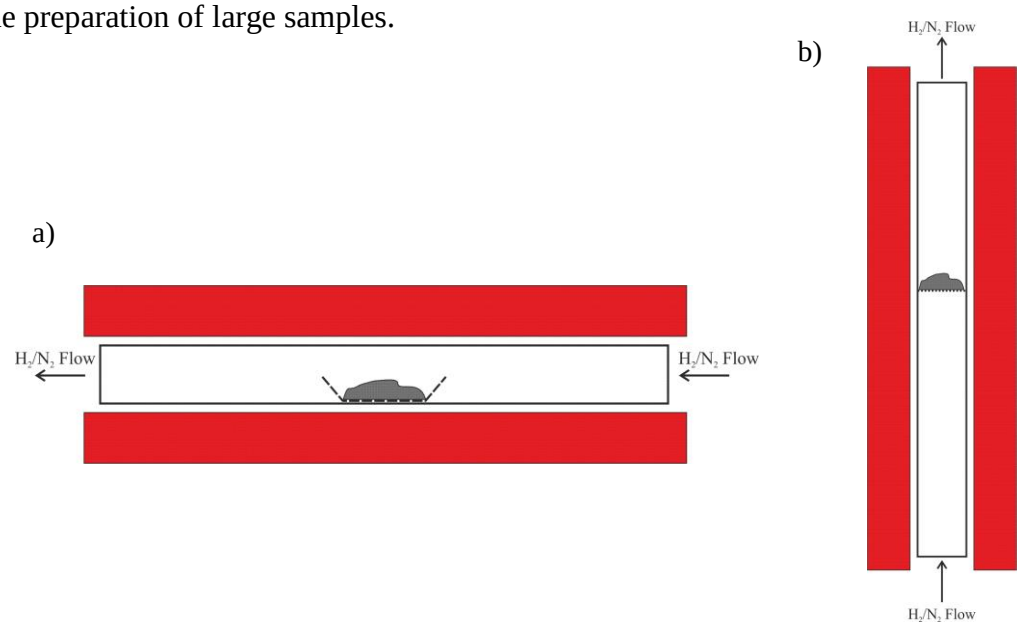

Figure 3.8: a) "Horizontal" set-up for the hydrogen gas reduction reaction b) "Vertical set-up for the hydrogen gas reduction reaction

These results show that reduction with hydrogen gas is effective and does an excellent job of synthesising metastable phases while removing the need from extra processing. However, this comes at the cost of increased reactivity which causes decomposition. This decomposition is not as extensive as that caused by the washing process discussed above and a larger sample of Sr_2FeIrO_4 was made this way for complete analysis (Chapter 4). While it is better than reduction with metal hydrides it is not without faults, most notably it cannot be relied upon to make pure samples. This makes full characterisation much more difficult.

3.3.2.3 Success of the zirconium getter

The final reduction method we used was a zirconium getter. This reaction is not a direct reaction of the reagents, instead the zirconium metal reacts with and draws away the partial pressure of oxygen formed at the surface of the parent oxide when it is heated. This results in the formation of zirconium oxide and conversion of the parent into a metastable phase.

This is a gentle reduction reaction compared to the reduction with hydrogen gas and does not produce by-products that need to be removed from the reaction mixture. Consequently, zirconium getter reactions were used to reduce the Ruddlesden-Popper parent oxides $Sr_2Fe_{0.5}Ir_{0.5}O_4$ and $La_xSr_{2-x}Co_{0.5}Ir_{0.5}O_4$ (x = 0, 0.5) with the expectation that we would be able to make larger, purer sample of their respective metastable phases. As discussed in Sections 3.2.4.3 and 3.2.5.3, and Chapters 6 and 8 this was largely successful. Using a zirconium getter a sample of $Sr_2Fe_{0.5}Ir_{0.5}O_3$ was made and samples of $La_xSr_{2-x}Co_{0.5}Ir_{0.5}O_3$ (x = 0, 0.5) were synthesised with some decomposition occurring during reaction. The results of these reductions show that for large samples the zirconium

getter method is highly effective and allowed fragile oxides to be reduced with relative ease and minimal processing.

The advantages of the zirconium getter method are quite clear, especially for fragile systems. During the reaction a pacifying layer of zirconium oxide forms on the surface of the zirconium reducing its reactivity over time. This works very well in tandem with the formation of metastable phases as it reduces the ability of the zirconium to react with the desired reduced phases. This is similar to the effect observed in hydride reactions however it is exaggerated due to the separation of the reactants. Thus we are given a greater window of time to observe and isolate the unusual phases we are pursuing.

3.3.2.4 Summary of reduction methods

The reductions we have conducted reaffirm that the group I/II metal hydrides are powerful reducing agents. However we have also shown that as research moves to more fragile oxide systems these hydrides may not be appropriate. To fill this void we have developed the use of hydrogen and zirconium as viable alternative reducing agents from topochemical reductions. Neither of these methods are without disadvantage but they are highly effective and should be given due consideration in future research.

3.3.3 Perovskite vs Ruddlesden-Popper parent phases

The comparative stability of the perovskite and Ruddlesden-Popper oxides with respect to reduction is one of the more curious results of this work. This is highlighted by the difference in reactivity of $La_xSr_{2-x}CoIrO_6$ (x= 0, 1) and $La_xSr_{2-x}Co_{0.5}Ir_{0.5}O_4$ (x= 0, 0.5). The reactions we have conducted show that no metastable phase derived from $LaSrCoIrO_6$ exists but reduction of $La_{0.5}Sr_{1.5}Co_{0.5}Ir_{0.5}O_4$ resulted in the synthesis of $La_{0.5}Sr_{1.5}Co_{0.5}Ir_{0.5}O_3$. The only significant difference between these two compounds is their structures, which are shown in Figure 3.9.

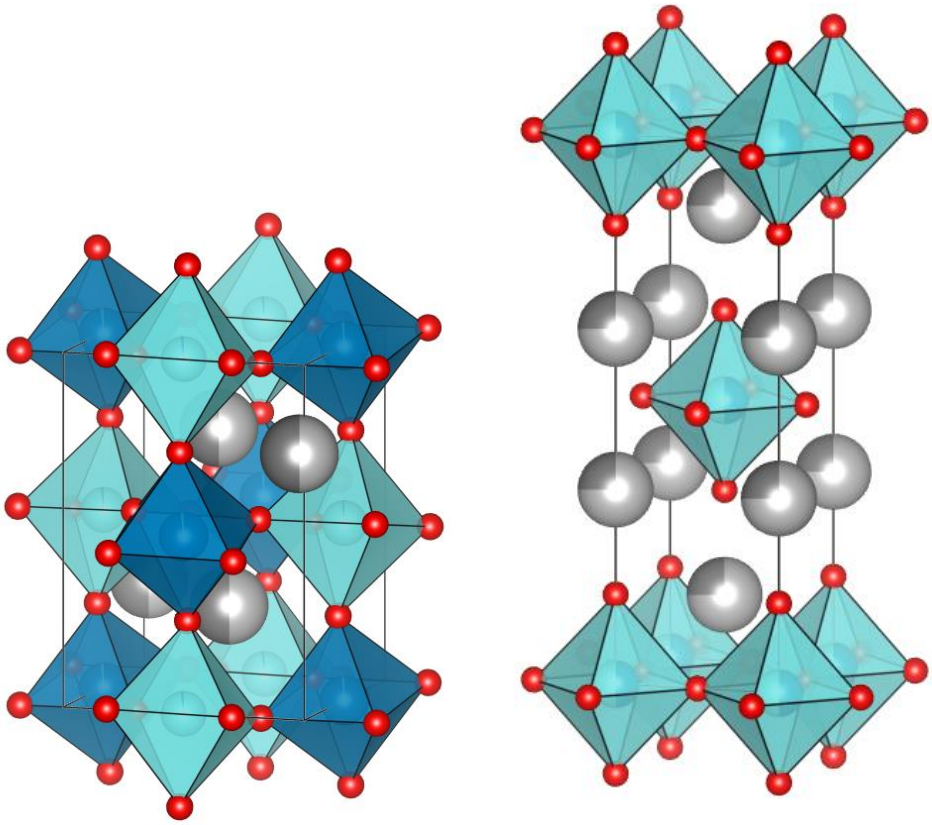

Figure 3.9: The unit cells of $LaSrCoIrO_6$ and $La_{0.5}Sr_{1.5}Co_{0.5}Ir_{0.5}O_4$

The n=1 Ruddlesden-Popper structure that $La_{0.5}Sr_{1.5}Co_{0.5}Ir_{0.5}O_4$ adopts can be regarded as ABO_3 perovskite blocks separated by rock salt layers of AO. In the case of $La_xSr_{2-x}Co_{0.5}Ir_{0.5}O_4$ (x= 0, 0.5) a layer of SrO is inserted into the structure which adds Sr^{2+} into the system. It is clear from the results discussed in Sections 3.2.3 and 3.2.5 that the addition of this rock salt layer increases the stability of the system such that a metastable phase can be isolated. We can consider why this rock salt layer increases the stability of a structure from a purely electrostatic view. The addition of Sr^{2+} increases the number of positively charged ions in the system which in turn increases the average positive charge experienced by each O^{2-} anion. This higher average charge increases the stability of the anion lattice which makes the structure more robust. This increased durability of the anion lattice acts to support the weak Ir-O lattice, adds an additional strengthening feature which gives stability to the structure and allows for the synthesis of a metastable phase

analogous to the infinite-layer phases previously observed. From these results we can posit that reduction of a Ruddlesden-Popper phase will increase the chances of a metastable phase with unique oxidation states and co-ordination geometries is possible where it is not possible to achieve the analogous metastable phase from the related perovskite. However previous experiments reported in the literature suggest the case is not this simple. The reductions of the Ruddlesden-Popper phases $Sr_2Fe_{0.5}Ru_{0.5}O_4$ and $Sr_2(Fe_{0.5}Ru_{0.5})_2O_7$[46] have been shown to be far more difficult than the analogous reduction of the perovskite $SrFe_{0.5}Ru_{0.5}O_3$. It appears impossible to isolate samples of $Sr_2Fe_{0.5}Ru_{0.5}O_3$ and $Sr_2(Fe_{0.5}Ru_{0.5})_2O_5$[46], which are regarded as "fully reduced" compounds. Instead the reactions result in samples with mixtures of reduced phases with different oxide contents. This is in stark contrast to the reduction of $SrFe_{0.5}Ru_{0.5}O_3$ and is attributed to B-site cation disorder. This disorder results in inhomogeneous samples which do not react uniformly with reducing agents. It is therefore more accurate to conclude that the addition of a rock-salt layer to an oxide system will increase its stability with respect to reduction if the samples are homogeneous have a near uniform reactivity with reducing agents In future this observation can be exploited to increase the chances of isolating reduced states.

3.4 Conclusions

The reactions of $CaMn_{0.5}Ir_{0.5}O_3$, Sr_2MIrO_6 (M = Fe, Co), $LaSrMIrO_6$ (M = Co, Ni), $Sr_2Fe_{0.5}Ir_{0.5}O_4$ and $La_xSr_{2-x}Co_{0.5}Ir_{0.5}O_4$ (x = 0, 0.5) with group I/II metal hydrides either resulted in total decomposition or the formation of a metastable phase. The isolation of these metastable phases proved impossible due to the chemical incompatibility of the washing procedures and the reduced products. In response to this two alternative reduction procedures were developed: reaction with flowing 95%/5% N_2/H_2 and reaction using a zirconium getter. Using these methods samples of reduced phases were produced

for complete characterisation. Both of these new procedures overcome the main disadvantage of the group I/II hydride method by removing the need for extra processing, however neither was able to produce a phase pure sample. This highlights how fragile the iridium-containing oxides are with respect to topochemical reduction. This work also showed that moving from the perovskite structure to the Ruddlesden-Popper structure increases the chances of isolating a reduced phase. This is because the extra ions in the rock salt layer add more charge to the system which increases the lattice energy.

Chapter 4 – Topochemical Reduction of Sr_2FeIrO_6

4.1 Introduction

In an attempt to make novel materials, a wide range of metastable phases containing low oxidation-state first-row transition metal cations, such as Mn^{I} [50], Fe^{II} [47], Co^{I} [49] and Ni^{I} [42], have been synthesised by topochemically reducing transition metal oxides with binary metal hydrides. In recent years this approach has been extended to include perovskite oxides containing the second row transition element ruthenium. It has been demonstrated that if ruthenium is the sole B-site cation, reduction results in complete decomposition. However coupling a ruthenium sub-lattice with another sub-lattice containing a 3*d* element has resulted in the synthesis of $SrFe_{0.5}Ru_{0.5}O_2$[44], $Na_2La_2Ti_2RuO_{10-x}$[90] and $LaSrNiRuO_4$[87].

The successful synthesis of novel, metastable phases containing ruthenium has provided a blueprint for the possibility of exploring the reduction chemistry of oxides containing 5*d* elements. The topochemical reduction of iridium complex oxides is of particular interest due to the large spin-orbit coupling Ir exhibits, the large number of parent phases that have been reported and the ease with which they can be made. Synthesis of metastable phases containing iridium would allow us to extend this work into the third row of the periodic table and observe how spin-orbit coupling affects the structure, electronic behaviour and magnetic properties of such materials.

Reduction of iridium-containing complex oxides also presents another vehicle with which we can explore the properties of 3*d*-5*d* mixed metal oxides. As previously outlined in this thesis (Chapter 1), 3*d*-5*d* mixed metal oxides exhibit a variety of interesting properties due to the contrasting localised and delocalised electronic behaviour of 3*d* and 5*d* cations

respectively. Topochemical reduction of such oxides will allow us to investigate if and how these behaviours change, and what properties arise as a result.

It has been demonstrated that $SrFeO_3$ can be readily reduced to form $SrFeO_2$[47] and that this metastable lattice is robust enough to stabilise the fragile ruthenium lattice in $SrFe_{0.5}Ru_{0.5}O_2$[44]. Consequently Sr_2FeIrO_6[22] is an ideal candidate as a parent phase and excellent starting point to explore the topochemical reduction chemistry of the complex oxides of iridium.

4.2 Synthesis

4.2.1 Synthesis of Sr_2FeIrO_6

A sample of Sr_2FeIrO_6 was prepared using a citrate gel method. Appropriate quantities of $SrCO_3$ (99.994%) and Fe (99.99%) were dissolved in a minimal quantity of a 1:1 mixture of conc. nitric acid and distilled water, then the required amount of IrO_2 (99.99%, dried at 700 ^oC for 2 hours) was added. Citric acid and analar ethylene glycol were added and the solution was heated whilst being stirred. The gel thus formed was allowed to dry and then combust in air. The subsequent product was ground into a fine powder, placed in an alumina crucible and heated at 1000 ^oC in air at a rate of 1 $^oC\ min^{-1}$ to remove the organic components of the sample. The resulting powder was pressed into a 13 mm diameter pellet and heated in air for two cycles of 2 days at 1100 ^oC.

The resulting powders were observed to be phase-pure by laboratory X-ray powder diffraction, with lattice parameters a = 5.55143(9) Å, b = 5.5733(8) Å, c = 7.84031(9) Å, α = 89.974(3)^o, β = 90.051(3)^o, γ = 90.142(1)^o, in good agreement with values reported in the literature (a = 5.54996(3) Å , b = 5.57847(3) Å , c = 7.84165(3) Å, α = 89.990(1) ^{o}, β = 90.059(1) ^{o}, γ = 90.079(1) ^{o}) [22].

4.2.2 Synthesis of Sr_2FeIrO_{6-x}

A full discussion on the reduction chemistry of iridium-containing oxides and the challenges this process presents, including that of Sr_2FeIrO_6, is given in Chapter 3. A sample of Sr_2FeIrO_{6-x} made for analysis by neutron powder diffraction was prepared by reacting approximately 1.25g of Sr_2FeIrO_6 with flowing 5%/95% N_2/H_2 using the method described in Chapter 2, Section 2.5. The sample was heated for 4 periods of 24 hours at 390 ^oC. Between heating cycles the samples were taken into an Ar filled glovebox, without being exposed to air, and ground with an agate pestle and mortar.

4.3 Results

4.3.1 Thermogravimetric analysis

To confirm the composition of the product of reduction, an oxidative thermogravimetric experiment was conducted. A small quantity of the reduced sample was heated under a flow of oxygen to reform Sr_2FeIrO_6, as confirmed by X-ray powder diffraction. During this reaction the sample gained 5.8% of its initial mass, an increase that is consistent with a composition of $Sr_2FeIrO_{4.11}$ for the reduced phase (Figure 4.1)

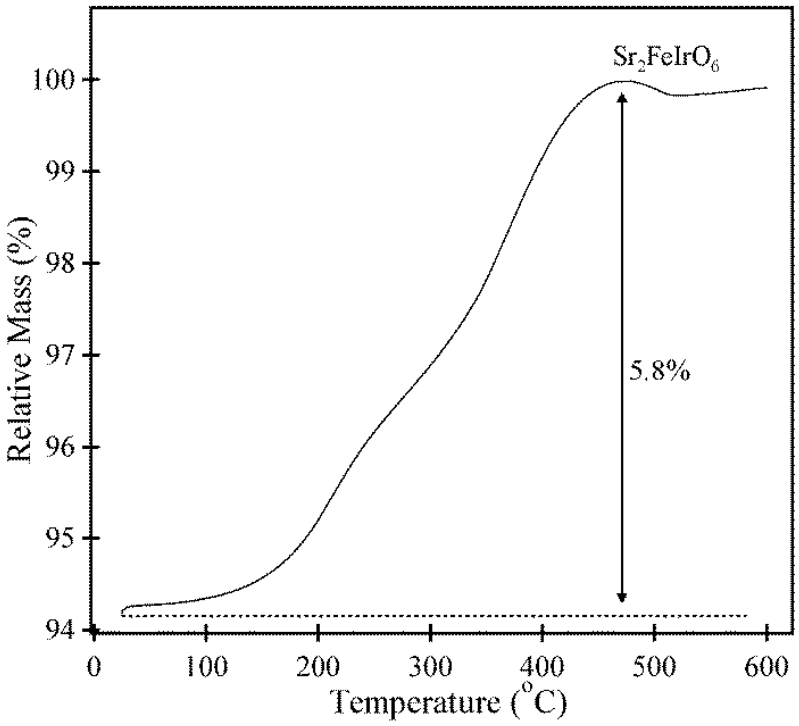

Figure 4.1: Thermogravimetric data collected during the oxidation of Sr_2FeIrO_{6-x} to Sr_2FeIrO_6

4.3.2. Structural characterisation of Sr_2FeIrO_4

4.3.2.1 Room temperature Synchrotron X-ray powder diffraction

X-ray powder diffraction data collected from the product of reaction of Sr_2FeIrO_6 with 5%/95% H_2/N_2, henceforth referred to as Sr_2FeIrO_4, could be indexed on the basis of a body-centred tetragonal unit cell with approximate lattice parameters a = 5.63 Å and c = 7.07 Å. These lattice parameters are similar to those of $LaSrNiRuO_4$, the product of the topochemical reduction of $LaSrNiRuO_6$, (a = 5.652(3) Å and c = 6.9151(4) Å) [87], suggesting Sr_2FeIrO_4 has a structure analogous to $LaSrNiRuO_4$.

High resolution X-ray powder diffraction data were collected from Sr_2FeIrO_4 using instrument I11 at the Diamond Light Source Ltd (Chapter 2, Section 2.7.1.2). A series of models were constructed based on the structural model of $LaSrNiRuO_4$[87] to determine the structure of Sr_2FeIrO_4. As the differences in the structures lie in the distortions of the

oxygen lattice, a subtle difference that would be difficult for X-ray diffraction data to determine in the presence of high electron count elements, the highest symmetry *I4/mmm* model was refined against the data to yield a good statistical fit. The observed, calculated and difference plots for the *I4/mmm* refinement are shown in Figure 4.2 and full details of the structural parameters are given in Table 4.1.

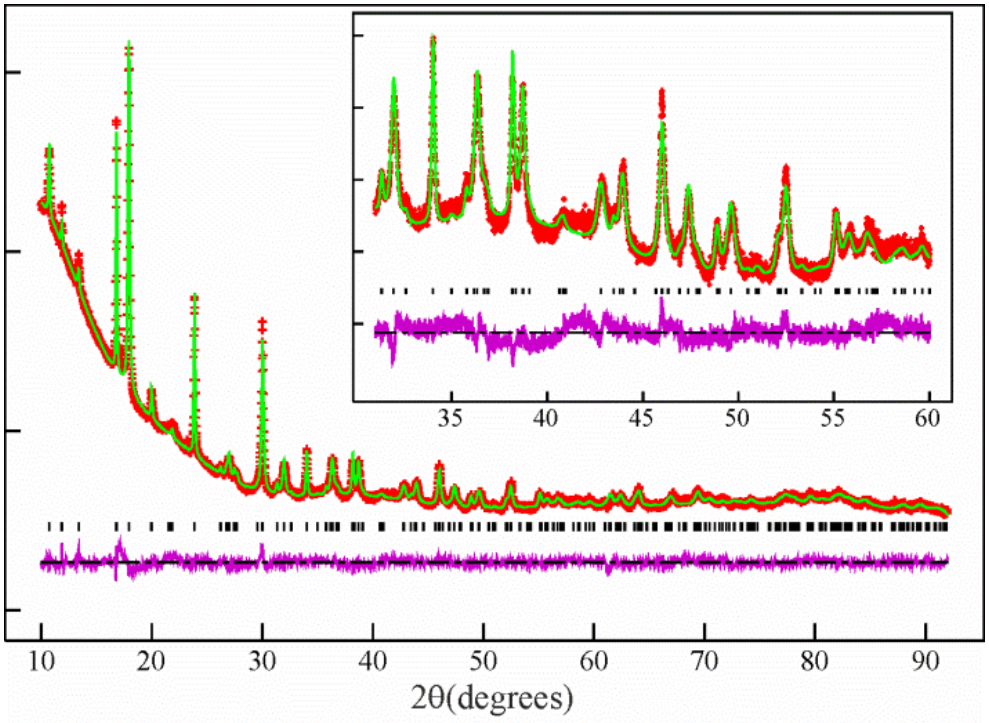

Figure 4.2: Observed, calculated and difference plots from the refinement of the *I4/mmm* structural model of Sr_2FeIrO_4 against synchrotron powder diffraction data collected at room temperature using the I11 instrument.

Atom	site	*x*	*y*	*z*	Fraction	U_{iso} (Å^2)
Sr	4*d*	½	0	¼	1	0.0050(5)
Fe/Ir(1)	2*a*	0	0	0	0.93/0.07	0.0055(3)
Ir/Fe(2)	2*b*	½	½	0	0.93/0.07	0.0055(3)
O	8*h*	0.2427(6)	0.2427(6)	0	1	0.0105(4)
Sr_2FeIrO_4 - Space Group: *I4/mmm* (# 139) Formula weight = 487.30 g mol^{-1}, Z = 2 *a* = 5.6469(1) Å, *c* = 7.0818(2) Å, volume = 225.82(1) Å^3						
Radiation source: Synchrotron X-ray, λ = 0.82626(1) Temperature: 300 K χ^2 = 5.35; *wRp*= 1.83 %; *Rp* = 1.36 %.						

Table 4.1: Parameters from the structural refinement of Sr_2FeIrO_4 against synchrotron powder diffraction data collected at room temperature.

4.3.2.2 Neutron Powder Diffraction

4.3.2.2.1 High temperature neutron powder diffraction data

Neutron powder diffraction data were collected from Sr_2FeIrO_4 at 150 K using the WISH instrument at ISIS (Chapter 2, Section 2.7.2.1). Magnetisation data (Section 4.3.3.1) indicates that there is no magnetically ordered state at T > 115 K, thus we can conclude all peaks in these diffraction data are structural. Neutron diffraction data allow us to rigorously interrogate the oxygen lattice of Sr_2FeIrO_4, due to the differences in neutron scattering lengths, in a way X-ray diffraction data do not.

The infinite-layer structure is able to twist and distort much like its parent the perovskite structure. This means that there are different possible structures infinite-layer phases can adopt. For example, $LaSrNiRuO_4$ adopts an *I2/m* structure in which the MO_4 units are diamonds with C_{2h} point symmetry and adopt an $a^oa^oc^-$ twisting regime, whereas $SrFe_{0.5}Ru_{0.5}O_2$ has an undistorted *P4/mmm* structure with perfectly square, untwisted MO_4 units with D_{4h} point symmetry. To determine the structure of Sr_2FeIrO_4 a series of models based on the B-site cation ordered infinite-layer structure of $LaSrNiIrO_4$ were constructed. These models are shown in Figure 4.3 and each exhibit varying degrees of distortion from the ideal symmetric infinite layer structure. All of these structures are defined by differences in the anion lattice. The *I4/mmm* model is the B-site rock salt cation ordered variant of the *P4/mmm* model that describes the structure of $SrFe_{0.5}Ru_{0.5}O_2$. In this model the MO_4 square planes are undistorted and do not rotate. The *I4/m* model also has square planes that remain symmetric but they are allowed to adopt an $a^oa^oc^-$ twisting pattern. The $P2_1$ model permits the MO_4 units to adopt a distorted

described above the *I2/m* model has MO_4 units that are allowed to distort from square co-ordination to diamond and these units are able to adopt an $a^oa^oc^-$ twisting regime.

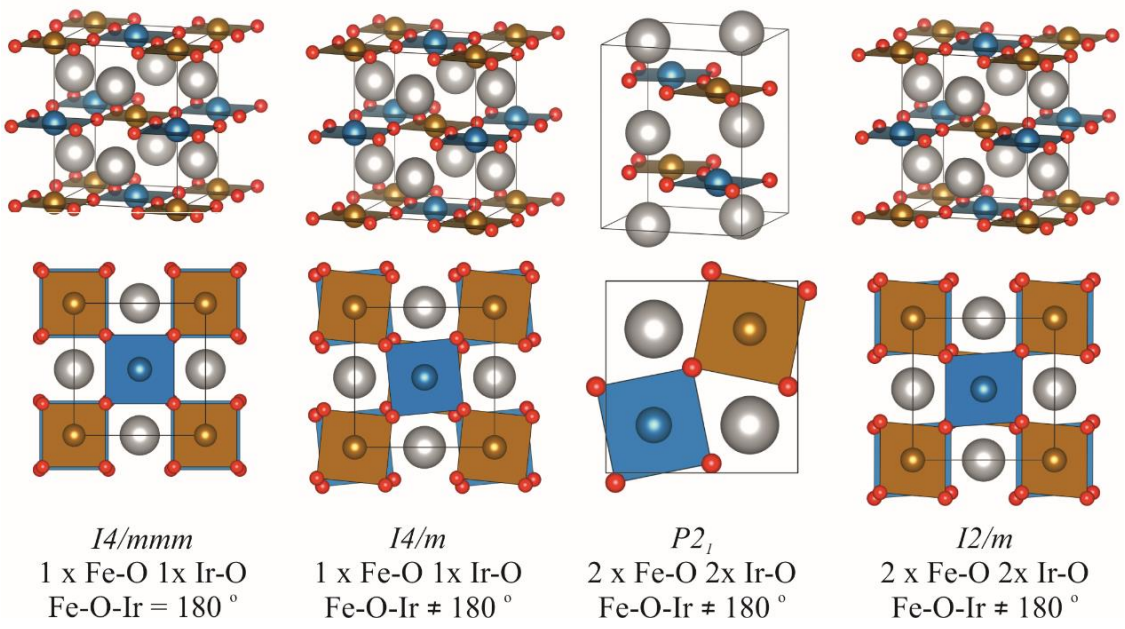

Figure 4.3: Structural models of the four possible structures of Sr_2FeIrO_4. Blue and gold spheres are iridium and iron respectively. The difference between the *P*2$_1$ and *I2/m* models are the opposing rotations. In *P*2$_1$ the rotation is in-phase and in *I2/m* the rotation is out of phases.

Each of these models was refined against the data collected at 150 K in order to determine the high temperature crystal structure of Sr_2FeIrO_4. The neutron scattering lengths of Fe and Ir are very similar (9.94(3) fm and 10.6(3) fm respectively[72]), as such the occupation of the two B-sites in each of the models was fixed to the values extracted from the refinement of synchrotron X-ray powder diffraction data. The data exhibited extra peaks associated with Ir, SrO and $Sr_2Fe_2O_5$ impurity phases, as such models of these phases were added to the refinement. Each refinement converged to give a good statistical fit. The fitting statistics from each of these refinements are shown in Table 4.2.

The best fit was achieved by refinement of the *I4/mmm* model against the data, which is consistent with the refinement conducted against the synchrotron X-ray powder

diffraction data. The observed, calculated and difference plots for the refinement of the *I4/mmm* model against each bank of the data are shown in Figure 4.4. Full details of the structural parameters and selected bond lengths are given in Tables 4.3 and 4.6 respectively.

Space Group	χ^2	wRp (%)	Rp (%)
*I*4/*mmm* (#139)	6.89	2.24	1.67
*I*4/*m* (#87)	6.92	2.25	1.68
$P12_11$ (#4)	7.12	2.35	1.79
*I*112/*m* (#12)	6.92	2.26	1.68

Table 4.2: Fitting statistics from the structural refinement of $SrFeIrO_4$ against neutron diffraction data collected at 150 K.

Atom	site	*x*	*y*	*z*	Fraction	U_{iso} (Å^2)
Sr	4*d*	½	0	¼	1	0.0050(5)
Fe/Ir(1)	2*a*	0	0	0	0.93/0.07	0.0055(3)
Ir/Fe(2)	2*b*	½	½	0	0.93/0.07	0.0055(3)
O	8*h*	0.2431(4)	0.2431(4)	0	1	0.0105(4)
Sr_2FeIrO_4 - Space Group: *I*4/*mmm* (# 139) Formula weight = 487.30 g mol^{-1}, Z = 2 *a* = *b* = 5.64555(8) Å, *c* = 7.0598(2) Å, volume = 225.013(8) Å^3 Phase fraction = 91.9(2) weight %						
Atom	site	*x*	*y*	*z*	Fraction	U_{iso} (Å^2)
Ir	4*a*	0	0	0	1	0.0010(1)
Ir – Space group: *Fm*-3*m* (# 225) Formula weight = 192.22 g mol^{-1}, Z = 4 *a* = *b* = *c* = 3.851(2) Å, volume = 57.12(10) Å^3 Phase fraction = 2.8(3) weight %						
Atom	site	*x*	*y*	*z*	Fraction	U_{iso} (Å^2)
Sr	4*a*	0	0	0	1	0.0010(1)
O	4*b*	½	0	0	1	0.0010(1)
SrO – Space group: *Fm*-3*m* (# 225) Formula weight = 103.61 g mol^{-1}, Z = 4 *a* = *b* = *c* = 5.161(1) Å, volume = 137.47(5) Å^3 Phase fraction = 1.1(2) weight %						
Atom	site	*x*	*y*	*z*	Fraction	U_{iso} (Å^2)
Sr(1)	8*h*	0.516	0.609	0	1	0.0025(1)
Fe(1)	4*a*	0	0	0	1	0.0025(1)
Fe(2)	8*i*	0.568	¼	0.458	½	0.0025(1)
O(1)	8*g*	¼	0.990	¼	1	0.0025(1)
O(2)	8*h*	0.0513	0.140	0	1	0.0025(1)
O(3)	8*i*	0.641	¼	0.123	½	0.0025(1)
$Sr_2Fe_2O_5$ – Space group: *Icmm* (# 74) Formula weight = 366.92 g mol^{-1}, Z = 4 *a* = 5.855(8) Å, *b* = 15.502(8) Å, *c* = 5.369(6) Å, volume = 487.3(8) Å^3 Phase fraction = 4.2(3) weight %						
Radiation source: Neutron Time of flight Temperature: 150 K χ^2 = 6.89; *wRp*= 2.24 %; *Rp* = 1.67 %.						

Table 4.3: Parameters from the structural refinement of Sr_2FeIrO_4 against neutron powder diffraction data collected at 150 K.

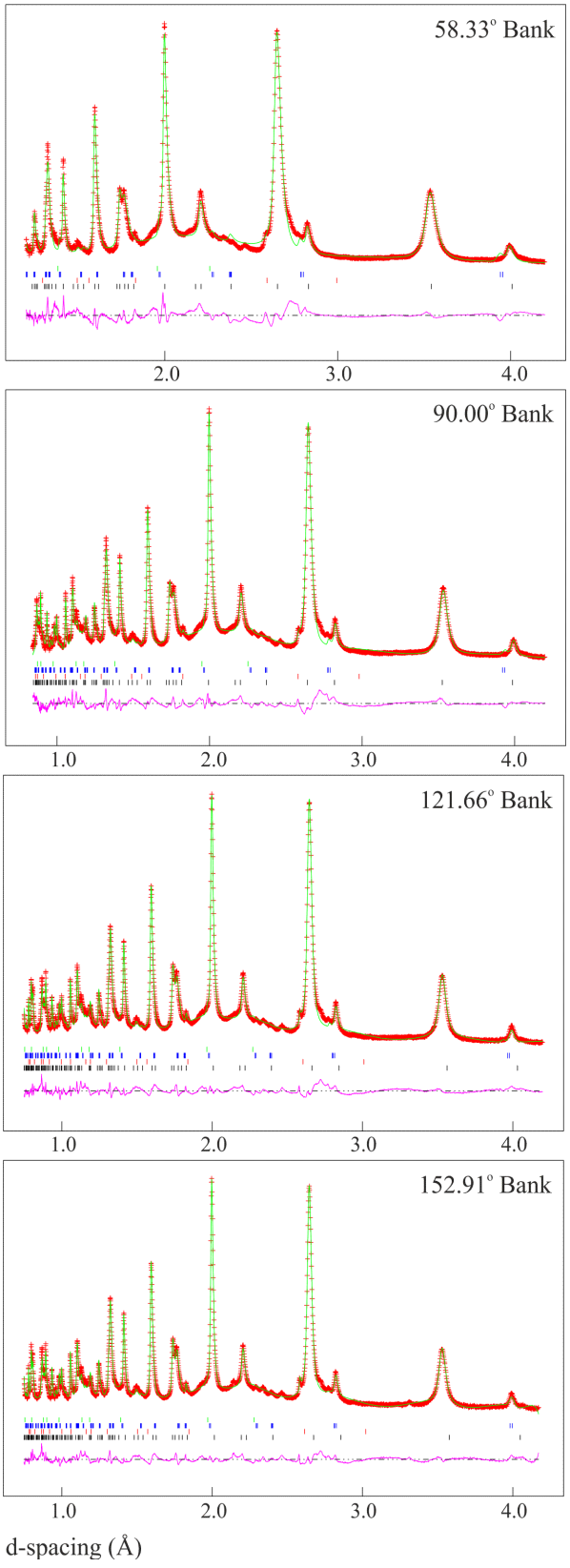

Figure 4.4: Observed, calculated and difference plots from the of the *I4/mmm* structural model of Sr_2FeIrO_4 against neutron powder diffraction data collected at 150 K using the WISH instrument. Tick marks correspond to the following: Green= $Sr_2Fe_2O_5$; Blue= SrO; Red= Ir and Black= Sr_2FeIrO_4

4.3.2.2.2 Low temperature neutron powder diffraction data

A further set of neutron powder diffraction data was collected from Sr_2FeIrO_4 at 1.5 K. Comparison of this data set with that collected at 150 K revealed two significant changes. Firstly the addition of Bragg peaks associated with long range magnetic order (see Section 4.3.3.2), and secondly the splitting of peaks that are structurally diagnostic. The splitting of these peaks is indicative of a lowering of the symmetry of the crystal structure of Sr_2FeIrO_4 and suggested a structural change had occurred. The logical explanation is that the structure distorted either by allowing the MO_4 square planes to change geometry or allowing these units to twist, or indeed both. The possible structural models that allow these distortions were discussed in Section 4.3.3.2.1 and are shown in Figure 4.3. To determine the low temperature structure each of these models was refined against the data collected at 1.5 K along with a model that accounted for the magnetic Bragg peaks (see Section 4.3.3.2). Each refinement converged to give a good statistical fit. The fitting statistics from each of these refinements are shown in Table 4.4.

Space Group	χ^2	wRp (%)	Rp (%)
I4/mmm (#139)	21.89	3.35	2.41
I4/m (#87)	21.37	3.32	2.37
$P12_11$(#4)	24.37	3.89	3.12
I112/m	18.45	2.94	2.08

Table 4.4: Fitting statistics from the structural refinement of $SrFeIrO_4$ against neutron diffraction data collected at 1.5 K.

The best fit was achieved by refinement of the *I2/m* model against the data, proving the structure distorted such that the previous square MO_4 units became diamonds and they twisted in an $a^oa^oc^-$ pattern. The observed, calculated and difference plots for the refinement of the *I2/m* model against each bank of the data are shown in Figure 4.5. Full details of the structural parameters and selected bond lengths are given in Tables 4.5 and 4.6 respectively.

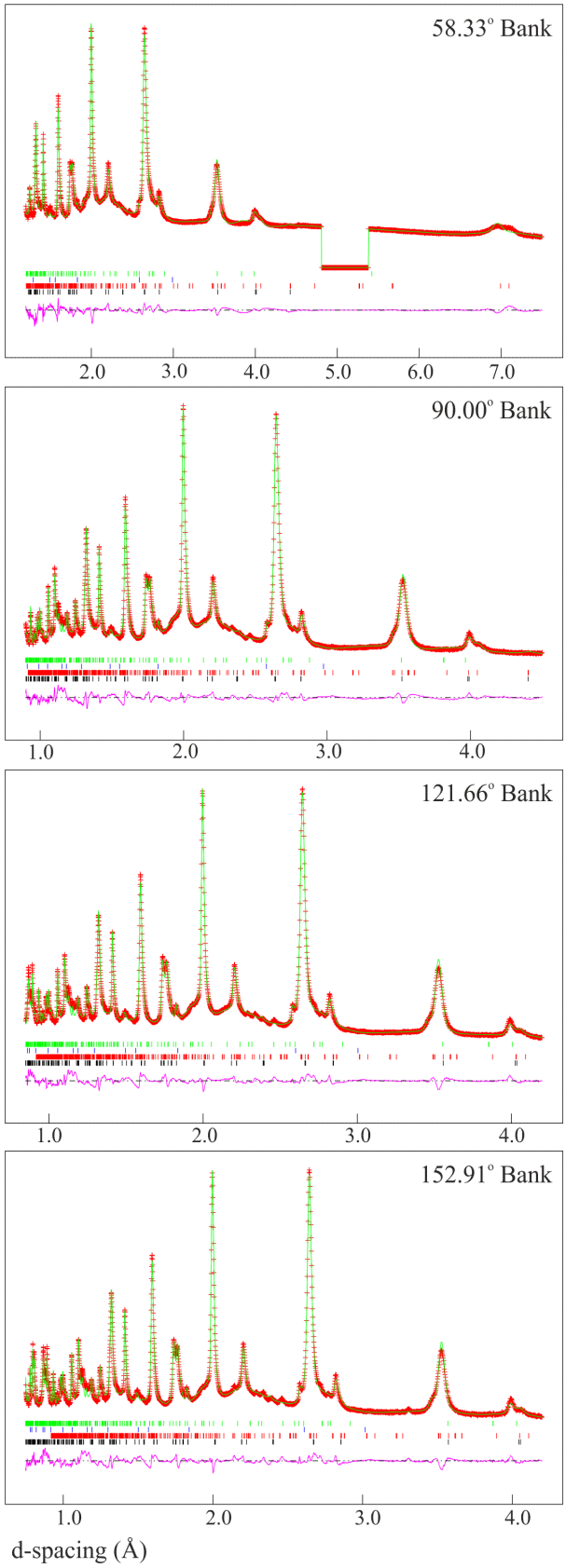

Figure 4.5: Observed, calculated and difference plots from the refinement of the *I2/m* structural model of Sr_2FeIrO_4 against neutron powder diffraction data collected at 1.5 K using the WISH instrument. Tick marks correspond to the following: Orange= Magnetic Unit Cell Green= $Sr_2Fe_2O_5$; Blue= SrO; Red= Ir and Black= Sr_2FeIrO_4

Atom	site	*x*	*y*	*z*	Fraction	U_{iso} (Å^2)
Sr	4*h*	½	0	0.249(1)	1	0.0028(4)
Fe/Ir(1)	2*a*	0	0	0	0.93/0.07	0.0055(3)
Ir/Fe(2)	2*b*	½	½	0	0.93/0.07	0.0055(3)
O(1)	4*i*	0.234(1)	0.745(1)	0	1	0.0077(4)
O(2)	4*i*	0.236(1)	0.247(1)	0	1	0.0077(4)
Sr_2FeIrO_4 - Space Group: *I* 1 1 2/*m* (# 12) Formula weight = 487.30 g mol^{-1}, Z = 2 *a* = 5.6446(1) Å *b* = 5.6435(1) Å, *c* = 7.0513(1) Å, γ = 89.830(4) volume = 224.623(9) Å^3 Phase fraction = 91.9 weight %						
Atom	site	*x*	*y*	*z*	Fraction	U_{iso} (Å^2)
Ir	4*a*	0	0	0	1	0.0010(1)
Ir – Space group: *Fm*-3*m* (# 225) Formula weight = 192.22 g mol^{-1}, Z = 4 *a* = *b* = *c* = 3.850(3) Å, volume = 57.07(8) Å^3 Phase fraction = 2.8 weight %						
Atom	site	*x*	*y*	*z*	Fraction	U_{iso} (Å^2)
Sr	4*a*	0	0	0	1	0.0010(1)
O	4*b*	½	0	0	1	0.0010(1)
SrO – Space group: *Fm*-3*m* (# 225) Formula weight = 103.61 g mol^{-1}, Z = 4 *a* = *b* = *c* = 5.141(1) Å, volume = 135.88(5) Å^3 Phase fraction = 1.1 weight %						
Atom	site	*x*	*y*	*z*	Fraction	U_{iso} (Å^2)
Sr(1)	8*h*	0.516	0.609	0	1	0.0025(1)
Fe(1)	4*a*	0	0	0	1	0.0025(1)
Fe(2)	8*i*	0.568	¼	0.458	½	0.0025(1)
O(1)	8*g*	¼	0.990	¼	1	0.0025(1)
O(2)	8*h*	0.0513	0.140	0	1	0.0025(1)
O(3)	8*i*	0.641	¼	0.123	½	0.0025(1)
$Sr_2Fe_2O_5$ – Space group: *Icmm* (# 74) Formula weight = 366.92 g mol^{-1}, Z = 4 *a* = 5.832(8) Å, *b* = 15.501(8) Å, *c* = 5.353(7) Å, volume = 483.9(9) Å^3 Phase fraction = 4.2 weight %						
Radiation source: Neutron Time of flight Temperature: 1.5 K χ^2 = 18.45; *wRp*= 2.94 %; *Rp* = 2.08 %.						

Table 4.5: Parameters from the structural refinement of Sr_2FeIrO_4 against neutron powder diffraction data collected at 1.5 K.

	Bond lengths (Å)		
	150 K	1.5 K	
Cation (M)	M-O	M-O(1)	M-O(2)
Fe	1.938(3)	1.950(7)	1.931(7)
Ir	2.054(3)	2.038(7)	2.067(7)
	Bond Angles (°)		
	150 K	1.5 K	
	Fe-O-Ir	Fe-O(1)-Ir	Fe-O(2)-Ir
	180	175.1(3)	177.4(3)

Table 4.6 Selected bond length and angles from the refined structures of Sr_2FeIrO_4 at 150 K and 1.5 K

4.3.3 Magnetic Characterisation of Sr_2FeIrO_4

4.3.3.1 SQUID Magnetometry

Magnetisation data were collected from Sr_2FeIrO_4 in an applied field of 100 Oe in the temperature range $5 \leq T / K \leq 300$. The zero-field cooled (ZFC) data, field cooled (FC) data and magnetisation-field isotherms collected at 300 K and 5 K are shown in Figure 4.6. At temperature exceeding 115 K the ZFC and FC data are weakly divergent. One cause of divergence between the ZFC and FC data would be the presence of a ferromagnetic impurity, in this case the prime suspect would be elemental iron. However the magnetisation isotherm collected at 300 K shows no hysteresis indicating this divergence is not due to iron or any other ferromagnetic impurity. At temperatures below 115 K the ZFC and FC data diverge strongly. The magnetisation isotherm collected at 5 K exhibits a small degree of hysteresis and is slightly offset from the origin. These observations indicate that at 115 K Sr_2FeIrO_4 undergoes a long range magnetic transition in which the system becomes an antiferromagnet with a degree of frustration.

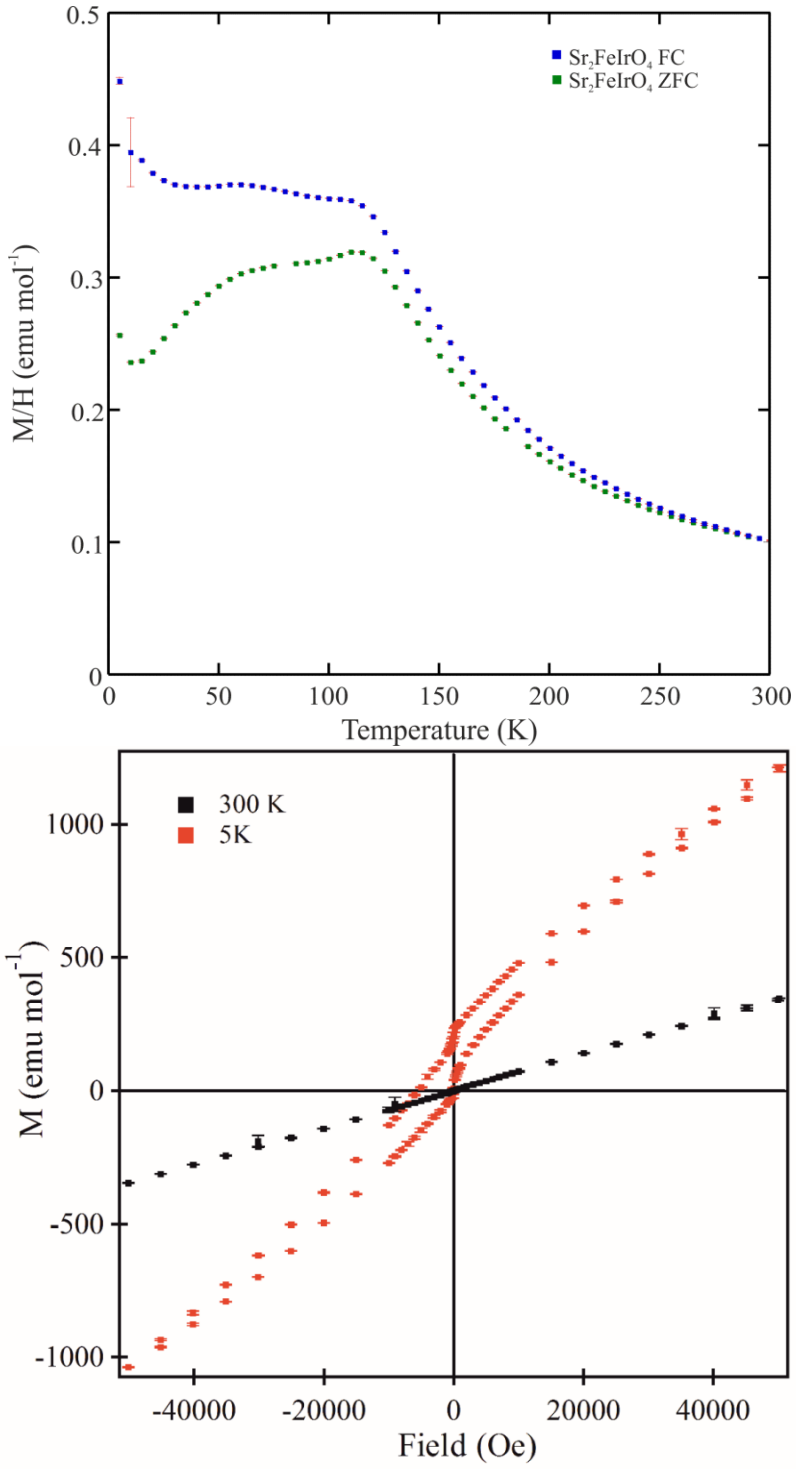

Figure 4.6: a) Zero-field cooled and field-cooled magnetisation data collected from Sr_2FeIrO_4. b) Magnetisation-field isotherms collected from Sr_2FeIrO_4

A ferrosubtraction measurement was conducted on the same sample of Sr_2FeIrO_4. The plots of the paramagnetic susceptibility and saturated ferromagnetic moment data extracted from the measurement are shown in Figure 4.7. The plot of the saturated ferromagnetic moment shows there is a steady increase in the moment at temperatures below 120 K. At 120 K the moment begins to plateau. At 25 K the moment increases dramatically. These results suggest that there are two events: one at 120 K which is the onset of antiferromagnetic order and another at 25 K which is the canting of the antiferromagnetic state. In contrast the paramagnetic susceptibility shows only one event. The susceptibility gently increases until 25 K and then decrease. The fact that the paramagnetic susceptibility does not exhibit the magnetic event at 120 K suggests Sr_2FeIrO_4 does not obey the Curie-Weiss law and is frustrated.

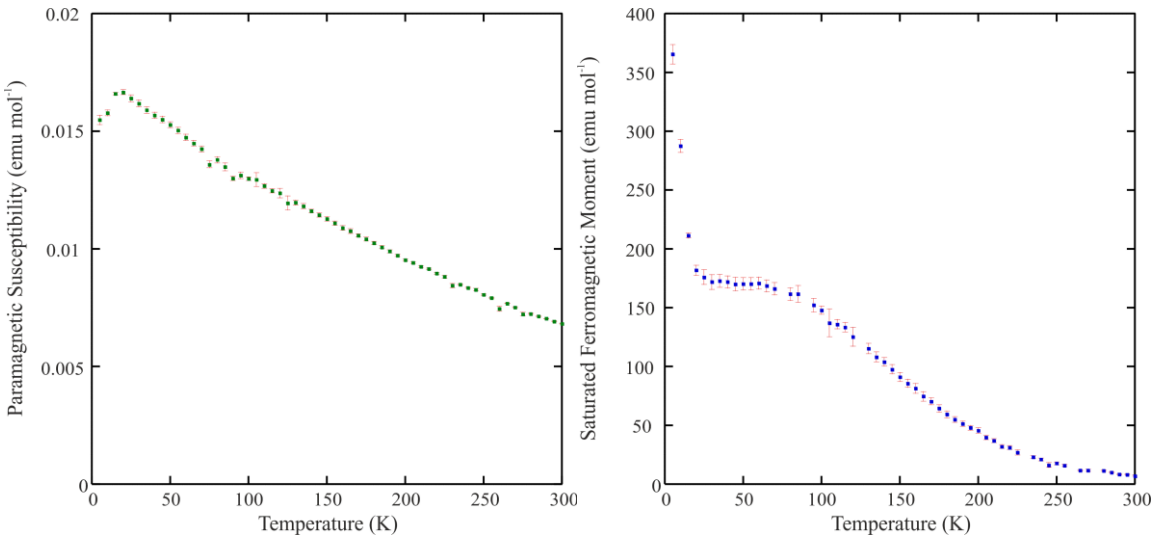

Figure 4.7: a) Paramagnetic susceptibility extracted from a ferrosubtraction measurement carried out on Sr_2FeIrO_4 b) Saturated ferromagnetic moment extracted from a ferrosubtraction measurement carried out on Sr_2FeIrO_4.

4.3.3.2 Neutron powder diffraction data

Comparison of the neutron diffraction data collected at 150 K and 1.5 K showed that the 1.5 K data had additional peaks not present in the 150 K data. These additional peaks were attributed to magnetic order due to the magnetisation behaviour exhibited in the SQUID magnetization data (section 4.3.3.1). The peaks could be indexed on the basis of a $\sqrt{2}\,x\,\sqrt{2}\,x\,2$ expansion of the refined crystallographic unit cell. A series of possible magnetic models were constructed using this unit cell. Their diffraction patterns were simulated and compared to the observed magnetic peaks. Models which contained spin contributions from only the iron cations did not correctly account for the magnetic peaks present in the data. The best match to the data was achieved by using the model shown in Figure 4.8 in which the Fe and Ir lattices are G-type antiferromagnetically ordered with the spins aligned such that they lie in the MO_4 planes. This magnetic model was refined against the neutron powder diffraction data collected at 1.5 K to give an excellent fit. The ordered magnetic moments were refined to be 2.84(7) μ_B per Fe centre and 1.09(12) μ_B per Ir centre. Figure 4.9 shows the observed, calculated and difference plots for the combined magnetic and structural refinement against the 58° bank data. The refined nuclear and magnetic structural parameters are detailed in Table 4.7.

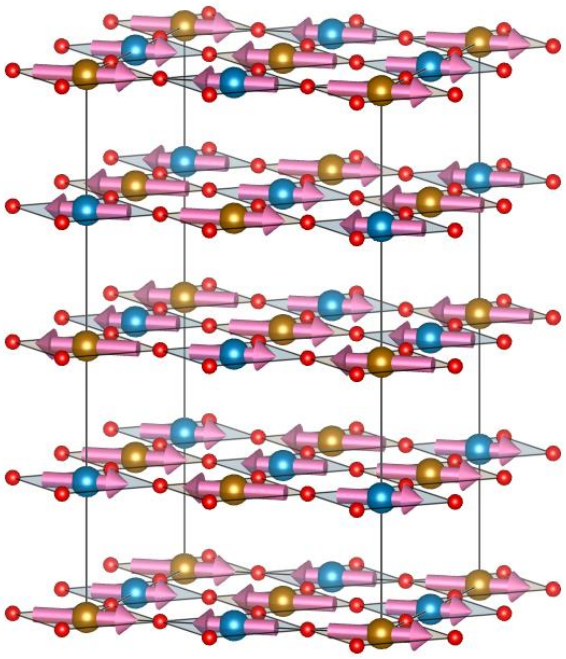

Figure 4.8 The refined magnetic unit cell of Sr_2FeIrO_4. The blue and gold spheres are iridium and iron respectively.

Atom	*x*	*y*	*z*	M_x	M_y	M_z
Fe(1)	0	0	0	2.84(7)	0	0
Fe(2)	½	½	0	-2.84(7)	0	0
Fe(3)	½	0	¼	-2.84(7)	0	0
Fe(4)	0	½	¼	2.84(7)	0	0
Fe(5)	0	0	½	-2.84(7)	0	0
Fe(6)	½	½	½	2.84(7)	0	0
Fe(7)	½	0	¾	2.84(7)	0	0
Fe(8)	0	½	¾	-2.84(7)	0	0
Ir(1)	½	0	0	1.09(12)	0	0
Ir(2)	0	½	0	-1.09(12)	0	0
Ir(3)	0	0	¼	-1.09(12)	0	0
Ir(4)	½	½	¼	1.09(12)	0	0
Ir(5)	½	0	½	-1.09(12)	0	0
Ir(6)	0	½	½	1.09(12)	0	0
Ir(7)	0	0	¾	1.09(12)	0	0
Ir(8)	½	½	¾	-1.09(12)	0	0

Table 4.7: The magnetic model refined for Sr_2FeIrO_4 against neutron powder diffraction data collected at 1.5 K.

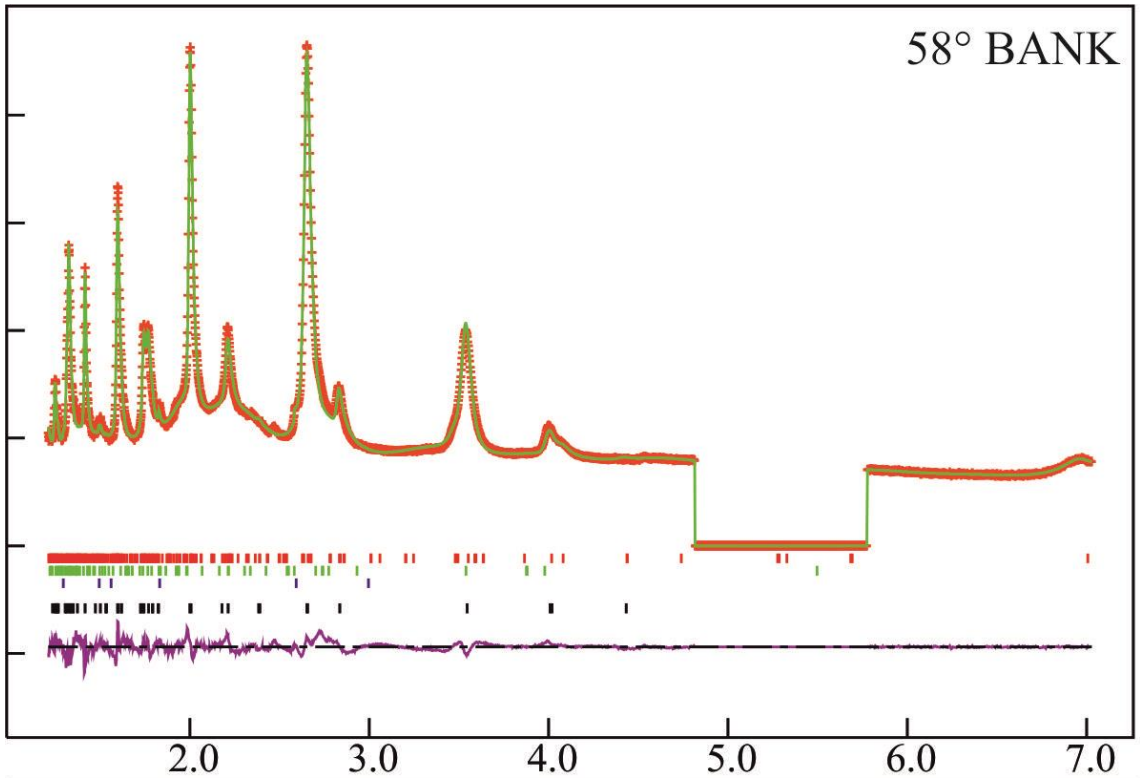

Figure 4.9: Observed, calculated and difference plots from the 58 º bank for refinement of the *I2/m* structural model of Sr_2FeIrO_4 against neutron powder diffraction data collected at 1.5 K using the WISH instrument. Tick marks correspond to the following: Orange= Magnetic Unit Cell Green= $Sr_2Fe_2O_5$; Blue= SrO; Red= Ir and Black= Sr_2FeIrO_4

4.3.3.3 Variable temperature neutron powder diffraction data

Neutron powder diffraction data were collected from Sr_2FeIrO_4 at various temperatures between 1.5 K and 150 K. The patterns collected at 115 K and below are all similar, varying only in the intensity of the Bragg peaks associated with magnetic order. The ordered moment was refined to zero for both iron and iridium in patterns collected above 115 K. Furthermore the distortion of the MO_4 units was quantified by comparing the Ir-O and Fe-O bond lengths extracted from each of the refinements. Figure 4.10 shows the evolution of the refined magnetic moment and MO_4 unit distortion as a function of temperature.

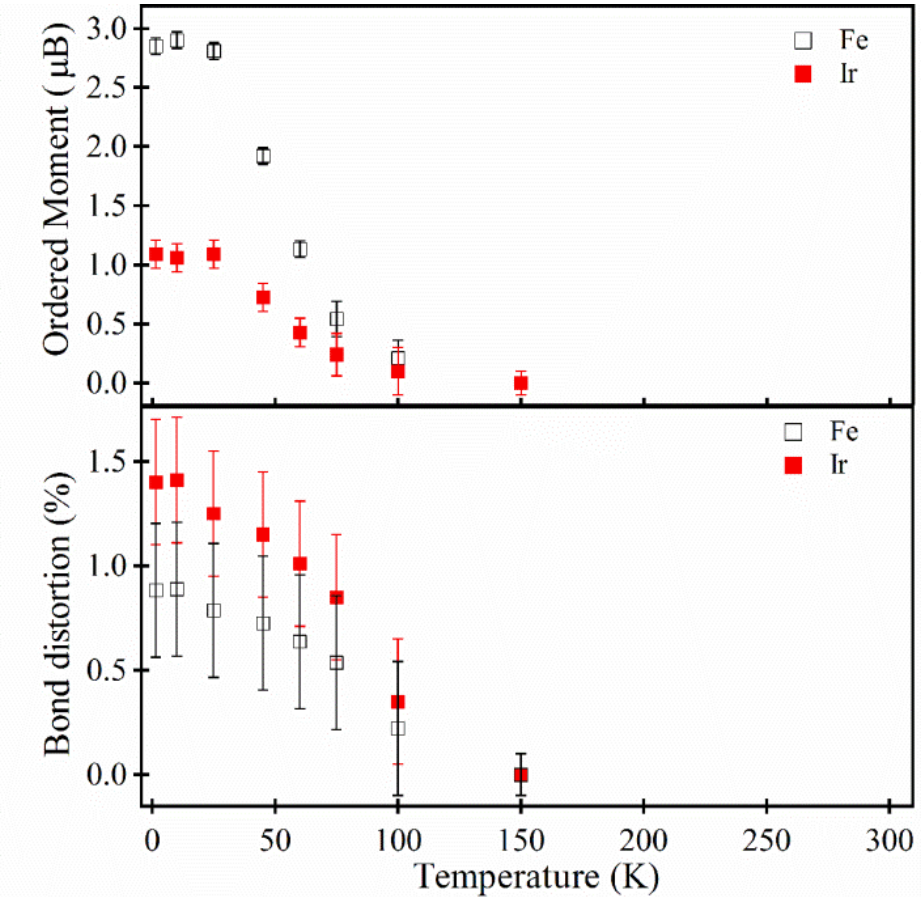

Figure 4.10: The ordered magnetic moment on Fe and Ir centres and bond distortion index defined as [[M-O(1)]-[M-O(2)]]/[0.5x[[M-O(1)+[M-O(2)]]] extracted from fits to neutron diffraction data

4.4 Discussion

4.4.1 Stability of Sr_2FeIrO_4

The stability of Sr_2FeIrO_4 is, in many respects, remarkable. The composition and magnetic data clearly indicated that both the iron and iridium cations have an oxidation state of +2. Ir^{II} is, in general, a rare oxidation state and to the best of our knowledge has never been reported in an extended oxide material. In extended oxide materials the most prevalent oxidation states of iridium are Ir^{IV} and Ir^{V} of which there are numerous examples with a variety of structures[21-22, 24, 66, 91-94]. The dominance of high oxidation states is a salient feature of the oxide chemistry of 5*d* elements, a feature that further highlights how unique Sr_2FeIrO_4 is. In contrast to the solid state mononuclear organometallic complexes containing Ir^{II} centres have been reported[95-97], in fact this is the only field in which this oxidation state of iridium appears in the literature. However, they are nowhere near as prevalent as their Ir^{I} and Ir^{III} counterparts, of which there are numerous examples. Furthermore to date no data has been published on the electrochemical potential of aqueous Ir^{II} so its stability has not been quantified. This lack of data and scarcity of examples suggest Ir^{II} is an unstable species. This instability is not surprising if we consider the electronic configuration of Ir^{II} shown in Figure 4.11. In the square planar co-ordination the $d_{xz/yz}$ orbital is partially occupied. This is a precarious state as it is close to the energetically desirable d^8 configuration that is dominant in square planar compounds. Consequently Ir^{II} compounds are likely to disproportionate to square planar Ir^{I} and low spin octahedral Ir^{III} both of which are far lower in energy and thus preferable. This instability of Ir^{II} is directly analogous to the instability of Pt^{III} and the dominance of the +2 and +4 oxidation states in platinum chemistry[98].

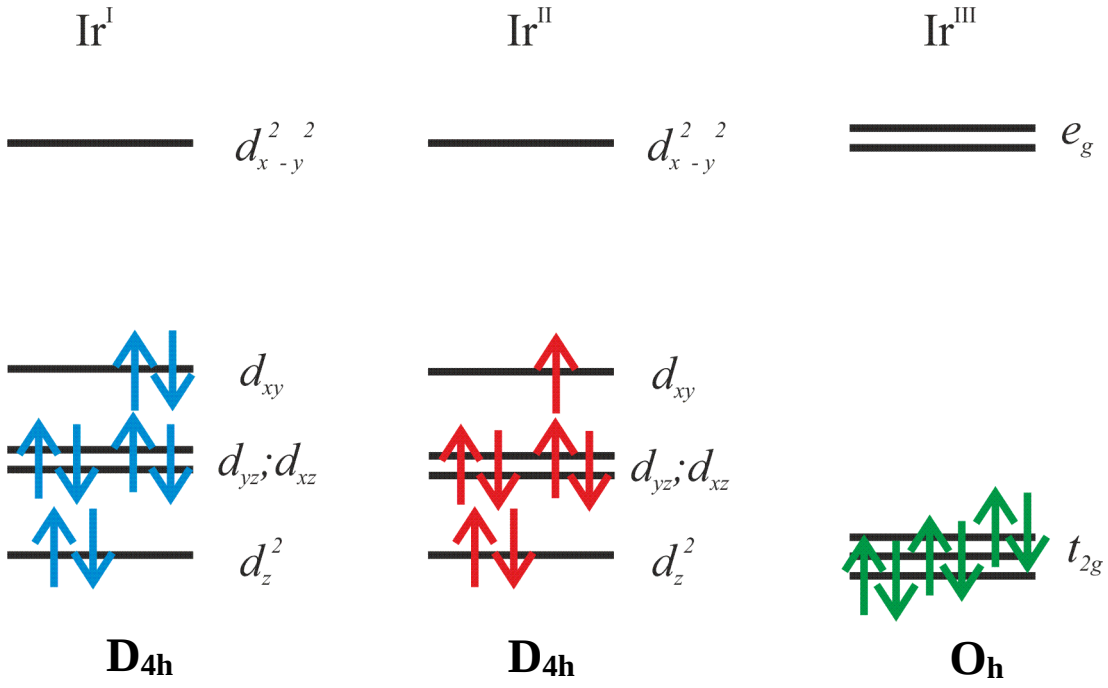

Figure 4.11: The proposed electronic states of square planar Ir^{II}, square planar Ir^{I} and octahedral Ir^{III} in an oxide ligand field

The instability and sparsity of Ir^{II} compounds presented in the literature highlights the exceptionality of Sr_2FeIrO_4. It is clear that the stability of Ir^{II} in Sr_2FeIrO_4 must be due to the imposition of kinetic stability by the Fe^{II} lattice. However the stability of this iron sub-lattice is also surprising. Metastable phases containing $Fe^{II}O_4$ units have previously been reported. The most notable of these is $SrFeO_{2+\delta}$[47], which was the first example of square planar Fe^{II} and can be regarded as one of the sublattices of Sr_2FeIrO_4. These compounds are very stable but they either contain exclusively iron on the B-site[47, 53, 99] or are derived from solid solutions of iron and ruthenium compounds with a 1:1 distribution of iron and ruthenium on the B-site[44, 46]. Previous attempts synthesise an iron-based metastable phase with a doped A-site or a B-site which is partially occupied by other 3*d* metals failed[100], presumably because the doping disrupted the stability of the lattice. Consequently,

Sr_2FeIrO_4 is the first metastable phase to have ordered iron and an element on the B-site not from group 8, as well as being the first reported extended oxide to contain Ir^{II}.

The extraordinary stability of Sr_2FeIrO_4 is further illustrated by its decomposition, most notably when the reduction is conducted using CaH_2 as a reducing agent (Chapter x). In contrast to other metastable infinite-layer phases Sr_2FeIrO_4 does not survive the washing process required to remove calcium-containing products from the reaction mixture. It is evident that Sr_2FeIrO_4 is markedly less stable than $SrFeO_2$, $SrFe_{0.5}Ru_{0.5}O_2$ and $LaSrNiRuO_4$, all with which Sr_2FeIrO_4 shares chemical and/or structural features. This indicates that the iridium-oxygen lattice is far more fragile than the analogous iron and ruthenium lattices and that the stable $SrFeO_2$ sublattice is only just able to hold together the $SrIrO_2$ sublattice. The comparative stabilities of $SrFe_{0.5}Ru_{0.5}O_2$ and Sr_2FeIrO_4 are surprising as ruthenium and iridium are equally electronegative (χ = 2.0 Pauling units) thus we might expect analogous compounds containing either ruthenium or iridium to behave similar with respect to reduction chemistry. In the specific case of $SrFe_{0.5}Ru_{0.5}O_2$ vs Sr_2FeIrO_4 one might have expected the latter to be more stable due to the cation order of Sr_2FeIrO_4 reducing the prevalence of iridium-rich areas which would be less stable due to the absence of the robust, stabilising iron lattice. This rationale only considers the behaviours of the cations which is too simple an assumption in an extended oxide phase. The difference in stabilities lies in the strength of the B-O bonds. The reported values for the bond enthalpies of Ru-O and Ir-O are 528 kJ mol^{-1} and 414 kJ mol^{-1} respectively[89] clearly showing that Ru-O bonds are stronger than Ir-O, a difference attributed to the better overlap of the Ru 4d and O 2p orbitals compared to that of the more radially extended Ir 5*d* orbitals. Whilst these values are derived from thermodynamic reactions they still provide valuable insight. It is therefore not surprising that $SrFe_{0.5}Ru_{0.5}O_2$ and $LaSrNiRuO_4$ are chemically far more stable than Sr_2FeIrO_4.

4.4.2 High temperature structure and magnetism

The refinement of room temperature X-ray synchrotron data and neutron diffraction data collected at 150 K confirm that Sr_2FeIrO_4 is an infinite-layer phase that retains the B-site cation order present in the parent phase, Sr_2FeIrO_6. Structural characterisation conducted clearly shows that above the magnetic ordering temperature Sr_2FeIrO_4 adopts a highly symmetric tetragonal structure described by a model with *I4/mmm* space symmetry (Section 4.3.3.2.1) The average co-planar bond lengths in Sr_2FeIrO_6, the bond lengths of Sr_2FeIrO_4 and $SrFeO_{2+\delta}$ are shown in Table 4.8. Sr_2FeIrO_4 is the second reported compound that contains square planar Ir, the first being Na_4IrO_4[101].

Compound	Fe-O Bond length (Å)	Ir-O Bond length (Å)
Sr_2FeIrO_4	1.938(3)	2.054(3)
$SrFeO_{2+\delta}$	1.995	-
Sr_2FeIrO_6	1.981	1.969

Table 4.8: Average Fe-O and Ir-O bond lengths in Sr_2FeIrO_4, $SrFeO_{2+\delta}$ and Sr_2FeIrO_6

Comparison of these bond lengths shows that upon reduction the average Ir-O bond length increases whereas the average Fe-O bond length decreases. Furthermore the Fe-O bond in Sr_2FeIrO_4 is shorter than that in $SrFeO_{2+\delta}$ indicating that the $FeIrO_4$ layers are under compression.

Magnetisation data (Figure 4.6) shows that above 115 K the zero-field-cooled and field-cooled traces are divergent. This break from classical Curie-Weiss behaviour indicates that there is either a magnetic impurity in the sample, in this case, iron metal is the obvious candidate, or that the spins in Sr_2FeIrO_4 are strongly interacting. A magnetisation isotherm collected as a function of the field at 300 K (Figure 4.6) is a straight line passing through the origin clearly showing that no ferromagnetic impurity is present in the compound. Consequently, it is apparent that the atypical magnetic behaviour of Sr_2FeIrO_4 observed is most likely due to the spins in the system not being dilute or interacting

weakly, as assumed by the Curie-Weiss law. The paramagnetic susceptibility data extracted from the ferrosubtraction measurement conducted on Sr_2FeIrO_4 could not be fit to the Curie-Weiss law and suggests that the spins in Sr_2FeIrO_4 are strongly interacting but frustrated.

4.4.3 Low temperature structure and magnetism

At low temperatures, Sr_2FeIrO_4 exhibits highly unusual behaviour. Magnetisation data (Figure 4.6), data extracted from a ferrosubtraction measurement (Figure 4.7) and refinement of neutron diffraction data (Section 4.3.3) illustrate that at 120 K Sr_2FeIrO_4 undergoes a magnetic transition to an antiferromagnetically ordered state that is described by the magnetic unit cell shown in Figure 4.8 that becomes canted at 25 K. Upon initial inspection this unit cell appears to be highly unusual especially when we consider the coupling regime shown in Figure 4.12. The Goodenough-Kanamori rules predict that both the in-plane $Fe(d_{x^2-y^2})^1$-O2p-$Ir(d_{x^2-y^2})^0$ superexchange (J_1) and the interlayer $Fe(d_{xz/yz})^2$-$Ir(d_{xz/yz})^4$ direct exchange (J_2) should be ferromagnetic, resulting in a ferromagnetically ordered ground state. Neutron diffraction data clearly shows this is not the case and that the magnetic ground state is far more complex. First let us consider the nearest neighbour couplings in the ab-plane. Along the b-axis the nearest neighbour Fe-Ir coupling (J_{1y}) is indeed ferromagnetic; however the coupling along the a-axis is antiferromagnetic (J_{1x}).This is clearly not the simple ferromagnetic coupling predicted. Now let us consider the coupling along the c-axis. The interaction between the cations in the c=0 layer with those in the c = ¼ layer (J_{2a}) is ferromagnetic, as expected, but the coupling between the cations in the c = ¼ and the c = ½ layers (J_{2b}) is antiferromagnetic. These conflicting interactions are clear evidence that the magnetic ground state cannot be defined by the nearest neighbour Fe-Ir interactions. Consequently we must consider other exchange pathways to account for the magnetic ground state. Figure 4.12 shows the magnetic unit

cell of Sr_2FeIrO_4 split into its constituent Fe and Ir sublattices. Each of these sublattices is a G-type antiferromagnetic lattice in which the nearest neighbour Fe-Fe, or Ir-Ir, interaction is antiferromagnetic. In the magnetic unit cell of Sr_2FeIrO_4 these interactions are the next-nearest neighbour interactions. The uniformity of the Ir-Ir and Fe-Fe couplings, in contrast to the frustrated nearest-neighbour interactions, suggest that it in fact is these interactions that define the magnetic ground state.

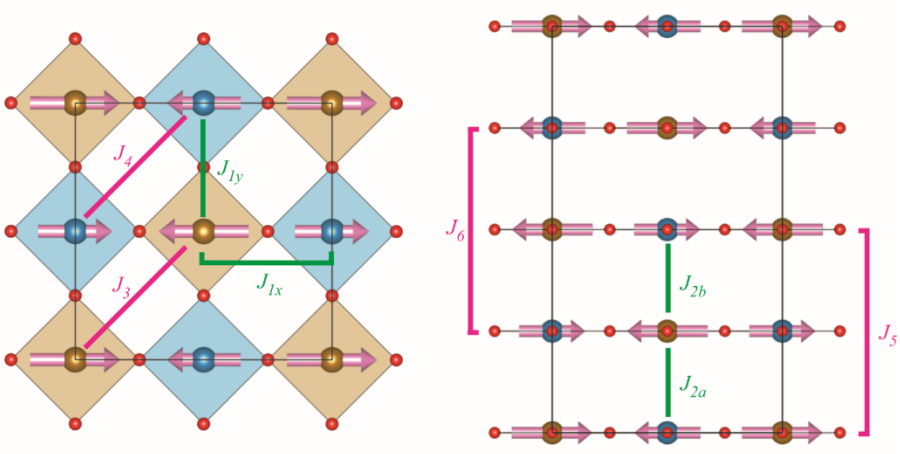

Figure 4.12: The magnetic coupling scheme of Sr_2FeIrO_4. Blue and gold spheres are iridium and iron respectively.

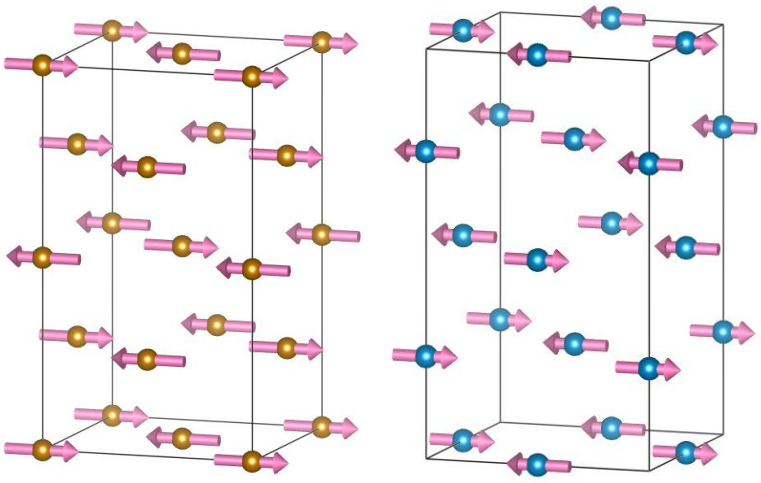

Figure 4.13: The iron and iridium magnetic sublattices of Sr_2FeIrO_4. Blue and gold spheres are iridium and iron respectively.

To fully understand why this ground state in dominant we must consider the subtle interplay of the different couplings. Figure 4.14 shows a representation of the ab-plane of Sr_2FeIrO_4's magnetic structure and defines three key interactions: J_α is the Fe-Ir nearest neighbour interaction, which we will assume is equal in both a and b; J_β is the next-nearest Fe-Fe coupling; and J_γ is the next-nearest neighbour Ir-Ir coupling. If we consider the strength of these couplings relative to each other we can describe four distinct magnetic states, the three most significant of which are shown in Figure 4.15.

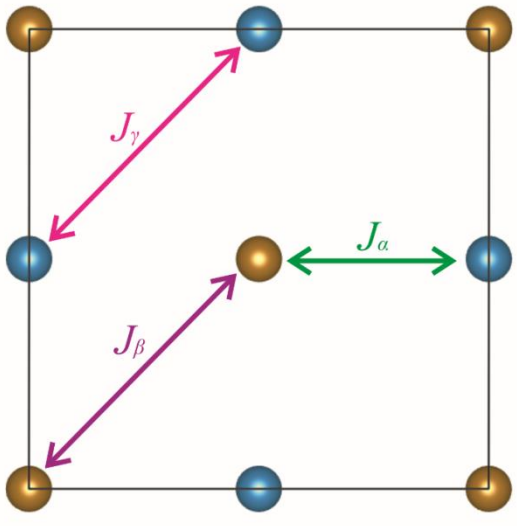

Figure 4.14: The three key magnetic couplings in the *ab*-plane of Sr_2FeIrO_4. Blue and gold spheres are iridium and iron respectively.

If all three couplings are roughly the same we would expect the system to be a spin glass as full resolution of these couplings is impossible within the constraints imposed by the symmetry of the structure. The presence of magnetic Bragg peaks proves this cannot be the case. If $J_\alpha > J_\beta, J_\gamma$ the result would be the simple ferromagnetic state predicted by the Goodenough-Kanamori rules. As previously discussed, this is not the ground state and as such we can be certain that $J_\beta, J_\gamma > J_\alpha$. But what of the relationship between J_β and J_γ? If $J_\beta > J_\gamma$, or vice versa, and both remain greater than J_α, we would expect to see sequential magnetic order, with the strongest coupling lattice ordering at the highest temperature.

This type of magnetic behaviour has been observed in many 3*d*-5*d* mixed metal oxides, especially in those containing Os (Sr_2FeOsO_6[102] and Sr_2CoOsO_6[103]). This behaviour arises in these compounds as the energy difference between the 3*d* cation and the 5*d* cation is large owing to the significant difference in oxidation states between the two. Consequently the 3*d*-5*d* orbital interaction is minimal. This results in the dominance of the 3*d*-3*d* and 5*d*-5*d* interactions, one of which is often much stronger than the other which in turn results in sequential magnetic order. The magnetisation data collected from Sr_2FeIrO_4 shows no evidence of sequential order (Section 4.3.4) and as such we can say J_β is not greater than J_γ. The final possibility is that in which $J_\beta \approx J_\gamma > J_\alpha$. In this case we would expect both the Fe and Ir lattice to order at the same temperature. Above this ordering temperature the spins are competing against thermal fluctuations and the symmetry restrictions imposed by the tetragonal structure, thus we would expect there to be frustration. The SQUID magnetisation data and variable temperature neutron diffraction data (Sections 3.3.4.1 and 3.3.4.2 respectively) both indicate that the Fe and Ir lattices order at the same temperature. Furthermore, the divergence in the ZFC and FC SQUID data, and lack of hysteresis in the 300 K magnetisation isotherms, are clear indications that above the ordering temperature the system's spins are strongly interacting and frustrated. We can therefore conclude that $J_\beta \approx J_\gamma > J_\alpha$. These observations, twinned with those drawn from the structure of the magnetic unit cell, clearly suggest that Sr_2FeIrO_4 has a unique combination of coupling constants that lead to an unorthodox magnetisation behaviour and a unique magnetic structure.

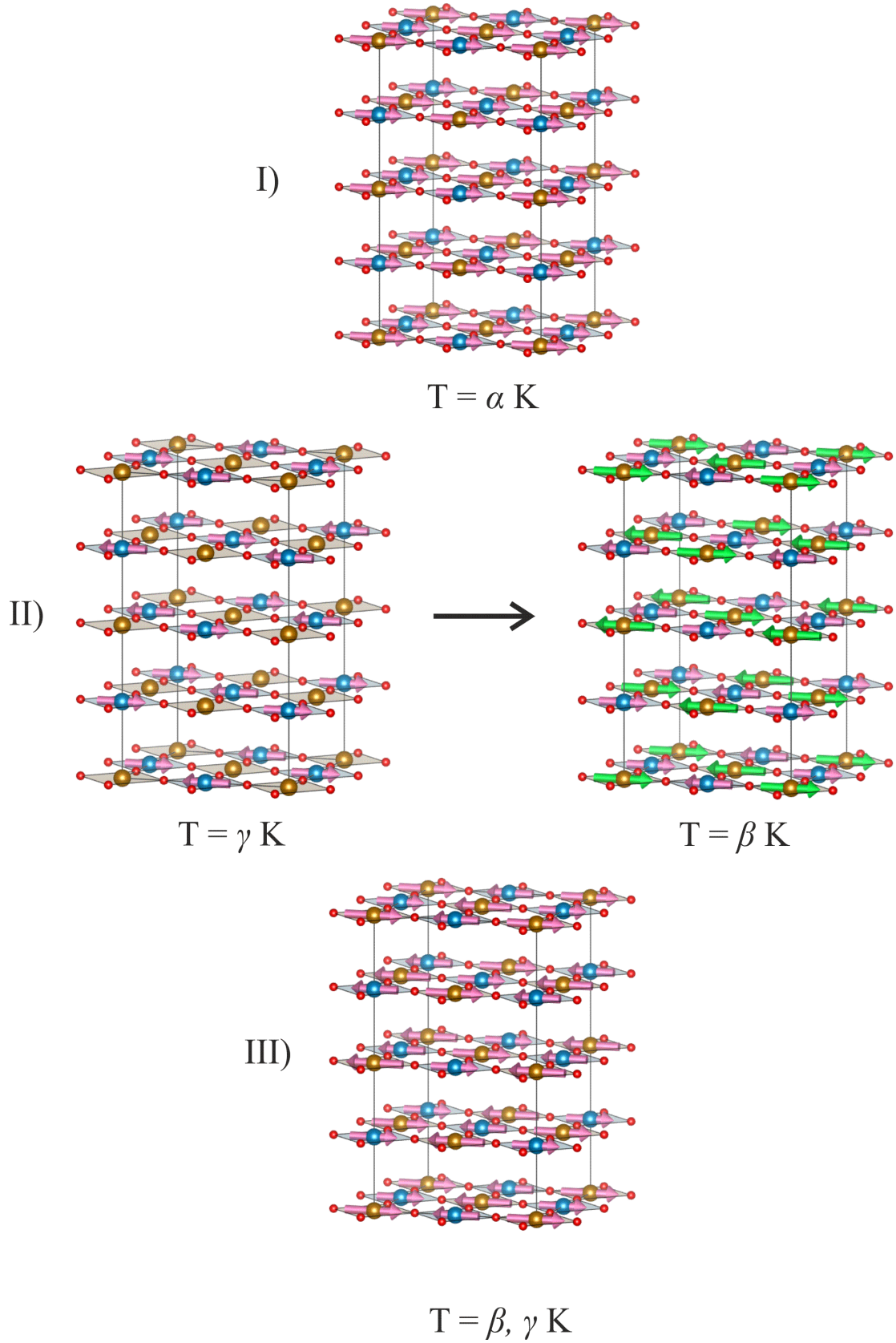

Figure 4.15: The three key magnetic ground states that arise from different magnitudes of the coupling constants shown in Figure 4.13. I) Is if $J_\alpha > J_\beta, J_\gamma$ II) Is if $J_\gamma > J_\beta > J_\alpha$ and III) Is if $J_\beta \approx J_\gamma > J_\alpha$

The unique magnetic behaviour of Sr_2FeIrO_4 has a direct impact on its structure. The "high temperature" tetragonal *I*4*/mmm* structure is in conflict with the magnetic structure as its 4-fold rotation axis forbids J_{1x} and J_{1y} from being different. Thus the *I*4*/mmm* structure further frustrates the spin interactions. To alleviate this frustration the structure must change to one with a lower symmetry which allows for the x and y axes to be inequivalent. This can be achieved by magnetostriction, a process in which cations with opposing spins moved closer together with the onset of magnetic order. This structural change lowers the symmetry and occurs at the same time as long range magnetic order. The variable temperature neutron diffraction data (Section 4.3.3.3) clearly shows that above the magnetic ordering temperature Sr_2FeIrO_4 remains *I*4*/mmm*. It also shows that the structural transition to the lower symmetry monoclinic *I*2*/m* structure happens at the magnetic ordering temperature and the distortion of the MO_4 units increases as the refined magnetic moment increases (Figure 4.10). These observations are clear evidence of the structural transition and magnetic order occurring simultaneously. Consequently we can conclude that this structural transition is driven by magnetostriction in the ab-plane. Furthermore as the signs of the J_{2a} and J_{2b} couplings are opposite, we would expect to see magnetostriction along the c axis resulting in alternating smaller and larger interlayer separations. Table 4.4 (Section 4.3.3.2.2) shows that refinement of a $P112_1$ symmetry structural model does not give a fit that is statistically better than that of *I*2*/m* and resulted in a structure in which the interlayer distances were equal within error. This suggests that if there is further lowering of symmetry as one might expect the atomic displacements are small and the data we have does not have the resolution required to highlight them.

4.4.3.1 Low temperature magnetic frustration

The magnetisation isotherm collected after field-cooling at 5 K from Sr_2FeIrO_4 (Figure 4.6) is very clearly displaced from the origin. Usually this would be a clear indication that the low temperature magnetic state is a spin glass, however the neutron diffraction data we collected at 1.5 K clearly show that at low temperatures Sr_2FeIrO_4 adopts an antiferromagnetic state. The apparent conflict of these observations can be resolved by considering the effects of antisite disorder in Sr_2FeIrO_4. The initial study of Sr_2FeIrO_6[22] and our refinement of Sr_2FeIrO_6 both show that Sr_2FeIrO_6 has an ordered B-site with around 7% antisite disorder. This small amount of disorder is retained by Sr_2FeIrO_4 and has a significant effect on the ordered magnetic state.

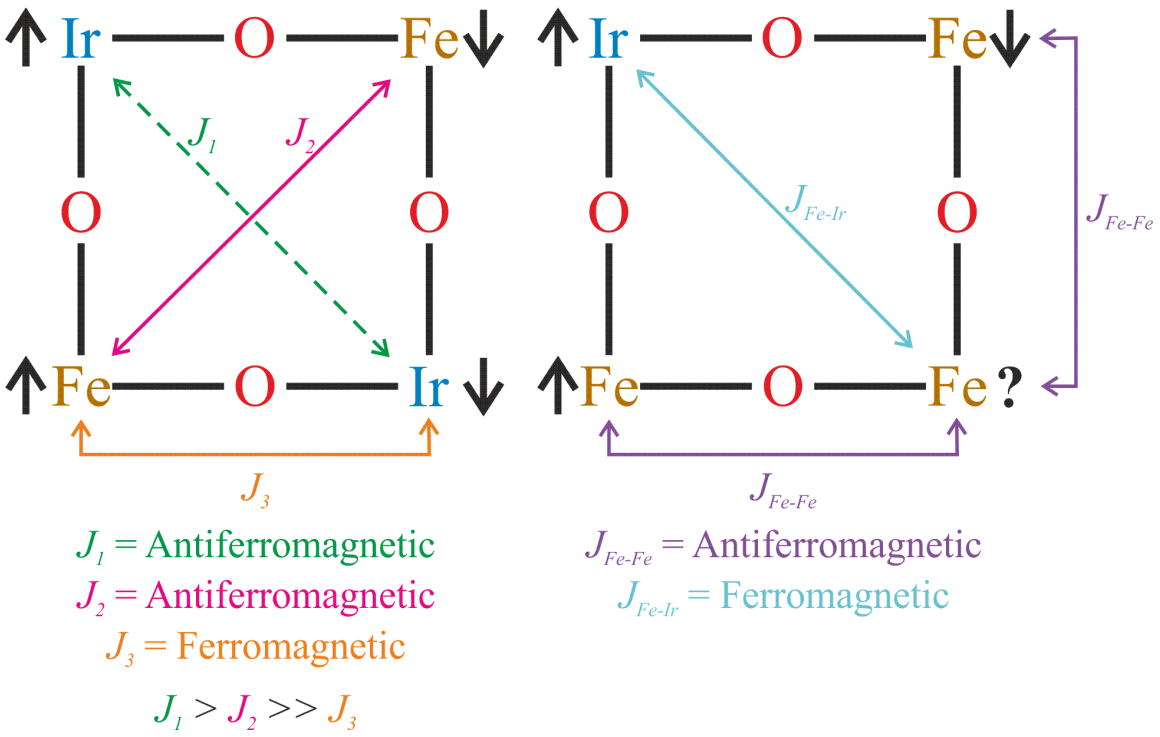

Figure 4.16: The three key magnetic couplings in the *ab*-plane of Sr_2FeIrO_4. Blue and gold spheres are iridium and iron respectively

Figure 4.16 shows the coupling regime of an ordered portion of Sr_2FeIrO_4 from the magnetic couplings extracted from the magnetic unit cell of Sr_2FeIrO_4. The dominant couplings are the same species super-superexchange interactions which lead to

ferromagnetic chains that are antiferromagnetically stacked. If we replace an iridium cation with an iron cation results in a frustration as shown in Figure 4.17. In this situation the nearest-neighbour Fe-Fe interaction is ferromagnetic and the next-nearest-neighbour Fe-Ir interaction is ferromagnetic. Assuming the cations that remain in place have the same spin orientations they had before the replacement, either only one nearest-neighbour interaction can be satisfied or one nearest-neighbour interaction and the next-nearest-neighbour can be satisfied. This results in frustration. The structural refinements show that there is a degree of disorder thus this frustration must be in the system and would account for the displaced magnetisation isotherm collected at 5 K.

4.5 Conclusion

The reaction of Sr_2FeIrO_6 with 95%/5% N_2/H_2 results in the deintercalation of oxide and formation of Sr_2FeIrO_4 which we believe to be the first reported example of Ir^{2+} in an extended oxide phase. Refinement of synchrotron diffraction data shows that Sr_2FeIrO_4 is an infinite layer phase that retains the rigorous B-site cation order of the parent phase. This is further confirmed by refinement of neuron data which also shows that at high temperatures Sr_2FeIrO_4 adopts a highly symmetric tetragonal *I4/mmm* structure. However, at lower temperatures there is a phase transition to a lower symmetry monoclinic *I2/m* structure which has distorted MO_4 units. SQUID magnetometry indicates that at 115 K Sr_2FeIrO_4 becomes magnetically ordered and is frustrated above 115 K. Low temperature neutron diffraction data indicates this ordered state is an antiferromagnetic state that can be described using a magnetic unit cell that is a $\sqrt{2}\ x\ \sqrt{2}\ x\ 2$ expansion of the crystallographic unit cell. This magnetic state consists of ordered Fe an Ir spins but the coupling regime is complex. The dominate couplings are those between like cations (i.e. Fe-Fe and Ir-Ir) rather than the expected nearest-

neighbour couplings. Furthermore comparison of the potential magnitude of the different couplings shows that the Fe-Fe and Ir-Ir couplings are roughly equal, which results in the exotic magnetic behaviour exhibited by Sr_2FeIrO_4. The magnetisation data and magnetic refinement suggest that the structural transition observed in driven by magnetostriction that alleviates the equivalency of x and y couplings in the ab plane. Magnetostriction along the *c* axis is not observed.

Chapter 5 – Synthesis and Characterisation of Doped Sr_2FeIrO_6

5.1 Introduction

Complex mixed metal oxides that contain iridium have recently undergone a renaissance in the function materials community owing to the large spin-orbit coupling present in iridium. In an octahedral ligand field this strong spin orbit coupling splits the t_{2g} orbital set creating a triplet state and a singlet state. This orbital arrangement, shown in Figure 5.1, has a marked effect on the physical properties of iridium containing oxides, for example Sr_2RhO_4[65-66] is a metallic compound whereas Sr_2IrO_4[20, 66, 69] is an insulator. The greater radial extension of the 5d orbitals means one would expect broader bands to be formed in Sr_2IrO_4 than in Sr_2RhO_4 and it would therefore also be a metal, however the splitting of the t_{2g} orbitals results in a band gap and the formation of two narrower bands. The literature is replete with research concerning Ir^{IV} containing species. This is mostly due to this cation having a partially occupied singlet state resulting in unusual magnetic behaviours. In contrast oxides containing Ir^{V} have received much less attention. Ir^{V} is a d^4 cation thus has a fully occupied triplet state and is a $j_{eff} = 0$ ion which is diamagnetic. Consequently, it is difficult to envisage materials containing Ir^{V} having any interesting magnetic properties beyond those that have not already been explored[23-24, 104].

We have extensively explored the reduction chemistry of Sr_2FeIrO_6 as discussed in Chapter 4, but its structure and physical properties remain the subject of debate in the literature. Various structures have been proposed and many conflicting results published. To clarify this situation, we decided to thoroughly analyse the structure and magnetic properties of Sr_2FeIrO_6. We also took the opportunity to explore the doping chemistry of

Sr_2FeIrO_6 as doping can have a marked effect on the structure and physical properties of oxides[61]. This gave us the opportunity to rigorously explore the chemistry of Sr_2FeIrO_6 and interrogate the j_{eff}= 0 state of Ir^V.

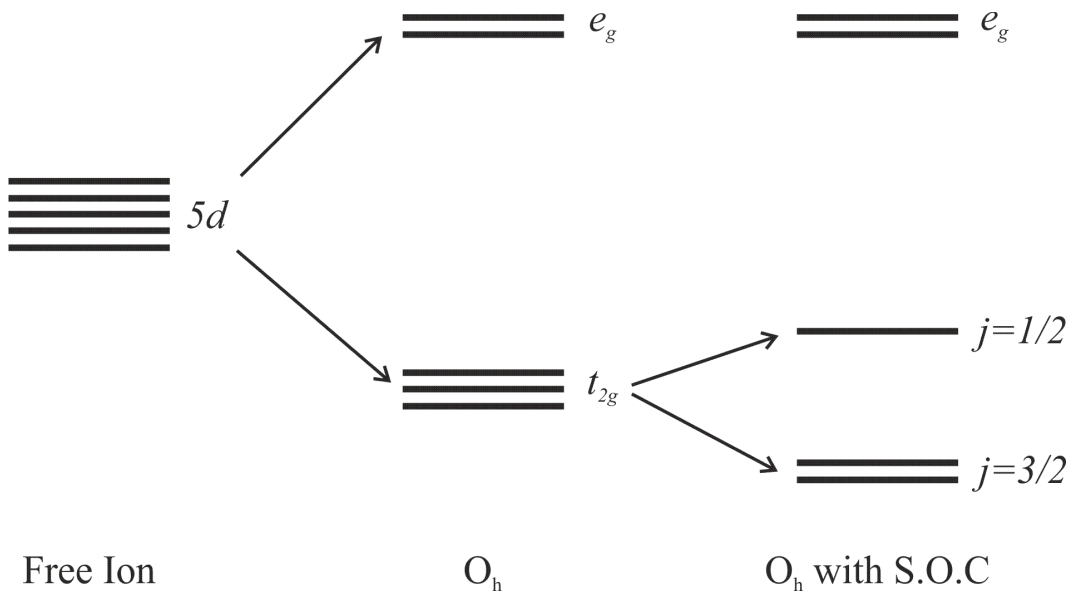

Figure 5.1: The orbital arrangements of a) an iridium free ion, b) iridium in octahedral co-ordination c) Ir^{IV} d^5 low spin in octahedral co-ordination with spin-orbit coupling

5.2 Synthesis

5.2.1 Synthesis of $Sr_{2-x}A_xFeIrO_6$ (A = Ca, Ba, La) and $Sr_2Fe_{0.95}Ga_{0.05}IrO_6$

Samples of Sr_2FeIrO_6, $La_xSr_{2-x}FeIrO_6$ (x= 0.025 and 0.05), $Ca_{0.05}Sr_{1.95}FeIrO_6$, $Ca_{0.185}Ba_{0.315}Sr_{1.95}FeIrO_6$ and $Sr_2Ga_{0.05}Fe_{0.95}IrO_6$ were prepared using the citrate gel method (Chapter 2, Section 2.1.2). Appropriate quantities of $SrCO_3$ (99.994%), La_2O_3 (99.999%), $CaCO_3$ (99.999%), $BaCO_3$ (99.997%), Ga_2O_3 (99.999%) and Fe (99.99%) were dissolved in a 1:1 mixture of conc. nitric acid and distilled water. After dissolution was complete the required amount of IrO_2 (99.99%, dried at 700 ^oC for 2 hours) was added. Citric acid and analar ethylene glycol were added and the solutions were heated whilst being stirred. The gel thus formed was dried and then allowed to combust in air. The subsequent products were ground into fine powders, placed in alumina crucibles and

heated at 1000 °C in air at a rate of 1 °C min^{-1} to remove the organic components of the sample. The resulting powders were pressed into 13 mm diameter pellets and heated in air for two cycles of 2 days at 1100 °C.

The resulting powders were observed to be phase-pure by laboratory X-ray powder diffraction. The lattice parameters of these phases were initially measured using CMPR[78] and are detailed in Table 5.1. The lattice parameters of Sr_2FeIrO_6 in good agreement with values reported in the literature (a = 5.54996(3) Å, b = 5.57847(3) Å, c = 7.84165(3) Å, α = 89.990(1) °, β = 90.059(1) °, γ = 90.079(1) °)[22]. The lattice parameters of the other samples were consistent with pure phases.

	a (Å)	b (Å)	c (Å)
Sr_2FeIrO_6	5.55	5.57	7.84
$La_{0.025}Sr_{1.975}FeIrO_6$	5.55	5.58	7.85
$La_{0.05}Sr_{1.95}FeIrO_6$	5.55	5.58	7.85
$Ca_{0.05}Sr_{1.95}FeIrO_6$	5.54	5.58	7.85
$Ba_{0.0185}$ $Ca_{0.0335}Sr_{1.95}FeIrO_6$	5.56	5.59	7.86
$Sr_2Ga_{0.05}Fe_{0.95}IrO_6$	5.56	5.58	7.86

Table 5.1: Lattice parameters of Sr_2FeIrO_6 and all doped phases extracted from CMPR

5.3 Results

5.3.1 Structural Characterisation of Sr_2FeIrO_6 and $La_{0.05}Sr_{1.95}FeIrO_6$

5.3.1.1 Sr_2FeIrO_6 Synchrotron X-ray Powder Diffraction Data

X-ray powder diffraction data collected from a sample of Sr_2FeIrO_6 using laboratory diffractometers could be indexed on the basis of either a monoclinic or triclinic unit cell. Furthermore, the data could be fit to a unit cell with either body-centring or primitive symmetry.

To determine the structure of Sr_2FeIrO_6 high resolution synchrotron X-ray powder diffraction data were collected using instrument I11 at the Diamond Light Source Ltd

(Section 2.7.1.2). In the literature there are three proposed structures for Sr_2FeIrO_6: $I\bar{1}$ [22, 105], $P2_1/n$[106-107] and $I2/m$[107-108]. These models are very similar. Each has rigorous rock salt B-site cation order, but a different octahedral rotation pattern as outlined below in Table 5.2 and shown in Figure 5.2. Refinement of each model against the data converged to give a good statistical fit. The fitting statistics from each of these refinements are shown in Table 5.3.

The best fit was achieved by refinement of the $I\bar{1}$ model against the data, a result consistent with that published in the initial study conducted by Battle et al.[22]. The observed, calculated and difference plots for the refinement against the $I\bar{1}$, $P2_1/n$ and $I2/m$ models are shown in Figure 5.3.

Space Group	Twisting Pattern (Glazer Notation)
$I\bar{1}$ (#2)	$a^-b^-c^-$
$I2/m$ (#12)	$a^0b^-b^-$
$P2_1/n$ (#14)	$a^-a^-c^+$

Table 5.2: Possible structures of Sr_2FeirO_6 and their octahedral twisting patterns

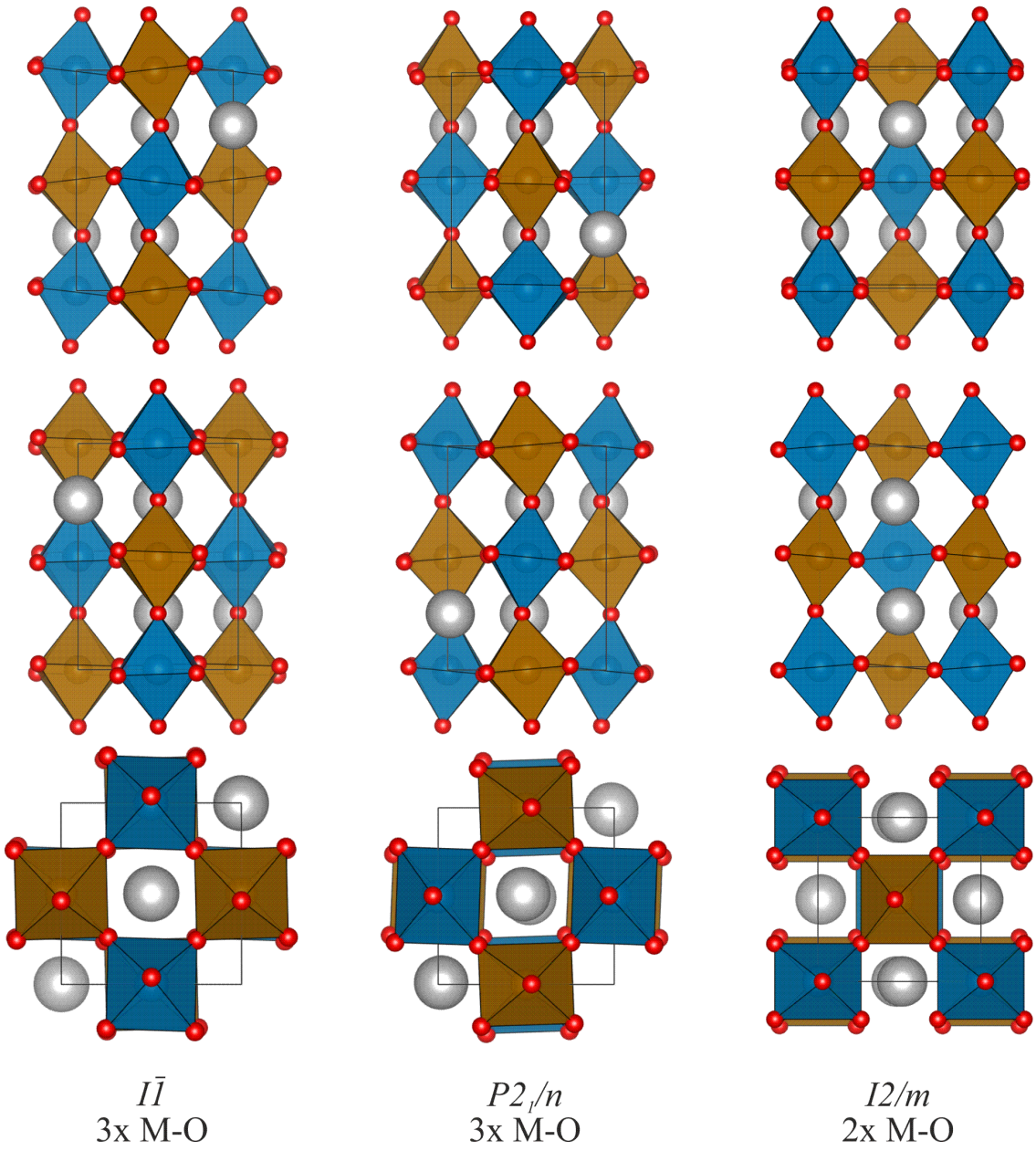

Figure 5.2: Structural models of the three possible structures of Sr_2FeIrO_6. Blue and brown spheres are iridium and iron respectively.

Space Group	χ^2	wRp (%)	Rp (%)
$I\bar{1}$ (#2)	14.13	2.55	1.70
I2/m (#12)	20.98	3.12	2.01
$P2_1/n$ (#14)	20.79	3.10	2.00

Table 5.3: Fitting statistics from the structural refinements of Sr_2FeIrO_6 against synchrotron diffraction data collected at room temperature.

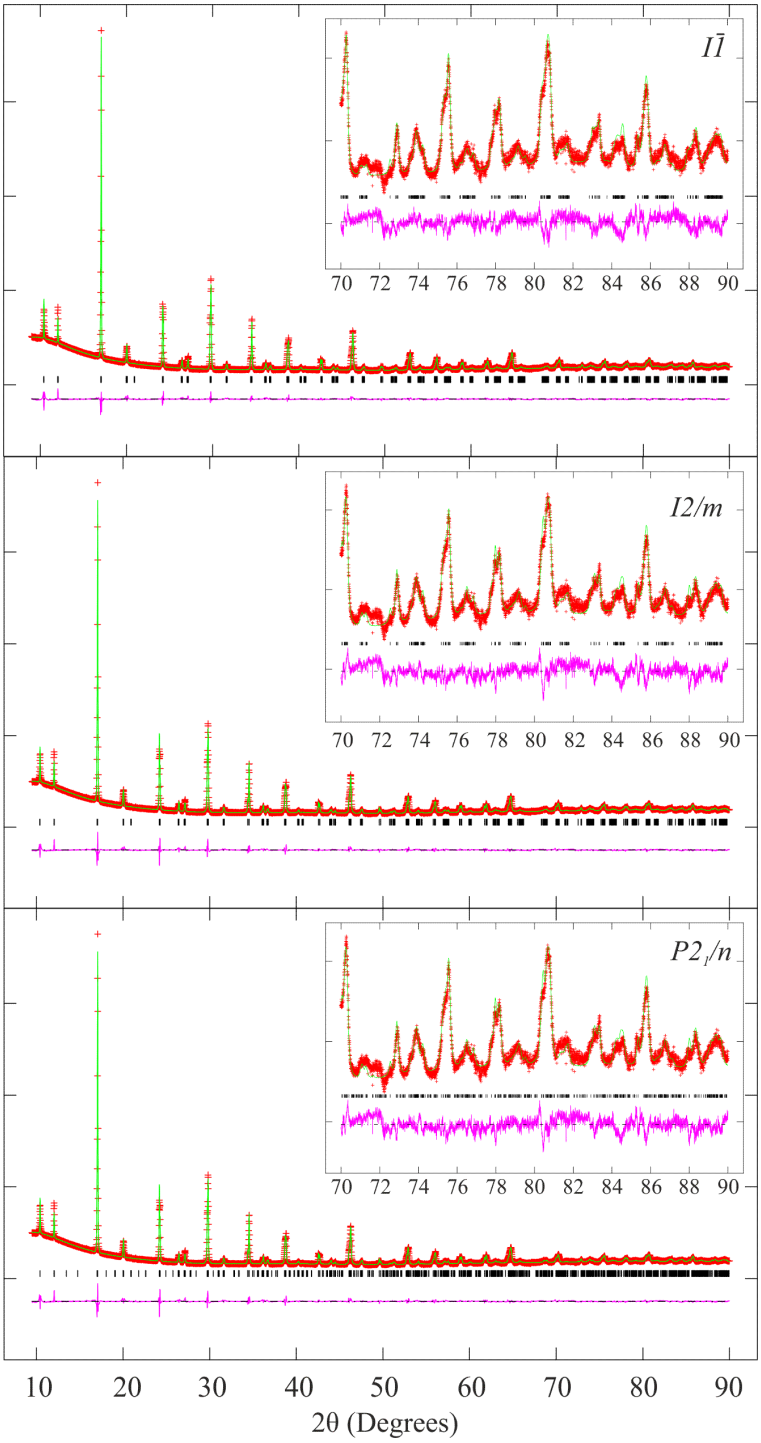

Figure 5.3: Observed, calculated and difference plots from the refinement of the *I*$\bar{1}$, *I2/m* and *P2₁/n* structural models of Sr_2FeIrO_6 against synchrotron powder diffraction data collected at room temperature using the I11 instrument.

5.3.1.2 $La_{0.05}Sr_{1.95}FeIrO_6$ synchrotron X-ray powder diffraction data

X-ray powder diffraction data collected from a sample of $La_{0.05}Sr1_{.95}FeIrO_6$ from laboratory diffractometers could be indexed on the basis of either a monoclinic or triclinic unit cell. Furthermore it could be indexed with body-centred or primitive symmetry.

High resolution synchrotron X-ray powder diffraction data were collected from $La_{0.05}Sr_{1.95}FeIrO_6$ using instrument I11 at the Diamond Light Source Ltd (Section 2.7.1.2). Models of $La_{0.05}Sr_{1.95}FeIrO_6$ were constructed based on the three structural models proposed for Sr_2FeIrO_6. Each model was refined against the data to give a good statistical fit. The fitting statistics from each refinement are shown in Table 5.4. The observed, calculated and difference plots for the refinement against the $I\bar{1}$, $P2_1/n$ and $I2/m$ models are shown in Figure 5.4.

Space Group	χ^2	wRp (%)	Rp (%)
$I\bar{1}$ (#2)	6.164	1.83	1.32
$I2/m$ (#12)	7.007	1.94	1.39
$P2_1/n$ (#14)	6.792	1.91	1.37

Table 5.4: Fitting statistics from the structural refinements of $La_{0.05}Sr_{1.95}FeIrO_6$ against synchrotron diffraction data collected at room temperature.

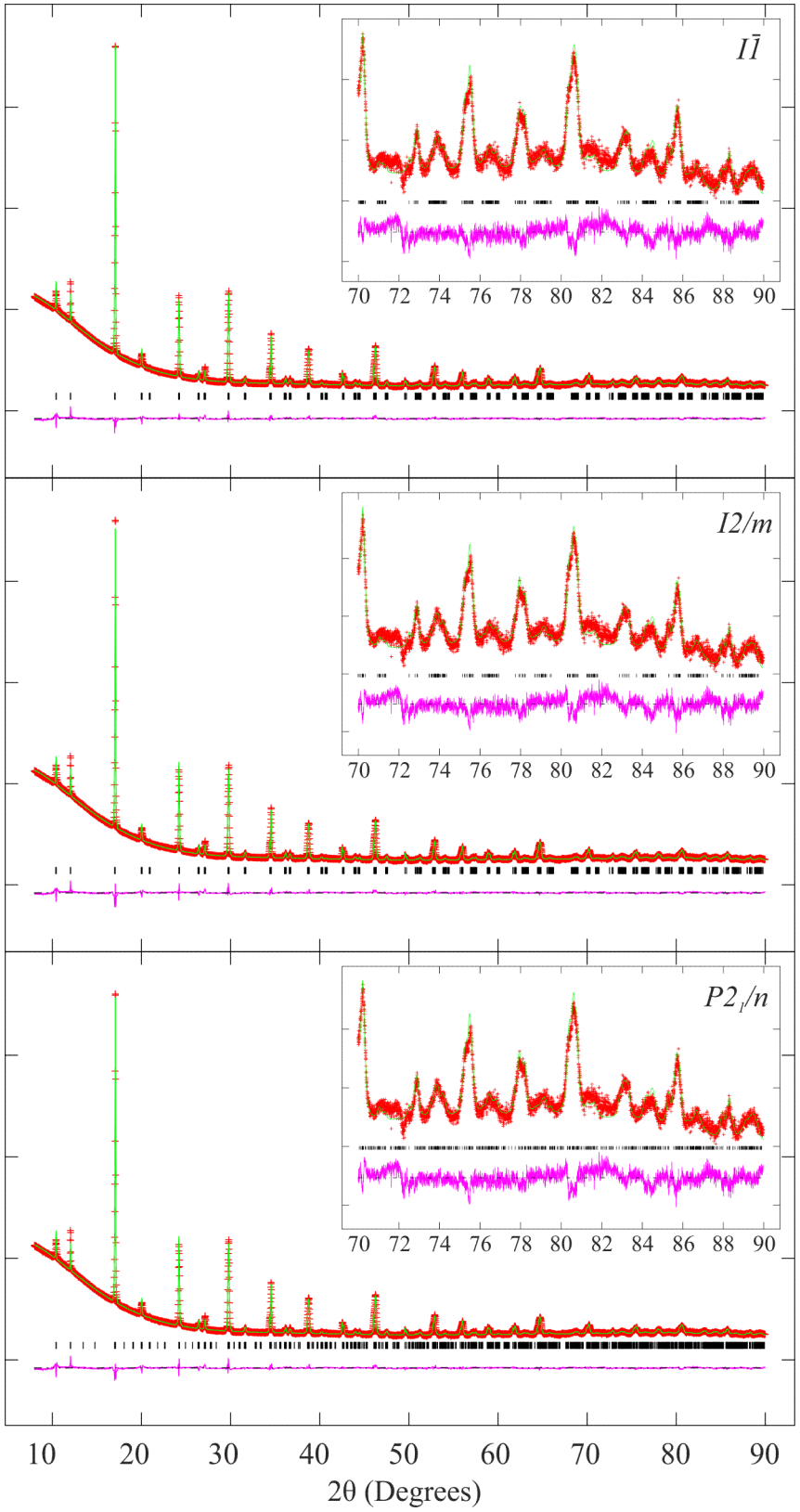

Figure 5.4: Observed, calculated and difference plots from the refinement of the $I\bar{1}$, *I2/m* and $P2_1/n$ structural models of $La_{0.05}Sr_{1.95}FeIrO_6$ against synchrotron powder diffraction data collected at room temperature using the I11 instrument.

The best fits were achieved by refinement of the $I\bar{1}$ and $P2_1/n$ models, with the $I\bar{1}$ model giving a marginally better fit. The difference between these two fits is minimal and nowhere near as clear as the respective fits for the structural refinements of Sr_2FeIrO_6 (see Table 5.3). Upon closer inspection of the $70 \leq \theta^{o} \leq 90$ sections of the refinements, it is clear that each of the models does a better job of accounting for certain peaks than the other. This is an indication that more than one phase is present in the sample.

To determine if there are two phases present in the sample two multiphase refinements were conducted: one in which the $I\bar{1}$ and $P2_1/n$ models were refined and one in which the $I2/m$ and $P2_1/n$ models were refined. The fitting statistics from each refinement are shown in Table 5.5. The observed, calculated and difference plots for the refinement against the $I\bar{1}$ + $P2_1/n$ models and $I2/m$ + $P2_1/n$ models are shown in Figure 5.5.

The fitting statistics of the multiphase refinements are better than those of the single phase refinements, a result that proves that there are indeed two phases in the sample: one with a primitive structure and one with a body-centred structure. Of the two multiphase refinements the best fit was achieved by the refinement of the $I\bar{1}$ and $P2_1/n$ models against the data. Figure 5.5 shows the $70 \leq \theta^{o} \leq 90$ section of the $I\bar{1}$ and $P2_1/n$ of the refinement. Comparing it to the same section for the single phase $I\bar{1}$ and $P2_1/n$ refinements in Figures 5.3 it is evident that, as expected, the combined refinement does a much better job of fitting peaks that are otherwise unaccounted for in the single-phase refinements.

Space Groups	χ^2	wRp (%)	Rp (%)
$I\bar{1}$ (#2) + $P2_1/n$ (#14)	5.782	1.81	1.24
$I2/m$ (#12)+ $P2_1/n$ (#14)	6.298	1.89	1.27

Table 5.5: Fitting statistics from the structural two-phase refinements of $La_{0.05}Sr_{1.95}FeIrO_6$ against synchrotron diffraction data collected at room temperature.

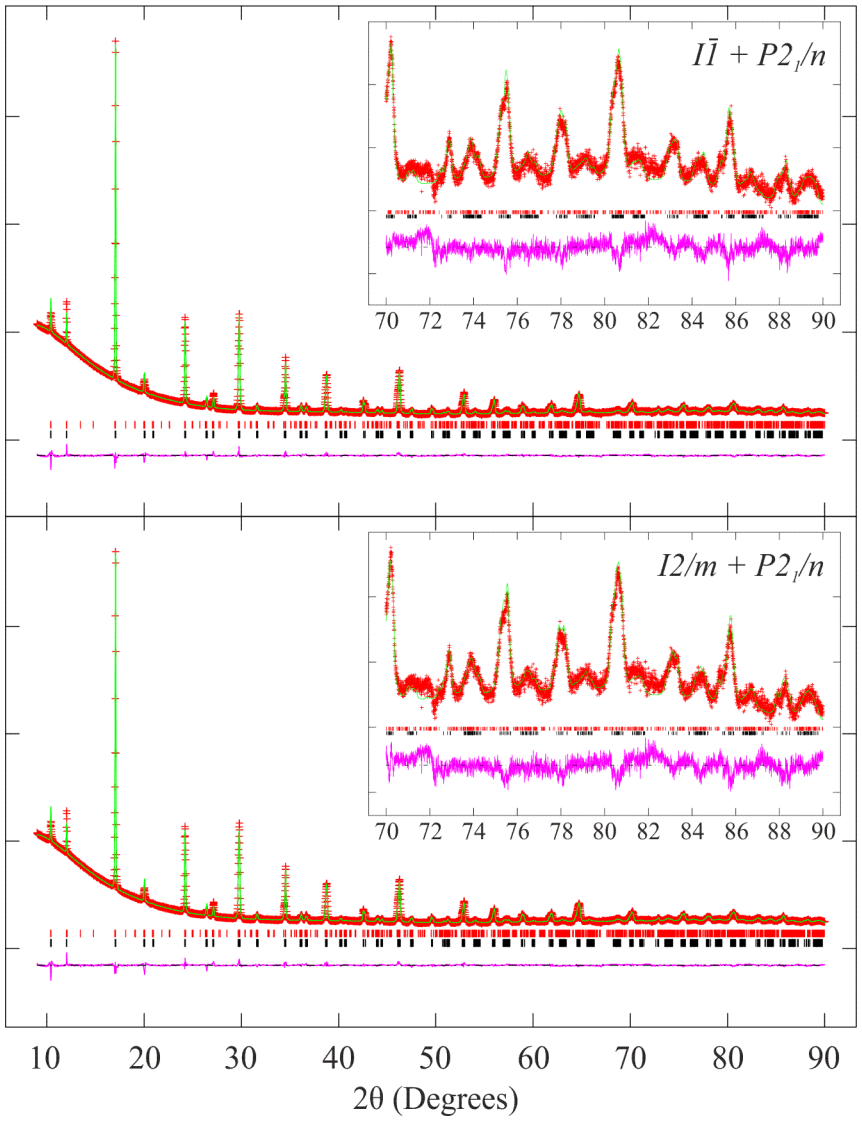

Figure 5.5: Observed, calculated and difference plots from the refinement of the $I\bar{1}$ + $P2_1/n$ and $I2/m$ + $P2_1/n$ two-phase structural models of $La_{0.05}Sr_{1.95}FeIrO_6$ against synchrotron powder diffraction data collected at room temperature using the I11 instrument.

5.3.1.3 $La_{0.05}Sr_{1.95}FeIrO_6$ variable temperature synchrotron X-ray powder diffraction data

High resolution synchrotron X-ray powder diffraction data were collected from $La_{0.5}Sr_{1.95}FeIrO_6$ over a temperature range of $100 \leq T / K \leq 300$ using the I11 instrument at the Diamond Light Source (Section 2.7.1.2). The $I\bar{1}$ and $P2_1/n$ models that discussed in Sections 5.3.1.1 and 5.3.1.2 were refined against each data set. The refinements all converged to give excellent statistical fits. The lattice parameters extracted from these refinements are given as a function of temperature in Figure 5.6.

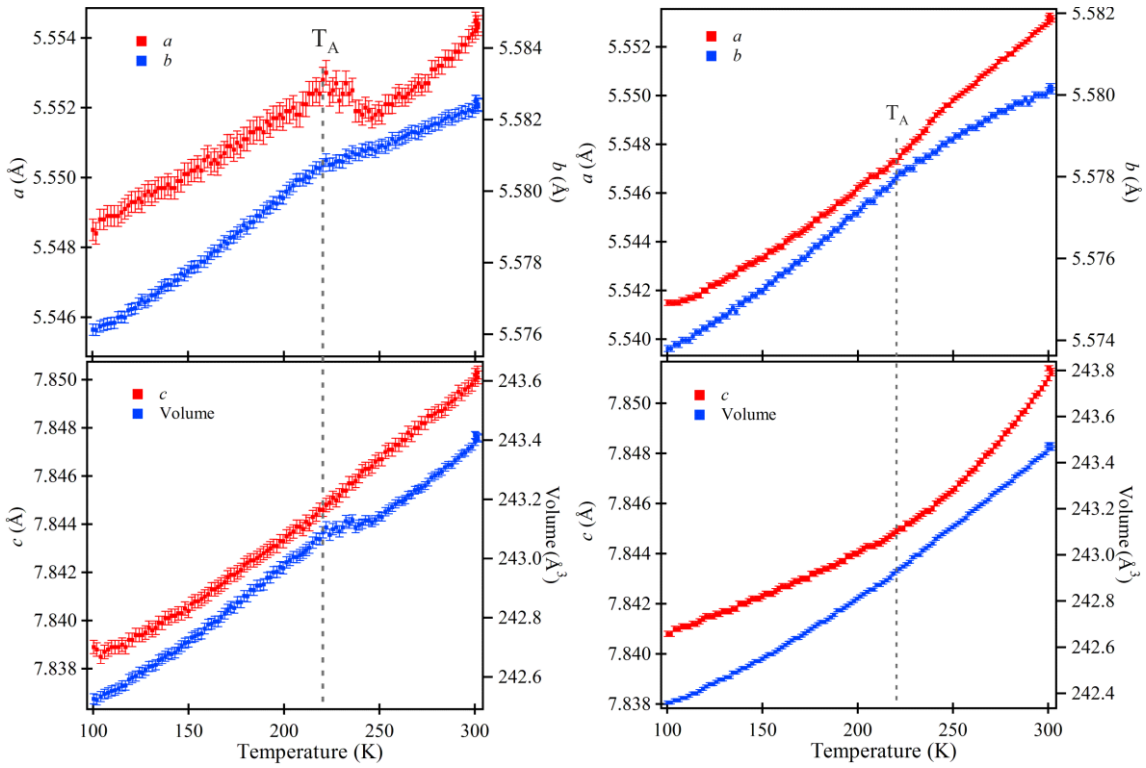

Figure 5.6: The lattice parameters extracted from the refinement of synchrotron X-ray diffraction data collected from $La_{0.5}Sr_{1.95}FeIrO_6$ in the temperature range $100 \leq T / K \leq 300$. Left) $I\bar{1}$ phase Right) $P2_1/n$ phase.

5.3.1.4 $La_{0.05}Sr_{1.95}FeIrO_6$ Neutron Powder Diffraction Data

Neutron powder diffraction data were collected from a sample of $La_{0.05}Sr_{1.95}FeIrO_6$ at 250K using the using the WISH instrument at ISIS (Chapter 2, Section 2.7.2.1). Magnetisation data (Section 5.3.2.1) indicates that there is no magnetically ordered state at T > 225 K, thus we can assume all peaks in these diffraction data are structural. The data could be indexed using the triclinic $I\bar{1}$ model that is based on the structure of Sr_2FeIrO_6. However upon closer inspection this model does not account for a series of very small peaks, highlighted in Figure 5.7.

These small peaks can be accounted for by indexing the data using the $P2_1/n$ model previously mentioned in Sections 5.3.1.1 and 5.3.1.2. This is consistent with the results collected from X-ray diffraction data (Section 5.3.1.2). Refinement of the synchrotron data collected from $La_{0.05}Sr_{1.95}FeIrO_6$ clearly indicates that there are two phases present, an $I\bar{1}$ phase and a $P2_1/n$ phase. To confirm this is the case a multiphase refinement was conducted in which the $I\bar{1}$ and $P2_1/n$ models were refined against the neutron diffraction data. The refinement converged to give a good statistical fit. The observed, calculated and difference plots for all data banks are shown in Figure 5.8. Full details of the structural parameters and selected bond lengths are given in Tables 5.6 and 5.7 respectively.

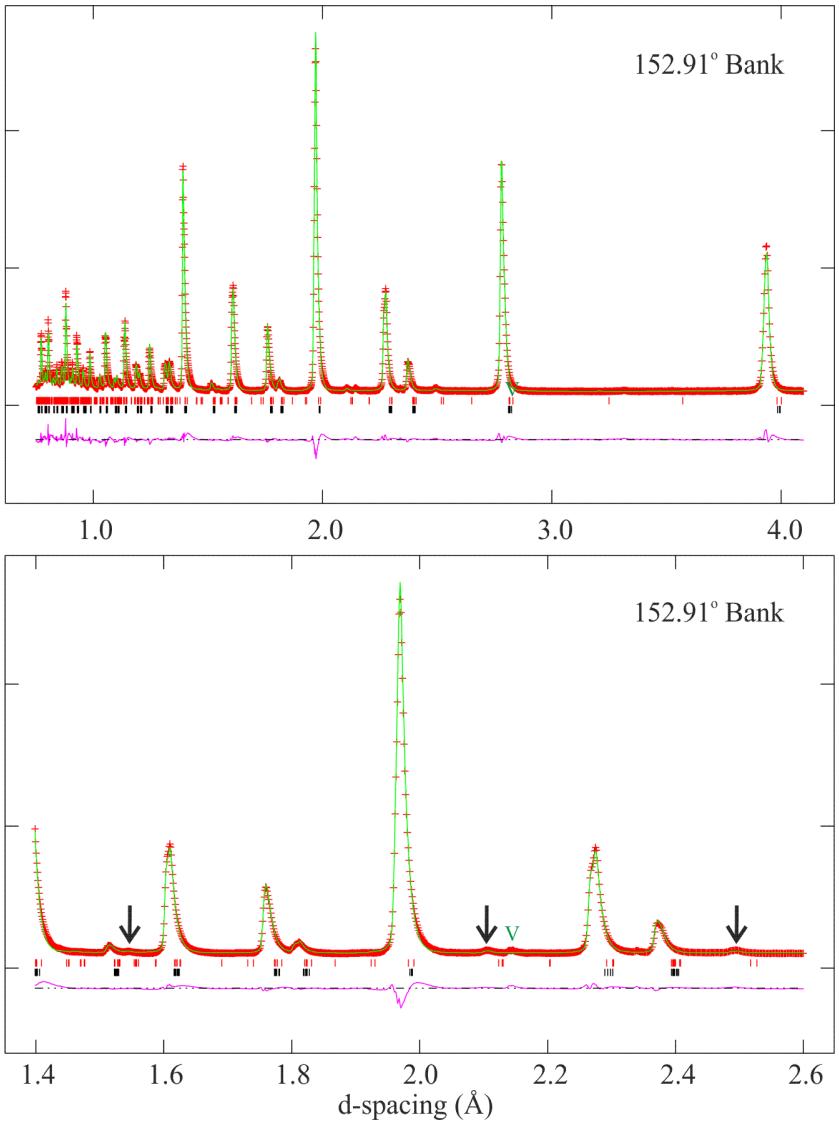

Figure 5.7: Observed, calculated and difference plots from the 152.91 º bank for refinement of the $I\bar{1}$ + $P2_1/n$ structural model of $La_{0.05}Sr_{1.95}FeIrO_6$ against neutron powder diffraction data collected at 1.5 K using the WISH instrument. The arrows highlight weak primitive peaks.

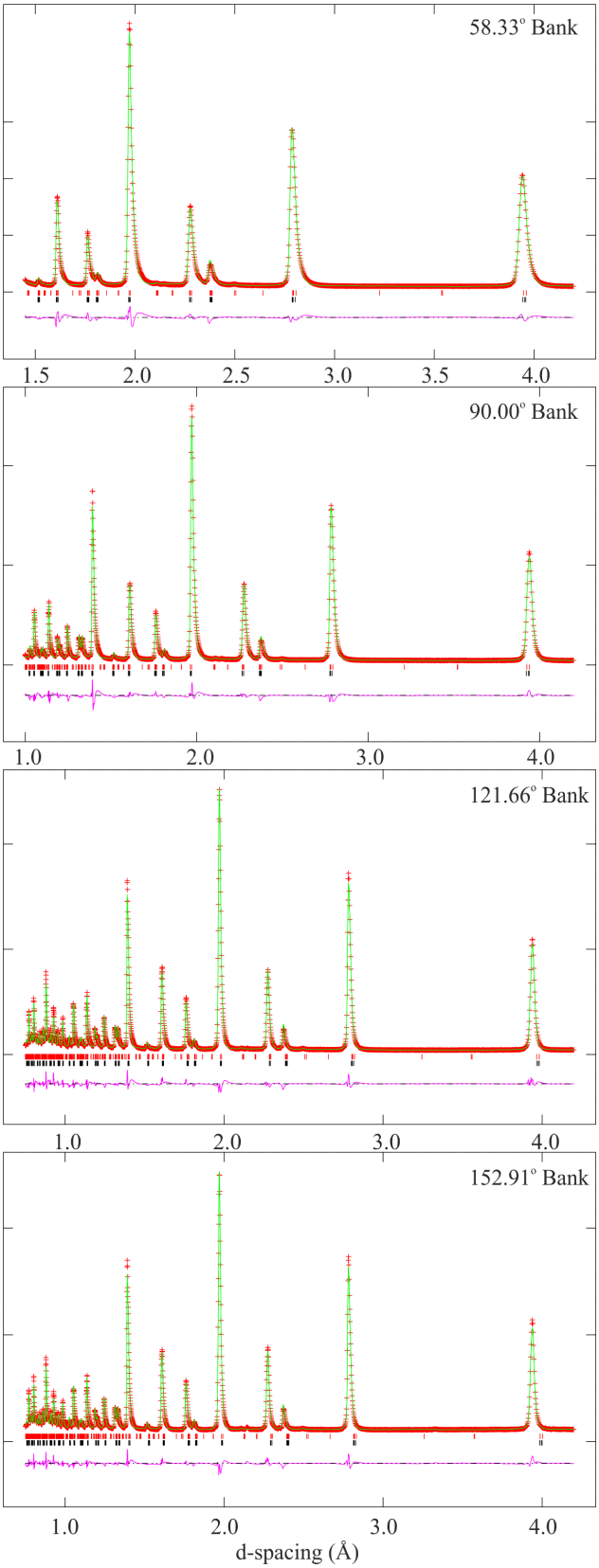

Figure 5.8: Observed, calculated and difference plots from the 152.91 º bank for refinement of the *I2/m* structural model of Sr_2FeIrO_6 against neutron powder diffraction data collected at 1.5 K using the WISH instrument. Tick marks correspond to the following: Black= $I\bar{1}$ Red= $P2_1/n$

Atom	site	*x*	*y*	*z*	Fraction	U_{iso} (Å^2)
Sr		0.499(1)	0.499(1)	0.250(1)	1	0.0048(3)
Fe/Ir(1)		0	½	0	0.92/0.08	0.045(3)
Ir/Fe(2)		½	0	0	0.92/0.08	0.045(3)
O(1)		0.258(1)	0.259(1)	0.984(1)	1	0.047(42)
O(2)		0.247(1)	0.756(1)	0.025(1)	1	0.014(5)
O(3)		0.502(1)	0.036(1)	0.250(1)	1	0.002(2)
Sr_2FeIrO_6 - Space Group: $I\bar{1}$ (# 2) Formula weight = 519.31 g mol^{-1} *a* = 5.5497(1) Å *b* = 5.5781(1) Å, *c* = 7.8463(1) Å, α = 89.99(1) °, β = 90.06(1) °, γ = 90.07(2) ° volume = 242.90(1) Å^3 Phase fraction = 45.5(1) weight %						
Atom	site	*x*	*y*	*z*	Fraction	U_{iso} (Å^2)
Sr/La	*4e*		0.000(1)	0.266(1)	0.95/0.05	0.0088(3)
Fe/Ir(1)	*2c*	½	0	½	0.18(6)/0.81(6)	0.0068(3)
Ir/Fe(2)	*2d*	½	0	0	0.18(6)/0.81(6)	0.0107(22)
O(1)	*4e*	0.227(1)	0.224(1)	0.020(1)	1	0.009(2)
O(2)	*4e*	0.246(1)	0.758(1)	0.013(1)	1	0.045(3)
O(3)	*4e*	0.970(1)	0.502(2)	0.251(2)	1	0.0088(3)
$La_{0.1}Sr_{1.9}FeIrO_6$ – Space group: $P2_1/n$ (# 14) Formula weight = 521.8745 g mol^{-1} *a* = 5.5515(1) Å *b* = 5.5810(1) Å, *c* = 7.8462(1) Å, β = 90.08(1) °, volume = 243.10(1) Å^3 Phase fraction = 54.4(1) weight %						
Radiation source: Neutron Time of flight Temperature: 250 K χ^2 = 71.46; *wRp*= 6.89%; *Rp* = 4.83%.						

Table 5.6: Parameters from the two-phase structural refinement of $La_{0.05}Sr_{1.95}FeIrO_6$ against neutron powder diffraction data collected at 250 K.

	Bond lengths (Å)					
	$I\bar{1}$			$P2_1/n$		
Cation (M)	M-O(1)	M-O(2)	M-O(3)	M-O(1)	M-O(2)	M-O(3)
Fe	1.969(20)	1.988(21)	1.972(8)	1.996(6)	1.987(6)	1.977(16)
Ir	1.978(20)	1.964(20)	1.972(8)	1.971(6)	1.955(6)	1.961(16)
	Bond Angles (°)					
	$I\bar{1}$			$P2_1/n$		
	Fe-O(1)-Ir	Fe-O(2)-Ir	Fe-O(3)-Ir	Fe-O(1)-Ir	Fe-O(2)-Ir	Fe-O(3)-Ir
	171.73(32)	168.42(32)	168.29(45)	165.59(32)	173.46(32)	170.27(91)

Table 5.7 Selected bond length and angles from the refined structures of $La_{0.05}Sr_{1.95}FeIrO_6$ at 250 K

5.3.2 Magnetic characterisation of $La_{0.05}Sr_{1.95}FeIrO_6$ and Sr_2FeIrO_6

5.3.2.1 SQUID Magnetometry of $La_{0.05}Sr_{1.95}FeIrO_6$ and Sr_2FeIrO_6

Magnetisation data were collected from a sample of $La_{0.05}Sr_{1.95}FeIrO_6$ in an applied field of 100 Oe in the temperature range $5 \leq T / K \leq 300$. The zero-field cooled (ZFC) and field cooled (FC) data and magnetisation-field isotherms collected at 300 K, 200 K and 5 K are shown in Figure 5.9. At temperatures above 225 K the zero-field cooled and field cooled measurements are the same. Neither data set could fit to the Curie-Weiss law over any significant temperature range. At temperatures between $120 \leq T / K \leq 225$ the zero-field cooled and field cooled measurements are divergent, however the magnetisation isotherms collected at 200 K and 300 K show no hysteresis indicating this is not due to detectable magnetic order or a ferromagnetic impurity. At temperatures below 120 K the zero-field and field cooled measurements remain divergent but the rate at which they diverge changes. The magnetisation isotherm collected at 5 K shows a small amount of hysteresis. These results indicate that $La_{0.05}Sr_{1.95}FeIrO_6$ undergoes a transition to a magnetically ordered state at 120 K but the magnetic behaviour observed at temperatures between $120 \leq T / K \leq 225$ remains ambiguous.

Magnetisation data were collected from a sample of Sr_2FeIrO_6 in an applied field of 100 Oe in the temperature range $5 \leq T / K \leq 300$. The zero-field cooled (ZFC) and field cooled (FC) data are shown in Figure 5.10. The results of ZFC and FC experiments are consistent with those published in the study conducted by Battle et al.[22]. At temperatures above 125 K the ZFC and FC plots are the same and can roughly be fit to the Curie-Weiss law. At 125 K the ZFC and FC plots reach a local maxima before beginning to rise again at 90 K.

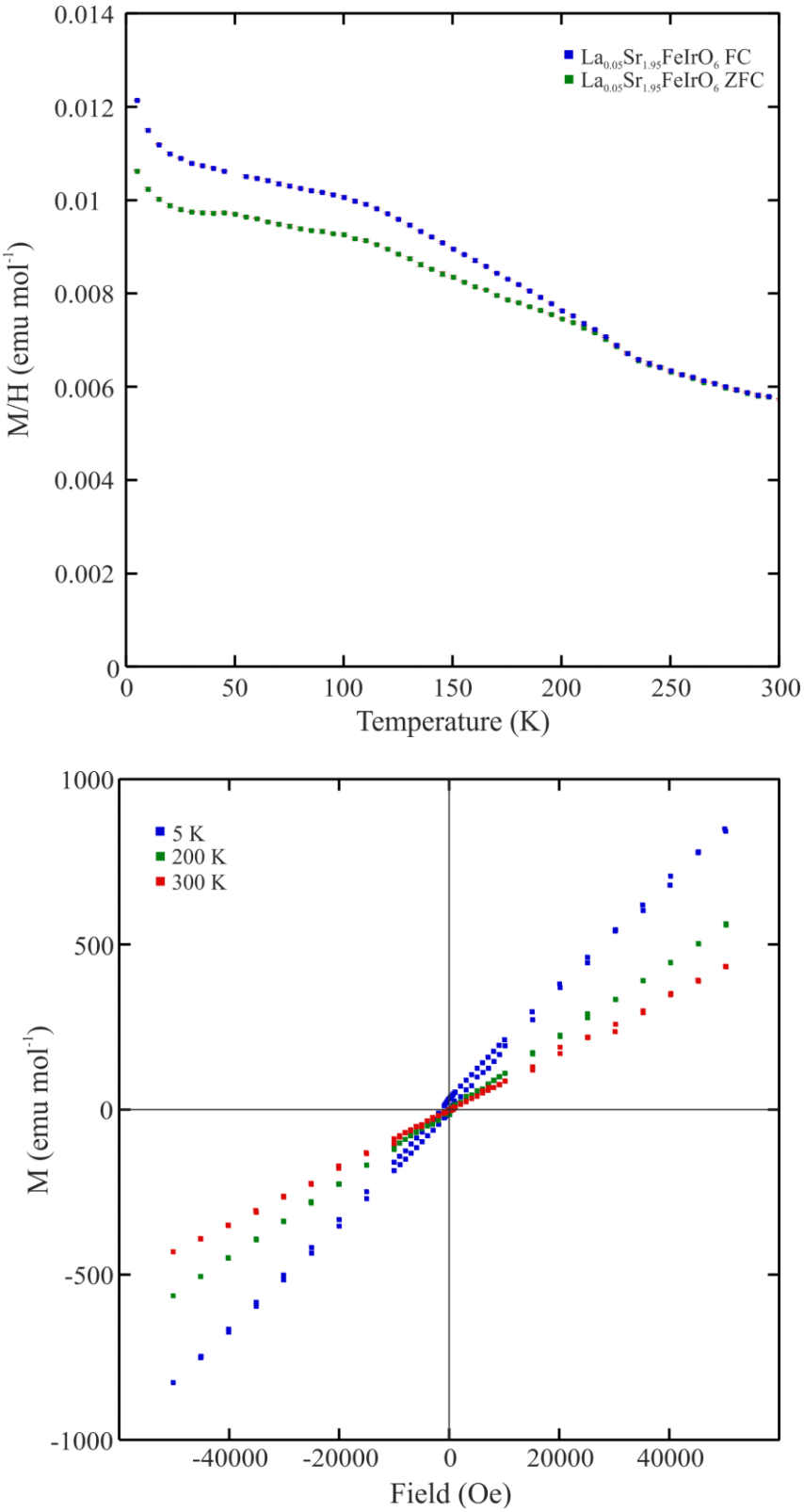

Figure 5.9: a) Zero-field cooled and field-cooled magnetisation data collected from $La_{0.05}Sr_{1.95}FeIrO_6$. b) Magnetisation-field isotherms collected from $La_{0.05}Sr_{1.95}FeIrO_6$.

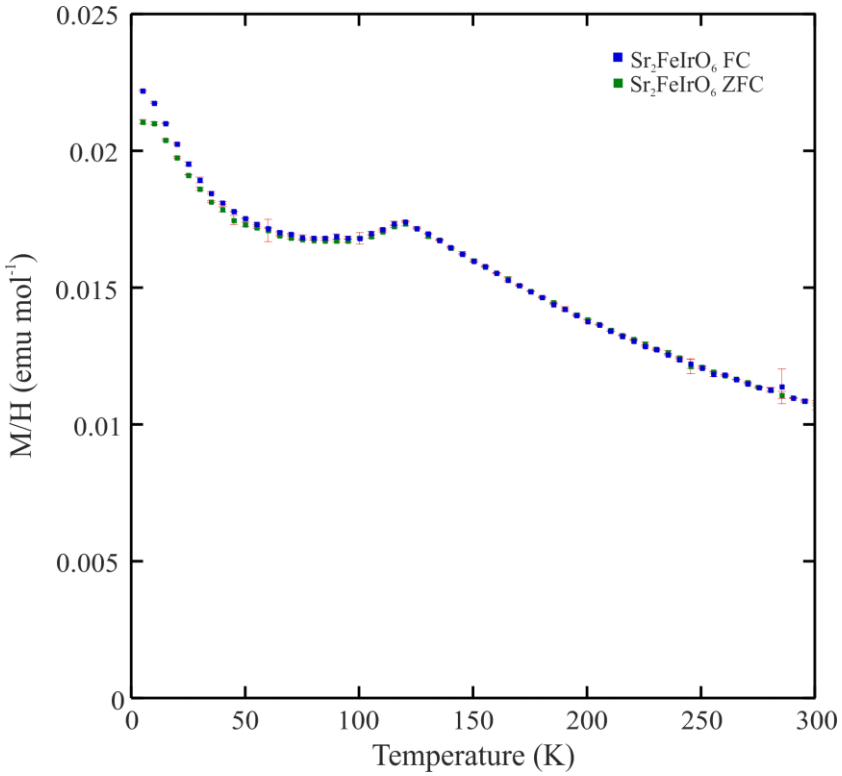

Figure 5.10: Zero-field cooled and field-cooled magnetisation data collected from Sr_2FeIrO_6

5.3.2.2 Neutron powder diffraction data

Comparison of neutron powder diffraction data collected at 250 K and 125 K showed that there is very little difference between the two data sets. In contrast comparison of the data collect at 1.5 K with the data collected at 250 K and 125 K showed that the 1.5 K data had additional peaks. The SQUID magnetisation data (Section 5.3.2.1) indicates that at 120 K $La_{0.05}Sr_{1.95}FeIrO_6$ undergoes a magnetic transition and as such these additional Bragg peaks were attributed to a magnetically ordered state. The peaks could be indexed on the basis of a 1 x 2 x 2 expansion of the refined crystallographic unit cell. This is the same expansion reported in the literature for the magnetic unit cell of Sr_2FeIrO_6[22]. A model for the magnetic unit cell based on that of Sr_2FeIrO_6 was constructed. The model, shown in Figure 5.11, consists of a diamagnetic iridium lattice and a G-type antiferromagnetically ordered iron lattice with the spins aligned along the z-axis.

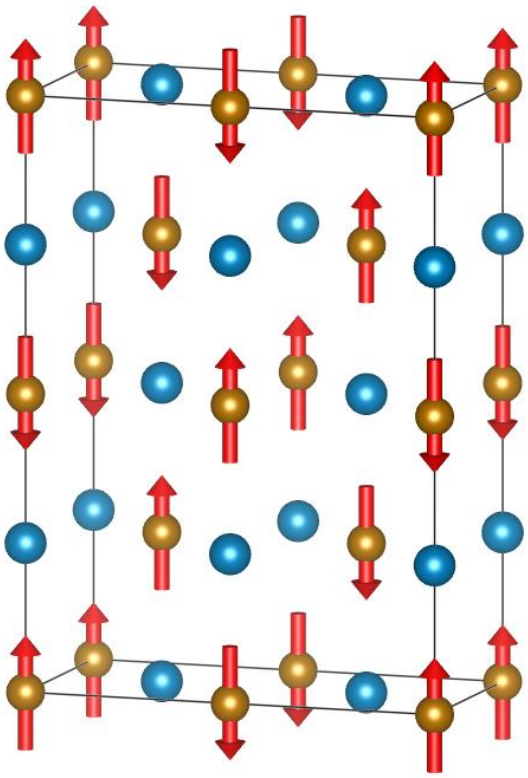

Figure 5.11 The refined magnetic unit cell of $La_{0.05}Sr_{1.95}FeIrO_6$. The blue and brown spheres are iridium and iron respectively

This magnetic model was refined against the neutron powder diffraction data collected at 1.5 K to give an excellent fit. The ordered magnetic moments were refined to be 2.45(1) μ_B per Fe centre. Figure 5.12 shows the observed, calculated and difference plots for the combined magnetic and structural refinement against the 58.33 º bank data. The refined nuclear and magnetic structural parameters are detailed in Table 5.8.

Atom	*x*	*y*	*z*	M_x	M_y	M_z
Fe(1)	0	0	0	0	0	2.45(1)
Fe(2)	0	½	0	0	0	-2.45(1)
Fe(3)	½	¼	¼	0	0	-2.45(1)
Fe(4)	½	¾	¼	0	0	2.45(1)
Fe(5)	0	0	½	0	0	-2.45(1)
Fe(6)	0	½	½	0	0	2.45(1)
Fe(7)	½	¼	¾	0	0	2.45(1)
Fe(8)	½	¾	¾	0	0	-2.45(1)

Table 5.8: The magnetic model refined for $La_{0.05}Sr_{1.95}FeIrO_6$ against neutron powder diffraction data collected at 1.5 K.

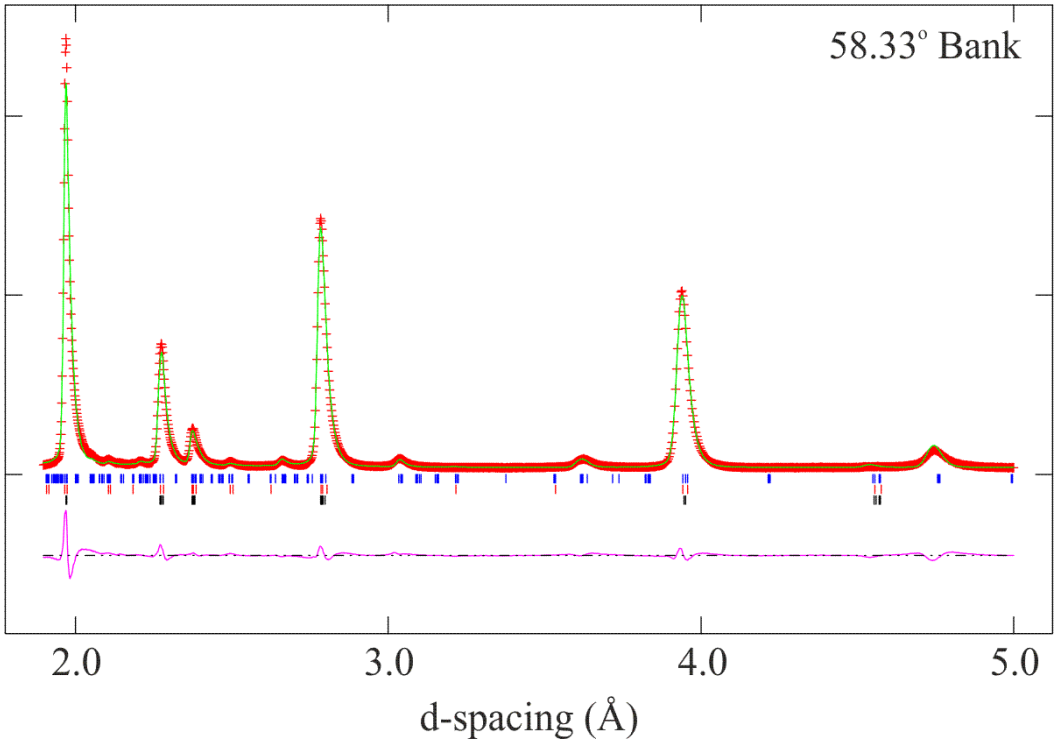

Figure 5.12: Observed, calculated and difference plots from the 152.91 º bank for refinement of the $I\bar{1}$ + $P2_1/n$ structural model of $La_{0.05}Sr_{1.95}FeIrO_6$ against neutron powder diffraction data collected at 1.5 K using the WISH instrument. Tick marks correspond to the following: Black= $I\bar{1}$ Red= $P2_1/n$ Blue= Magnetic model

5.3.2.3 Variable temperature neutron powder diffraction data

Neutron powder diffraction data were collected from $La_{0.05}Sr_{1.95}FeIrO_6$ at various temperatures between 1.5 K and 250 K. The patterns collected at 120 K and below are all similar varying only in the intensity of the Bragg peaks associated with magnetic order. The ordered moment was refined to zero for data collected above 120 K. Figure 5.13 shows the evolution of the refined magnetic moment compared to the SQUID magnetometry data.

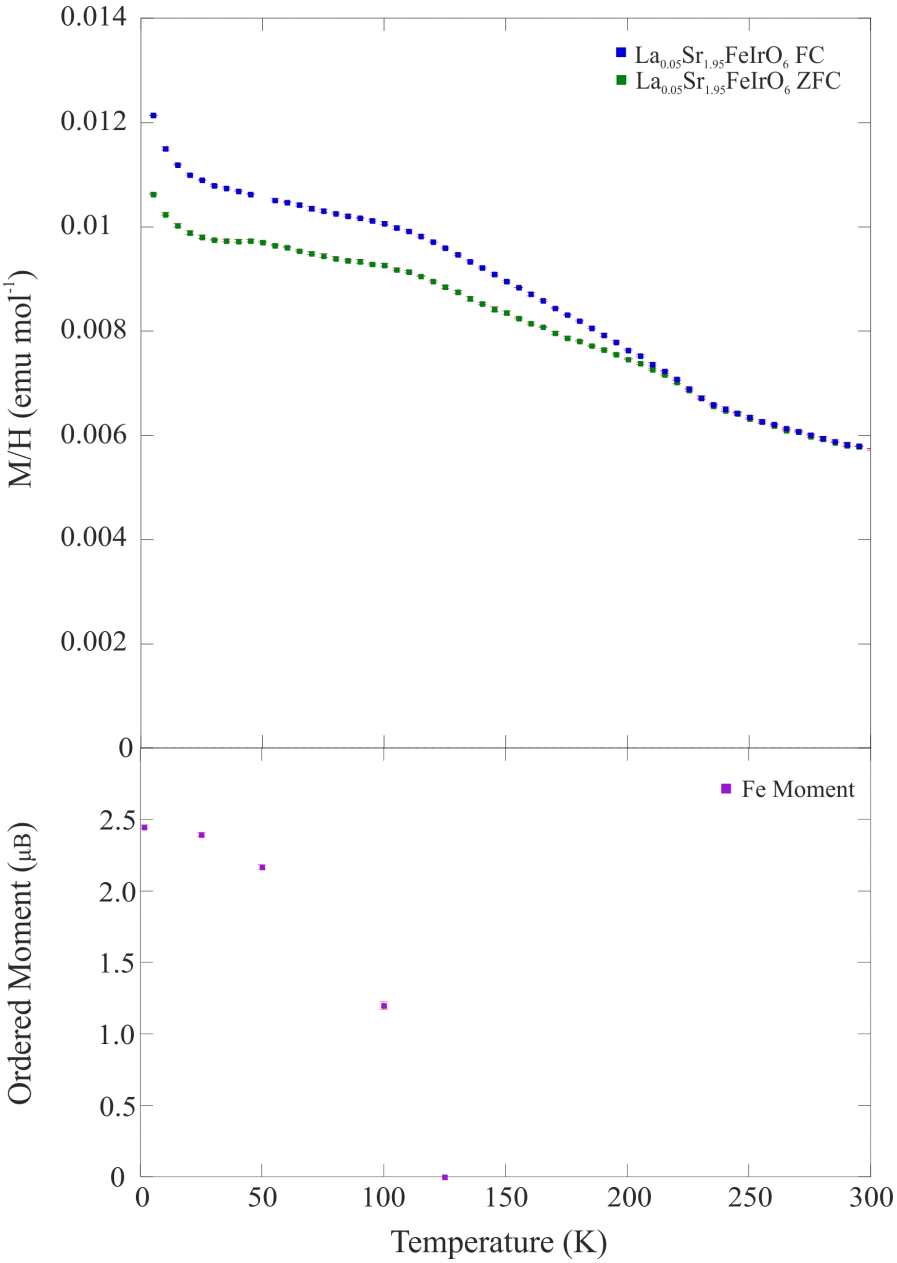

Figure 5.13: The zero-field cooled and field-cooled magnetisation data of $La_{0.05}Sr_{1.95}FeIrO_6$ and the refined ordered moments extracted from refinements of neutron diffraction data.

5.3.3 ^{57}Fe Mössbauer Spectroscopy of $La_{0.05}Sr_{1.95}FeIrO_6$

^{57}Fe Mössbauer spectra were collected from a sample of $La_{0.05}Sr_{1.95}FeIrO_6$ at 293 K, 200 K and 10 K and are shown in Figure 5.14. The spectra collected at 293 K and 200 K could be fit by two signals: a sharp singlet, which is consistent with Fe^{3+} in a symmetric site, and a broader doublet, which is consistent with Fe^{3+} in a more distorted co-ordination

centre. The spectrum collected at 10 K could be fit to two magnetic sextets. Table 5.9 details the parameters extracted from the fits to each of the spectra.

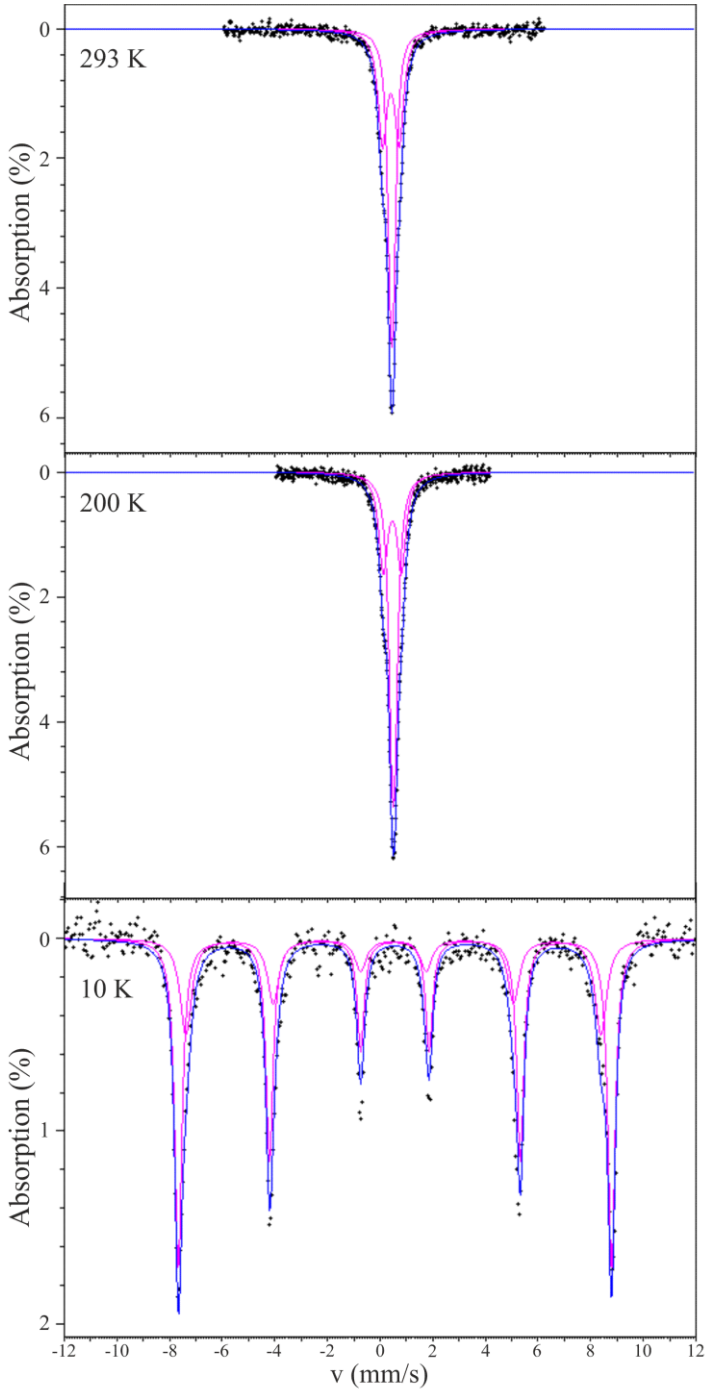

Figure 5.14: ^{57}Fe Mössbauer spectra collected at 293 K, 200 K and 10 K.

T (K)	Site 1					Site 2					χ^2
	CS (mm/s)	Δ (mm/s)	B_{hf} (T)	HWHM (mm/s)	%	CS (mm/s)	Δ (mm/s)	B_{hf} (T)	HWHM (mm/s)	%	
293	0.400(6)	0.634(3)	0	0.205(1)	47.0(6)	0.437(2)	0.115(1)	0	0.134(2)	53.0(6)	0.595
200	0.459(5)	0.691(2)	0	0.201(1)	39.9(5)	0.496(1)	0.122(1)	0	0.148(2)	60.1(5)	0.572
10	0.507(22)	-	48.90(3)	0.265(5)	31(8)	0.563(2)	-	51.05(5)	0.164(1)	68(7)	0.709

Table 5.9: Fitting statistics extracted from the ^{57}Fe Mössbauer spectra collected at 293 K, 200 K and 10 K.

5.3.4 Structural characterisation of $Sr_{2-x}A_xFeIrO_6$ (A= La, Ca, Ba) and $Sr_2Ga_{0.05}FeIrO_6$

5.3.4.1 $Sr_{2-x}A_xFeIrO_6$ (A= La, Ca, Ba) synchrotron X-ray powder diffraction data

Similarly to Sr_2FeIrO_6 (Section 5.3.1.1) and $La_{0.05}Sr_{1.95}FeIrO_6$ (Section 5.3.1.2) X-ray powder diffraction data collected from samples of $La_{0.025}Sr_{1.975}FeIrO_6$, $Ca_{0.05}Sr_{1.95}FeIrO_6$, $Ca_{0.185}Ba_{0.315}Sr_{1.95}FeIrO_6$ and $Sr_2Ga_{0.05}Fe_{0.95}IrO_6$ from laboratory diffractometers could be indexed on the basis of either a monoclinic or triclinic unit cell with body-centred or primitive symmetry.

High resolution synchrotron X-ray powder diffraction data were collected from samples of $La_{0.025}Sr_{1.975}FeIrO_6$, $Ca_{0.05}Sr_{1.95}FeIrO_6$, $Ca_{0.185}Ba_{0.315}Sr_{1.95}FeIrO_6$ and $Sr_2Ga_{0.05}Fe_{0.95}IrO_6$ using instrument I11 at the Diamond Light Source Ltd (Chapter 2, Section 2.7.1.2). Structural models were constructed based on the three structural models proposed for Sr_2FeIrO_6. As described in Section 5.3.1.1 these structural models are very similar but differ in the cooperative octahedral twisting patterns. The structures and their twisting patterns are shown in Figure 5.2 and described in Table 5.2. Each model was refined against each set of data to give a good statistical fit. The fitting statistics from each refinement are shown in Tables 5.10-x.13. The observed, calculated and difference

plots for the refinements against the $I\bar{1}$, $P2_1/n$ and $I2/m$ models are shown in Figures 5.14-5.17.

Space Group	χ^2	wRp (%)	Rp (%)
$I\bar{1}$ (#2)	5.189	1.70	1.24
$I2/m$ (#12)	6.439	1.89	1.33
$P2_1/n$ (#14)	6.365	1.88	1.33

Table 5.10: Fitting statistics from the structural refinements of $La_{0.025}Sr_{1.975}FeIrO_6$ against synchrotron diffraction data collected at room temperature.

Space Group	χ^2	wRp (%)	Rp (%)
$I\bar{1}$ (#2)	18.57	2.58	1.78
$I2/m$ (#12)	22.90	2.87	1.92
$P2_1/n$ (#14)	22.89	2.87	1.92

Table 5.11: Fitting statistics from the structural two-phase refinements of $Ca_{0.05}Sr_{1.95}FeIrO_6$ against synchrotron diffraction data collected at room temperature.

Space Group	χ^2	wRp (%)	Rp (%)
$I\bar{1}$ (#2)	9.368	2.17	1.54
$I2/m$ (#12)	11.14	2.37	1.63
$P2_1/n$ (#14)	11.35	2.39	1.63

Table 5.12: Fitting statistics from the structural two-phase refinements of $Ba_{0.0185}Ca_{0.315}Sr_{1.95}FeIrO_6$ against synchrotron diffraction data collected at room temperature.

Space Group	χ^2	wRp (%)	Rp (%)
$I\bar{1}$ (#2)	13.00	2.36	1.62
$I2/m$ (#12)	18.64	2.65	1.90
$P2_1/n$ (#14)	18.75	2.66	1.91

Table 5.13: Fitting statistics from the structural two-phase refinements of $Sr_2Ga_{0.05}Fe_{0.95}IrO_6$ against synchrotron diffraction data collected at room temperature.

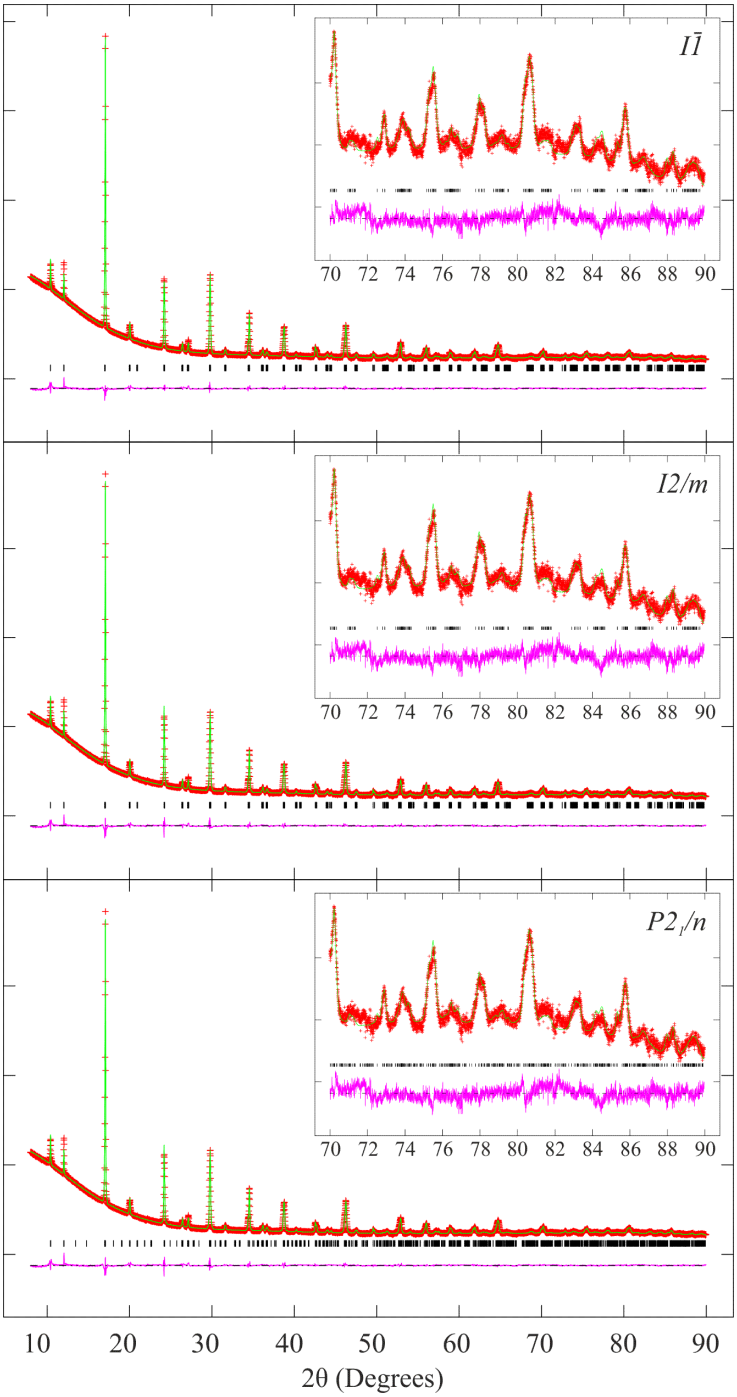

Figure 5.15: Observed, calculated and difference plots from the refinement of the $I\bar{1}$, $I2/m$ and $P2_1/n$ structural models of $La_{0.025}Sr_{1.975}FeIrO_6$ against synchrotron powder diffraction data collected at room temperature using the I11 instrument.

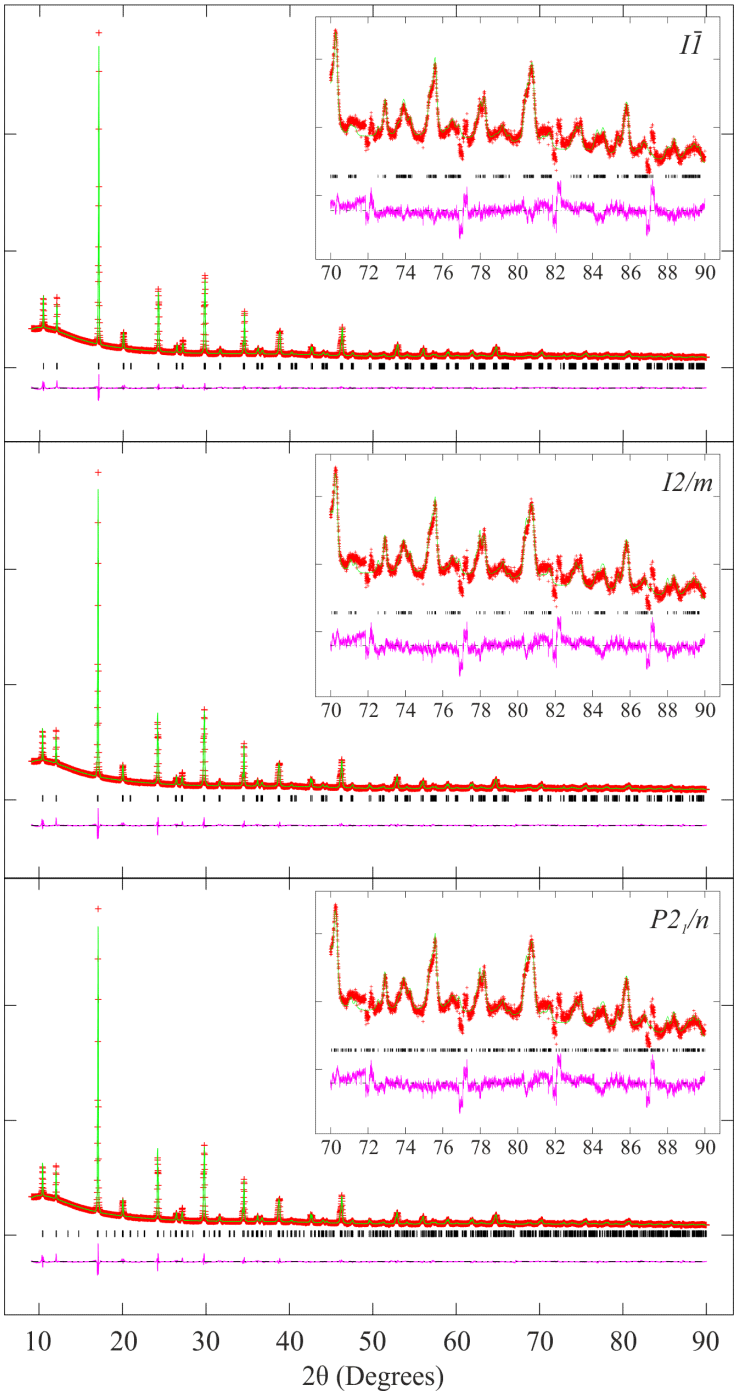

Figure 5.16: Observed, calculated and difference plots from the refinement of the $I\bar{1}$, *I2/m* and $P2_1/n$ structural models of $Ca_{0.05}Sr_{1.95}FeIrO_6$ against synchrotron powder diffraction data collected at room temperature using the I11 instrument.

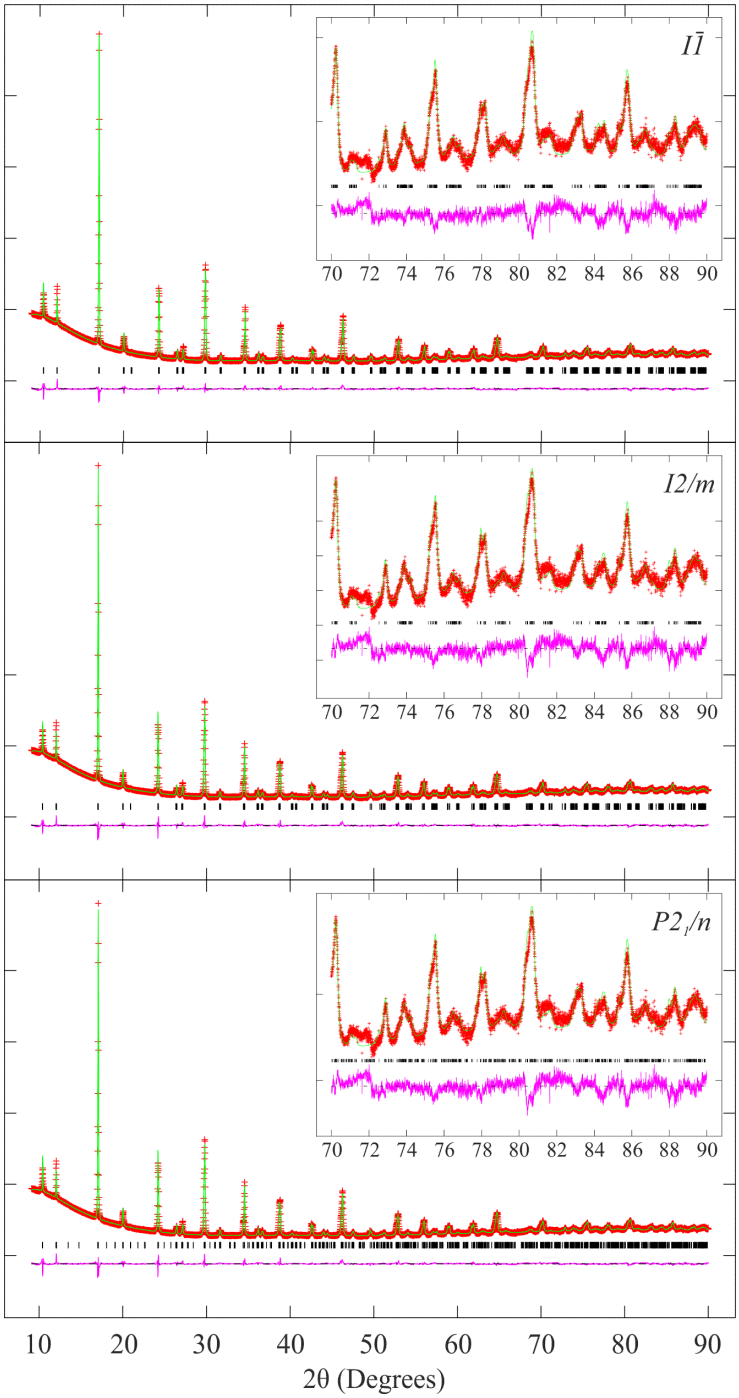

Figure 5.17: Observed, calculated and difference plots from the refinement of the $I\bar{1}$, *I2/m* and $P2_1/n$ structural models of $Ba_{0.0185}Ca_{0.315}Sr_{1.95}FeIrO_6$ against synchrotron powder diffraction data collected at room temperature using the I11 instrument.

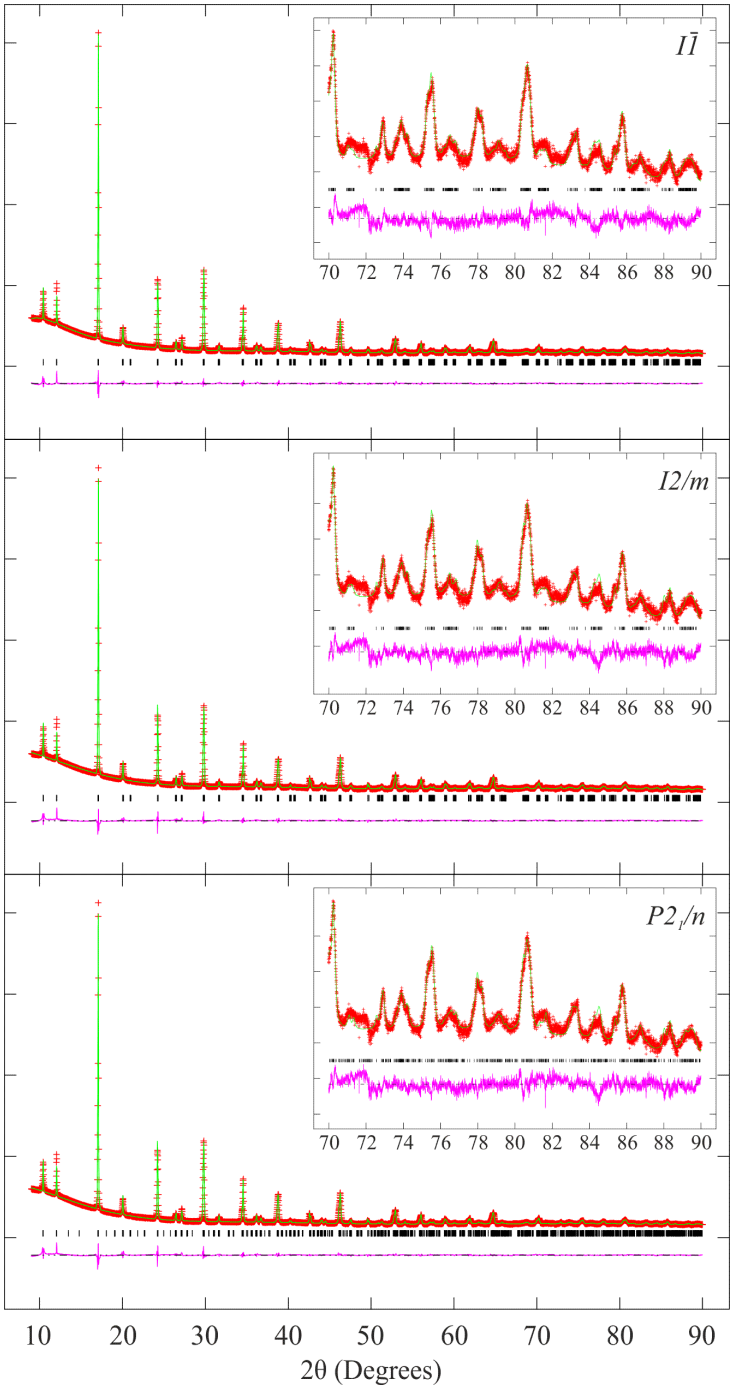

Figure 5.18: Observed, calculated and difference plots from the refinement of the $I\bar{1}$, *I2/m* and $P2_1/n$ structural models of $Sr_2Ga_{0.05}Fe_{0.95}IrO_6$ against synchrotron powder diffraction data collected at room temperature using the I11 instrument.

For each compound the narrative was much the same as it was for $La_{0.05}Sr_{1.95}FeIrO_6$ (Section 5.3.1.2). The best fit to each set of data was achieved with the $I\bar{1}$ models however the fits to the $P2_1/n$ models are also very good only being marginally worse than those of the $I\bar{1}$ models. Once again from inspection of the $70 \leq \theta\ ^{o} \leq 90$ sections of the refinements, it is clear that each of the models does a better job of accounting for certain peaks than the other. This is an indication that there are two phases in each of the samples, as there were in $La_{0.05}Sr_{1.95}FeIrO_6$.

To determine if there are two phases present in the sample two multiphase refinements for each sample were conducted: one in which the $I\bar{1}$ and $P2_1/n$ models were refined and one in which the $I2/m$ and $P2_1/n$ models were refined. The fitting statistics from each refinement are shown in Tables 5.14 - 5.17. The observed, calculated and difference plots for the refinements against the $I\bar{1}$ + $P2_1/n$ models and $I2/m$ + $P2_1/n$ models are shown in Figures 5.18 - 5.21.

Space Groups	χ^2	wRp (%)	Rp (%)
$I\bar{1}$ (#2) + $P2_1/n$ (#14)	4.032	1.54	1.14
$I2/m$ (#12)+ $P2_1/n$ (#14)	4.742	1.67	1.19

Table 5.14: Fitting statistics from the structural two-phase refinements of $La_{0.025}Sr_{1.975}FeIrO_6$ against synchrotron diffraction data collected at room temperature.

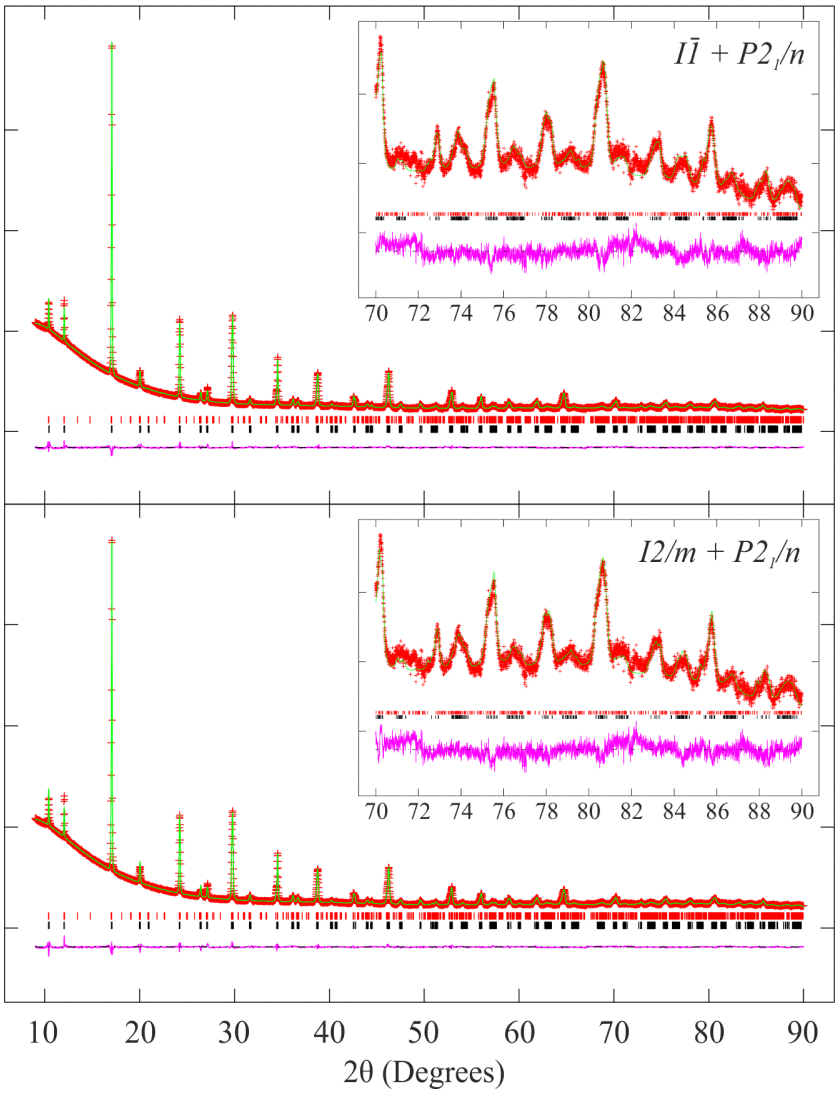

Figure 5.19: Observed, calculated and difference plots from the refinement of the $I\bar{1}$ + $P2_1/n$ and $I2/m$ + $P2_1/n$ two-phase structural models of $La_{0.025}Sr_{1.975}FeIrO_6$ against synchrotron powder diffraction data collected at room temperature using the I11 instrument.

Space Groups	χ^2	wRp (%)	Rp (%)
$I\bar{1}$ (#2) + $P2_1/n$ (#14)	16.45	2.43	1.70
$I2/m$ (#12)+ $P2_1/n$ (#14)	17.73	2.53	1.77

Table 5.15: Fitting statistics from the structural two-phase refinements of $Ca_{0.05}Sr_{1.95}FeIrO_6$ against synchrotron diffraction data collected at room temperature.

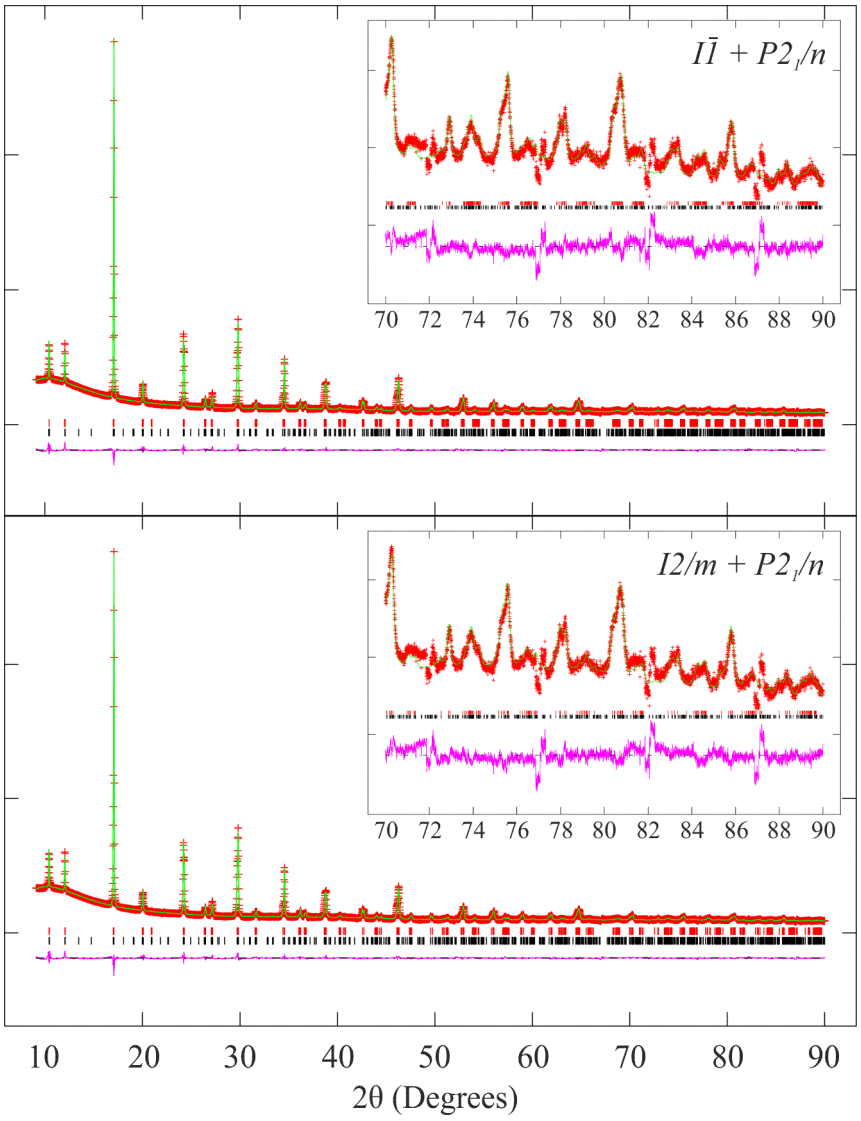

Figure 5.20: Observed, calculated and difference plots from the refinement of the $I\bar{1}$ + $P2_1/n$ and $I2/m$ + $P2_1/n$ two-phase structural models of $Ca_{0.05}Sr_{1.95}FeIrO_6$ against synchrotron powder diffraction data collected at room temperature using the I11 instrument.

Space Groups	χ^2	wRp (%)	Rp (%)
$I\bar{1}$ (#2) + $P2_1/n$ (#14)	8.565	2.04	1.49
$I2/m$ (#12)+ $P2_1/n$ (#14)	9.026	2.14	1.53

Table 5.16: Fitting statistics from the structural two-phase refinements of $Ba_{0.0185}Ca_{0.315}Sr_{1.95}FeIrO_6$ against synchrotron diffraction data collected at room temperature.

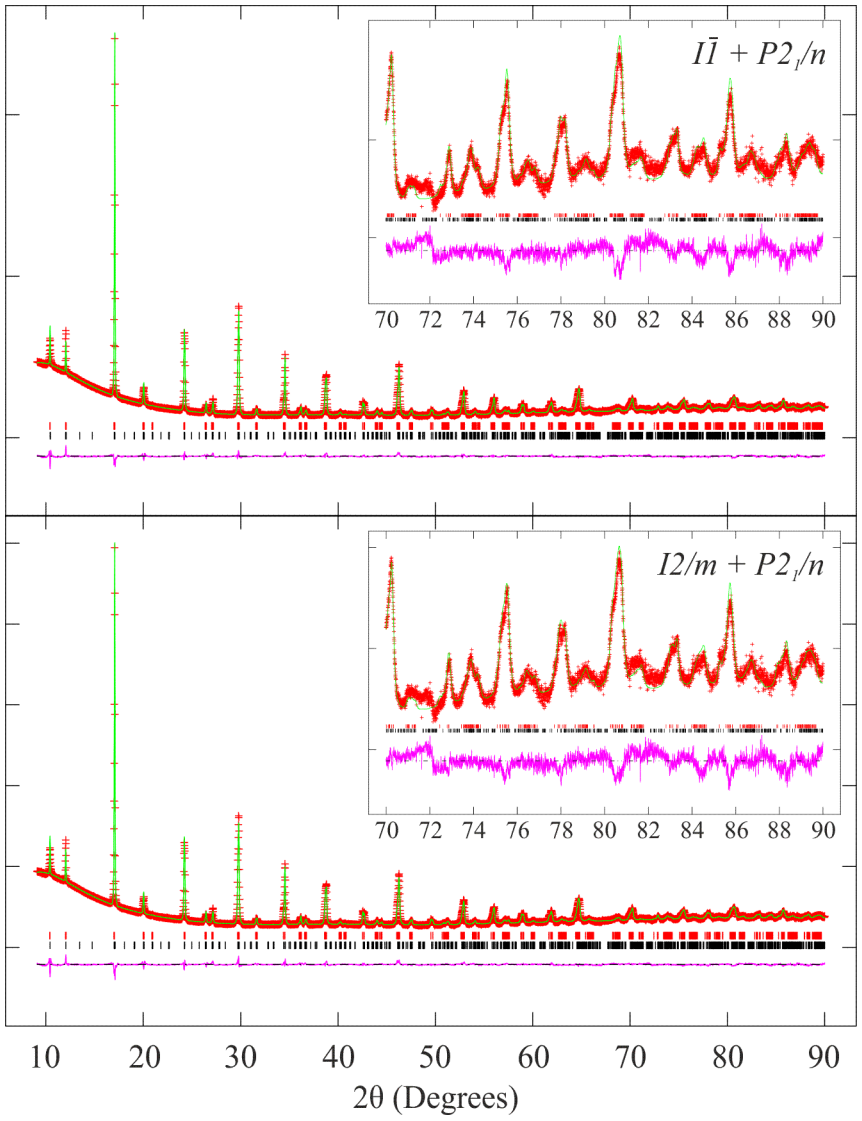

Figure 5.21: Observed, calculated and difference plots from the refinement of the $I\bar{1}$ + $P2_1/n$ and $I2/m$ + $P2_1/n$ two-phase structural models of $Ba_{0.0185}Ca_{0.315}Sr_{1.95}FeIrO_6$ against synchrotron powder diffraction data collected at room temperature using the I11 instrument.

Space Groups	χ^2	wRp (%)	Rp (%)
$I\bar{1}$ (#2) + $P2_1/n$ (#14)	10.01	2.07	1.47
$I2/m$ (#12)+ $P2_1/n$ (#14)	11.10	2.18	1.52

Table 5.17: Fitting statistics from the structural two-phase refinements of $Sr_2Ga_{0.05}Fe_{0.95}IrO_6$ against synchrotron diffraction data collected at room

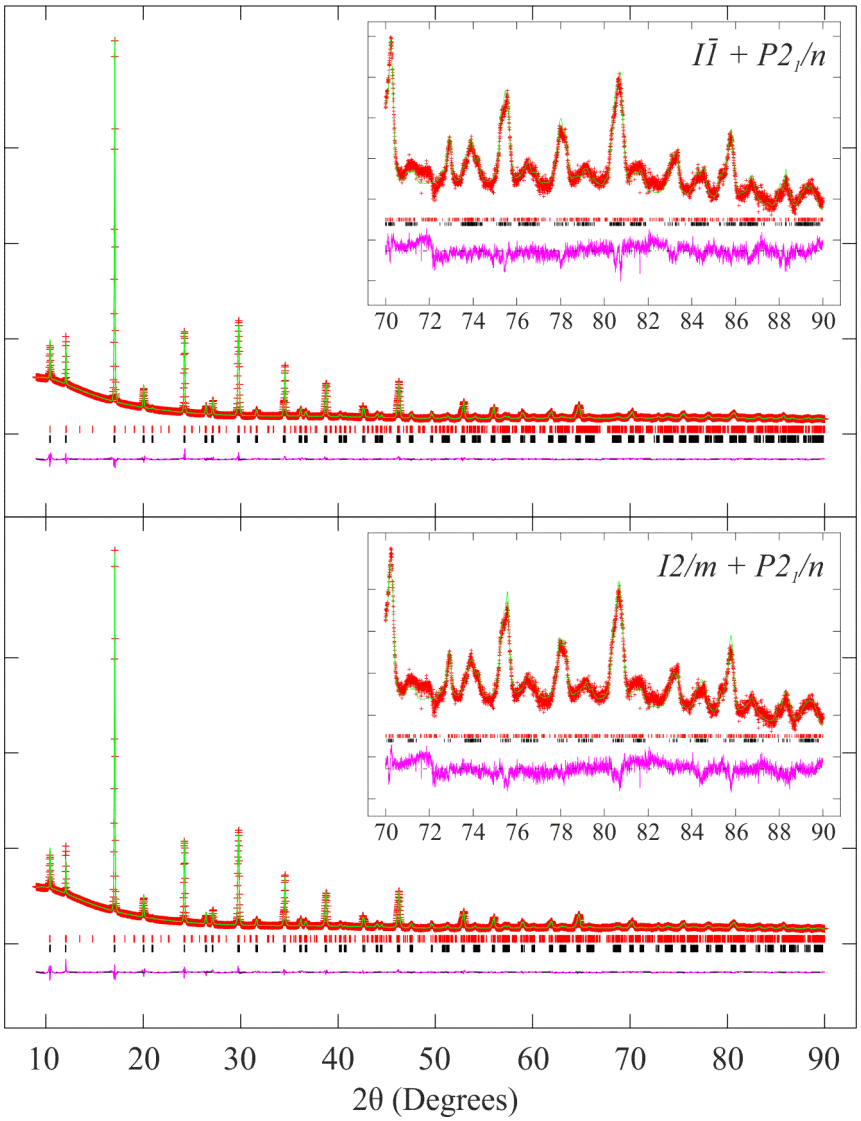

Figure 5.22: Observed, calculated and difference plots from the refinement of the $I\bar{1}$ + $P2_1/n$ and $I2/m$ + $P2_1/n$ two-phase structural models of $Sr_2Ga_{0.05}Fe_{0.95}IrO_6$ against synchrotron powder diffraction data collected at room temperature using the I11 instrument.

The fitting statistics of the multiphase refinements for each sample are better than those of the single phase refinements, a result that once again suggests that there are two phases in

each sample: one with a primitive structure and one with a body-centred structure. For each compound, of the two multiphase refinements the best fit was achieved by the refinement of the $I\bar{1}$ and $P2_1/n$ models. Figures 5.18 - 5.21 show the $70 \leq \theta\ ^{o} \leq 90$ section of the $I\bar{1}$ and $P2_1/n$ of the refinements. Comparing them to the same sections for the single phase $I\bar{1}$ and $P2_1/n$ refinements in Figures 5.14 – 5.17 it is evident that, as expected, the combined refinements do a much better job of fitting peaks that are otherwise unaccounted for in the single phase refinements. These conclusions are consistent with those drawn from similar analysis conducted on a sample of $La_{0.05}Sr_{1.95}FeIrO_6$.

5.3.5 Magnetic characterisation of $Sr_{2-x}A_xFeIrO_6$ (A= La, Ca, Ba) and $Sr_2Ga_{0.05}FeIrO_6$

5.3.5.1 SQUID magnetisation data

Magnetisation data were collected from samples of $La_{0.025}Sr_{1.975}FeIrO_6$, $Ca_{0.05}Sr_{1.95}FeIrO_6$, $Ca_{0.185}Ba_{0.315}Sr_{1.95}FeIrO_6$ and $Sr_2Ga_{0.05}FeIrO_6$ in an applied field of 100 Oe in the temperature range $5 \leq T\ /\ K \leq 300$. The zero-field cooled (ZFC) data, field cooled (FC) data and magnetisation-field isotherms collected at 300 K and 5 K for each sample are shown in Figure 5.23 alongside magnetisation data collected from Sr_2FeIrO_6 and $La_{0.05}Sr_{1.95}FeIrO_6$. The data collected from each sample have the same features as that collected from $La_{0.05}Sr_{1.95}FeIrO_6$ (Section 5.3.2.1), differing only in the magnitude of the magnetisation. At temperatures between $300 \leq T\ /\ K \leq 225$ K the zero-field cooled and field cooled measurements are the same. No data set could be fit to the Curie-Weiss law over any significant temperature range. At temperatures between $120 \leq T\ /\ K \leq 225$ the zero-field cooled and field cooled measurements diverge and at temperatures below 120 K the zero-field and field cooled measurements remain divergent but at a different rate.

The magnetisation isotherms collected at 5 K shows a small amount of hysteresis (Figure 5.24). Similarly to $La_{0.05}Sr_{1.95}FeIrO_6$, these results indicate that the doped samples undergo a transition to a magnetically ordered state at 120 K.

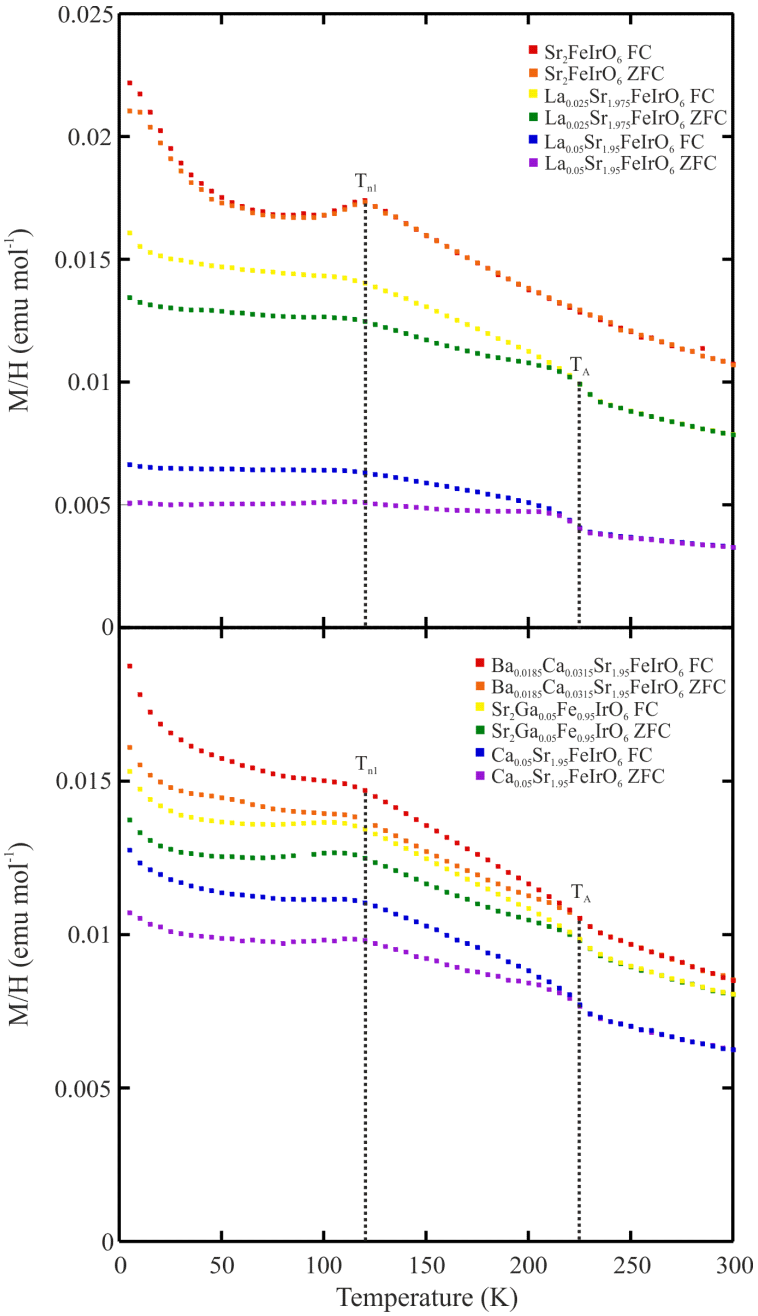

Figure 5.23: Zero-field cooled and field-cooled magnetisation data collected from Sr_2FeIrO_6 and all other doped samples.

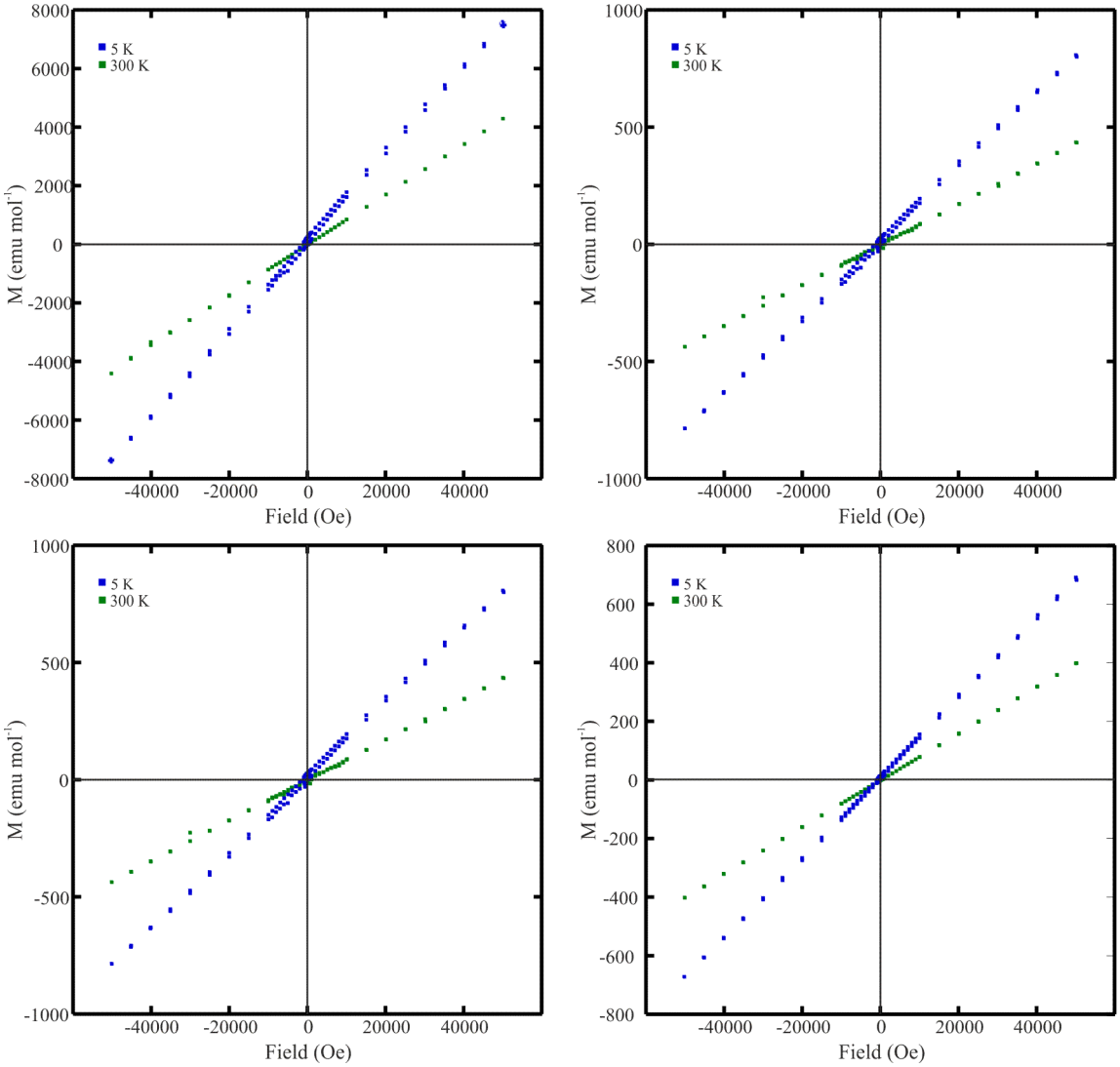

Figure 5.24: Magnetisation-field isotherms collected from a) $La_{0.025}Sr_{1.95}FeIrO_6$ b) $Ca_{0.05}Sr_{1.95}FeIrO_6$ c) $Ba_{0.0185}Ca_{0.0315}FeIrO_6$ d) $Sr_2Ga_{0.05}Fe_{0.95}IrO_6$

5.4 Discussion

5.4.1 The structure of Sr_2FeIrO_6

The structure of S_2FeIrO_6 has been a topic of significant debate in the literature. The initial study conducted by Battle et al.[22], in which structural refinement was conducted using high resolution neutron powder diffraction data, concluded that the structure of Sr_2FeIrO_6 was best described by a triclinic model with $I\bar{1}$ symmetry (Section 5.3.1.1, Table 5.1). Since this first report there have been no fewer than five papers that concern

Sr_2FeIrO_6 and its structure, the majority of which dispute the original structural classification.

The study conducted by Qasim et al.[108] states that their synchrotron X-ray powder diffraction data and neutron powder diffraction data show no evidence of Sr_2FeIrO_6 having a triclinic $I\bar{1}$ structure. Instead they suggest that Sr_2FeIrO_6 adopts a monoclinic *I2/m* structure. This conclusion was supported by a paper by Kayser et al.[109], once again based on the refinement against synchrotron X-ray powder diffraction data and neutron powder diffraction data. An investigation conducted by Bufaiçal et al.[106] initially concluded that Sr_2FeIrO_6 has a monoclinic $P2_1/n$ structure, on the basis of synchrotron X-ray powder diffraction data. However a second investigation conducted by the same group concludes that the structure of Sr_2FeIrO_6 is dependent on how it is made[107]. They promulgate that synthesis by heating at 1100 ^oC results in the structure with $P2_1/n$ symmetry but heating a sample progressively at temperatures between 975 – 1100 ^oC results in the *I2/m* structure. Finally the most recent study concerning the structure of Sr_2FeIrO_6 was published by Kharkwal et al [105]. and returns to the original assertion that it has an $I\bar{1}$ structure. The problem with each of these subsequent studies is that the data they present are entirely inconsistent with that published in the original paper published by Battle et al. A number of the papers report the presence of Fe_2O_3 or IrO_2 in their samples and those that don't present suspicious data which clearly shows their samples contain ferromagnetic impurities. These conflicting sets of data lead us to conclude that the samples from the studies that followed Battle et al. were not phase pure. This assertion is supported by the experimental data and results we obtained. The magnetisation data we collected from Sr_2FeIrO_6 (Section 5.3.2.1) is identical to that reported by Battle et al., a clear indication our phase is the same as theirs. Refinement of synchrotron X-ray powder diffraction data against each of the $I\bar{1}$, *I2/m* and $P2_1/n$ models

(Section 5.3.1.1) shows that we have a phase pure sample and yields two significant results illustrated in Table 5.3 and Figure 5.3. Firstly, it shows that the best fit to the data was achieved by refinement of the $I\bar{1}$ model against the data. The efficacy of this is clear from both the fitting statistics of the refinement and how well the peaks at $70 \leq 2\theta\ ^{o} \leq 90$ are fit compared to the other refinements. The second key result is that the $I\bar{1}$ structure is only slightly better than the *I2/m* and $P2_1/n$. This result is not surprising if we examine the structures. Figure 5.2 in Section 5.3.1.1 shows the unit cells of each structure and Table 5.2 states the MO_6 octahedral twisting patterns permitted by each structure. Inspection of the unit cells reveals they are very similar. The differences lie in how the MO_6 octahedra subtly twist and as these twist are phenomena that are defined by the oxygen positions it can be difficult to establish the true structure with X-ray diffraction data, especially in this case where the cations have significantly higher electron counts than oxygen. It is therefore not entirely surprising that the *12/m* and $P2_1/n$ models can do a very good job at fitting the $I\bar{1}$ structure or Sr_2FeIrO_6. The closeness of fit of all of these models will be a key point in determining the structure of the doped phases and understanding the results reported by the other studies.

5.4.2 Structure of doped Sr_2FeIrO_6

The refinement of data diffraction collected from $La_{0.05}Sr_{1.95}FeIrO_6$ show that it has a complex and unique structure. As with Sr_2FeIrO_6 the X-ray and neutron diffraction data could be fit very well to the *I2/m*, $P2_1/n$ and $I\bar{1}$ structural models, with the $I\bar{1}$ model fitting best. However further analysis proved that the sample consists of two phases: an $I\bar{1}$ phase and a $P2_1/n$ phase. This phase separation was confirmed by a ^{57}Fe Mössbauer spectrum collected at 300 K. Similar analysis was conducted on the synchrotron X-ray diffraction data collected from samples of $La_{0.025}Sr_{1.975}FeIrO_6$, $Ca_{0.05}Sr_{1.95}FeIrO_6$, $Ca_{0.185}Ba_{0.315}Sr_{1.95}FeIrO_6$ and $Sr_2Ga_{0.05}Fe_{0.95}IrO_6$ which yielded the same results. From

this we can conclude that the behaviour of $La_{0.05}Sr_{1.95}FeIrO_6$ is the same as that of the other doped samples and extrapolate the results we obtained from neutron diffraction and apply them to the doped samples.

The refinements of the doped samples yielded several key results that are of interest. The structural parameters extracted from the refinements of the doped samples are all very similar for the $I\bar{1}$ phase and are in turn all very similar to those extracted from the refinement of Sr_2FeIrO_6 whereas those of the $P2_1/n$ phase are more varied, as shown in Tables 5.18 and 5.19. This would suggest that the $I\bar{1}$ phase in all samples is Sr_2FeIrO_6, and that the dopants are entirely contained in the $P2_1/n$ phase. The implication of this is that the $I\bar{1}$ phase is fragile and any change in stoichiometry results in the extrusion of a secondary phase with the $P2_1/n$ structure. This assertion is supported by the variety of cations used to dope Sr_2FeIrO_6 and their structural or chemical function. We have made aliovalent and isovalent substitutions using La^{3+} and Ca^{2+}, Ba^{2+}. We have reduced the tolerance factor using La^{3+} and Ca^{3+}, and maintained it using Ca^{2+}/Ba^{3+}. Finally we have made isovalent B-site substitution using Ga^{3+}. Each of these substitutions leads to phase separation. This is clear evidence that the $I\bar{1}$ structure of Sr_2FeIrO_6 is highly sensitive and only stable when stoichiometry is rigorously maintained. This sensitivity provides an explanation for the conflicting results reported in the literature discussed in Section 5.4.1. Iridium can be volatile in the presence of oxygen. Consequently iridium deficient samples ($Sr_2FeIr_{1-x}O_6$) can easily be made if care is not taken to avoid iridium loss. The findings discussed above suggest that these non-stoichiometric samples would phase separate into a mixture of $I\bar{1}$ and $P2_1/n$, a complex state that requires high resolution diffraction data to deconvolute.

	$I\bar{1}$		
	a (Å)	b (Å)	c (Å)
Sr_2FeIrO_6	5.55194(4)	5.57793(4)	7.84457(5)
$La_{0.05}Sr_{1.95}FeIrO_6$	5.5499(3)	5.57843)	7.8458(4)
$La_{0.025}Sr_{1.975}FeIrO_6$	5.55596(7)	5.58366(6)	7.85434(8)
$Ca_{0.05}Sr_{1.95}FeIrO_6$	5.5610(1)	5.5827(1)	7.8563(1)
$Ba_{0.0185}Ca_{0.0315}Sr_{1.95}FeIrO_6$	5.55746(9)	5.58843(6)	7.8561(1)
$Sr_2Ga_{0.05}Fe_{0.95}IrO_6$	5.5587(1)	5.58995(9)	7.8584(1)

Table 5.18: Lattice parameters of the $I\bar{1}$ phase extracted from two-phase refinement of synchrotron X-ray diffraction data collected from Sr_2FeIrO_6 and doped variants.

	$P2_1/n$		
	a (Å)	b (Å)	c (Å)
Sr_2FeIrO_6	-	-	-
$La_{0.05}Sr_{1.95}FeIrO_6$	5.5562(3)	5.5837(3)	7.8488(3)
$La_{0.025}Sr_{1.975}FeIrO_6$	5.5642(1)	5.5928(1)	7.8614(1)
$Ca_{0.05}Sr_{1.95}FeIrO_6$	5.5566(1)	5.5908(1)	7.8533(2)
$Ba_{0.0185}Ca_{0.0315}Sr_{1.95}FeIrO_6$	5.56179(1)	5.5800(1)	7.8572(3)
$Sr_2Ga_{0.05}Fe_{0.95}IrO_6$	5.58186(8)	5.56024(8)	7.8575(1)

Table 5.19: Lattice parameters of the $P2_1/n$ phase extracted from two-phase refinement of synchrotron X-ray diffraction data collected from Sr_2FeIrO_6 and doped variants.

Another key finding from the structural refinement of $La_{0.05}Sr_{1.95}FeIrO_6$ is the local co-ordination geometries of the B-site cations. Table 5.20 details a number of A_2BIrO_6 compounds reported in the literature that adopt an $I\bar{1}$ structure, along with their bond lengths. The bond lengths of these compounds show the octahedra in these compounds are quite symmetric. The literature is replete with examples of extended oxides which contain Ir^{V} [23-24, 110] and one of the results emphasised by many of these studies is that when in a six co-ordinate environment Ir^{V} sits in a highly symmetric octahedral site. This has been attributed to the strong spin orbit coupling splitting the t_{2g} orbital set resulting in the J_{eff} = 0 electronic ground state shown in Figure 5.26. The local co-ordination environments of the majority Fe and Ir sites in both the $P2_1/n$ and $I\bar{1}$ structures extracted from the refinement of neutron diffraction data collected from $La_{0.05}Sr_{1.95}FeIrO_6$ are

shown in Figure 5.25. The bond lengths shown in Table 5.20 and Figure 5.25 appear to corroborate this assertion with the exception of Ba_2BiIrO_6[104]. Closer inspection of the bond lengths in Figure 5.25 shows that the octahedra of the $P2_1/n$ structure are slightly less symmetric than those of the $I\bar{1}$ structure. This observation is consistent with the ^{57}Fe Mössbauer spectra collected at 293 K and 200 K which show there are two unique iron environments (Section 5.3.3). This may seem a pedantic observation however this subtle distinction in the co-ordination environments has significant implications on the observed magnetic behaviour of the doped samples and will be discussed in depth in Section 5.4.3.4.

$AA'BIrO_6$	B-O Bond Lengths (Å)	Ir-O Bond Lengths (Å)
$BaLaCoIrO_6$	2.051(8)	1.972(8)
	2.053(9)	1.971(9)
	2.038(11)	1.96(11)
Ba_2LaIrO_6	2.345(7)	1.960(7)
	2.334(8)	1.968(8)
	2.331(7)	1.975(7)
Ba_2BiIrO_6	2.455(18)	1.960(7)
	2.332(12)	1.968(8)
	2.306(13)	1.807(18)
Sr_2FeIrO_6	1.971(7)	1.977(7)
	1.991(8)	1.960(8)
	1.973(9)	1.972(9)

Table 5.20: Reported bond lengths of iridium containing double perovskites with an $I\bar{1}$ structure.

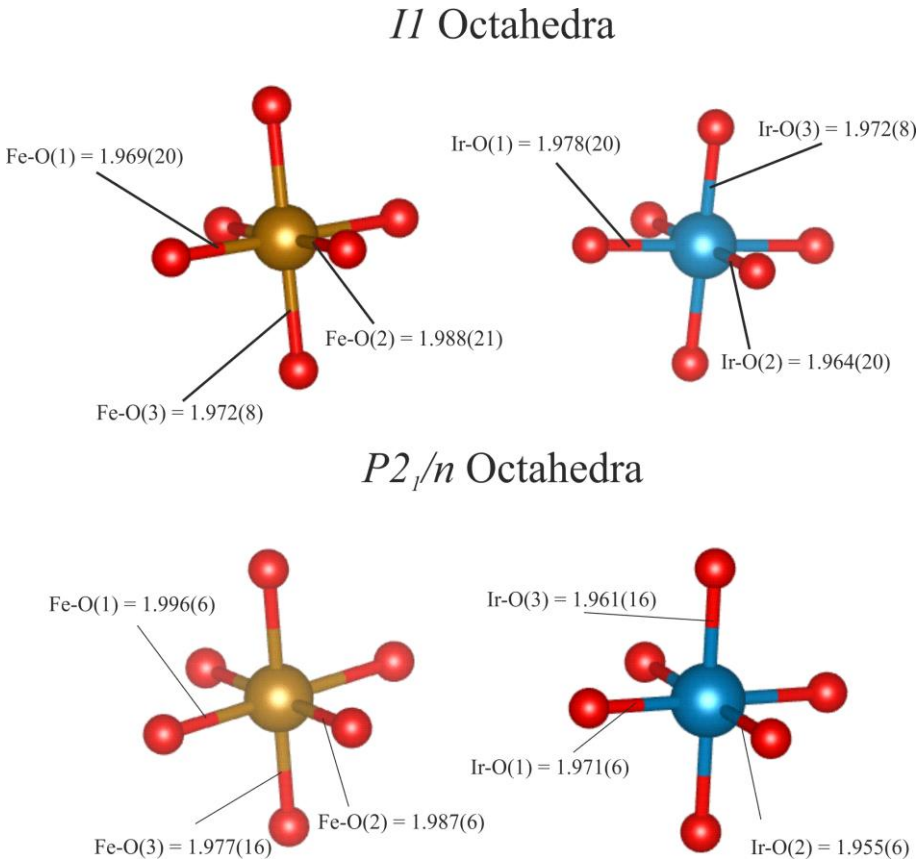

Figure 5.25: MO_6 bond lengths extracted from refinement of neutron diffraction data collected from the WISH instrument at 250 K. The Blue and brown spheres are iron and iridium respectively.

Finally, the synchrotron X-ray powder diffraction data collected at temperatures in the range $100 \leq T\ /K \leq 300$ reveal a significant difference between the $I\bar{1}$ and $P2_1/n$ phases. Figure 5.6 (Section 5.3.1.3) shows that upon cooling the lattice parameters of the $I\bar{1}$ phases decrease at a roughly uniform rate with no clearly observable anomalies. This is not the case for the $P2_1/n$ phase. The data presented in Figure 5.6 clear show that at around 220 K the rate at which the *a* and *b* lattice parameters decrease changes resulting in clearly observable anomaly, this also results in a change in the rate at which the volume of the unit cell decreases. These changes in the rate at which the lattice parameters decrease suggest that there is an event around 220 K that results in a structural deviation in the $P2_1/n$ phase. The temperature at which this structural deviation occurs in

coincident with the first magnetic anomaly observed in the magnetisation data collected from all of the doped samples (Section 5.3.5.1). Either the coincidence of these events is unrelated, which is unlikely, or they are related.

5.4.3 Magnetism of Doped Sr_2FeIrO_6

5.4.3.1 Magnetic properties of Sr_2FeIrO_6

To fully understand the magnetic properties of $La_{0.05}Sr_{1.95}FeIrO_6$, $La_{0.025}Sr_{1.975}FeIrO_6$, $Ca_{0.05}Sr_{1.95}FeIrO_6$, $Ca_{0.185}Ba_{0.315}Sr_{1.95}FeIrO_6$ and $Sr_2Ga_{0.05}Fe_{0.95}IrO_6$ we must first understand the magnetic properties of Sr_2FeIrO_6. Figure 5.10 in Section 5.3.2.1 shows the zero-field-cooled (ZFC) and field cooled (FC) measurements we conducted on a sample of Sr_2FeIrO_6. It shows that Sr_2FeIrO_6 undergoes a magnetic ordering transition to a canted antiferromagnetic state at 120 K, findings that are in agreement with the original study conducted by Battle et al[22]. This original study also solved the low temperature magnetic structure of Sr_2FeIrO_6 and showed the magnetic state is a type-II antiferromagnetic state in which the Fe lattice orders. This magnetic unit cell is shown is shown in Figure 5.28 and the electronic spin states of the cations are shown in Figure 5.26. The refined magnetic unit cell proves that the Ir cations have no ordered moment and that the dominant coupling interaction is the Fe-Ir- Fe interaction. If we consider the spin sates of these cations we can see that the coupling occurs through the Ir^V e_g orbitals and is thus a π-exchange. This magnetic state has also been observed in $BaLaCoIrO_6$[23].

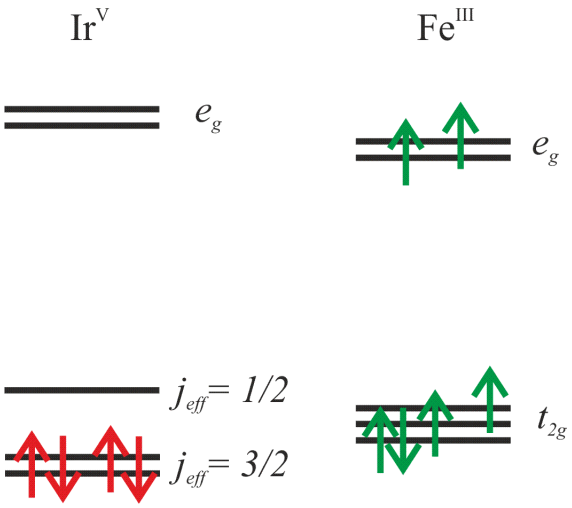

Figure 5.26: The electronic states of Ir^{V} and Fe^{III} in Sr_2FeIrO_6

5.4.3.2 Magnetic properties of $La_{0.05}Sr_{1.95}FeIrO_6$

The ZFC and FC experiments conducted on sample of $La_{0.05}Sr_{1.95}FeIrO_6$, outlined in Section 5.3.2.1 and shown in Figure 5.9, indicate the magnetism of this compound is far more complex than that of Sr_2FeIrO_6. The most striking observation extracted from these data is that there are two magnetic events: T_A at 225 K and T_{n1} at 120 K. Magnetisation isotherms collected from a sample of $La_{0.05}Sr_{1.95}FeIrO_6$ at temperatures between $120 \leq T\ K \leq 300$ K exhibit no hysteresis as shown in Figure 5.9, proving that this first event is not due to a ferromagnetic iron containing impurity. Furthermore the ^{57}Fe Mössbauer spectrum collected at 200 K shows little difference to that collected at 293 K and clearly shows the iron lattice is not ordered. This means that the magnetic event at T_A must originate from an iridium impurity or the iridium lattice. The most plausible iridium impurity phase would be Sr_2IrO_4 considering it has a transition to a canted antiferromagnetic state at around 240 K[20]. We calculated that to account for the weak magnetic signal at least 0.3 mole% would need to be present in the sample of $La_{0.05}Sr_{1.95}FeIrO_6$. Analysis of the X-ray synchrotron diffraction data and neutron diffraction reveal we would be confident in detecting levels of Sr_2IrO_4 as low as 0.03

mole%. Inspection of these diffraction data shows no evidence for the presence of Sr_2IrO_4. Figure 5.27 shows the simulation against the synchrotron X-ray diffraction data of $La_{0.05}Sr_{1.95}FeIrO_6$ with 0.3 mole% of Sr_2IrO_4 added as a second phase. The pattern shows diffraction peaks are clearly visible. Thus while it is impossible to state that no impurity is present, we can reasonably conclude the magnetic anomaly is not due to an iridium containing impurity.

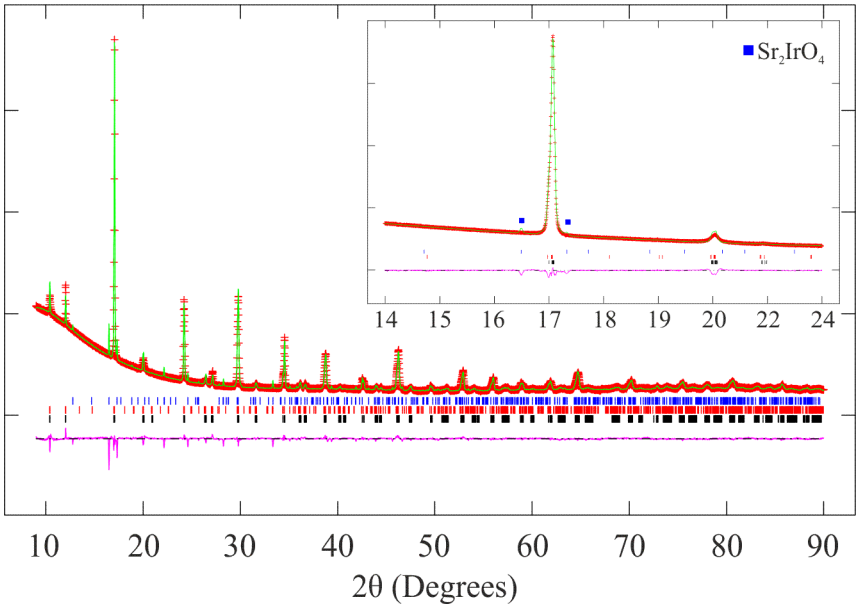

Figure 5.27: Observed, calculated and difference plots from the refinement of the $I\bar{1}$ + $P2_1/n$ and $I2/m$ + $P2_1/n$ two-phase structural models of $La_{0.05}Sr_{1.95}FeIrO_6$ against synchrotron powder diffraction data collected at room temperature using the I11 instrument with 0.03% weight fraction of Sr_2IrO_4. Tick marks correspond to the following: Black= $I\bar{1}$ Red= $P2_1/n$ Blue= Sr_2IrO_4

The magnetisation isotherm collected from $La_{0.05}Sr_{1.95}FeIrO_6$ at 5 K exhibits hysteresis indicating that the magnetic event at T_{n1} results in a canted antiferromagnetic state. The ^{57}Fe spectrum collected at 10 K can be fit to two sextets indicating that the iron lattices in both the $I\bar{1}$ and $P2_1/n$ phases are magnetically ordered (Section 5.3.3). Refinement against the neutron diffraction data collected from $La_{0.05}Sr_{1.95}FeIrO_6$ at 1.5 K shows that $La_{0.05}Sr_{1.95}FeIrO_6$ has a magnetically ordered state that can be described by the unit cell in Figure 5.28. Only one set of magnetic Bragg peaks were observed thus we can conclude

that both phases have the same ordered state. The unit cell in Figure 5.28 bears more than a passing resemblance to that of Sr_2FeIrO_6 and demonstrates that ostensibly $La_{0.05}Sr_{1.95}FeIrO_6$ has the same magnetically order state as Sr_2FeIrO_6. Once again the ordered magnetic state is a type-II antiferromagnetic state in which the dominant super exchange mechanism is the Fe-Ir-Fe exchange.

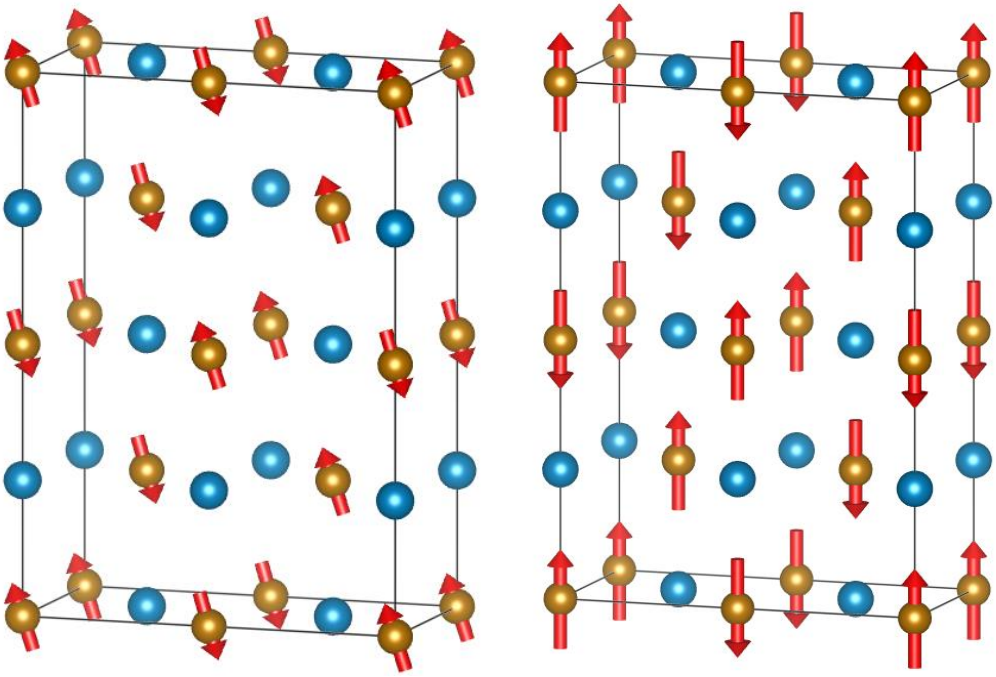

Figure 5.28: Left) The magnetic unit cell of Sr_2FeIrO_6 Right) The refined magnetic unit cell of $La_{0.05}Sr_{1.95}FeIrO_6$

Comparison of the neutron diffraction data collected from $La_{0.05}Sr_{1.95}FeIrO_6$ at temperatures between $120 \leq T\ K \leq 225$ to that collected at 1.5 K and 300 K showed that there were no additional Bragg peaks associated with magnetic order. This was confirmed by refinement against the data which indicated there was no detectable moment on Fe or Ir below 125 K (Section 5.3.2.3). This is consistent with the magnetisation data discussed earlier in this section.

5.4.3.3 Magnetisation of doped Sr_2FeIrO_6

Comparison of the magnetisation data collected from samples of doped Sr_2FeIrO_6 show that the topology of the ZFC and FC measurements are the same, highlighting they have identical magnetic events. We have already demonstrated in Section 5.3.4.1 that the chemistry and structural composition of these samples are nearly identical, it is therefore reasonable to conclude that their magnetic properties are the same, as evidenced by the magnetisation data.

Similarly to $La_{0.05}Fe_{1.95}FeIro_6$ there are no detectable impurities in any of these samples. The magnetisation isotherms collected from these samples show no displacement or hysteresis (Section 5.3.5.1) and the high-resolution synchrotron X-ray diffraction data only exhibit peaks that are associated with the $I\bar{1}$ and $P2_1/n$ structures (Section 5.3.4.1). The lack of any observable impurity and the difference in the magnitudes of the magnetisation of each sample suggest that the magnetic events are bulk effects. The event at T_{n1} is probably due to the onset of type-II antiferromagnetic order as demonstrated by the refinement of neutron diffraction data collected from $La_{0.05}Sr_{1.95}FeIrO_6$. These additional magnetisation data confirm that the magnetic event observed at T_A in all the data is a replicable phenomenon that most likely arises from iridium lattice in the $P2_1/n$ portion of the samples. Furthermore, the anomalies observed in the lattice parameters extracted from the refinements of the variable temperature synchrotron X-ray diffraction data are clearly coincident with the magnetic event at T_A as shown in Figure 5.29, a clear suggestion that the first event is a bulk event that originates from the $P2_1/n$ phase. This is a highly unusual scenario with little precedent.

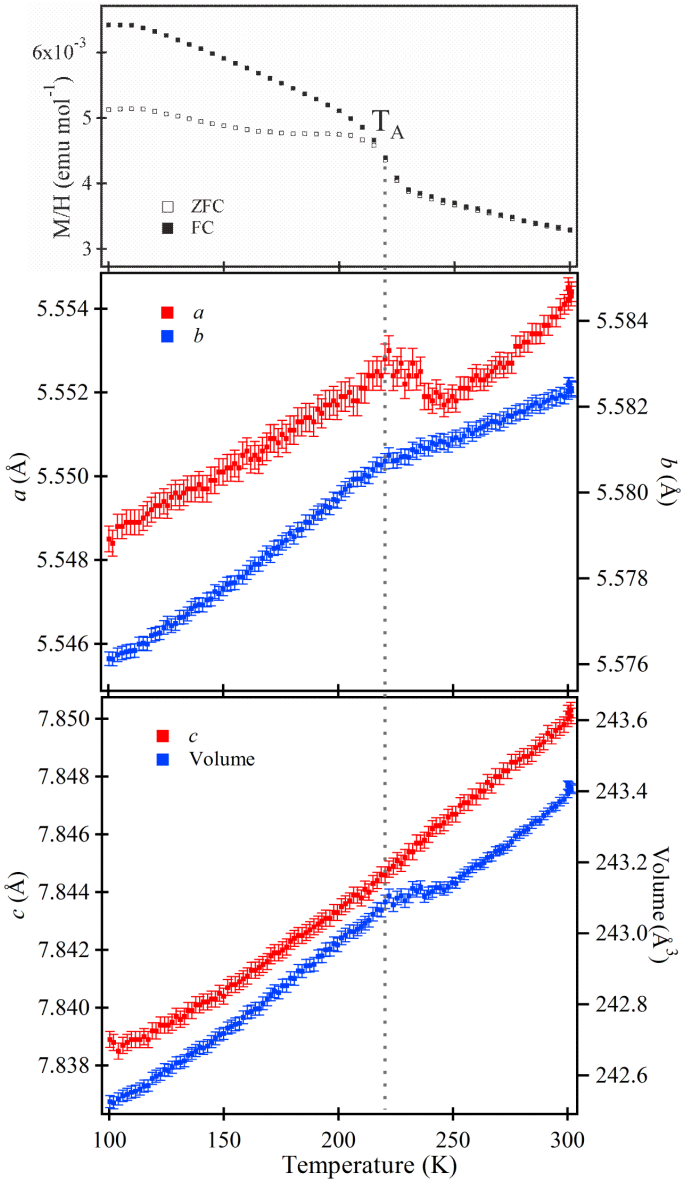

Figure 5.29: The lattice parameters extracted from the refinement of the P2$_1$/*n* model against synchrotron X-ray diffraction data collected from La$_{0.05}$Sr$_{1.95}$FeIrO$_6$ in the temperature range 100 ≤ T / K ≤ 300 compared to the magnetisation data of La$_{0.05}$Sr$_{1.95}$FeIrO$_6$.

5.4.3.4 The electronic state and magnetism of Ir^{v}

It is widely reported in the literature that Ir^{V} is diamagnetic. The strong spin orbit coupling splits the t_{2g} orbital set in iridium resulting in a singlet state and a triplet state. As Ir^{v} is a d^4 cation the triplet state orbitals become fully occupied resulting in no unpaired electrons, a state shown in Section 5.4.3.1, Figure 5.26. The lack of unpaired electrons means that Ir^{V} centres have no net moment and thus do not contribute to

magnetic order. There are numerous examples of Ir^{V} containing compounds that exhibit this behaviour, the most notable for this work being Sr_2FeIrO_6[22]. Considering the ubiquity of this state and the strength of evidence in its favour it is difficult to imagine an alternative state that could give rise to a magnetic response. However the evidence presented in previous sections of this discussion clearly indicates that there is a magnetic event that is, on balance of probabilities, due to iridium.

There are two ways in which we can approach these results. The first would be to axiomatically state Ir^{V} cannot have a magnetic moment and the unusual magnetic behaviour is a result of impurities in the sample. While there is a wealth of evidence proving Ir^{V} cannot have a magnetic moment, the second assertion that there are impurities is hard to prove, or indeed disprove. The refinements of the synchrotron X-ray powder diffraction data collected from each sample show that there are no peaks present that cannot be fit to either the $I\bar{1}$ or $P2_1/n$ structure. Furthermore the magnetisation isotherms collected from each sample show that there is no ferromagnetic impurity present in any of the samples (Sections 5.3.2.1 and 5.3.5.1). The data presented in Figure 5.29 clearly show that for $La_{0.05}Sr_{1.95}FeIrO_6$ there is a structural change to the $P2_1/n$ phase in the sample at the same temperature T_A occurs. This is either an unfortunate coincidence or, more likely, they are related. It is impossible to state unequivocally that there are no impurities in these samples however we took great care synthesising the samples and the extensive analysis we have conducted on them, all of which indicates there are no impurities, are the strongest evidence to support that the samples are phase pure. In the absence of concrete evidence that there are impurities in the samples, and with clear evidence that there is a structural change at the same temperature as the magnetic event at T_A, it is reasonable to take the second approach in which we conclude that all magnetic events observed come from the sample bulk.

SQUID magnetometry data collected from stoichiometric Sr_2FeIrO_6 only exhibits a magnetic event analogous to the second observed in the doped samples. The structural analysis in Section 5.3.1.2 and 5.3.1.4.1 indicates that the $I\bar{1}$ phase in the doped samples is Sr_2FeIrO_6, thus the first magnetic event must arise from the $P2_1/n$ phase. The ^{57}Fe Mössbauer spectra collected at various temperatures (Section 5.3.3) show that the iron lattices in both structures are not magnetically ordered until after the second magnetic event, thus the first magnetic event must be due to the iridium lattice of the $P2_1/n$ phase.

These observations are very difficult to rationalise for all of the reasons previously outlined. The $I\bar{1}$ or $P2_1/n$ structures are very similar and as such we would not expect such a significant difference in behaviour. However there is one key difference between the two structures. The MO_6 of the $P2_1/n$ phase are slightly less symmetric than those of the $I\bar{1}$ phase, as highlighted in Figure 5.25, Section 5.4.2. In most compounds a small change in the co-ordination environment would not be particularly noteworthy however in recent years there has been debate in the literature about the interplay of co-ordination geometry and spin-orbit coupling in iridium containing oxides. It has been reported that the double perovskite Sr_2YIrO_6 undergoes a transition to an antiferromagnetic state at 1.5 K[111]. The structural characterisation of Sr_2YIrO_6 shows that the IrO_6 octahedra are compressed along the apical axis and as such is distorted from the ideal O_h co-ordination geometry that is strongly associated with Ir^V. To understand this magnetic state Cao et al. conducted a series of calculations that examined the relationship between the spin-orbit coupling of Ir^V and its co-ordination geometry. These calculations showed that the spin-orbit coupling of Ir^V can be quenched if it is forced into a sufficiently distorted octahedral site, which in turn would result in Ir^V adopting an electronic state with unpaired electrons[112]. There has been rigorous debate surrounding this report owing to the indisputable fact that Sr^{II} and Y^{III} are diamagnetic and the wealth of evidence that

suggests Ir^{v} must adopt a j_{eff} = 0 state[113]. The most compelling evidence that this state exists was published by T. Corredor et al. They have published heat capacity measurements collected from a single crystal of Sr_2YIrO_6 that are consistent with the onset of a magnetically ordered state at 1.5 K[114]. There remains division on the cause of this order as other studies have suggested that the distortion in Sr_2YIrO_6 is not enough to quench the spin-orbit coupling[115]. It is clear this is a burgeoning area of interest for the functional materials community and much more investigation is required to confirm and understand a magnetic state that arises from an Ir^{V} lattice. Unfortunately for this work it means that there is no concrete evidence or precedent presented in the literature to support the highly unusual magnetic behaviour these doped variants of Sr_2FeIrO_6 Therefore to fully understand these behaviours in depth density functional theory calculations and data collected from single crystals are likely required. While we cannot come to well-rounded conclusions, the careful work we have conducted shows that the transitions at T_A are not caused by impurities present in the samples and are most likely a result of Ir^{V} order in the $P2_1/n$ phases.

5.5 Conclusions

In this work we have successfully synthesised Sr_2FeIrO_6 and a variety of samples doped with low levels of La, Ca, Ba and Ga. We have shown using high resolution synchrotron X-ray diffraction data that Sr_2FeIrO_6 adopts an $I\bar{1}$ structure and that reports that suggest otherwise have measured samples that do not maintain the 1:1 Fe to Ir ratio and contain Fe_2O_3. High resolution synchrotron X-ray diffraction data collected from samples of the doped Sr_2FeIrO_6 species can be fit well to the same $I\bar{1}$ structural model, however the best fits were achieved by refinement of a combination of $I\bar{1}$ and $P2_1/n$ structural models against the data. The results of these refinements are supported by the same results drawn

from refinement of neutron powder diffraction data collected from $La_{0.05}Sr_{1.95}FeIrO_6$. These refinements prove that the $I\bar{1}$ structure is very fragile and the slightest change in stoichiometry results in the extrusion of a $P2_1/n$ phase. Magnetisation data collected from the doped samples undergo two magnetic transitions: T_A at 225 K and T_{n1} at 120 K. Refinement of neutron diffraction data collected at 1.5 K and a ^{57}Fe Mössbauer spectrum collected at 5 K show that the transition at T_{n1} is due to the ordering of the iron lattices which adopt a type-II canted antiferromagnetic state similar to that of Sr_2FeIrO_6. The transition at T_{n1} is caused not by the iron lattices as shown by ^{57}Fe Mössbauer spectra and refinement of neutron diffraction data. Careful inspection of all diffraction data collected from the doped samples shows that we can be confident to a reasonable degree that there are no impurities present in the samples. Consequently, the transition at T_A must come from the Ir^v lattice.

Chapter 6 – Synthesis and Topochemical reduction of $Sr_2Fe_{0.5}Ir_{0.5}O_4$

6.1 Introduction

Chapter 4 of this thesis describes the synthesis and reduction of the double perovskite Sr_2FeIrO_6 to form Sr_2FeIrO_4, the first example of a complex oxide that contains Ir^{II}. The success of this reaction proves that the coupling of an iron and an iridium lattice can successfully be exploited to make a metastable compound with highly unusual properties. Thus we wanted to extend this work to include other oxides that contain iron and iridium.

The n = 1 Ruddlesden-Popper structure is a layered analogue of the perovskite structure that can be regarded as layers of perovskite blocks separated by rock salt layers (Chapter 1, Section 1.4.3). Phases that adopt the Ruddlesden-Popper structure have similar chemistries to their related perovskite compounds due to their structural similarities. This similarity extends to topochemical reduction. It has been shown that complex oxides with Ruddlesden-Popper structures can be reduced to form oxide deficient phases by deploying the same synthetic methods used to reduce compounds with the perovskite structure. Notable examples of these reactions include the reductions of Sr_2FeO_4[99], Sr_3FeO_7[53], $Sr_2Fe_{0.5}Ru_{0.5}O_4$ and $Sr_2(Fe_{0.5}Ru_{0.5})_2O_7$[46].

On the basis of the precedent outlined above, we decided to further explore the reduction chemistry of iron and iridium containing complex oxides, and oxides that adopt the n = 1 Ruddlesden-Popper structure. To do this we synthesised and reduced $Sr_2Fe_{0.5}Ir_{0.5}O_4$, the n = 1 Ruddlesden-Popper analogue of Sr_2FeIrO_6.

6.2 Synthesis

6.2.1 Synthesis of $Sr_2Fe_{0.5}Ir_{0.5}O_4$

A sample of $Sr_2Fe_{0.5}Ir_{0.5}O_4$ was prepared using the citrate gel method (Chapter 2, Section 2.1.2). Appropriate quantities of $SrCO_3$ (99.994%) and Fe (99.99%) were dissolved in a minimal quantity of a 1:1 mixture of conc. nitric acid and distilled water, then the required amount of IrO_2 (99.99%, dried at 700 ^oC for 2 hours) was added. Citric acid and analar ethylene glycol were added and the solution was heated whilst being stirred. The gel thus formed was allowed to dry and then combust in air. The subsequent product was ground into a fine powder, placed in an alumina crucible and heated at 1000 ^oC in air at a rate of 1 $^oC\ min^{-1}$ to remove the organic components of the sample. The resulting powder was pressed into a 13 mm diameter pellet and heated in air for two cycles of 2 days at 1000 ^oC and one cycle of 2 days at 1050 ^oC.

The resulting powders were observed to be phase-pure by laboratory X-ray powder diffraction, with lattice parameters a = 3.90 Å, c = 12.58 Å.

6.2.2 Synthesis of $Sr_2Fe_{0.5}Ir_{0.5}O_{4-x}$

A full discussion on the reduction chemistry of iridium-containing oxides and the challenges this process presents, including that of $Sr_2Fe_{0.5}Ir_{0.5}O_4$, is given in Chapter 3. A sample of $Sr_2Fe_{0.5}Ir_{0.5}O_{4-x}$ made for analysis by neutron powder diffraction was prepared by reacting approximately 1.25g of $Sr_2Fe_{0.5}Ir_{0.5}O_4$ with zirconium using the method described in Chapter 2, Section 2.6. The sample was heated for 2 periods of 7 days at 400 ^oC and a final heating cycle of 7 days at 410 ^oC. Between heating cycles the samples were taken into an Ar filled glovebox, without being exposed to air, and ground with an agate pestle and mortar.

6.3 Results

6.3.1 Structural characterisation of $Sr_2Fe_{0.5}Ir_{0.5}O_4$

6.3.1.1 Synchrotron powder X-ray diffraction data

High resolution powder X-ray diffraction data were collected from a sample of $Sr_2Fe_{0.5}Ir_{0.5}O_4$ using instrument I11 at the Diamond Light Source (Chapter 2, Section 2.7.1.2). Owing to the similarities in lattice parameters and composition of $Sr_2Fe_{0.5}Ru_{0.5}O_4$ and $Sr_2Fe_{0.5}Ir_{0.5}O_4$, a structural model based on that of $Sr_2Fe_{0.5}Ru_{0.5}O_4$ with *I4/mmm* symmetry was constructed and refined against the synchrotron powder X-ray diffraction data. The unit cell of the model is shown in Figure 6.1. The refinement converged to give an excellent statistical fit. In the pattern there are very small peaks attributed to an impurity that could not be indexed. The lattice parameter with which this impurity can be indexed suggests it might be a perovskite with an indeterminable composition. The observed, calculated and difference plots for the refinement are shown in Figure 6.2.

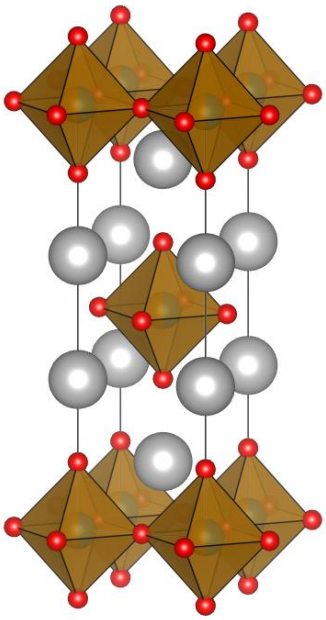

Figure 6.1: The structural unit cell of $Sr_2Fe_{0.5}Ir_{0.5}O_4$ with *I4/mmm* space symmetry. The blue and gold spheres are iridium and iron respectively.

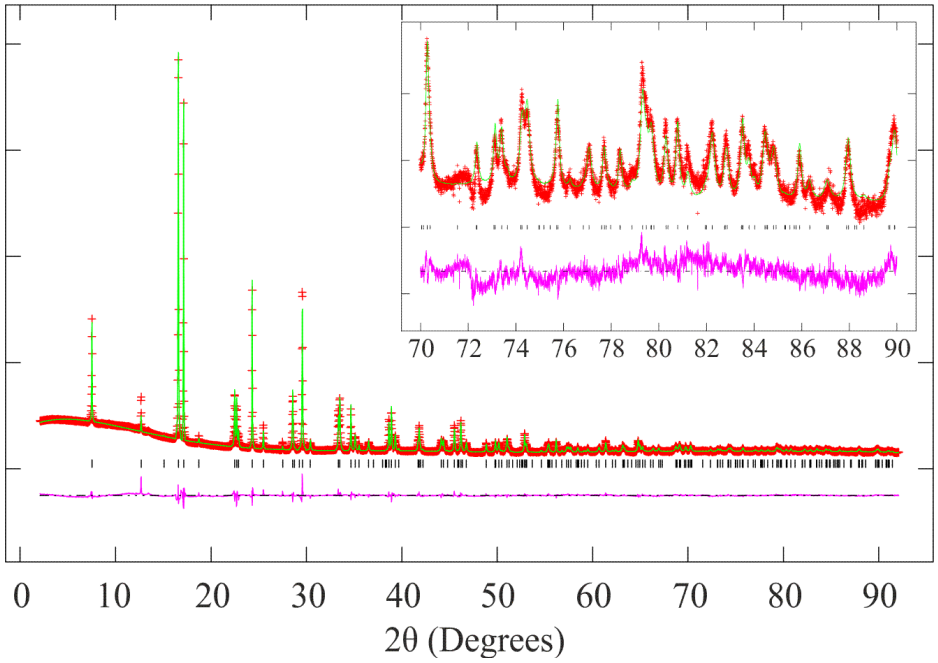

Figure 6.2: Observed, calculated and difference plots from the refinement of the *I4/mmm* structural model of $Sr_2Fe_{0.5}Ir_{0.5}O_4$ against synchrotron powder diffraction data collected at room temperature using the I11 instrument.
χ^2 = 155.9, wR_p = 5.43% and R_p = 3.23%; *a* = *b* = 3.91762(4) Å, *c* = 12.5845(1) Å

6.3.1.2 Neutron powder diffraction data

Neutron powder diffraction data were collected from a sample of $Sr_2Fe_{0.5}Ir_{0.5}O_4$ using the D2B instrument at the ILL (Chapter 2, Section 2.7.1.2) at room temperature and 5 K. The data collected at room temperature could be fully indexed using CMPR[78] to the same lattice parameters extracted from the refinement of the synchrotron powder diffraction data. The same *I4/mmm* model shown in Figure 6.1 was refined against the neutron powder diffraction data collected at room temperature to give an excellent statistical fit. The observed, calculated and difference plot for the refinement is shown in Figure 6.3 and full details of the structural parameters are given in Table 6.1. Selected bond lengths extracted from the refinements of the room temperature and 5 K data are given in Table 6.2.

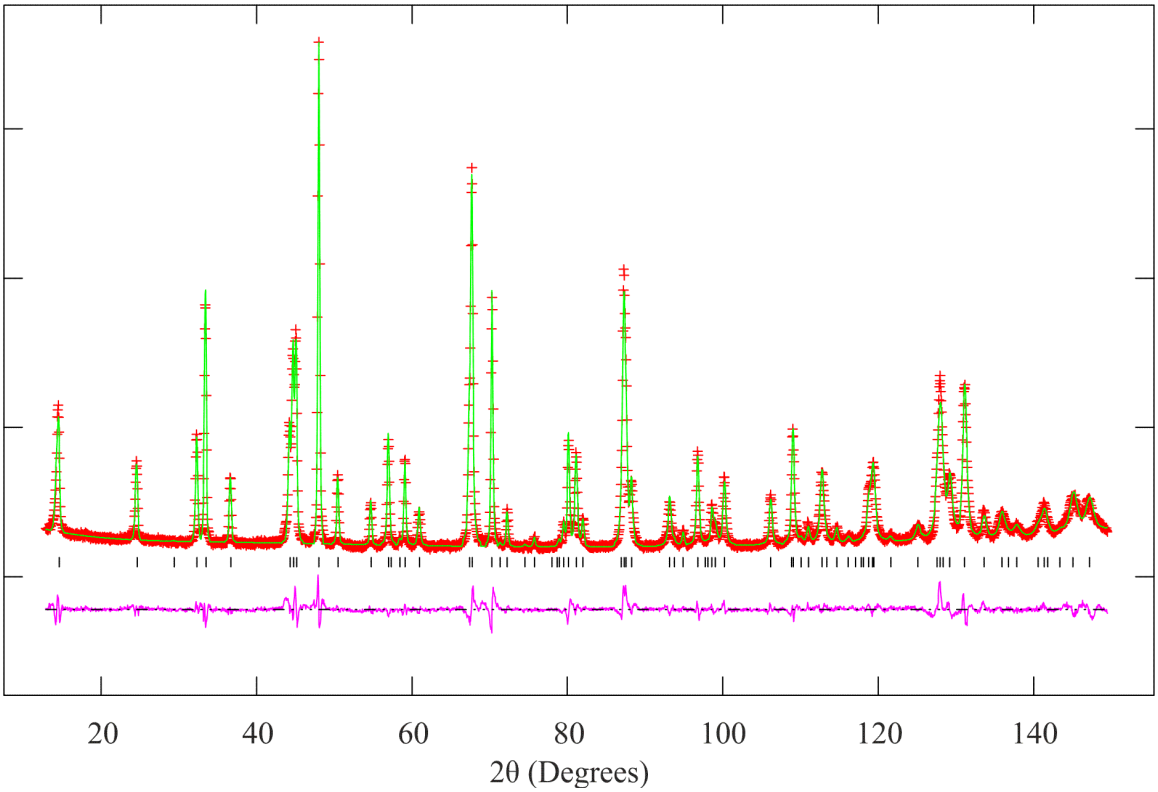

Figure 6.3: Observed, calculated and difference plots from the of the *I*4/*mmm* structural model of $Sr_2Fe_{0.5}Ir_{0.5}O_4$ against the neutron powder diffraction data collected at room temperature using the D2B instrument.

Atom	site	*x*	*y*	*z*	Fraction	U_{11} (Å^2)	U_{22} (Å^2)	U_{33} (Å^2)
Sr	4*e*	0	0	0.3546(1)	1	0.0029(4)	0.0029(4)	0.0021(6)
Fe/Ir	2*a*	0	0	0	0.5/0.5	0.0005(4)	0.0005(4)	0.0029(7)
O(1)	4*e*	0	0	0.1600(1)	1	0.0072(4)	0.0072(4)	0.0005(1)
O(2)	4*c*	0	½	0	1	0.0134(4)	0.0030(4)	0.0117(5)
$Sr_2Fe_{0.5}Ir_{0.5}O_4$ - Space Group: *I*4/*mmm* (#139) Formula weight = 363.275 g mol^{-1} *a* = *b* = 3.91663(6) Å, *c* = 12.5781(2) Å, volume = 192.949(9) Å^3								
Radiation source: Constant wavelength, λ = 1.54 Å Temperature: Room Temperature χ^2 = 5.882; *wRp*= 5.70 %; *Rp* = 4.38 %.								

Table 6.1: Parameters from the structural refinement of $Sr_2Fe_{0.5}Ir_{0.5}O_4$ against neutron powder diffraction data collected at room temperature.

	Bond lengths (Å)	
Temperature	M-O(1)	M-O(2)
Room Temperature	2.013(1)	1.958(3)
5 K	2.009(7)	1.953(5)

Table 6.2: Selected bonds length from the refined structures of $Sr_2Fe_{0.5}Ir_{0.5}O_4$ at room temperature and 5 K

6.3.2 Magnetic characterisation of $Sr_2Fe_{0.5}Ir_{0.5}O_4$

6.3.2.1 SQUID magnetometry

Magnetisation data were collected from a sample of $Sr_2Fe_{0.5}Ir_{0.5}O_4$ in an applied field of 100 Oe in the temperature range $5 \leq T / K \leq 300$. The zero-field cooled (ZFC) and field cooled (FC) data and magnetisation-field isotherms collected at 300 K, 100 K and 5 K are shown in Figure 6.4. At temperatures above 170 K the zero-field cooled and field cooled measurements are convergent however neither data set could fit to the Curie-Weiss law even with a large temperature independent parameter. At temperatures between $50 \leq T / K \leq 170$ the zero-field cooled and field cooled measurements are divergent. Magnetisation isotherms collected at 100 K and 300 K do not show any detectable hysteresis, indicating the divergence is not due to a ferromagnetic impurity. At temperatures below 50 K the zero-field and field cooled measurements remain divergent but the rate at which they diverge increases. The magnetisation isotherm collected at 5 K after field-cooling the sample shows a small amount of hysteresis. This indicate that $Sr_2Fe_{0.5}Ir_{0.5}O_4$ undergoes a transition to either a magnetically ordered state at 50 K or a spin glass state.

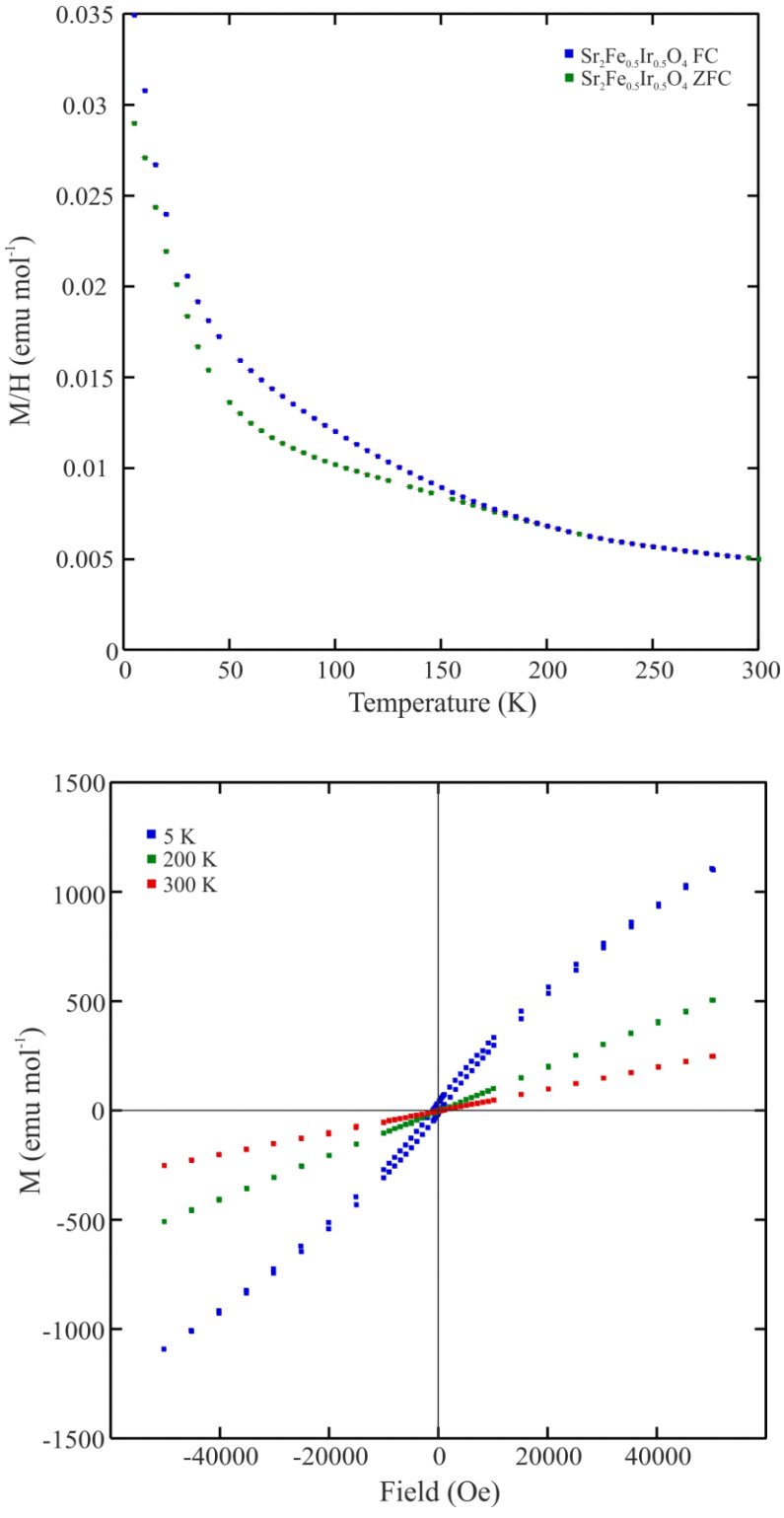

Figure 6.4: a) Zero-field cooled and field-cooled magnetisation data collected from $Sr_2Fe_{0.5}Ir_{0.5}O_4$. b) Magnetisation-field isotherms collected from $Sr_2Fe_{0.5}Ir_{0.5}O_4$

6.3.2.2 Neutron diffraction data

Comparison of the neutron diffraction data collected from $Sr_2Fe_{0.5}Ir_{0.5}O_4$ at room temperature and 5 K did not reveal additional diffraction peaks that could not be attributed to the closed-circuit refrigeration system the sample was cooled in. Furthermore refinement of simple ferromagnetic unit cells against the data collected at 5 K did not converge. These results indicate $Sr_2Fe_{0.5}Ir_{0.5}O_4$ does not have a magnetically ordered state that can be detected by diffraction. The observed, calculated and difference plot for the refinement is shown in Figure 6.5 and full details of the structural parameters are given in Table 6.2.

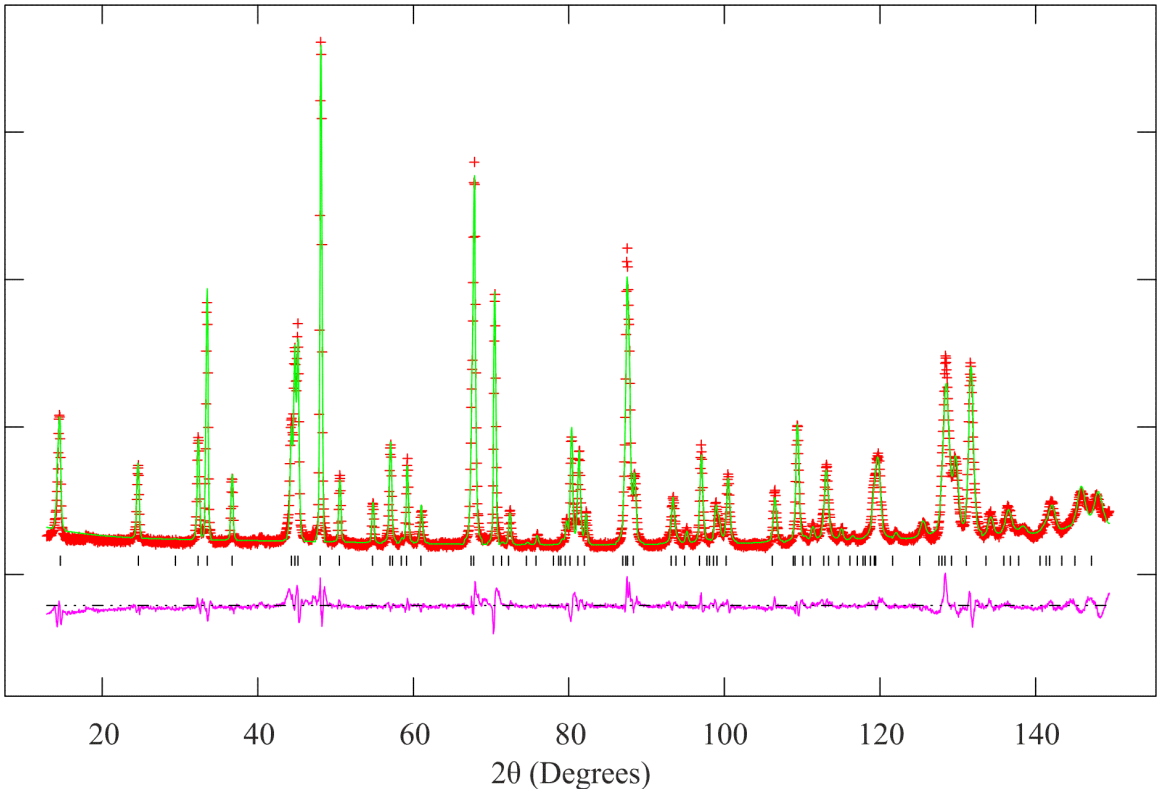

Figure 6.5: Observed, calculated and difference plots from the of the *I4mmm* structural model of $Sr_2Fe_{0.5}Ir_{0.5}O_4$ against the neutron powder diffraction data collected at 5 K using the D2B instrument.

Atom	site	*x*	*y*	*z*	Fraction	U_{11} (Å^2)	U_{22} (Å^2)	U_{33} (Å^2)
Sr	4*e*	0	0	0.3547(1)	1	0.002(1)	0.002(1)	0.001(1)
Fe/Ir	2*a*	0	0	0	0.5/0.5	0.0002(1)	0.0002(1)	0.006(3)
O(1)	4*e*	0	0	0.1612(1)	1	0.0002(3)	0.0002(3)	0.0005(2)
O(2)	4*c*	0	½	0	1	0.008(1)	0.001(4)	0.001(2)
$Sr_2Fe_{0.5}Ir_{0.5}O_4$ - Space Group: *I*4/*mmm* (#139) Formula weight = 363.275 g mol^{-1}, Z = 2 *a* = *b* =3.90776(9) Å, *c* = 12.5547(4) Å, volume = 191.72(1) Å^3								
Radiation source: Constant wavelength, λ = 1.54 Å Temperature: 5 K χ^2 = 12.06; *wRp* = 8.15 %; *Rp* = 6.15 %.								

Table 6.2: Parameters from the structural refinement of $Sr_2Fe_{0.5}Ir_{0.5}O_4$ against neutron powder diffraction data collected at room temperature.

6.3.3 Structural characterisation of $Sr_2Fe_{0.5}Ir_{0.5}O_{4-x}$

6.3.3.1 Thermogravimetric analysis of $Sr_2Fe_{0.5}Ir_{0.5}O_{4-x}$

An oxidative thermogravimetric experiment was conducted to confirm the oxygen content of $Sr_2Fe_{0.5}Ir_{0.5}O_{4-x}$. A small quantity of the reduced sample was heated under a flow of oxygen to reform $Sr_2Fe_{0.5}Ir_{0.5}O_4$, as confirmed by X-ray powder diffraction. During this reaction the sample gained 3.73 % of its initial mass, an increase that is consistent with a composition of $Sr_2Fe_{0.5}Ir_{0.5}O_{3.15}$ for the reduced phase (Figure 6.6). From this point on $Sr_2Fe_{0.5}Ir_{0.5}O_{4-x}$ will be referred to as $Sr_2Fe_{0.5}Ir_{0.5}O_3$.

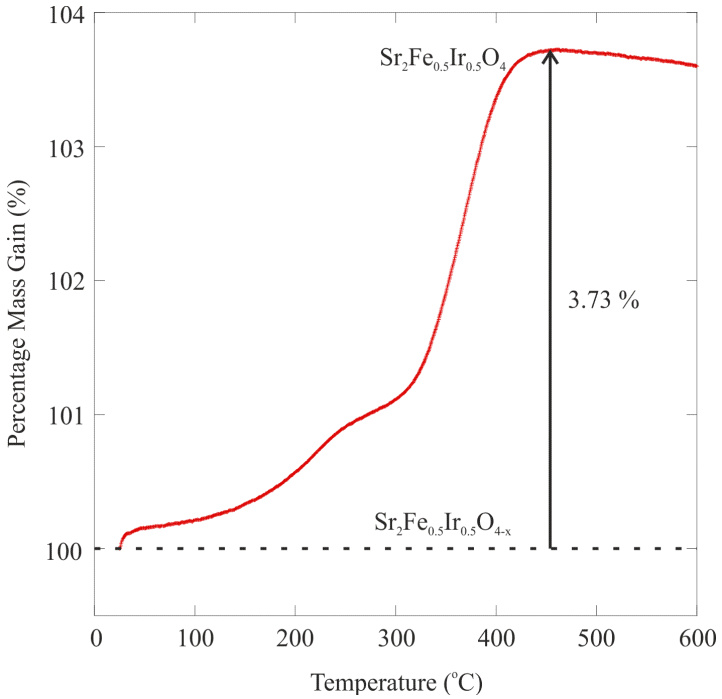

Figure 6.6: Thermogravimetric data collected during the oxidation of $Sr_2Fe_{0.5}Ir_{0.5}O_{4-x}$ to $Sr_2Fe_{0.5}Ir_{0.5}O_4$

6.3.3.2 Synchrotron powder X-ray diffraction data

High resolution powder X-ray diffraction data were collected from a sample of $Sr_2Fe_{0.5}Ir_{0.5}O_3$ using instrument I11 at the Diamond Light Source (Chapter 2, Section 2.7.1.2). The vast majority of the diffraction pattern could be indexed to an orthorhombic unit cell. Additional peaks could not be indexed and were attributed to unknown impurities. A structural model with *Immm* symmetry was constructed based on those of Sr_2FeO_3 and $Sr_2Fe_{0.5}Ru_{0.5}O_3$, and refined against the synchrotron X-ray diffraction data. The unit cell of the model is shown in Figure 6.8. The refinement gave a good statistical fit. The observed, calculated and difference plots for the refinement are shown in Figure 6.7.

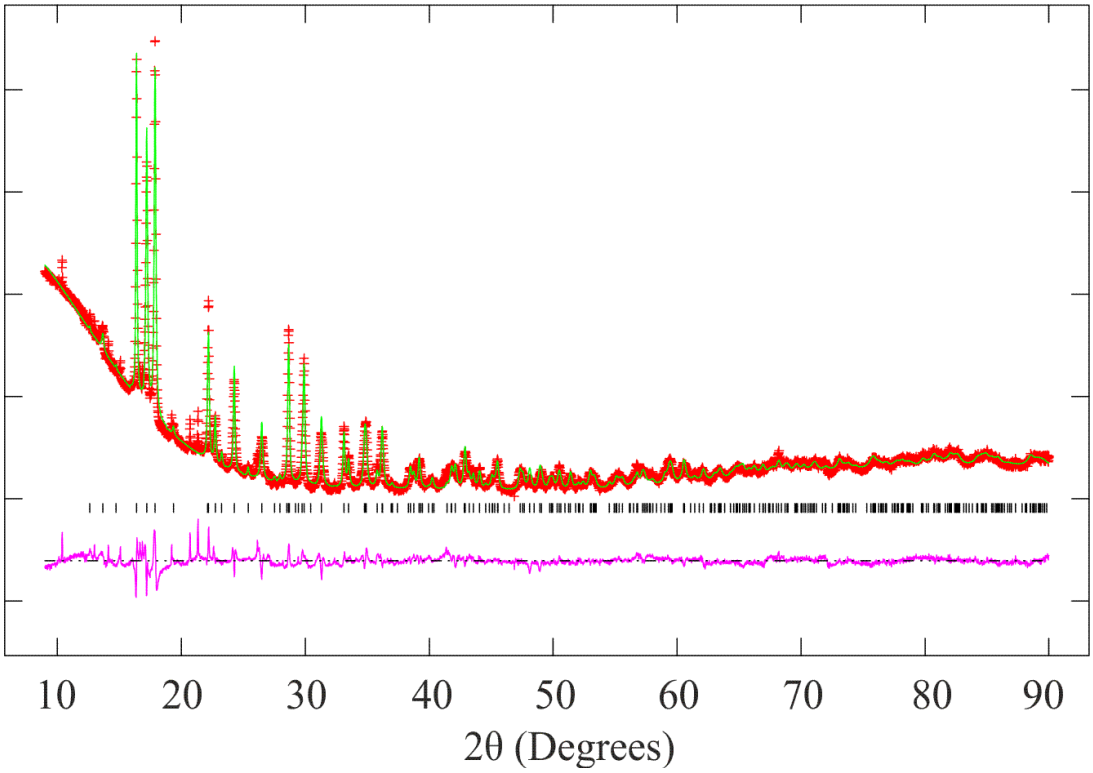

Figure 6.7: Observed, calculated and difference plots from the refinement of the *Immm* structural model of $Sr_2Fe_{0.5}Ir_{0.5}O_3$ against synchrotron powder diffraction data collected at room temperature using the I11 instrument.
χ^2 = 39.98, wR_p = 3.37% and R_p = 2.24%; *a* = 3.9232(1) Å, *b* = 3.6426 (1) Å, *c* = 12.8486(4) Å

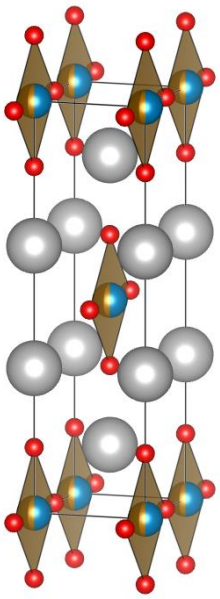

Figure 6.8: The structural unit cell of $Sr_2Fe_{0.5}Ir_{0.5}O_3$ with *Immm* space symmetry. The blue and gold spheres are iridium and iron respectively.

6.3.3.3 Neutron powder diffraction data

Neutron powder diffraction data were collected from a sample of $Sr_2Fe_{0.5}Ir_{0.5}O_3$ using the D2B instrument at the ILL (Chapter 2, Section 2.7.1.2) at room temperature and 5 K. The data collected at room temperature could be fully indexed using CMPR[78] to the same lattice parameters extracted from the refinement of the synchrotron powder diffraction data. The *Immm* model shown in Figure 6.8 was refined against the neutron powder diffraction data collected at room temperature to give a good statistical fit. The observed, calculated and difference plots for the refinement is shown in Figures 6.9 and full details of the structural parameters are given in Tables 6.4. Selected bond lengths extracted from the refinements are given in Table 6.5.

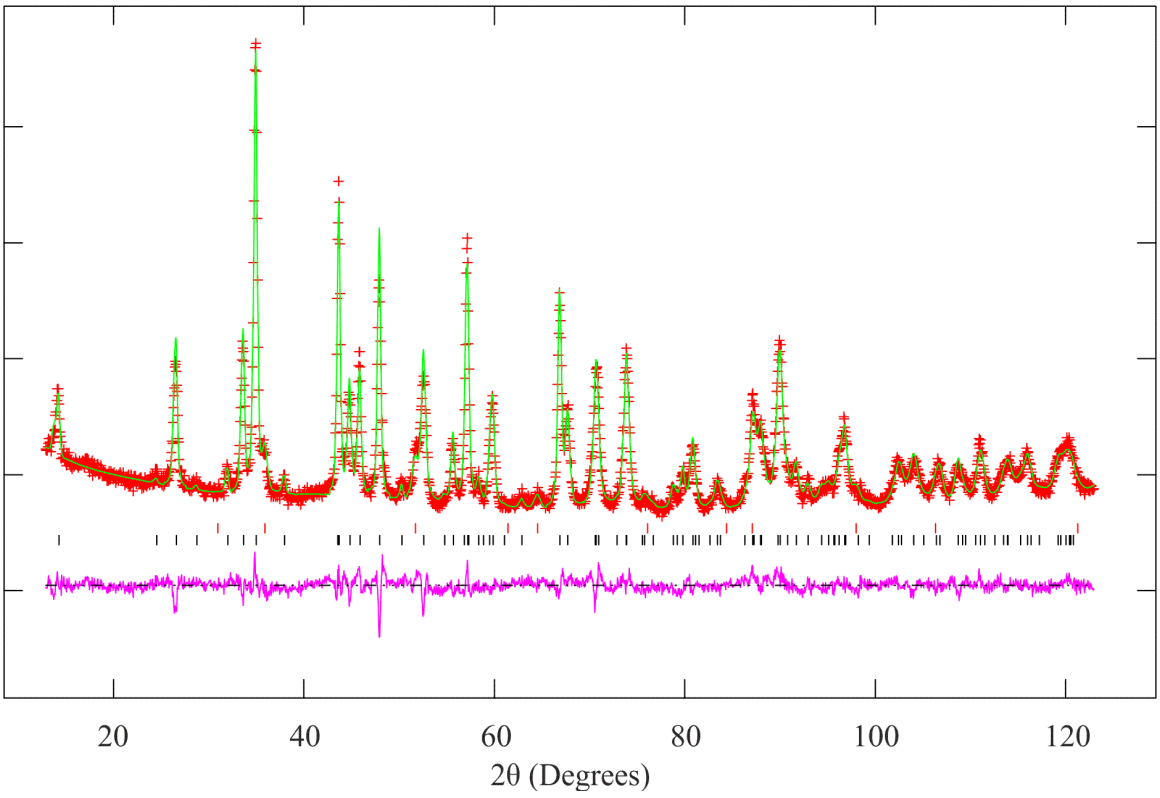

Figure 6.9: Observed, calculated and difference plots from the of the *Immm* structural model of $Sr_2Fe_{0.5}Ir_{0.5}O_3$ against the neutron powder diffraction data collected at room temperature using the D2B instrument. The tick marks correspond to the following: Black = $Sr_2Fe_{0.5}Ir_{0.5}O_3$; Red = SrO

Atom	site	*x*	*y*	*z*	Fraction	U_{11} (Å^2)	U_{22} (Å^2)	U_{33} (Å^2)
Sr	4*i*	0	0	0.3512(1)	1	0.002(1)	0.0018(1)	0.0029(1)
Fe/Ir	2*a*	0	0	0	0.5/0.5	0.0006(1)	0.005(1)	0.0049(1)
O(1)	4*i*	0	0	0.1590(2)	1	0.005(2)	0.010(2)	0.001(1)
O(2)	4*f*	½	0	0	1	0.009(1)	0.005(1)	0.001(1)
$Sr_2Fe_{0.5}Ir_{0.5}O_3$ - Space Group: *Immm* (#71) Formula weight = 347.275 g mol^{-1}, Z = 2; Weight Fraction = 94.5% *a* = 3.9252(2) Å, *b* = 3.5999(2) Å, *c* = 12.8538(6) Å, volume = 181.63(2) Å^3								
Atom	site	*x*	*y*	*z*	Fraction	U_{iso} (Å^2)		
Sr	4*b*	½	½	½	1	0.0095(1)		
O(1)	4*a*	0	0	0	1	0.0095(1)		
SrO - Space Group: $Fm\bar{3}m$ (#225) Formula weight = 487.30 g mol^{-1}, Z = 2; Weight Fraction = 5.5% *a* = *b* = *c* = 5.174(1) Å, volume = 138.55(8) Å^3								
Radiation source: Constant wavelengthc Temperature: Room Temperature χ^2 = 2.210; *wRp* = 4.55 %; *Rp* = 3.63 %								

Table 6.4: Parameters from the structural refinement of $Sr_2Fe_{0.5}Ir_{0.5}O_3$ against neutron powder diffraction data collected at room temperature.

	Bond lengths (Å)	
Temperature	M-O(1)	M-O(2)
Room Temperature	1.9625(1)	2.044(3)
5 K	1.9579(1)	2.045(2)

Table 6.5: Selected bond lengths from the refined structures of $Sr_2Fe_{0.5}Ir_{0.5}O_3$ at room temperature and 5 K

6.3.4 Magnetic characterisation of $Sr_2Fe_{0.5}Ir_{0.5}O_3$

6.3.4.1 SQUID magnetometry

Magnetisation data were collected from a sample of $Sr_2Fe_{0.5}Ir_{0.5}O_3$ in an applied field of 100 Oe in the temperature range $5 \leq T / K \leq 300$. The zero-field cooled (ZFC) and field cooled (FC) data and magnetisation-field isotherms collected at 300 K and 5 K are shown in Figure 6.10. At temperatures above 45 K the zero-field cooled and field cooled measurements diverge slightly, similarly to the divergence observed in Sr_2FeIrO_4 (Chapter 4, Section 4.3.4.1). One cause of divergence between the ZFC and FC data would be the presence of a ferromagnetic impurity, in this case the prime suspect would be elemental iron. However the magnetisation isotherm collected at 300 K shows no

hysteresis indicating this divergence is not due to iron or any other ferromagnetic impurity. At 45 K the ZFC-FC measurements become more strongly divergent suggesting the onset of either a spin glass state or a canted antiferromagnetic state. A magnetisation isotherm collected at 5 K after field-cooling showed hysteresis and displacement from the origin suggesting at $Sr_2Fe_{0.5}Ir_{0.5}O_3$ has a transition to a spin glass state or a canted antiferromagnetic state with a significant component of frustration.

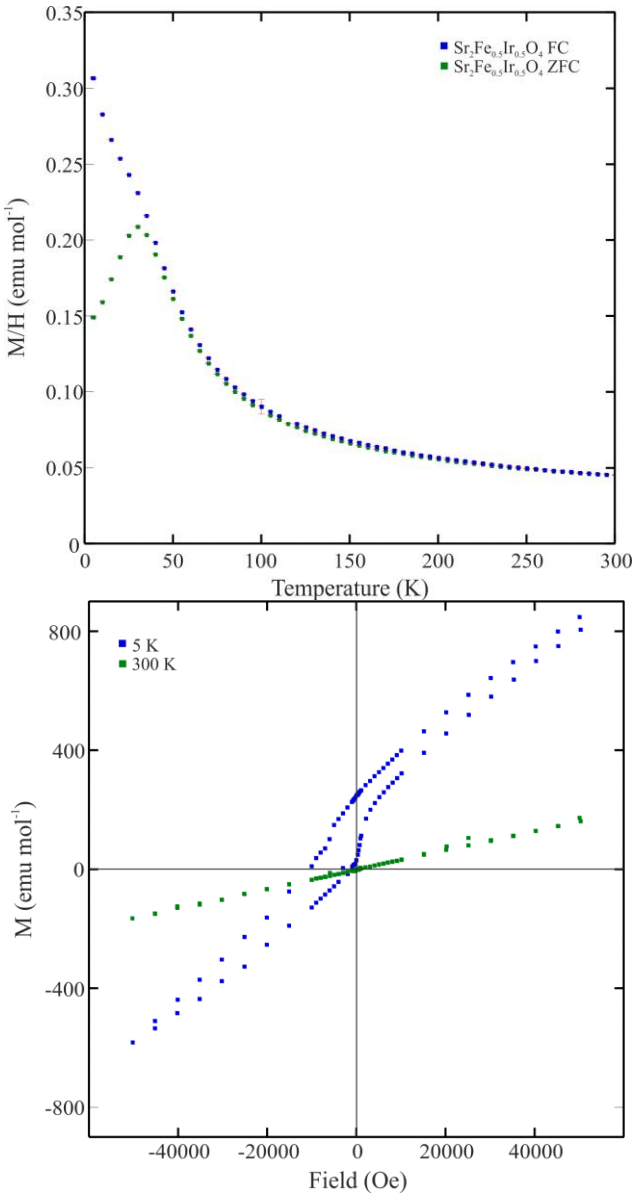

Figure 6.10: a) Zero-field cooled and field-cooled magnetisation data collected from $Sr_2Fe_{0.5}Ir_{0.5}O_3$. b) Magnetisation-field isotherms collected from $Sr_2Fe_{0.5}Ir_{0.5}O_3$

6.3.4.2 Neutron diffraction data

Comparison of the neutron diffraction data collected from $Sr_2Fe_{0.5}Ir_{0.5}O_3$ at room temperature and 5 K did not reveal additional diffraction peaks that could not be attributed to the closed-circuit refrigeration system the sample was cooled in. A series of ferromagnetic unit cells were constructed and refined against the data collected at 5 K. The refinement of the model in which the spins aligned along the *b*-axis converged to give a small moment of around 0.8(5) μ_B. Magnetisation data suggests that at room temperature $Sr_2Fe_{0.5}Ir_{0.5}O_3$ is not magnetically ordered. Thus the analysis was repeated for the data collected at room temperature to determine whether the result is real. The refinement converged to give a moment of around 0.3(2) μ_B suggesting the result is not real. The observed, calculated and difference plots for the refinement is shown in Figures 6.11 and full details of the structural parameters are given in Tables 6.6.

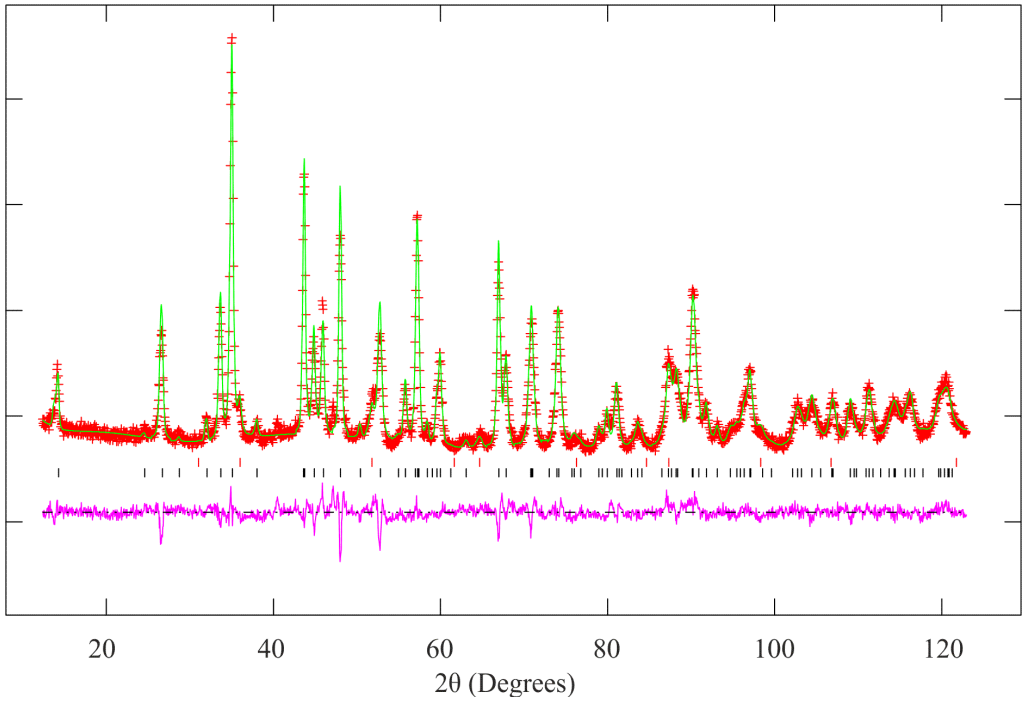

Figure 6.11: Observed, calculated and difference plots from the of the *Immm* structural model of $Sr_2Fe_{0.5}Ir_{0.5}O_3$ against the neutron powder diffraction data collected at 5 K using the D2B instrument. The tick marks correspond to the following: Black = $Sr_2Fe_{0.5}Ir_{0.5}O_3$; Red = SrO

Atom	site	*x*	*y*	*z*	Fraction	U_{11} (Å^2)	U_{22} (Å^2)	U_{33} (Å^2)	U_{iso} (Å^2)
Sr	4*i*	0	0	0.3511(1)	1	-	-	-	0.003(1)
Fe/Ir	2*a*	0	0	0	0.5/0.5	0.0019(1)	0.0003(1)	0.0002(1)	-
O(1)	4*i*	0	0	0.1592(2)	1	0.001(2)	0.007(2)	0.004(1)	-
O(2)	4*f*	½	0	0	1	0.005(1)	0.002(1)	0.00005(1)	-
$Sr_2Fe_{0.5}Ir_{0.5}O_3$ - Space Group: *Immm* (#71) Formula weight = 347.275 g mol^{-1}, Z = 2; Weight Fraction = 94.5% *a* = 3.9159(2) Å, *b* = 3.5872(2) Å, *c* = 12.8396(8) Å, volume = 180.36(3) Å^3									
Atom	site	*x*	*y*	*z*	Fraction	U_{iso} (Å^2)			
Sr	4*b*	½	½	½	1	0.00009 (1)			
O(1)	4*a*	0	0	0	1	0.00009 (1)			
SrO - Space Group: *Fm*$\bar{3}$*m* (#225) Formula weight = 487.30 g mol^{-1}, Z = 2; Weight Fraction = 5.5% *a* = *b* = *c* = 5.163(1) Å, volume = 137.64(9) Å^3									
Radiation source: Constant wavelength, λ = 1.54 Å Temperature: 5K χ^2 = 2.840; *wRp* = 5.32 %; *Rp* = 4.14 %									

Table 6.6: Parameters from the structural refinement of $Sr_2Fe_{0.5}Ir_{0.5}O_3$ against neutron powder diffraction data collected at 5 K.

6.4 Discussion

6.4.1 Structure and magnetism of $Sr_2Fe_{0.5}Ir_{0.5}O_4$

6.4.1.1 Structure $Sr_2Fe_{0.5}Ir_{0.5}O_4$

Refinements of synchrotron powder X-ray diffraction data and neutron powder diffraction data (Sections 6.3.1.1 and 6.3.1.2) show that the structure of $Sr_2Fe_{0.5}Ir_{0.5}O_4$ is best described by a tetragonal unit cell with *I*4/*mmm* space symmetry (Figure 6.2).

The bond lengths of $Sr_2Fe_{0.5}Ir_{0.5}O_4$, $Sr_2Fe_{0.5}Ru_{0.5}O_4$, Sr_2FeO_4 and their related perovskites are given in Table 6.7. Comparison of these bond lengths shows that in the Ruddlesden-Popper phases the apical M-O bond is longer than that of the M-O bond (M-O(1)) in the *ab*-plane (M-O(2)). Furthermore it is longer than the equivalent bond in the related perovskite. This clearly shows that in the Ruddlesden-Popper structure there is far less, or even no, compression along the *c*-axis compared to the equivalent perovskite structure. This is because the positively charged AO layer in the Ruddlesden-Popper structure

draws the negatively charged apical oxide ions away from the B-site. This structural feature is not present in the perovskite structure.

	Bond Length (Å)		
Compound	M-O(1)	M-O(2)	M-O(3)
$SrFeO_3$[116]	1.913(14)	1.921(5)	-
Sr_2FeO_4[117]	1.950(9)	1.932(1)	-
$SrFe_{0.5}Ru_{0.5}O_3$[46]	I .97(3)	1.97(2)	-
$Sr_2Fe_{0.5}Ru_{0.5}O_4$[118]	2.009	1.951	-
Sr_2FeIrO_6 (M = Fe)[22]	1.938(3)	1.950(7)	1.931(7)
Sr_2FeIrO_6 (M = Ir)[22]	2.054(3)	2.038(7)	2.067(7)
$Sr_2Fe_{0.5}Ir_{0.5}O_4$	2.013(1)	1.958(3)	-

Table 6.7: The Bond lengths of selected iron-containing oxide phases.

The unit cell that describes the structure of $Sr_2Fe_{0.5}Ir_{0.5}O_4$ has a disordered array of iron and iridium cations which is in contrast to the perovskite analogue, Sr_2FeIrO_6, which has rigorous B-site Cation order (Chapter 4). The key difference between these two structures, besides the cation order, is the connectivity along the *c*-axis as shown in Figure 6.12.

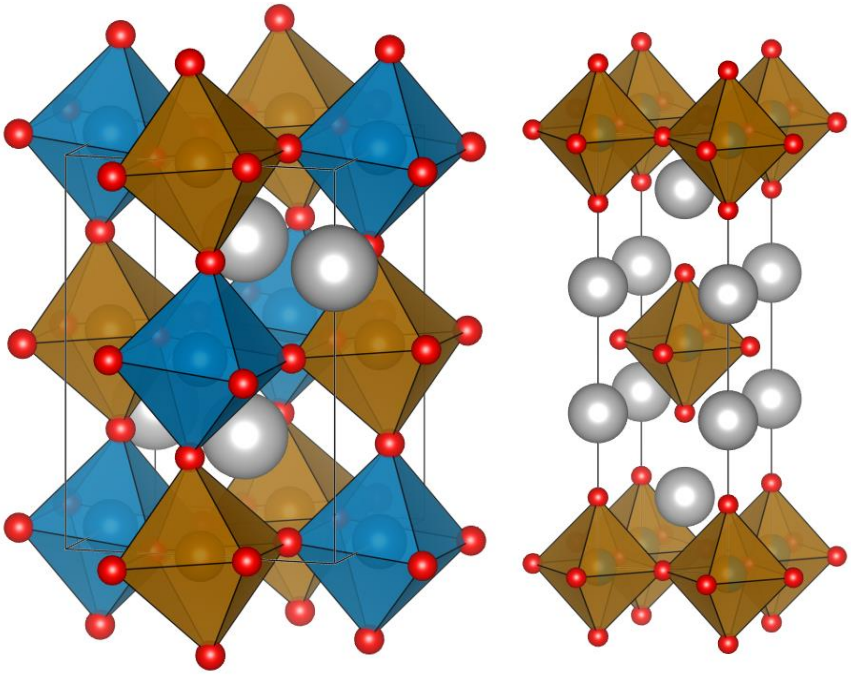

Figure 6.12: The unit cells of Sr_2FeIrO_6 (left) and $Sr_2Fe_{0.5}Ir_{0.5}O_4$ (right). The blue and gold spheres are iridium and iron respectively.

The breaking of the connectivity along the crystallographic *c*-axis has two key consequences. The first is that a B-site cation in the Perovskite structure has 6 neighbours whereas an equivalent cation in the *n =1* Ruddlesden-Popper structure has 4 B-site neighbours. Extensive work has been conducted by Woodward et al. into the factors that cause cation order[34]. They found that order occurs when B-site cations have significant differences either cation radius or charge, with charge having the greatest effect; when the difference is large enough the cations order to reduce local strain. The reduced number of B-site neighbours in the *n =1* Ruddlesden-Popper structure means that the effects of strain are restricted to the two-dimensional *ab*-plane and is lower compared to the analogous perovskite. Consequently compounds with the *n* = 1 Ruddlesden-Popper structure are often B-site cation disordered when the analogous Perovskite exhibits B-site cation order. This phenomenon is exemplified by Sr_2FeMoO_6[119] and $Sr_2Fe_{0.5}Mo_{0.5}O_4$[120].

The second consequence of breaking the connectivity along the *c*-axis is that the symmetry relation between layers in broken. This means that the layers can be disordered along the *c*-axis while the B-site cations are ordered within the layers (Figure 6.13). This is known as paracrystallinity and is exemplified by La_4LiMnO_8 and $La_3SrLiMnO_8$[41]. Due to the disorder between the layers paracrystallinity does not result in an expansion of the conventional disordered unit cell that describes the *n* = 1 Ruddlesden-Popper structure, thus no extra peaks are present in the diffraction patterns of paracrystalline compounds. This means that the diffraction patterns collected from paracrystalline compounds are fit best to models that have B-site cation disorder despite this not actually being the case. In the case of $Sr_2Fe_{0.5}Ir_{0.5}O_4$ we need to examine its bulk properties to help determine whether its structure is paracrystalline or B-site cation disordered.

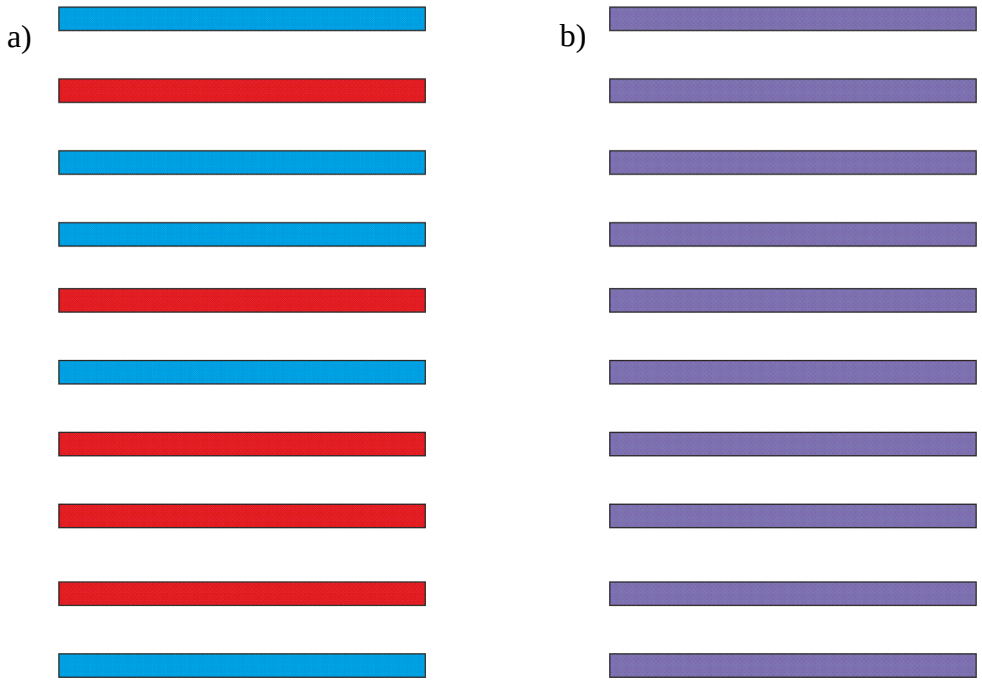

Figure 6.13: A cartoon representation of paracrystallinity: a) a disordered arrangement of ordered layers, b) the disordered structure "seen" by diffraction

6.4.1.2 Magnetic properties of $Sr_2Fe_{0.5}Ir_{0.5}O_4$

The SQUID magnetisation data collected from $Sr_2Fe_{0.5}Ir_{0.5}O_4$ as a function of temperature is shown in Section 6.3.2.1 and illustrates that $Sr_2Fe_{0.5}Ir_{0.5}O_4$ has unusual magnetic properties. The zero-field-cooled and field-cooled measurements have two points of divergence: one at 170 K and a second at 50 K. The synchrotron X-ray powder diffraction data shown in Section 6.3.1.1 shows that there is a very small amount of an unidentifiable impurity in the sample which could have a magnetically ordered state. This would result in a magnetisation profile that causes divergence between the ZFC and FC measurements. However the magnetisation isotherm collected at 100 K doesn't exhibit any detectable hysteresis, displacement or other feature that would be indicative of a magnetically ordered state. One cause of this behaviour could be due to the iron lattice undergoing two ordering events: one to an antiferromagnetic state and a second to a canted-antiferromagnetic state. There is an alternative explanation. The same magnetisation

phenomena are observed in the doped variants of Sr_2FeIrO_6 which are discussed in Chapter 5. The work presented in Chapter 5 shows that small deviations from the strict stoichiometry of Sr_2FeIrO_6 result in the formation and separation of two phases. The secondary phase has a $P2_1/n$ structure and two magnetic transitions. Comparing the magnetic properties of the doped Sr_2FeIrO_6 variants and $Sr_2Fe_{0.5}Ir_{0.5}O_4$ it is clear that they have similar properties. This suggests that the two magnetic events observed in the SQUID magnetisation of $Sr_2Fe_{0.5}Ir_{0.5}O_3$ data are not inconsistent sequential order in which the iridium and iron lattices become magnetically ordered at different temperatures. The lack of magnetic Bragg peaks in the neutron powder diffraction data means it is not possible to determine the source of the unusual magnetisation behaviour of $Sr_2Fe_{0.5}Ir_{0.5}O_3$.

The magnetisation isotherm collected from $Sr_2Fe_{0.5}Ir_{0.5}O_4$ at 5 K has a small degree of hysteresis which suggests $Sr_2Fe_{0.5}Ir_{0.5}O_4$ undergoes a transition to a canted antiferromagnetic state. In contrast to the magnetisation data the neutron powder diffraction data collected at 5 K does not exhibit extra peaks associated with magnetic order compared to the data collected at room temperature. This result has significant implications with regards to the structure of $Sr_2Fe_{0.5}Ir_{0.5}O_4$ which will be discussed later in this chapter. Another key result of the lack of magnetic Bragg peaks is that it is not possible to accurately determine the magnetic structure of the canted antiferromagnetic state and thus accurate oxidation states for Fe and Ir cannot be determined.

6.4.1.3 Paracrystallinity of $Sr_2Fe_{0.5}Ir_{0.5}O_4$

Magnetisation data discussed in Section 6.4.1.2 are consistent with the onset of a long range magnetically order state, either one in which the iridium and iron lattices order sequentially, or one in which the iron orders antiferromagnetically and then cants. For a

long range magnetic state to propagate through a compound the coupling of a given cation to its neighbours must be the same as those of the same cation elsewhere in the compound. For this to be the case the distribution of the B-site cations must be ordered rather than disordered. In Section 6.4.1.1 two explanations were given for the disordered structure of $Sr_2Fe_{0.5}Ir_{0.5}O_3$: either the B-site is truly disordered, or it is ordered within layers and the layers are disordered i.e. it is paracrystalline. The results of the magnetisation data clearly show that $Sr_2Fe_{0.5}Ir_{0.5}O_3$ must be ordered in the layers and therefore must be paracrystalline.

Studies pertaining to the onset of cation order in oxides conclude that for order to be present in a compound there must be a significant difference in cation radius and/or formal charge[34]. In order to maintain charge balance the two chemically reasonable options for the oxidation states of Fe and Ir in $Sr_2Fe_{0.5}Ir_{0.5}O_4$ are Fe^{IV}/Ir^{IV} or Fe^{III}/Ir^{V}. As previously discussed in this section for B-site cation order to occur there must be an appreciable difference in either the radii or the charge of the B-site cations. For the oxidation state combination to be Fe^{IV}/Ir^{IV} the radii of these cations would have to be very different. Comparison of these radii show this is simply not the case (Fe^{IV} = 0.729 nm and Ir^{IV} = 0.765 nm)[121]. In contrast the oxidation states of Fe and Ir in the Fe^{III}/Ir^{IV} pairing differ by 2 units. A difference of 2 units is regarded as borderline, that is it has the potential to lead to cation order. Given that $Sr_2Fe_{0.5}Ir_{0.5}O_4$ exhibits properties that require B-site cation order it is reasonable to conclude that the oxidation states of iron and iridium are +3 and +5 respectively and that the difference of 2 charge units results in order, as it does in Sr_2FeIrO_6[22].

6.4.1.4 $Sr_2Fe_{0.5}Ir_{0.5}O_4$ and doped Sr_2FeIrO_6

The structural and magnetic properties of $Sr_2Fe_{0.5}Ir_{0.5}O_4$ are in many ways similar to those of the doped variants of Sr_2FeIrO_6. This similarity is most notably manifest in the magnetic properties of $Sr_2Fe_{0.5}Ir_{0.5}O_4$ and doped Sr_2FeIrO_6. The evidence presented in Chapter 5 shows that upon doping Sr_2FeIrO_6 splits into two phases, one of which undergoes two magnetic transitions. The first of these transitions is attributed to the ordering of Ir^V, a situation that is highly usual and with little precedent. The magnetisation data presented in Section 6.3.2.1 and discussed in Section 6.4.1.1 suggest that $Sr_2Fe_{0.5}Ir_{.5}O_4$ has a similar magnetisation profile. One explanation for the magnetisation data of $Sr_2Fe_{0.5}Ir_{0.5}O_4$ would be sequential order of the Fe and Ir lattices in which the Ir is $j_{eff} \neq 0$. The only previously reported example of a compound with magnetically ordered Ir^V is Sr_2YIrO_6[111-112, 114]. The debate surround Sr_2YIrO_6 has been covered in Chapter 5, Section 5.4.3.4 of this thesis. In the literature it has been suggested Ir^V can become a $j_{eff} \neq 0$ cation when the IrO_6 octahedra are distorted.

Table 6.7 outlines the IrO bond lengths of the $I\bar{1}$ and $P2_1/n$ phases of $La_{0.05}Sr_{1.95}FeIrO_6$ and $Sr_2Fe_{0.5}Ir_{0.5}O_4$, all of which have been extracted from refinements against neutron powder diffraction data. Comparison of the bond lengths in Table 6.7 and the standard deviations in Table 6.8 show that the octahedra in $Sr_2Fe_{0.5}Ir_{0.5}O_4$ are more distorted than those in both phases of $La_{0.05}Sr_{1.95}FeIrO_6$. The distortion of the MO_6 octahedra of $Sr_2Fe_{0.5}Ir_{0.5}O_4$ suggests that the unusual magnetic behaviour observed in $Sr_2Fe_{0.5}Ir_{0.5}O_4$ could be due to sequential order of Ir and Fe.

	Bond lengths (Å)		
Compound	M-O(1)	M-O(2)	M-O(3)
$Sr_2Fe_{0.5}Ir_{0.5}O_4$	2.013(1)	1.958(3)	-
$La_{0.05}Sr_{1.95}FeIrO_6$ $I\bar{1}$ (M = Fe)	1.969(20)	1.988(21)	1.972(8)
$La_{0.05}Sr_{1.95}FeIrO_6$ $I\bar{1}$ (M = Ir)	1.978(20)	1.964(20)	1.972(8)
$La_{0.05}Sr_{1.95}FeIrO_6$ $P2_1/n$ (M = Fe)	1.996(6)	1.987(6)	1.977(16)
$La_{0.05}Sr_{1.95}FeIrO_6$ $P2_1/n$ (M = Ir)	1.971(6)	1.955(6)	1.961(16)

Table 6.7: Selected bond lengths from the refined structures of $Sr_2Fe_{0.5}Ir_{0.5}O_3$ and $La_{0.05}Sr_{1.95}FeIrO_6$

Compound	Mean (Å)	Variance (Å^2)	Standard Deviation (Å)
$Sr_2Fe_{0.5}Ir_{0.5}O_4$	1.976	6.72 x10^{-4}	0.0259
$La_{0.05}Sr_{1.95}FeIrO_6$ $I\bar{1}$ (M = Fe)	1.976	0.696 x10^{-4}	0.00834
$La_{0.05}Sr_{1.95}FeIrO_6$ $I\bar{1}$ (M = Ir)	1.971	0.329 x10^{-4}	0.00573
$La_{0.05}Sr_{1.95}FeIrO_6$ $P2_1/n$ (M = Fe)	1.987	0.602 x10^{-4}	0.00776
$La_{0.05}Sr_{1.95}FeIrO_6$ $P2_1/n$ (M = Ir)	1.962	0.436 x10^{-4}	0.00660

Table 6.8: The mean average, variance and standard deviation of the bond lengths extracted from the refined structures of $Sr_2Fe_{0.5}Ir_{0.5}O_3$ and $La_{0.05}Sr_{1.95}FeIrO_6$

The similarities between the magnetic properties of $Sr_2Fe_{0.5}Ir_{0.5}O_4$ and doped Sr_2FeIrO_6 are underpinned by subtle differences. Figure 6.14 shows the zero-field-cooled and field-cooled measurements of $Sr_2Fe_{0.5}Ir_{0.5}O_4$ and $La_{0.05}Sr_{1.95}FeIrO_6$. The topology of these measurements are the same, however the temperatures at which the magnetic transitions take place are different. Notably the temperatures at which $Sr_2Fe_{0.5}Ir_{0.5}O_4$ undergoes magnetic ordering are lower than those of $La_{0.05}Sr_{1.95}FeIrO_6$. The temperatures at which magnetic transitions occur in Ruddlesden-Poppers are often lower than those in their perovskite analogues. This occurs due to the lower number of nearest neighbours which reduces the strength of coupling between cations. The adherence of $Sr_2Fe_{0.5}Ir_{0.5}O_4$ and $La_{0.05}Sr_{1.95}FeIrO_6$ to the well-established trend is not inconsistent with $Sr_2Fe_{0.5}Ir_{0.5}O_4$ being an example of a compound in which Ir^V has a magnetic moment.

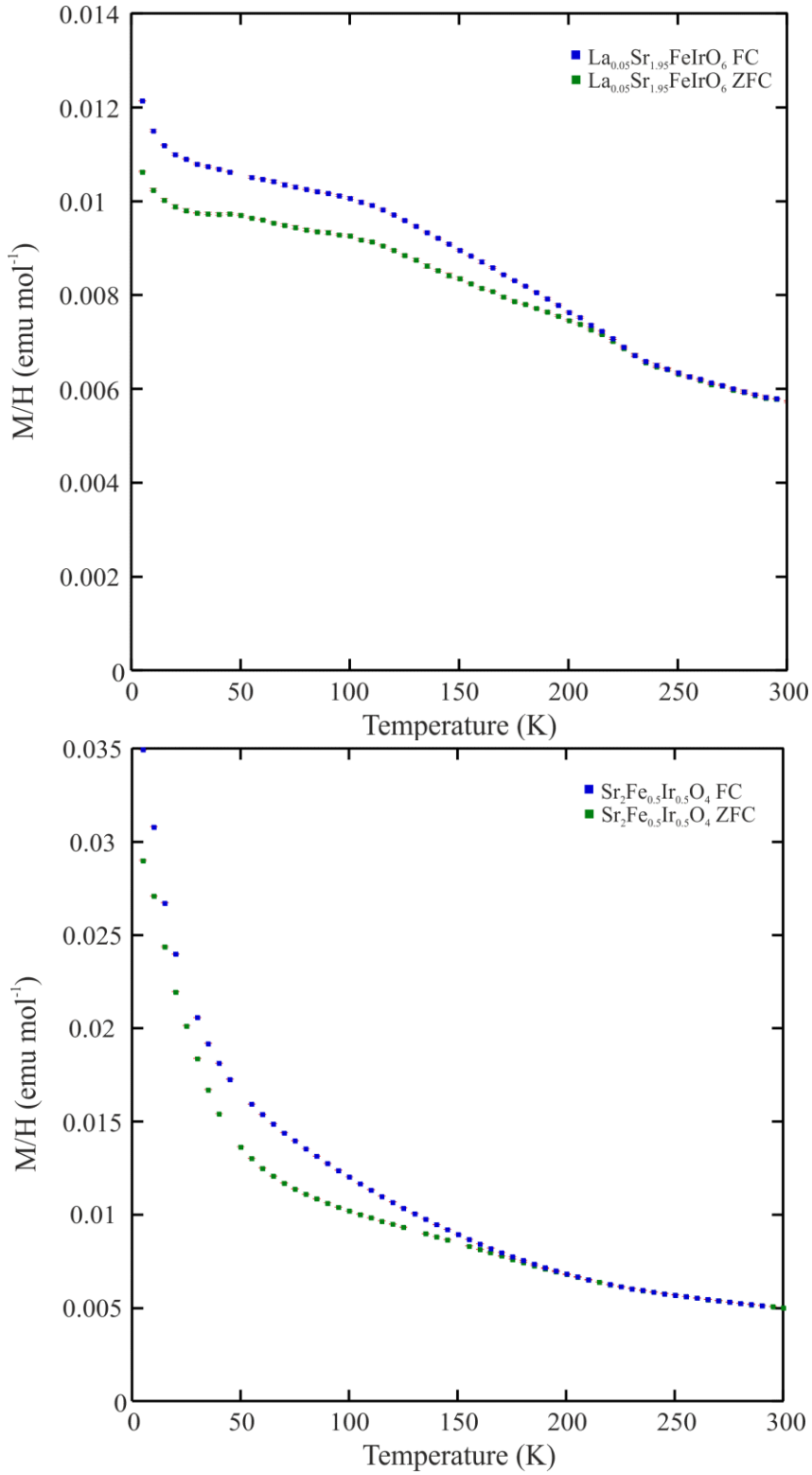

Figure 6.14: The ZFC-FC plots of $La_{0.05}Sr_{1.95}FeIrO_6$ (Top) and $Sr_2Fe_{0.5}Ir_{0.5}O_4$ (Bottom)

The paracrystalline structure of $Sr_2Fe_{0.5}Ir_{0.5}O_4$ makes it more difficult to interrogate the magnetic properties of $Sr_2Fe_{0.5}Ir_{0.5}O_4$ than those of the doped variants of Sr_2FeIrO_6. In a paracrystalline material ordering within the layers is masked by the disorder along the crystallographic *c*-axis thus the structure of the ordered state cannot be determined by neutron diffraction. Consequently we are unable to determine the magnetic properties of $Sr_2Fe_{0.5}Ir_{0.5}O_4$ in isolation. We can however understand the properties of $Sr_2Fe_{0.5}Ir_{0.5}O_4$ by considering them in tandem with those of the doped variants of Sr_2FeIrO_6. The comparison of these compounds suggests there is evidence for the existence of magnetically ordered $j_{eff} \neq 0$ Ir^V, a highly unusual state that is receiving increasing attention in the functional materials community.

6.4.2 Structure and magnetism of $Sr_2Fe_{0.5}Ir_{0.5}O_3$

6.4.2.1 Structure of $Sr_2Fe_{0.5}Ir_{0.5}O_3$

The refinements of the synchrotron X-ray powder diffraction data and neutron powder diffraction data collected from $Sr_2Fe_{0.5}Ir_{0.5}O_3$ at room temperature prove that $Sr_2Fe_{0.5}Ir_{0.5}O_3$ has an orthorhombic structure. The structure of $Sr_2Fe_{0.5}Ir_{0.5}O_3$ can be described by a unit cell with *Immm* space symmetry (Figure 6.8), analogous to those that describe Sr_2FeO_3 and $Sr_2Fe_{0.5}Ru_{0.5}O_{3+\delta}$. These refinements show that upon reduction the topology of much of the structure of $Sr_2Fe_{0.5}Ir_{0.5}O_4$ remains the same, most notably there is no change in position of the B-site cations, proving the reduction is topochemical and that $Sr_2Fe_{0.5}Ir_{0.5}O_3$ is paracrystalline. The lattice parameters of $Sr_2Fe_{0.5}Ir_{0.5}O_4$ and $Sr_2Fe_{0.5}Ir_{0.5}O_3$ are given in Table 6.9. Comparison of these parameters shows that there is a significant contraction along the axis oxide was removed and small expansions in the axes in which oxide remains. This result is consistent with the topochemical reductions of

other transition metal oxides with a Ruddlesden-Popper structure, as shown by the lattice parameters of some selected reductions in Table 6.9.

Compound	*a* (Å)	*b* (Å)	*c* (Å)
Sr_2FeO_4*	3.8642(1)	3.8642(1)	12.3968(2)
Sr_2FeO_3	3.5337(9)	3.9095(9)	12.9123(12)
$Sr_2Fe_2O_7$	3.8526(1)	3.8526(1)	20.1490(1)
$Sr_2Fe_2O_5$	3.514825(2)	3.95271(2)	20.9125(1)
$Sr_2Fe_{0.5}Ru_{0.5}O_4$$^+$	3.9025(1)	3.9025(1)	12.5943(3)
$Sr_2Fe_{0.5}Ru_{0.5}O_{3.25}$	3.6459(7)	3.9300(3)	12.898(2)
$Sr_2Fe_{0.5}Ru_{0.5}O_{3.44}$	3.7169(8)	3.9028(7)	12.856(2)
$Sr_2(Fe_{0.5}Ru_{0.5})_2O_7$$^+$	3.9187(1)	3.9187(1)	20.4146
$Sr_2(Fe_{0.5}Ru_{0.5})_2O_{5.50}$	3.6553(5)	3.9300(3)	20.815(2)
$Sr_2(Fe_{0.5}Ru_{0.5})_2O_{5.86}$	3.7164(5)	3.9208(4)	20.740(2)
$Sr_2Fe_{0.5}Ir_{0.5}O_4$	3.91663(6)	3.91663(6)	12.5781(2)
$Sr_2Fe_{0.5}Ir_{0.5}O_3$	3.9252(2)	3.5999(2)	12.8538(6)

Table 6.9: Lattice parameters of selected iron-based Ruddlesden-Popper structures and their reduced analogues. * Reported from X-ray powder diffraction data; $^+$ Reported from neutron powder diffraction data collected at 1.7 K.

The bond lengths of $Sr_2Fe_{0.5}Ir_{0.5}O_4$, $Sr_2Fe_{0.5}Ir_{0.5}O_3$ and other relevant oxides are given in Table 6.10. Comparison of these bond lengths shows that upon reduction the M-O bond that lies along the *c*-axis increases in length while the M-O bond that lies along the *b*-axis gets shorter. This is consistent with the bond lengths observed in the reduction of $Sr_2Fe_{0.5}Ru_{0.5}O_4$ but not that of Sr_2FeO_4. This would suggest that the $FeIrO_4$ chains are under compression along the *b*-axis but compression is relieved along the *c*-axis.

	Bond Length (Å)	
Compound	M-O(1)	M-O(2)
Sr_2FeO_4[117]	1.950(9)	1.932(1)
Sr_2FeO_3[99]	2.001	1.961
$Sr_2Fe_{0.5}Ru_{0.5}O_4$[118]	2.009	1.951
$Sr_2Fe_{0.5}Ru_{0.5}O_{3+\delta}$[46]	1.951(1)/1.947(1)	2.038(13)/2.089(10)
$Sr_2Fe_{0.5}Ir_{0.5}O_3$	1.9625(1)	2.044(3)
$Sr_2Fe_{0.5}Ir_{0.5}O_4$	2.013(1)	1.958(3)

Table 6.10: Selected bond lengths from the refined structures of iron-containing Ruddlesden-Popper phases and their reduced metastable phases

$Sr_2Fe_{0.5}Ir_{0.5}O_4$ is the n = 1 Ruddlesden-Popper analogue of Sr_2FeIrO_6, therefore $Sr_2Fe_{0.5}Ir_{0.5}O_3$ is the layered analogue of Sr_2FeIrO_4. Given that $Sr_2Fe_{0.5}Ir_{0.5}O_3$ and Sr_2FeIrO_4 are related it might be expected that they share some structural features. Specifically, we might expect the geometry of the MO_4 units to be similar. The M-O bond lengths of $Sr_2Fe_{0.5}Ir_{0.5}O_3$ and Sr_2FeIrO_4 extracted from refinements of neutron powder diffraction data are given below in Table 6.10.

	Bond lengths (Å)					
	Room Temperature			Low Temperature		
Compound	M-O(1)	M-O(2)	M-O(3)	M-O(1)	M-O(2)	M-O(3)
$Sr_2Fe_{0.5}Ir_{0.5}O_4$	2.013(1)	1.958(3)	-	2.009(7)	1.953(5)	-
$Sr_2Fe_{0.5}Ir_{0.5}O_3$	1.9625(1)	2.044(3)	-	1.9579(1)	2.045(2)	-
Sr_2FeIrO_6 (M = Fe)*	1.971(7)	1.991(8)	1.973(9)	-	-	-
Sr_2FeIrO_4 (M = Fe)	1.938(3)	-	-	1.931(7)	2.067(7)	-
Sr_2FeIrO_6 (M = Ir)*	1.977(7)	1.960(8)	1.972(9)	-	-	-
Sr_2FeIrO_4 (M = Ir)	2.054(3)	-	-	1.950(7)	2.038(7)	-

Table 6.11: Selected bond lengths from the refined structures of $Sr_2Fe_{0.5}Ir_{0.5}O_4$, $Sr_2Fe_{0.5}Ir_{0.5}O_3$, Sr_2FeIrO_6 and Sr_2FeIrO_4 at room and low temperature

Comparing the bond lengths of $Sr_2Fe_{0.5}Ir_{0.5}O_3$ and Sr_2FeIrO_4 highlights some key differences in the local structure of these compounds. The MO_4 units of $Sr_2Fe_{0.5}Ir_{0.5}O_4$ are not very symmetric at room temperature, that is do not have D_{4h} symmetry. Instead we can see that they have C_{2v} symmetry. Furthermore we can see that there is very little change in the geometry of the MO_4 units of $Sr_2Fe_{0.5}Ir_{0.5}O_3$ at low temperature. This is in sharp contrast to the structural properties of Sr_2FeIrO_4, as discussed in Chapter 4 and above in Table 6.10. The difference in co-ordination geometry of these related compounds stems from the difference in connectivity between the MO_4 units. Figure 6.15 shows the unit cells of $Sr_2Fe_{0.5}Ir_{0.5}O_3$ and Sr_2FeIrO_4. The unit cell of $Sr_2Fe_{0.5}Ir_{0.5}O_3$ shows that the anion vacancies order along the *b*-axis creating chains of MO_4 units in which only

one of the oxide ions sits between B-sites. The other oxide ion is only bonded to one B-site cation and as such has addition freedom to move along the *c*-axis without drastically altering the local co-ordination geometry or structure of $Sr_2Fe_{0.5}Ir_{0.5}O_3$ as a whole. In contrast the anion vacancies in Sr_2FeIrO_4 order along the *c*-axis resulting in planes of corner sharing MO_4 units in which both oxide ions form bonds with two B-site cations, a bonding regime that is far more restrictive.

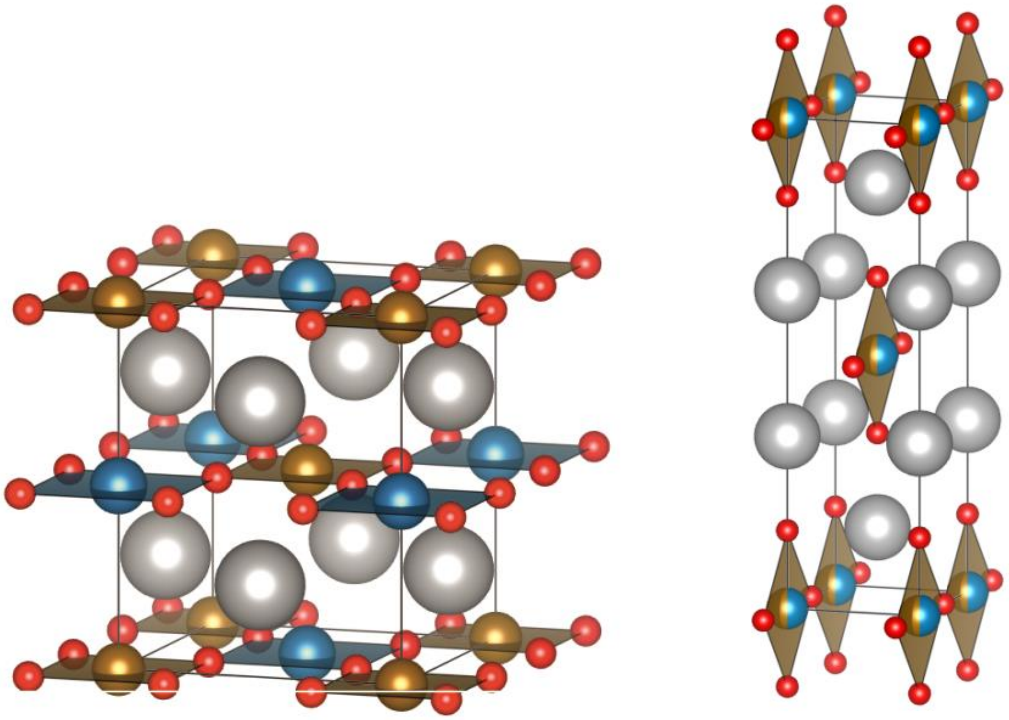

Figure 6.15: The unit cells of Sr_2FeIrO_4 (left) and $Sr_2Fe_{0.5}Ir_{0.5}O_3$ (right)

6.4.2.2 Magnetism of $Sr_2Fe_{0.5}Ir_{0.5}O_3$

Magnetisation data collected from $Sr_2Fe_{0.5}Ir_{0.5}O_3$ (Section 6.3.4.1, Figure 6.11) show that the zero-field-cooled and field-cooled measurements are weakly divergent at temperatures between $45 \leq T/K \leq 300$. There are two explanations for this behaviour. The first is that there is a small amount of a ferromagnetic impurity in the sample, the prime candidate in this case would be elemental iron. The magnetisation isotherm collected at

300 K (Section 6.3.4.1, Figure 6.11) proves this is not the case as it is a straight line that passes through the origin that displays no hysteresis. The second explanation is that the spins in $Sr_2Fe_{0.5}Ir_{0.5}O_3$ are interacting but not ordered. This would be the same magnetic regime that is observed in Sr_2FeIrO_4 (Chapter 4) and suggests that the magnetic couplings in $Sr_2Fe_{0.5}Ir_{0.5}O_3$ are frustrated and unable to order. The magnetisation data also indicate that at 45 K $Sr_2Fe_{0.5}Ir_{0.5}O_3$ undergoes a transition to an ordered magnetic state. The magnetisation isotherm collected at 5 K (Section 6.3.4.1, Figure 6.11) is displaced from the origin which suggests this state is either a spin glass state or a canted antiferromagnetic state with a significant component of frustration.

Analysis of the neutron diffraction data collected from $Sr_2Fe_{0.5}Ir_{0.5}O_3$ at 5 K indicates that there are no extra Bragg peaks associated with a magnetic structure. Furthermore, refinements of ferromagnetic unit cells against the neutron diffraction data did not give reasonable magnetic moments upon convergence. Normally this would suggest that we have a spin glass state however due to the paracrystallinity of $Sr_2Fe_{0.5}Ir_{0.5}O_3$ it remains possible that there may be magnetic order within the layers that is not related by symmetry to the order in the layers above and below. In the absence of data that can provide definitive answers regarding the magnetic behaviour of $Sr_2Fe_{0.5}Ir_{0.5}O_3$ it is necessary to contextualise its properties by comparing them to those of Sr_2FeIrO_4. Figure 6.16 shows the magnetisation isotherms of $Sr_2Fe_{0.5}Ir_{0.5}O_3$ and Sr_2FeirO_4 collected at 5 K. It can clearly be seen that they are quite similar. Both display hysteresis but most importantly they are both displaced from the origin. The similarity of these isotherms and the magnetisation behaviour discussed above would suggest that $Sr_2Fe_{0.5}Ir_{0.5}O_3$ and Sr_2FeIrO_4 have similar magnetic properties.

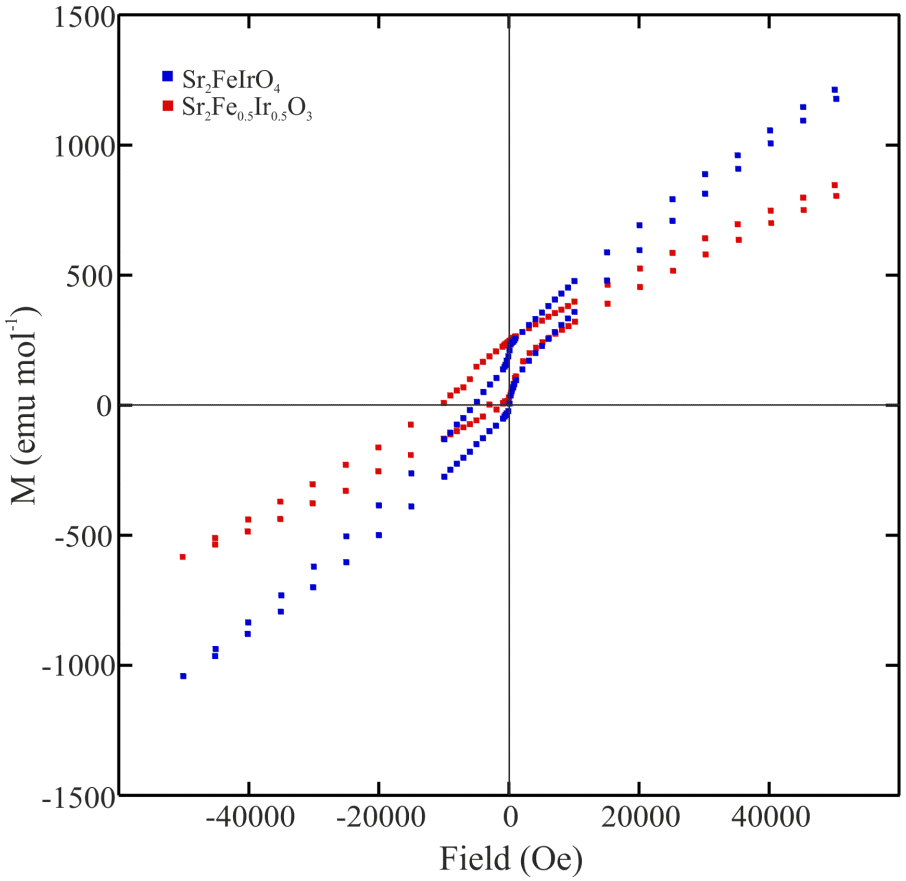

Figure 6.16: The magnetisation isotherms collected from Sr_2FeIrO_4 and $Sr_2Fe_{0.5}Ir_{0.5}O_3$ at 5 K

The magnetic behaviour of Sr_2FeIrO_4 is discussed in detail in Chapter 4 of this thesis. Data presented in Chapter 4 proves that above the temperature at which it orders Sr_2FeIrO_4 is magnetically frustrated. At the magnetic ordering temperature the structure of Sr_2FeIrO_4 distorts allowing a canted antiferromagnetic state to propagate through the material. The magnetisation isotherm collected from Sr_2FeIrO_4 at 5 K is offset, suggesting there is some frustration in the system. This frustration is due to the small amount of antisite disorder in the system. Figure 6.17 shows the magnetic couplings of ordered Fe and Ir in Sr_2FeIrO_4 and the frustrated couplings when an iron site is occupied by an iridium cation. The magnetisation data discussed previously suggests that the magnetic properties of $Sr_2Fe_{0.5}Ir_{0.5}O_3$ and Sr_2FeIrO_4 are very similar. This implies that at temperature above 50 K the iron and iridium spins of $Sr_2Fe_{0.5}Ir_{0.5}O_3$ are interacting but

frustrated. It would also suggest that at 50 K $Sr_2Fe_{0.5}Ir_{0.5}O_3$ undergoes a transition to a magnetically ordered state. The paracrystallinity of $Sr_2Fe_{0.5}Ir_{0.5}O_3$ means that order is restricted to the *ab*-plane such that the magnetic structure of one layer cannot be related by symmetry to that of its neighbours. Consequently the magnetic state cannot be observed by diffraction. However using what we know about the anti-site disorder and couplings in Sr_2FeIrO_4 we can hypothesise the nature of the magnetically order state in $Sr_2Fe_{0.5}Ir_{0.5}O_3$.

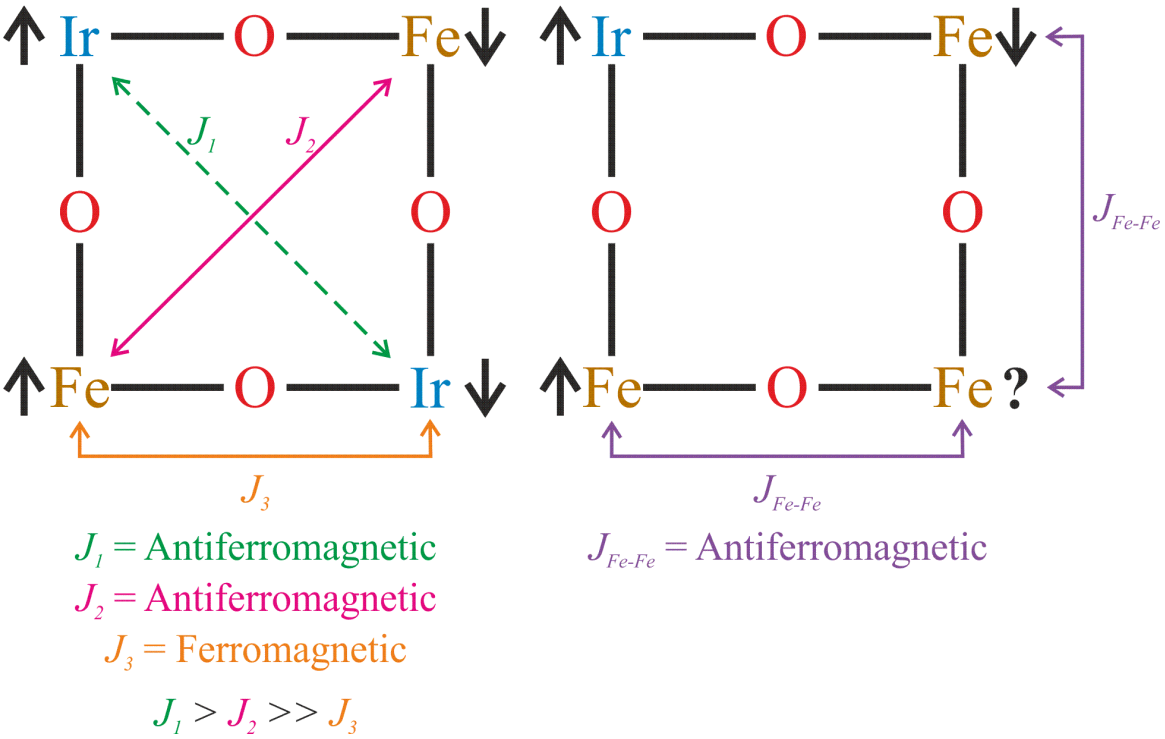

Figure 6.17: The coupling regime in Sr_2FeIrO_4 and the frustration present due to the 7% antisite disorder.

Figure 6.18 shows a possible coupling regime in the layers of $Sr_2Fe_{0.5}Ir_{0.5}O_3$ based on the magnetic structure of Sr_2FeIrO_4. The diagram shows that the ferromagnetic Fe-Ir superexchange and the antiferromagnetic direct exchange of Fe-Ir can be satisfied which results in antiferromagnetically stacked ferromagnetic chains. The paracrystallinity of $Sr_2Fe_{0.5}Ir_{0.5}O_3$ masks the order within the layers thus we cannot say with certainty how much antisite disorder there is in $Sr_2Fe_{0.5}Ir_{0.5}O_3$. However given the similarities of

$Sr_2Fe_{0.5}Ir_{0.5}O_3$ and Sr_2FeIrO_4 it is reasonable to assume there is a degree of antisite disorder in the layers of $Sr_2Fe_{0.5}Ir_{0.5}O_3$. Replacing one of the iridium cations with an iron cation frustration is introduced. This is because the antiferromagnetic direct Fe-Fe exchange and the antiferromagnetic Fe-Fe superexchange are in conflict. Both cannot be satisfied. This is similar to the frustration caused by the small degree of antisite disorder in Sr_2FeIrO_4 shown in Figure 6.17. This frustration would explain why the magnetisation isotherms of Sr_2FeIrO_4 and $Sr_2Fe_{0.5}Ir_{0.5}O_3$ collected at 5 K are offset from the origin, a clear indication there is frustration.

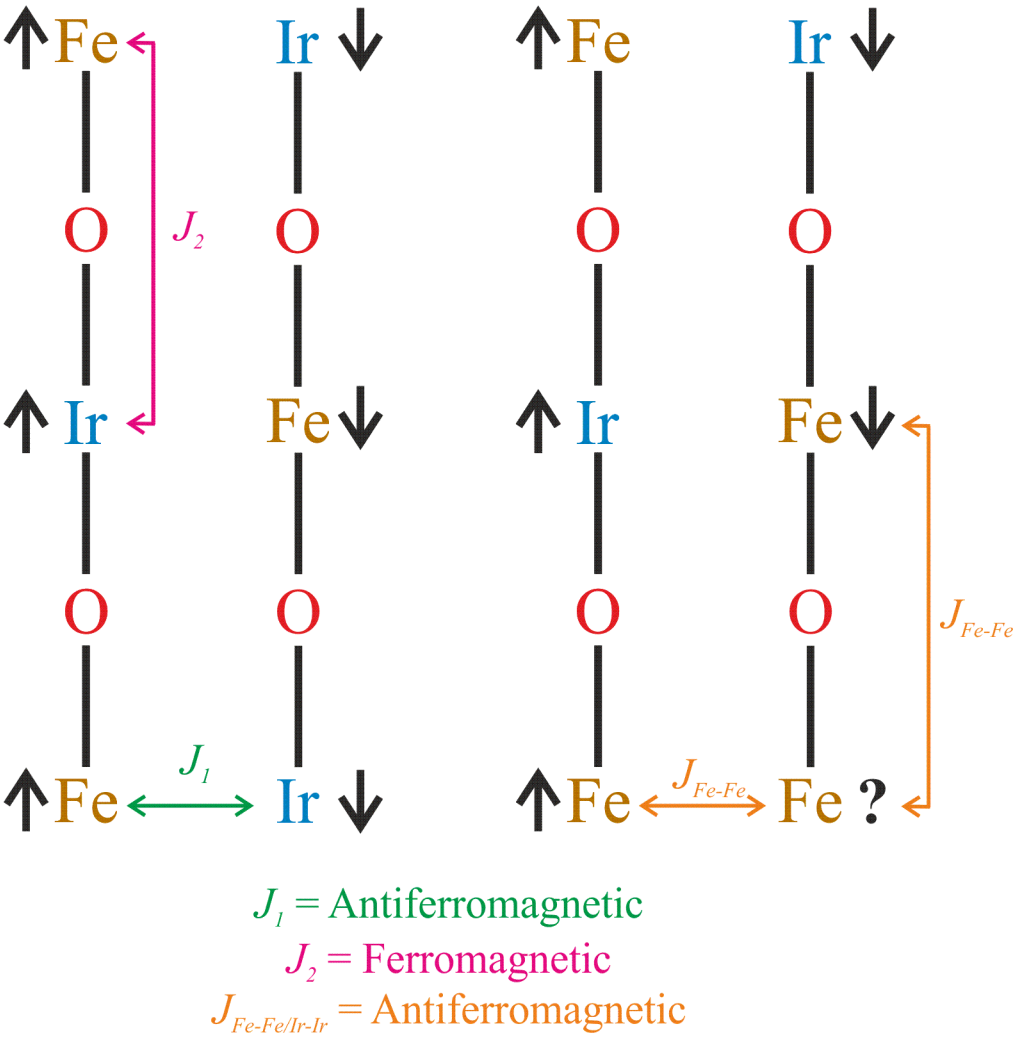

Figure 6.18: The coupling regime in $Sr_2Fe_{0.5}Ir_{0.5}O_3$ and the frustration present due to antisite disorder.

6.5 Conclusions

In this study we have successfully synthesised and reduced $Sr_2Fe_{0.5}Ir_{0.5}O_4$. We have shown that $Sr_2Fe_{0.5}Ir_{0.5}O_4$ has the archetypal tetragonal *I*4/*mmm* Ruddlesden-Popper structure. We have also shown by analysis and comparison of magnetisation data that $Sr_2Fe_{0.5}Ir_{0.5}O_4$ is paracrystalline, which is that there is B-site cation order within the layers but along the *c*-axis these layers are disordered. Magnetisation data collected from $Sr_2Fe_{0.5}Ir_{0.5}O_4$ show that it has two magnetic transitions, one at 170 K and another at 50 K. This is very similar to the doped variants of Sr_2FeIrO_6 discussed in Chapter 5 and suggests that $Sr_2Fe_{0.5}Ir_{0.5}O_4$ could be another example of an iridium containing oxide in which Ir^V cations have a $j_{eff} \neq 0$ state and magnetically order. This magnetisation behaviour could also be due to the iron lattice having two ordering events, thus further study to determine the true nature of the magnetic order is required. Neutron diffraction data collected at 5 K did not suggest that $Sr_2Fe_{0.5}Ir_{0.5}O_4$ has an ordered magnetic state that can be detected by diffraction methods. This is likely a consequence of the structure's paracrystallinity.

The reaction of $Sr_2Fe_{0.5}Ir_{0.5}O_4$ with zirconium using the getter method resulted in the formation of an oxide deficient phase. Compositional analysis proved this phase is $Sr_2Fe_{0.5}Ir_{0.5}O_3$. Refinement of diffraction data collected from $Sr_2Fe_{0.5}Ir_{0.5}O_3$ shows that it adopts an *Immm* structure analogous to that adopted by Sr_2FeO_3[99]. Magnetisation data indicate that $Sr_2Fe_{0.5}Ir_{0.5}O_3$ has a very similar magnetic behaviour to that of Sr_2FeIrO_4 (Chapter 4) with ZFC-FC plots that are consistently divergent. At 45 K the magnetisation data $Sr_2Fe_{0.5}Ir_{0.5}O_3$ becomes magnetically ordered. Similarly to $Sr_2Fe_{0.5}Ir_{0.5}O_4$, Neutron diffraction data collected at 5 K did not suggest that $Sr_2Fe_{0.5}Ir_{0.5}O_3$ has an ordered magnetic state that can be detected by diffraction methods. Although the magnetically ordered state of $Sr_2Fe_{0.5}Ir_{0.5}O_3$ cannot be analysed by diffraction, by considering the spin

exchange interactions present in the system we can posit that the magnetically ordered state consist of antiferromagnetically stacked ferromagnetic chains. This coupling regime also explains why the magnetisation isotherm collected from $Sr_2Fe_{0.5}Ir_{0.5}O_3$ 5 K is offset from the origin if we consider that there will be a degree of antisite B-site cation disorder in layers.

This study of $Sr_2Fe_{0.5}Ir_{0.5}O_4$ and $Sr_2Fe_{0.5}Ir_{0.5}O_3$ highlights the difficulty structural disorder can present when it comes to fully characterising complex oxide phases. Consequently to fully understand $Sr_2Fe_{0.5}Ir_{0.5}O_4$ and $Sr_2Fe_{0.5}Ir_{0.5}O_3$ it is necessary to consider its properties in comparison to similar systems that are not disordered, such as $Sr_2FreIrO_6$ and Sr_2FeIrO_4.

Chapter 7 – Topochemical Reduction of $CaMn_{0.5}Ir_{0.5}O_3$

7.1 Introduction

The reduction chemistry of ternary oxides that contain manganese as the sole B-site cation has been extensively explored with a variety of interesting results. By topochemically reducing a variety of manganese-containing oxides compounds which contain Mn^{I} [50], Mn^{II} [122] and Mn^{III} [2] have been isolated.

Notable examples of reduced manganese oxides include $CaMnO_{2.5}$[2], $Sr_3Mn_2O_{6+\delta}$[52] and $La_{0.5}Ba_{0.5}MnO_{2.5}$[122-123], the structures of which are shown in Figure 7.1. The structures shown in Figure 7.1 highlight that manganese is not as structurally flexible as other 3*d* ions such as iron and is sensitive to chemical composition. $CaMnO_{2.5}$ cannot be reduced beyond an oxide content of 2.5 and adopts an ordered oxide deficient structure of vertex sharing square pyramidal units. In contrast the structure of $La_{0.5}Ba_{0.5}MnO_{2.5}$ can be regarded as alternating layers of vertex-sharing octahedra and vertex-sharing tetrahedra. Finally, as discussed in Section 1.5.2, the structure of $Sr_3Mn_2O_{6+\delta}$ is unexpectedly different from that of $Sr_3Fe_2O_{6+\delta}$ despite their similar parent structures and compositions. These examples highlight that the structural results of the topochemical reduction of manganese oxides are unique. The structures of these topochemically reduced oxides are even more interesting if compared to the structures of topochemically reduced oxides that contain iron, cobalt and nickel. The infinite layer structure, exemplified by $LaNiO_2$[42], $SrFeO_{2+\delta}$[47] and $SrFe_{0.5}Ru_{0.5}O_2$[44], has not been observed in the reduced oxides of manganese. Furthermore, the *n=2* Ruddlesden-Popper structures $Sr_3Fe_2O_7$[117], which is isostructural with $Sr_3Mn_2O_7$[124], reduces to form an oxide that is isostoichiometric to $Sr_3Mn_2O_{6+\delta}$ but has a different structure[51].

Building on the precedent of reduced manganese oxides and the successes in reducing iridium-containing oxides discussed in Chapters 4 and 6 of this thesis, we decided to extend our work to include the manganese and iridium mixed-metal oxide, $CaMn_{0.5}Ir_{0.5}O_3$. In this work we also hope to extend our understanding of why manganese-containing topochemically reduced oxides adopt atypical structure types.

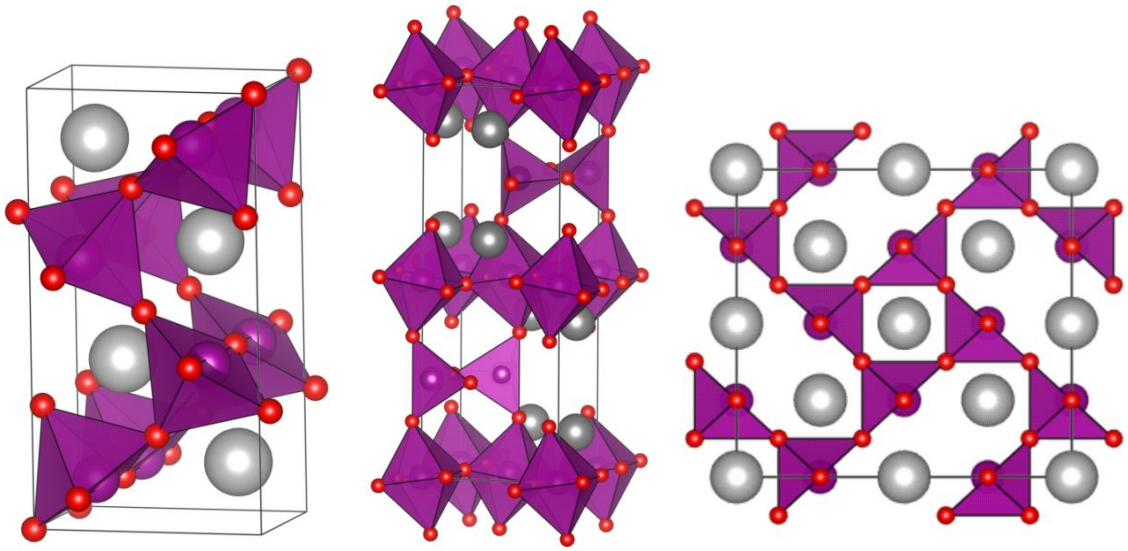

Figure 7.1: The crystal structures of $CaMnO_{2.5}$, $La_{0.5}Ba_{0.5}MnO_{2.5}$ and $Sr_3Mn_2O_{6+\delta}$

7.2 Synthesis

7.2.1 Synthesis of $CaMn_{0.5}Ir_{0.5}O_3$

A sample of $CaMn_{0.5}Ir_{0.5}O_3$ was prepared using a citrate gel method. Appropriate quantities of $CaCO_3$ (99.999%) and MnO_2 (99.997%) were dissolved in a minimal quantity of a 1:1 mixture of conc. nitric acid and distilled water, then the required amount of IrO_2 (99.99%, dried at 700 ^oC for 2 hours) was added. Citric acid and analar ethylene glycol were added and the solution was heated whilst being stirred. The gel thus formed was allowed to dry and then combust in air. The subsequent product was ground into a fine powder, placed in an alumina crucible and heated at 1000 ^oC in air at a rate of 1 ^oC

min^{-1} to remove the organic components of the sample. The resulting powder was pressed into a 13 mm diameter pellet and heated in air for two cycles of 2 days at 1100 ^{o}C.

The resulting powders were observed to be phase-pure by laboratory X-ray powder diffraction, with lattice parameters a = 5.37589(5) Å, b = 5.46997(6) Å, c = 7.64080(7) Å and space symmetry *Pnma*, in good agreement with values reported in the literature (a = 5.350 Å, b = 5.455 Å, c = 7.643 Å, note no error bars are given in the literature)[79].

7.2.2 Synthesis of $CaMn_{0.5}Ir_{0.5}O_{3-x}$

A full discussion on the reduction chemistry of iridium-containing oxides and the challenges this process presents, including that of $CaMn_{0.5}Ir_{0.5}O_3$, is given in Chapter 3. A sample of $CaMn_{0.5}Ir_{0.5}O_{3-x}$ for analysis by neutron powder diffraction was prepared by reacting approximately 1.25g of $CaMn_{0.5}Ir_{0.5}O_3$ with half a molar equivalent of NaH using the method described in Chapter 3, Section 3.2.6.2. The sample was heated for 4 periods of 7 days at temperatures between $180 \leq T / {}^{o}C \leq 210$. Between heating cycles the samples were taken into an Ar filled glovebox, without being exposed to air, ground with an agate pestle and mortar, and one molar equivalent of NaH was added.

7.3 Results

7.3.1 Thermogravimetric analysis of $CaMn_{0.5}Ir_{0.5}O_{3-x}$

An oxidative thermogravimetric experiment was conducted to confirm the oxygen content of $CaMn_{0.5}Ir_{0.5}O_{3-x}$. A small quantity of the reduced sample was heated under a flow of oxygen to reform $CaMn_{0.5}Ir_{0.5}O_3$, as confirmed by X-ray powder diffraction. During this reaction the sample gained 3.95 % of its initial mass, an increase that is consistent with a composition of $CaMn_{0.5}Ir_{0.5}O_{2.477}$ for the reduced phase (Figure 7.2). From now on $CaMn_{0.5}Ir_{0.5}O_{3-x}$ will be referred to as $CaMn_{0.5}Ir_{0.5}O_{2.5}$.

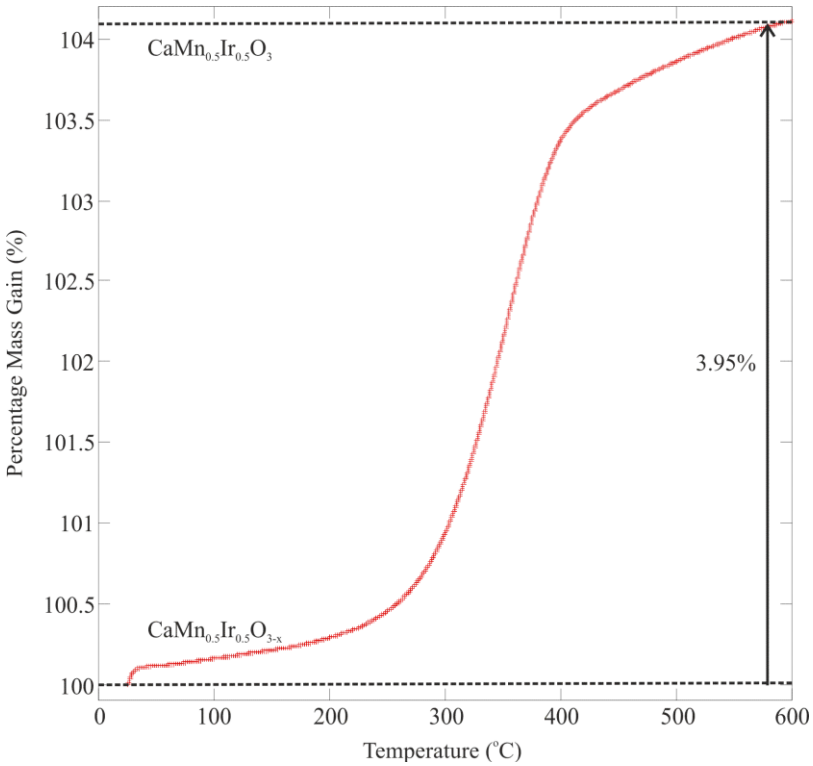

Figure 7.2: Thermogravimetric data collected during the oxidation of $CaMn_{0.5}Ir_{0.5}O_{2.5}$ to $CaMn_{0.5}Ir_{0.5}O_3$

7.3.2 Structural characterisation of $CaMn_{0.5}Ir_{0.5}O_{2.5}$

7.3.2.1 Synchrotron powder X-ray diffraction data

High resolution powder X-ray diffraction data were collected from a sample of $CaMn_{0.5}Ir_{0.5}O_{2.5}$ using instrument I11 at the Diamond Light Source (Section 2.7.1.2). The diffraction pattern could be indexed on the basis of a cubic unit cell. However, the neutron diffraction data collected from the same sample of $CaMn_{0.5}Ir_{0.5}O_{2.5}$ (Section 7.3.2.2) could not be fit to a unit cell with cubic symmetry. Closer inspection of the refinement of the synchrotron X-ray powder diffraction data show that some peaks are split, as shown in Figure 7.2.

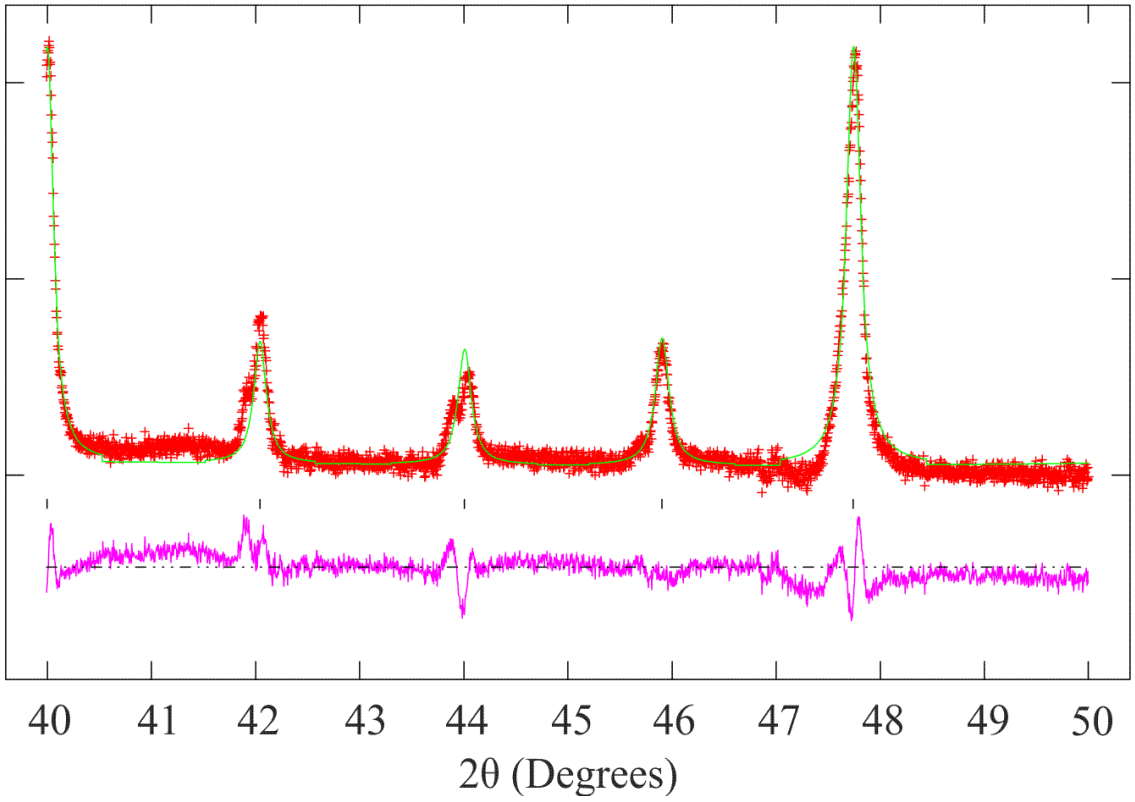

Figure 7.3: The 40 ≤ 2θ / º ≤ 50 portion of the refinement of a cubic model against the synchrotron X-ray powder diffraction data collected from $CaMn_{0.5}Ir_{0.5}O_{2.5}$.

An orthorhombic cell *Pnma* space symmetry was constructed (Figure 7.4) based on the cubic unit cell initially refined against the synchrotron X-ray powder diffraction data. A full explanation of this unit cell will be given in Section 7.3.2.2 alongside neutron powder diffraction data. The model shown in Figure 7.4 was refined against the synchrotron X-ray powder diffraction data. The refinement converged to give an excellent statistical fit that is better than that of the refinement of the cubic model. The observed, calculated and difference plots for the refinement are shown in Figure 7.5.

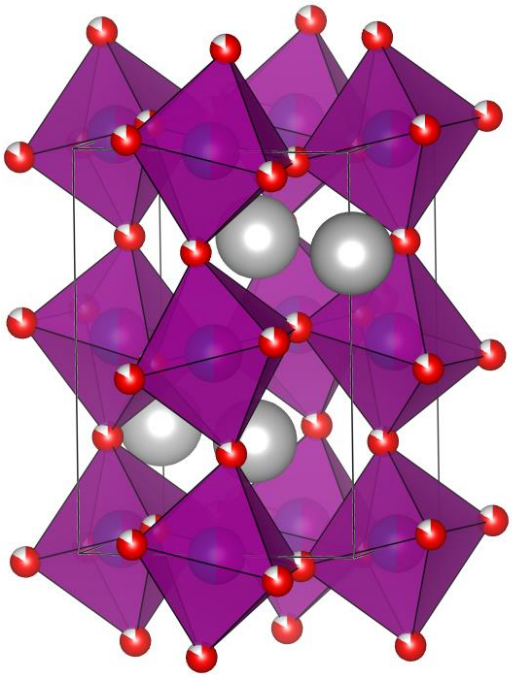

Figure 7.4: The structural unit cell of $CaMn_{0.5}Ir_{0.5}O_{2.5}$ with *Pnma* space symmetry in which the oxygen vacancies are evenly distributed across all O sites. The blue and purple spheres are iridium and manganese respectively.

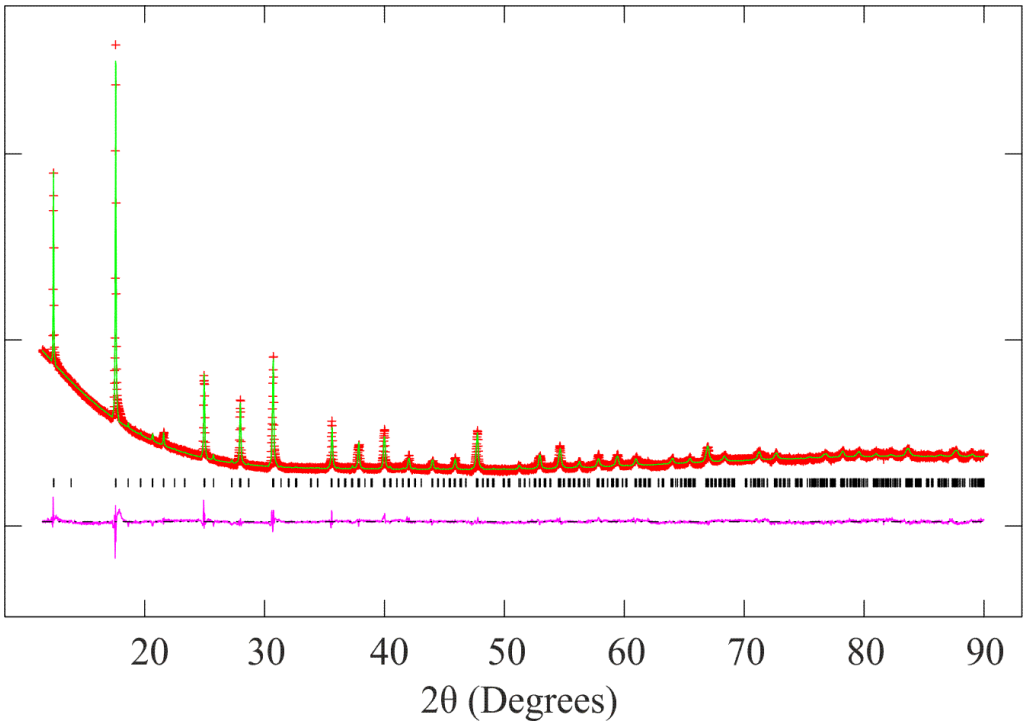

Figure 7.5: Observed, calculated and difference plots from the refinement of the *Pnma* structural model of $CaMn_{0.5}Ir_{0.5}O_{2.5}$ against synchrotron powder diffraction data collected at room temperature using the I11 instrument. χ^2 = 8.499, wRp = 2.08% Rp= 1.49%; a = 5.4087(1) Å, b = 7.6243(1) Å, c = 5.3953 (1) Å, V = 222.497(7) Å^3

7.3.2.2 Neutron powder diffraction data

Neutron powder diffraction data were collected from a sample of $CaMn_{0.5}Ir_{0.5}O_{2.5}$ using the D2B instrument at the ILL (Chapter 2, Section 2.7.2.2) at room temperature and 5 K. The neutron powder diffraction pattern could not be fully indexed using the cubic $Fm\bar{3}m$ unit cell used in the initial refinement of the synchrotron X-ray diffraction data (Section 7.3.2.1). The additional peaks in the neutron diffraction data could be indexed on the basis of a unit cell that is a $\sqrt{2}\ x\ 2\ x\ \sqrt{2}$ expansion of the cubic unit cell pictured in Figure 7.6. An orthorhombic unit cell with *Pnma* symmetry was constructed (Figure 7.6) and refined against the neutron powder diffraction data collected at room temperature. During the refinement the occupancies of the two oxide sites were allowed to vary. This resulted in one site being fully occupied and the other having an occupancy of around 75%. The refinement converged to give an excellent fit. The observed, calculated and difference plots for the refinement are shown in Figure 7.7 and full details of the structural parameters are given in Tables 7.1 and 7.2. Selected bond lengths extracted from refinement are given in Table 7.3 and the structure extracted from the refinement is shown in Figure 7.6. This structure is in essence the same as that of the unreduced starting material.

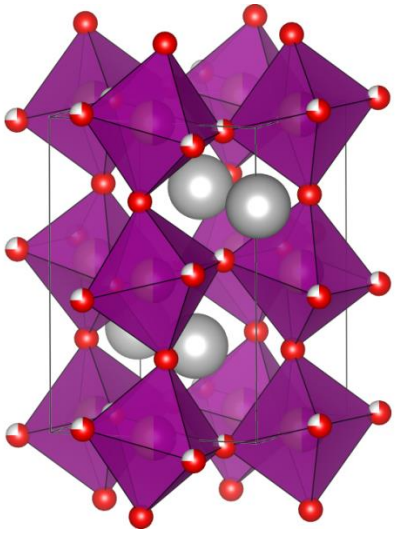

Figure 7.6: The structural unit cell of $CaMn_{0.5}Ir_{0.5}O_{2.5}$ with *Pnma* space symmetry extracted from the refinement shown in Figure 7.7. The blue and purple spheres are iridium and manganese respectively.

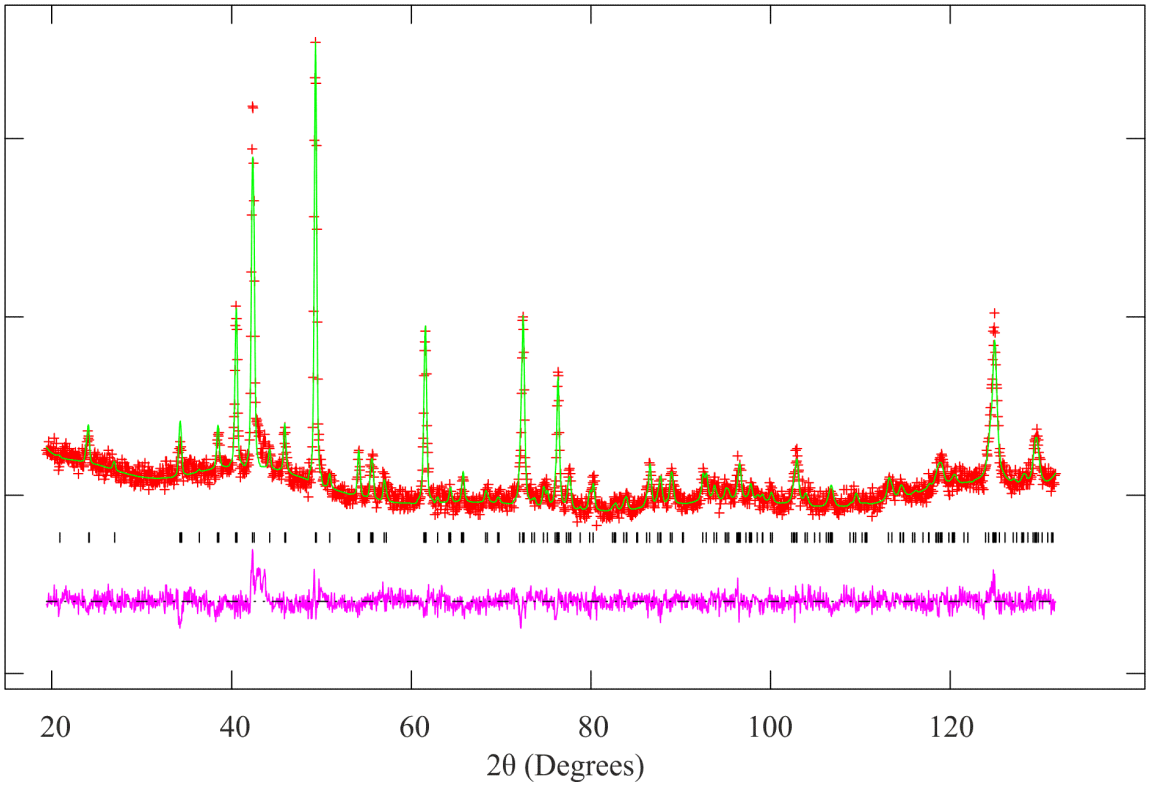

Figure 7.7: Observed, calculated and difference plots from the refinement of the *Pnma* structural model of $CaMn_{0.5}Ir_{0.5}O_{2.5}$ against neutron powder diffraction data collected at room temperature using the D2B instrument.

Atom	site	*x*	*y*	*z*	Fraction
Ca		0.028(1)	¼	0.999(3)	1
Mn/Ir		0	0	½	0.5/0.5
O(1)		0.475(2)	¼	0.052(2)	0.99(2)
O(2)		0.206(1)	0.5442(7)	0.216(1)	0.75(1)
$CaMn_{0.5}Ir_{0.5}O_{2.5}$ - Space Group: *Pnma* (#62) Formula weight = 203.66 g mol^{-1} *a* = 5.4160(7) Å, *b* = 7.6268(7) Å, *c* = 5.3892(6) Å, volume = 222.61(5) $Å^3$					
Radiation source: Constant wavelength, λ = 1.54 Å Temperature: Room temperature χ^2 = 1.588; *wRp*= 3.98 %; *Rp* = 3.10 %.					

Table 7.1: Parameters from the structural refinement of $CaMn_{0.5}Ir_{0.5}O_{2.5}$ against neutron powder diffraction data collected at room temperature.

Atom	U_{iso} ($Å^2$)	U_{11} ($Å^2$)	U_{22} ($Å^2$)	U_{33} ($Å^2$)	U_{12} ($Å^2$)	U_{13} ($Å^2$)	U_{23} ($Å^2$)
Ca	-	0.039(6)	0.0025(2)	0.012(4)	0	0.004(2)	0
Fe/Ir	0.006(1)	-	-	-	-	-	-
O(1)	-	0.060(8)	0.0046(5)	0.08(1)	0	0.012(9)	0
O(2)	-	0.033(4)	0.012(2)	0.014(3)	0.001(3)	0.029(2)	0.012(3)

Table 7.2: Thermal parameters from the structural refinement of $CaMn_{0.5}Ir_{0.5}O_{2.5}$ against neutron powder diffraction data collected at room temperature.

	Bond lengths (Å)			
	Room Temperature		5 K	
Cation (M)	M-O(1)	M-O(2)	M-O(1)	M-O(2)
Mn/Ir	1.931(1)	1.994(7)	1.939(2)	1.917(7)
	Bond Angles (°)			
	150 K		1.5 K	
	M-O(1)-M	M-O(2)-M	M-O(1)-M	M-O(2)-M
	161.7(8)	153.2(4)	157.7(7)	153.6(4)

Table 7.3 Selected bond length and angles from the refined structure of $CaMn_{0.5}Ir_{0.5}O_{2.5}$ at room temperature and 5 K

The mechanism of the reaction of NaH and $CaMn_{0.5}Ir_{0.5}O_3$ is not fully understood however the presence of hydride and possibly hydrogen gas means that there is the potential $CaMn_{0.5}Ir_{0.5}O_{2.5}$ is in fact an oxyhydride. The neutron scattering length of hydrogen is negative (-3.7390(11) fm[72]), therefore the presence of hydride in a lattice can be detected by close inspection of the refined occupancies and thermal parameters of the oxide sites. If $CaMn_{0.5}Ir_{0.5}O_{2.5}$ were $CaMn_{0.5}Ir_{0.5}O_{2.5}H_y$ ($y \leq 0$) we would expect the occupancies of the oxide sites to refine to low values that are chemically unreasonable

and/or for their thermal parameters to refine to negative, physically unreasonable values. Thus, refinements in which oxide site occupancy and thermal parameters were allowed to freely refine were conducted. Care had to be taken during these refinements to reduce the effects of parameter correlation. These refinements clearly showed that there are no hydride anions in the lattice. We can therefore conclude that $CaMn_{0.5}Ir_{0.5}O_{2.5}$ is not an oxyhydride.

7.3.3 Magnetic characterisation of $CaMn_{0.5}Ir_{0.5}O_{2.5}$

7.3.3.1 SQUID magnetometry

Magnetisation data were collected from a sample of $CaMn_{0.5}Ir_{0.5}O_{2.5}$ in an applied field of 100 Oe in the temperature range $5 \leq T / K \leq 300$. The zero-field cooled (ZFC) and field cooled (FC) data and magnetisation-field isotherms collected at 300 K and 5 K are shown in Figure 7.8. At temperatures above 110 K the zero-field cooled and field cooled measurements are convergent however neither data set could reasonably be fit to the Curie-Weiss law. At 110 K the ZFC-FC measurements become divergent suggesting the onset of either a spin glass state or a canted antiferromagnetic state. A magnetisation isotherm collected at after field cooling 5 K exhibits hysteresis and displacement from the origin suggesting at $CaMn_{0.5}Ir_{0.5}O_{2.5}$ has a transition to a frustrated canted-antiferromagnetic state or a spin glass state.

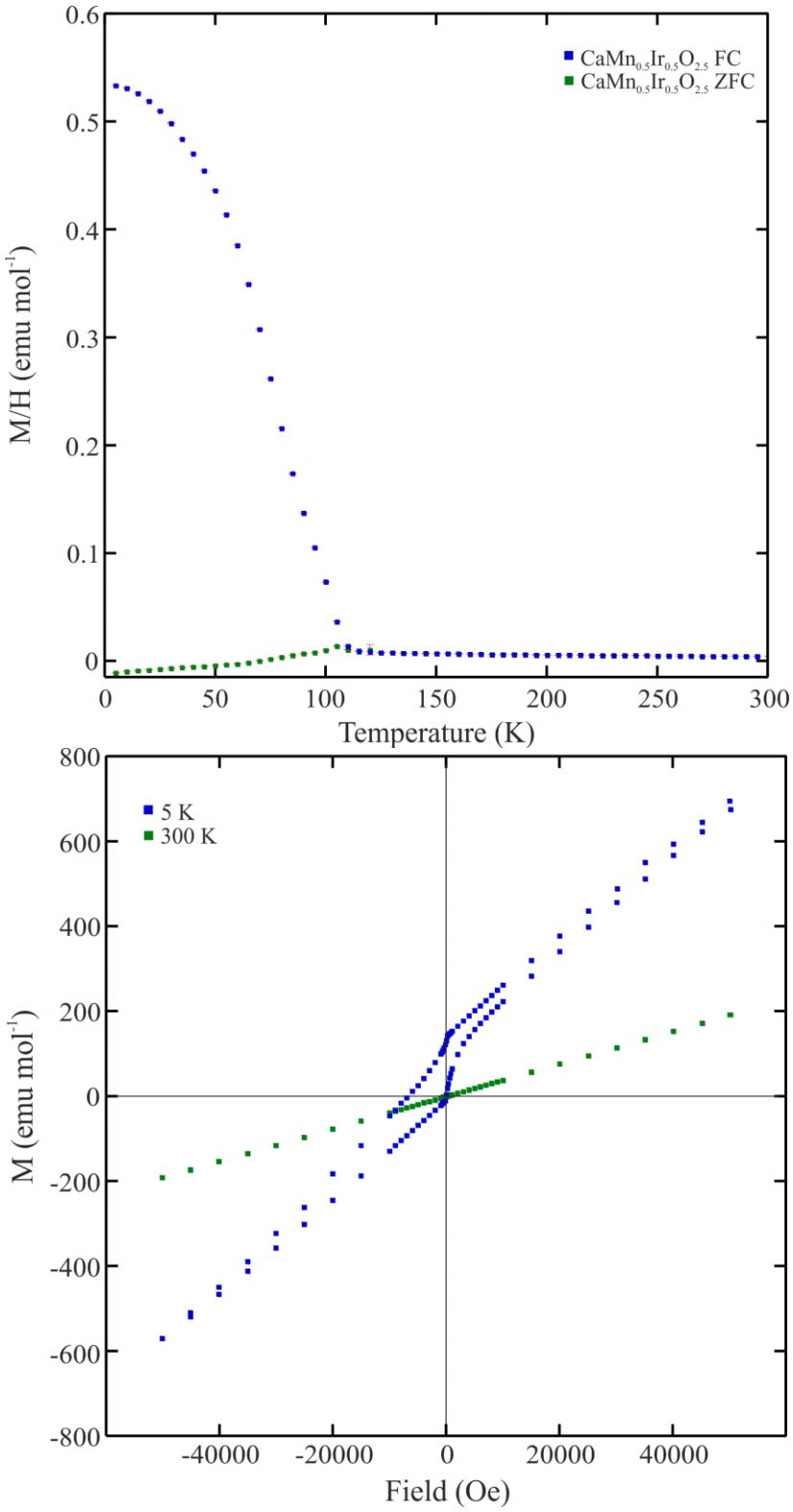

Figure 7.8: a) Zero-field cooled and field-cooled magnetisation data collected from $CaMn_{0.5}Ir_{0.5}O_{2.5}$. b) Magnetisation-field isotherms collected from $CaMn_{0.5}Ir_{0.5}O_{2.5}$

7.3.3.2 Neutron powder diffraction data

Comparison of the neutron diffraction data collected from $CaMn_{0.5}Ir_{0.5}O_{2.5}$ at room temperature and 5 K did not reveal additional diffraction peaks that could not be attributed to the closed-circuit refrigeration system in which the sample was cooled. Furthermore refinement of simple ferromagnetic unit cells against the data collected at 5 K did not converge. These results indicate $CaMn_{0.5}Ir_{0.5}O_{2.5}$ does not have a magnetically ordered state that can be detected by diffraction.

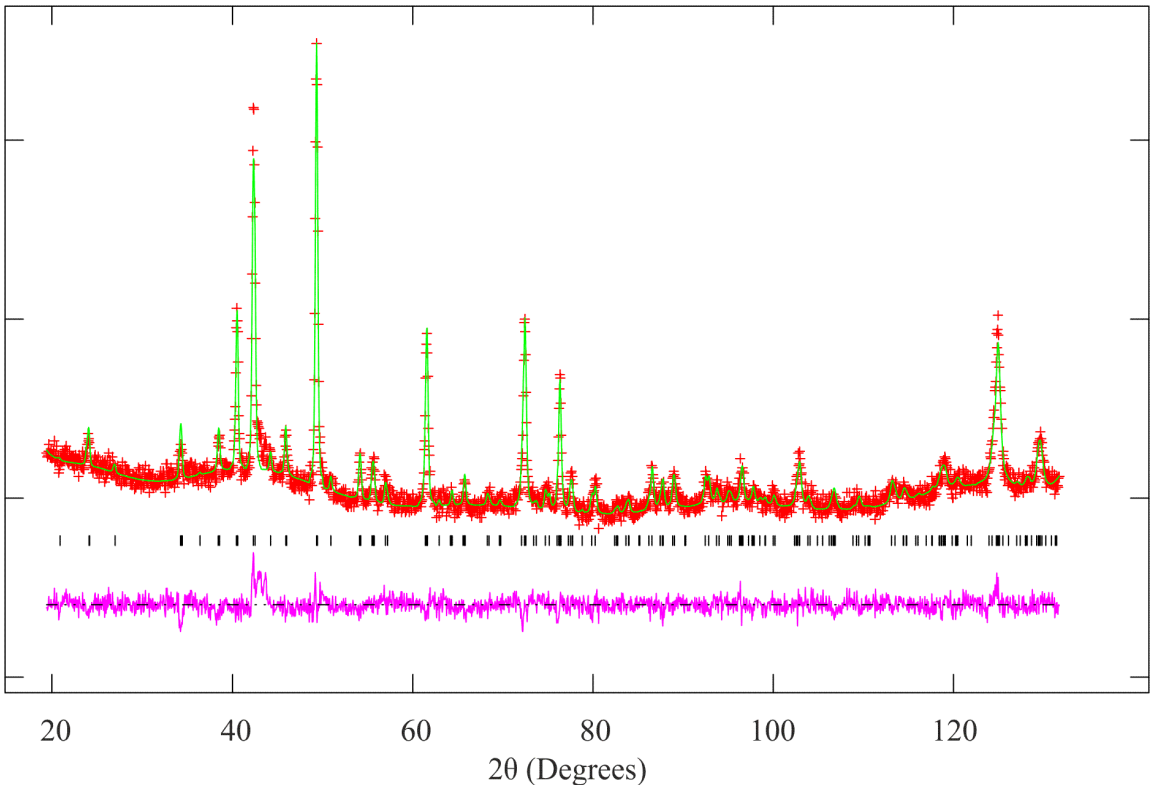

Figure 7.9: Observed, calculated and difference plots from the refinement of the *Pnma* structural model of $CaMn_{0.5}Ir_{0.5}O_{2.5}$ against neutron powder diffraction data collected at 5 K using the D2B instrument.

Atom	site	*x*	*y*	*z*	Fraction
Ca		0.030(1)	¼	0.999(3)	1
Mn/Ir		0	0	½	0.5/0.5
O(1)		0.476(2)	¼	0.065(2)	0.99(2)
O(2)		0.206(1)	0.5442(7)	0.216(1)	0.75(1)
$CaMn_{0.5}Ir_{0.5}O_{2.5}$ - Space Group: *Pnma* (#62) Formula weight = 203.66 g mol^{-1} *a* = 5.4126(7) Å, *b* = 7.6112(7) Å, *c* = 5.3785(6) Å, volume = 221.58(5) $Å^3$					
Radiation source: Constant wavelength, λ = 1.54 Å Temperature: 5 K χ^2 = 1.841; *wRp*= 3.98 %; *Rp* = 3.10 %.					

Table 7.4: Parameters from the structural refinement of $CaMn_{0.5}Ir_{0.5}O_{2.5}$ against neutron powder diffraction data collected at 5 K.

Atom	U_{iso} ($Å^2$)	U_{11} ($Å^2$)	U_{22} ($Å^2$)	U_{33} ($Å^2$)	U_{12} ($Å^2$)	U_{13} ($Å^2$)	U_{23} ($Å^2$)
Ca	-	0.051(6)	0.0025(1)	0.013(4)	0	0.004(1)	0
Fe/Ir	0.010(1)	-	-	-	-	-	-
O(1)	-	0.057(8)	0.0046(2)	0.09(1)	0	0.007(8)	0
O(2)	-	0.022(3)	0.006(2)	0.009(3)	0.004(3)	0.024(2)	0.011(3)

Table 7.5: Thermal parameters from the structural refinement of $CaMn_{0.5}Ir_{0.5}O_{2.5}$ against neutron powder diffraction data collected at 5 K.

7.4 Discussion

7.4.1 Oxidation states of $CaMn_{0.5}Ir_{0.5}O_3$

The refinement of the synchrotron X-ray powder diffraction data collected from $CaMn_{0.5}Ir_{0.5}O_3$ confirms that it has a B-site disordered perovskite structure with *Pnma* symmetry. The original study published by S. Mizusaki *et al.* suggests that $CaMn_{0.5}Ir_{0.5}O_3$ contains Mn^{III}/Ir^{V} and Mn^{IV}/Ir^{IV} in the following ratios, 0.276/0.276 and 0.224/0.224[79]. These are not extracted from the refinement of diffraction data or local probes such as XANES, XAFS or NMR, rather they are calculated from empirical equations derived from the volumes of related compounds that do not have mixed 3*d*/5*d* occupancy on the B-site. Consequently the conclusions drawn in the original studying pertaining to the oxidation states are not certain. It is important to try and understand the oxidation states of Mn and Ir in $CaMn_{0.5}Ir_{0.5}O_3$ in order to contextualise the structural properties of

$CaMn_{0.5}Ir_{0.5}O_{2.5}$. The requirements for cation order have been thoroughly discussed in Chapters 4, 5 and 6 of this thesis and been used to help rationalise the oxidation states in the oxidation states of B-site cations in ordered oxides. We can use the same rationale to help gain an understanding of the transition metal oxidation states in $CaMn_{0.5}Ir_{0.5}O_3$ in the absence of concrete characterisation. Table 7.6 outlines some relevant ionic radii[121].

Cation	Oxidation Sate	Ionic Radii (nm)
Mn	III	0.645
	IV	0.53
Fe	III	0.645
	IV	0.585
Ir	IV	0.625
	V	0.57

Table 7.6: The ionic radii of Mn, Fe and Ir in octahedral coordination geometries.

Comparing the ionic radii highlighted in Table 7.6 we can see the difference in radii of the Mn^{III}/Ir^{V} and Mn^{IV}/Ir^{IV} pairs are 0.075 nm and 0.095 nm respectively. These differences are very small and as such could both lead to B-site cation disorder on the basis of size. The values in Table 7.6 also show that Mn^{III} has the same ionic radius as Fe^{III}. The structure of Sr_2FeIrO_6 has been thoroughly discussed in Chapters 4 and 5 of this thesis but a key feature of this structure is the rigorous order of its Fe^{III} and Ir^{V} B-site cations. Considering the order in Sr_2FeIrO_6 and the similarities in ionic radii and charge difference of the Fe^{III}/Ir^{V} and Mn^{III}/Ir^{V} pairings, it is reasonable to expect that $CaMn_{0.5}Ir_{0.5}O_3$ would be ordered if the oxidation states of Mn and Ir were III and V respectively. This is clearly not the case, suggesting the oxidation states of Mn and Ir to be IV in both cases.

7.4.2 Structure of $CaMn_{0.5}Ir_{0.5}O_{2.5}$

The refinements of the synchrotron X-ray and neutron powder diffraction data show that $CaMn_{0.5}Ir_{0.5}O_{2.5}$ adopts an oxide deficient perovskite structure which can be described by an orthorhombic cell with *Pnma* symmetry (Section 7.3.2.2, Figure 7.6). The refined lattice parameters of $CaMn_{0.5}Ir_{0.5}O_{2.5}$ and the reported lattice parameters of $CaMn_{0.5}Ir_{0.5}O_3$ are given in Table 7.7 alongside the lattice parameters of a number of other parent oxides and their metastable reduced oxides.

Compound	a (Å)	b (Å)	c (Å)	V (Å^3)
$CaMn_{0.5}Ir_{0.5}O_3$*	5.350	7.714	5.404	223.06
$CaMn_{0.5}Ir_{0.5}O_{2.5}$	5.4160(7)	7.6268(7)	5.3892(6)	222.61(5)
$CaMnO_3$[125]	5.2771(10)	7.4403(14)	5.2616(11)	206.59
$CaMnO_{2.5}$[2]	5.43(1)	10.24(1)	3.74(1)	207.96
$SrFeO_3$[116]	3.851(1)	-	-	57.11
$SrFeO_{2+\delta}$[47]	3.99107(3)	3.99107(3)	3.47481(5)	55.35
$LaCoO_3$[126]	5.436(4)	5.436(4)	13.132(4)	336.06
$La_2Co_2O_5$[127]	5.4445(2)	15.8689(4)	5.6922(2)	491.80
$LaNiO_3$[#128]	5.4535(1)	5.4535(1)	13.1010(3)	337.43
La_2NiO_5[+129]	3.9193	-	-	60.20
$LaNiO_2$[42]	3.959(1)	3.959(1)	3.375(1)	52.90
$SrFe_{0.5}Ru_{0.5}O_3$[+130]	3.915	3.915	3.9386	241.80
$SrFe_{0.5}Ru_{0.5}O_2$[44]	3.9903(1)	3.9903(1)	3.4978(1)	55.69
Sr_2FeIrO_6[22]	5.54996(3)	5.57847(3)	7.84165(3)	242.78
Sr_2FeIrO_4	5.64555(8)	5.64555(8)	7.0598(2)	225.013(8)

Table 7.7: The lattice parameters of parent and reduced oxide phases. * = Errors not reported in the literature. [+] = Values are scaled to cubic values for comparison. [#] = Rhombohedral perovskite

Comparison of these lattice parameters shows that the change in parameters upon reduction to $CaMn_{0.5}Ir_{0.5}O_{2.5}$ is quite small. There is a small contraction along the "long" axis and in the square prismatic plane. This is unlike many of the other topochemical reductions published in the literature and discussed in this thesis (Chapters 4, 6 and 8) which show much larger changes in lattice parameters. Most notably the lattice parameters tend to change significantly along one axis, along which anion vacancies

order. The obvious examples are the infinite-layer phases[42, 44] in which we see a significant decrease in the *c* lattice parameter as the anion vacancies order along the *c*-axis. Another key example is the difference between $LaCoO_3$ and $La_2Co_2O_5$ in which we see a large increase in the c lattice parameter due to the layered ordering of octahedra and tetrahedra. The cause of this difference lies in the structural disorder present in $CaMn_{0.5}Ir_{0.5}O_3$ and $CaMn_{0.5}Ir_{0.5}O_{2.5}$.

The stoichiometry of $CaMn_{0.5}Ir_{0.5}O_{2.5}$ is not unusual. Isostoichiometric compounds have been shown to adopt a wide variety of anion ordered structures that reflect the coordination preferences of the cations present in the compound. The structures of $CaMnO_{2.5}$[2], $La_2Co_2O_5$[127], $La_2Cu_2O_5$[131], $La_2Ni_2O_5$[129] and $YBaCo_2O_5$[132] are shown in Figure 7.10. These structures highlight that the $A_2B_2O_5$ stoichiometry is versatile and can accommodate octahedral, tetrahedral, square planar and square pyramidal coordination geometries. To understand the structure of $CaMn_{0.5}Ir_{0.5}O_{2.5}$ we can examine the possible oxidation states of Mn and Ir in $CaMn_{0.5}Ir_{0.5}O_{2.5}$, and their preferred coordination geometries.

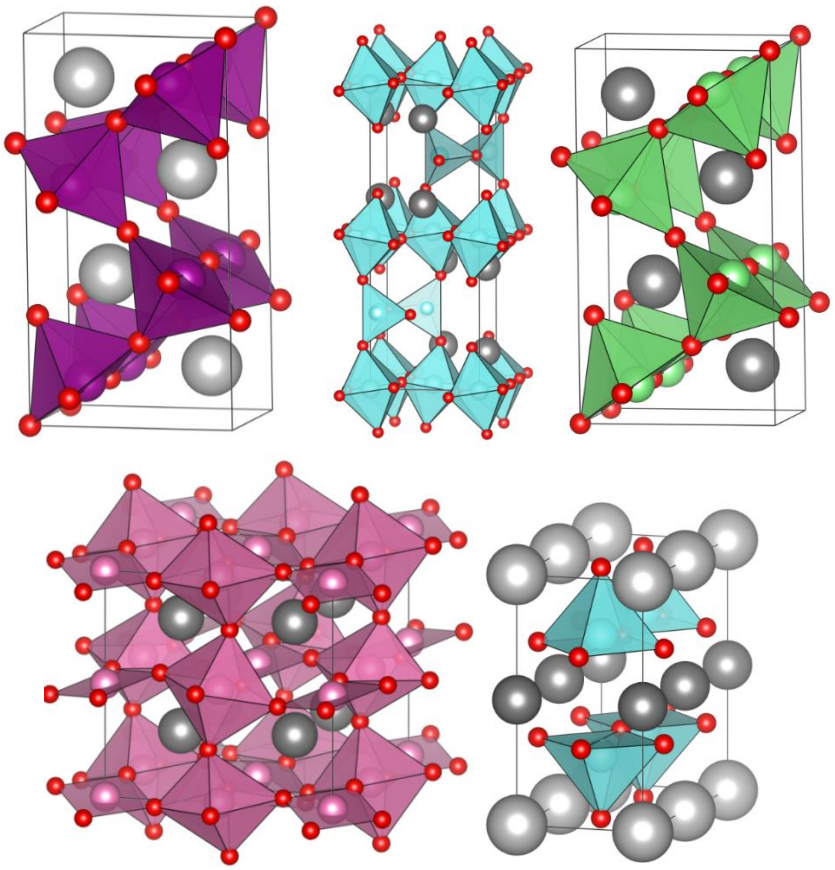

Figure 7.10: The crystal structures of $CaMnO_{2.5}$, $La_2Co_2O_5$, $La_2Cu_2O_5$, $La_2Ni_2O_5$ and $YBaCo_2O_5$

In Section 7.4.1 we suggested the oxidations states of Mn and Ir in $CaMn_{0.5}Ir_{0.5}O_{2.5}$ are Mn^{IV}/Ir^{IV}, thus $CaMn_{0.5}Ir_{0.5}O_{2.5}$ should have one of two oxidation state pairings: Mn^{II}/Ir^{IV} or Mn^{III}/Ir^{III}. The first oxidation state pairing to consider is Mn^{II}/Ir^{IV}. Mn^{II} is a high spin d^5 cation and as such has no coordination geometry preference as it will never gain ligand field stabilisation energy. Thus we would expect a compound that contains Mn^{II}/Ir^{IV} to adopt a structure that is driven by the coordination preferences of Ir^{IV} and be anion vacancy ordered. This is clearly not the case for $CaMn_{0.5}Ir_{0.5}O_{2.5}$ and would suggest that Mn^{II}/Ir^{IV} are not the oxidation states present in $CaMn_{0.5}Ir_{0.5}O_{2.5}$. The alternative is Mn^{III}/Ir^{III}. Ir^{III} is a low spin d^6 cation and therefore strongly favours octahedral coordination due to the high ligand field stabilisation energy that can be gained. To compliment six coordinate Ir^{III}, Mn^{III} would have to adopt four-coordinate geometry. The

electronic structures of Mn^{III} in a square planar coordination environment and a tetrahedral environment are shown in Figure 7.11. It isn't immediately clear that either would be particularly stable, a situation that is reinforced by the paucity of examples of either state existing in the solid state, in the case of square planar Mn no examples exist. In contrast $CaMnO_{2.5}$[2] and $Sr_3Mn_2O_{6+\delta}$[52] have structures that indicate that Mn^{III} prefers to adopt a five-coordinate square pyramidal geometry. It is clear based on electronic structure and precedent that Ir^{III} and Mn^{III} are in conflict, preferring six and five coordinate environments respectively.

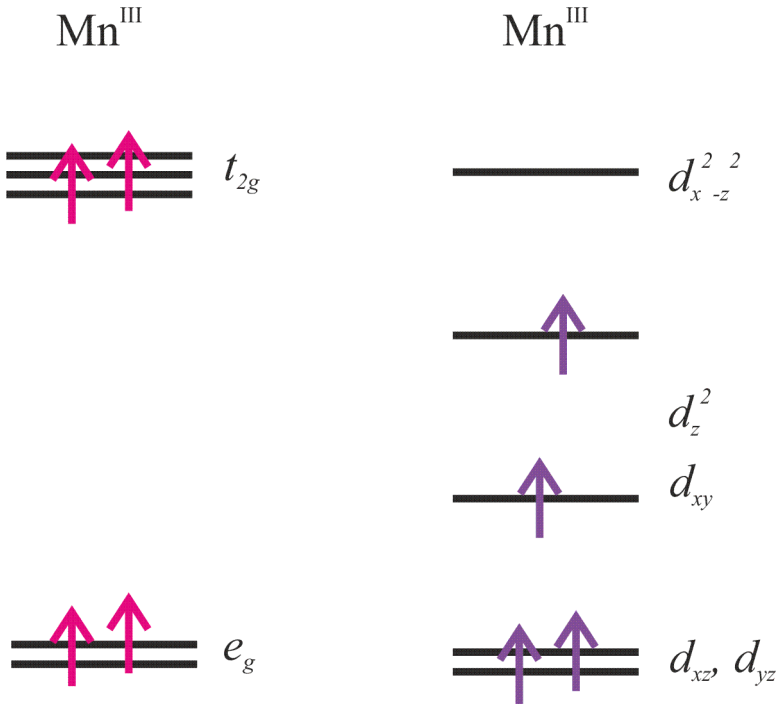

Figure 7.11: The electronic structures of tetrahedral and square pyramidal coordinated Mn^{III}

Due to the high ligand field stabilisation energy of low spin d^6 in an octahedral field one might expect the structure of $CaMn_{0.5}Ir_{0.5}O_{2.5}$ to be dominated by the coordination preference of Ir^{III}. The result of this Ir^{III} dominance would be that Mn^{III} would have a square planar or tetrahedral coordination environment. There is little precedent for manganese adopting a square planar geometry thus a $La_2Ni_2O_5$ structure is unlikely[129].

The only example of a compound that has manganese in a square planar coordination environment is $SrFe_{1-x}Mn_xO_2$ ($x \leq 0.3$)[100], however the low manganese content in this compound highlights that square planar coordinated manganese is not favourable. There are examples of Brownmillerite structures that contain manganese, most notably $La_{0.75}Ca_{0.25}MnO_{2.5}$[122] which has a *Pnma* structure that cannot exhibit charge order, therefore it must have some tetrahedrally coordinated Mn^{III}. Another possible structure in which octahedra and tetrahedra are ordered is the structure of $Ho_{0.2}Sr_{0.8}CoO_{2.75}$[133]. However the refinement of the neutron powder diffraction data collected from $CaMn_{0.5}Ir_{0.5}O_{2.5}$ clearly shows that $CaMn_{0.5}Ir_{0.5}O_{2.5}$ does not adopt a Brownmillerite structure, or any other anion ordered structure. This is because there is a key difference between the compounds shown in Figure 7.12 and $CaMn_{0.5}Ir_{0.5}O_{2.5}$. The B-cation lattice of $CaMn_{0.5}Ir_{0.5}O_{2.5}$ is not ordered. The anion ordered structures shown in Figure 7.12 require a cation lattice that has a structure that reliably repeats and propagates over a length scale much larger than that of the unit cell. This is not the case in $CaMn_{0.5}Ir_{0.5}O_{2.5}$. The disorder in $CaMn_{0.5}Ir_{0.5}O_{2.5}$ manifests as a statistical distribution of Mn and Ir across the B-sites of the sample. Thus if Ir^{III} and Mn^{III} had six and four coordinate geometries respectively there would significant strain between Ir-rich and Mn-rich areas of the sample. Furthermore, in the areas of the sample where the proportions of Ir and Mn are roughly equal but randomly distributed it is difficult to envisage a structure that maintains MO_x connectivity without moving the B-site cations to different positions in the unit cell that describes the structure. The structure extracted from refinement clearly shows that $CaMn_{0.5}Ir_{0.5}O_{2.5}$ is structurally frustrated. Our analysis suggests the combination of the cation coordination preferences and B-site cation disorder causes this frustration. To relieve this frustration a compromise must be met. The refined structure of $CaMn_{0.5}Ir_{0.5}O_{2.5}$ suggests that the compromise that is struck is that both Mn^{III} and Ir^{III} five

coordinate geometries in which the oxide vacancies are retained in the *ac*-plane. The preference of Mn^{III} to adopt a square pyramidal geometry is well established in the literature[2, 52, 123] thus it would appear the coordination preference of Mn^{III} wins out over that Ir^{III} in order to preserve the structural integrity of the compound.

7.4.2.1 Local structure of $CaMn_{0.5}Ir_{0.5}O_{2.5}$

Close inspection of the refinement of the neutron powder diffraction data collected from $CaMn_{0.5}Ir_{0.5}O_{2.5}$ highlights that the background is not flat. The rolling background of the data is an indication that $CaMn_{0.5}Ir_{0.5}O_{2.5}$ has a short-range structure that is ordered within the wider disordered structure. The existence of a localised structure would suggest that on the local level the previously discussed structural disorder is soluble. This has previously been observed in $La_{1-x}Ca_xMnO_{2+\delta}$ ($0.6 \leq x \leq 1$)[50] which has a complex structure in which the tetrahedral MnO_4 units do not order to form an anion vacancy ordered structure. The complex structure was solved using pair distribution and reverse Monte-Carlo analysis. To conduct these analyses Time of Flight neutron powder diffraction data are need, as such we are not able to use the neutron powder diffraction data collected from D2B to determine the local anion order of $CaMn_{0.5}Ir_{0.5}O_{2.5}$. However as per the discussion in Section 7.4.2 the geometries of the Mn and Ir cations are likely square pyramidal so we can posit that the structure is likely a disordered version of the compositionally-related $CaMnO_{2.5}$ structure.

The structural analysis we have conducted suggests that $CaMn_{0.5}Ir_{0.5}O_{2.5}$ has a structure similar to that of $CaMnO_{2.5}$, but why aren't the anion vacancies ordered in $CaMn_{0.5}Ir_{0.5}O_{2.5}$? Clearly the main difference between these compounds is the presence of iridium on the B-site. In Section 7.4.2 we established that the Ir^{III} in $CaMn_{0.5}Ir_{0.5}O_{2.5}$ strongly favours octahedral coordination geometry due to the high ligand field

stabilisation energy it will gain. However this is not possible so it is forced to adopt a square pyramidal geometry. In order to retain as much ligand field stabilisation energy as possible the Ir^{III} cations will favour a highly symmetric square pyramid in which bonds are of equal lengths such that the e_g orbital manifold is minimally split. The bond lengths and angles of the MnO_5 square pyramidal units in $CaMnO_{2.5}$ are shown in table 7.8.

Oxide Anion	Mn-O(n) Bond Length (Å)
O(1)	1 .883(5)
O(2)	2.093(88)
O(3)	1.927(4)

Table 7.8: The reported Mn-O bond lengths from $CaMnO_{2.5}$[2]

The structure of $CaMnO_{2.5}$ is set up to the Mn-O(2) bond is the "apical" bond, that is it is the point of the pyramid. The bond lengths in Table 7.8 clearly show that this apical bond is elongated in the MnO_5 unit. Once again this puts the Mn and Ir in conflict: the Mn square pyramid favours an elongated apical bond, as expects, whereas the Ir square pyramid favours a shorter apical bond. If there were B-site cation order in $CaMn_{0.5}Ir_{0.5}O_{2.5}$ this conflict could be resolved by a cooperative distortion that would allow the lattice to twist to accommodate these bond preferences. However, $CaMn_{0.5}Ir_{0.5}O_{2.5}$ is disordered. This means that the conflict in bond lengths will lead to a build-up in structural strain in the sample, we will refer to this strain as bond strain. One way in which the bond strain in the system can be reduced in by breaking the structure into smaller domains, thus minimising the number of bonds that are strained. However in each domain the apical bonds can orient themselves in one of 4 directions, none of which is preferred over another. Consequently each of the domains will have one of four possible ordered structures. As there is no way the structure of one domain can affect another, all four will be present in the sample. A cartoon depiction of this is shown in

Figure 7.12. This would explain the rolling background in the neutron diffraction data collected from $CaMn_{0.5}Ir_{0.5}O_{2.5}$.

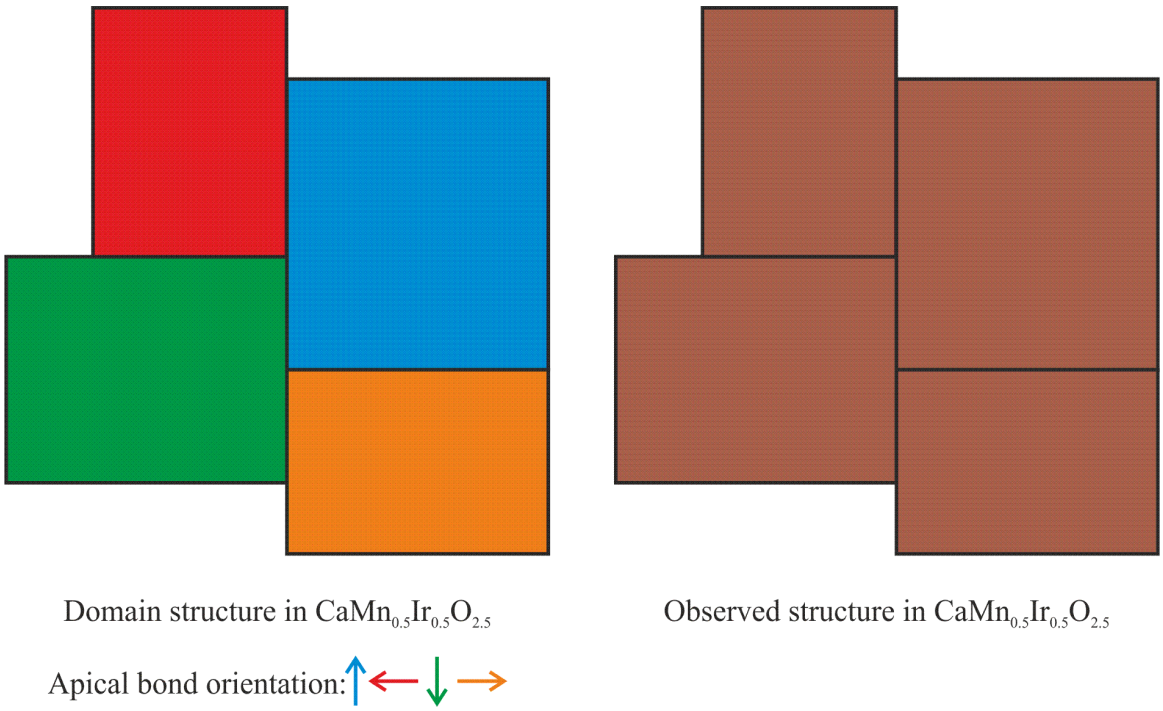

Figure 7.12: The proposed microstructure of $CaMn_{0.5}Ir_{0.5}O_{2.5}$ and the observed structure of $CaMn_{0.5}Ir_{0.5}O_{2.5}$

7.4.2.2 The prevalence of Ir^{III}

The structural analysis discussed previously in this section clearly suggests that Mn and Ir both have oxidation states of III in $CaMn_{0.5}Ir_{0.5}O_{2.5}$. Mn^{III} has previously been observed as the sole cation in the topochemically reduced oxides $CaMnO_{2.5}$[2] and $Sr_3Mn_2O_{6+\delta}$[52], and in other topochemically reduced oxides as part of mixed valent systems[122]. In contrast the existence of Ir^{III} is not as well established in the literature. A study by D. Weber *et al.*[134] reports the synthesis and characterisation of $K_{0.75}Na_{0.25}IrO_2$ and IrOOH which are layered oxides that are purported to contain Ir^{III}. However to date there are no reports in the literature that claim the existence of Ir^{III} in a topochemically reduced oxide. As such, $CaMn_{0.5}Ir_{0.5}O_{2.5}$ is the third example of a topochemically reduced oxide, as presented in

this thesis, and the first to contain Ir^{III}. Furthermore $CaMn_{0.5}Ir_{0.5}O_{2.5}$ is the first example of an extended oxide phase that contains Ir^{III} in square pyramidal coordination geometry.

7.4.3 Magnetic behaviour of $CaMn_{0.5}Ir_{0.5}O_{2.5}$

The magnetisation data presented in Section 7.3.3.1 clearly indicate that $CaMn_{0.5}Ir_{0.5}O_{2.5}$ undergoes a transition at 110 K to either a canted antiferromagnetic state or a spin glass state. The neutron diffraction data collected from $CaMn_{0.5}Ir_{0.5}O_{2.5}$ at 5 K do not exhibit additional peaks, as shown in Section 7.3.2.2. This proves $CaMn_{0.5}Ir_{0.5}O_{2.5}$ adopts a spin glass state. For a compound to adopt a spin glass state there are two criteria: the spins in the system must be frustrated and there must be disorder in the system. If we examine the structure of $CaMn_{0.5}Ir_{0.5}O_{2.5}$ we can clearly see why $CaMn_{0.5}Ir_{0.5}O_{2.5}$ adopts a spin glass state. The structure of $CaMn_{0.5}Ir_{0.5}O_{2.5}$ (Section 7.4.2) is highly disordered. Not only are the B-site cation sites are disordered, a feature inherited from $CaMn_{0.5}Ir_{0.5}O_3$, but the oxide lattice is also disordered. The disorder accounts for the second criterion that leads to a spin glass state but doesn't explain if the spins in the system are frustrated. In Section 7.4.2.1 we suggested the short range structure of $CaMn_{0.5}Ir_{0.5}O_{2.5}$ resembles the structure of $CaMnO_{2.5}$. Figure 7.13 shows the electronic configurations of Mn^{III} and Ir^{III} in square pyramidal coordination. The dominant superexchange interactions in this system are the d_z^2 - $d_{x^2-y^2}$ and the $d_{x^2-y^2}$- $d_{x^2-y^2}$ interactions. The diagram in Figure 7.14 shows that for Mn - Mn coupling the d_z^2 - $d_{x^2-y^2}$ exchange is ferromagnetic and the $d_{x^2-y^2}$- $d_{x^2-y^2}$ exchange is antiferromagnetic. These couplings lead to an antiferromagnetic state, part of which is shown in Figure 7.15. In contrast both the d_z^2 - $d_{x^2-y^2}$ and the $d_{x^2-y^2}$- $d_{x^2-y^2}$ superexchange interactions for Mn – Ir coupling are antiferromagnetic. This is the source of the frustration in $CaMn_{0.5}Ir_{0.5}O_{2.5}$. Replacement of a Mn cation with an Ir cation results in a change in the coupling regime. The ferromagnetic couplings become antiferromagnetic couplings. This change results in a regime that cannot be resolved as 2 of the sites

neighbouring the substituted sit have spins that have an opposing orientation to the third site but all sites have the same, antiferromagnetic superexchange couplings. This is a very clearly frustrated set up that, combined with the chemical disorder, would lead to a spin glass state.

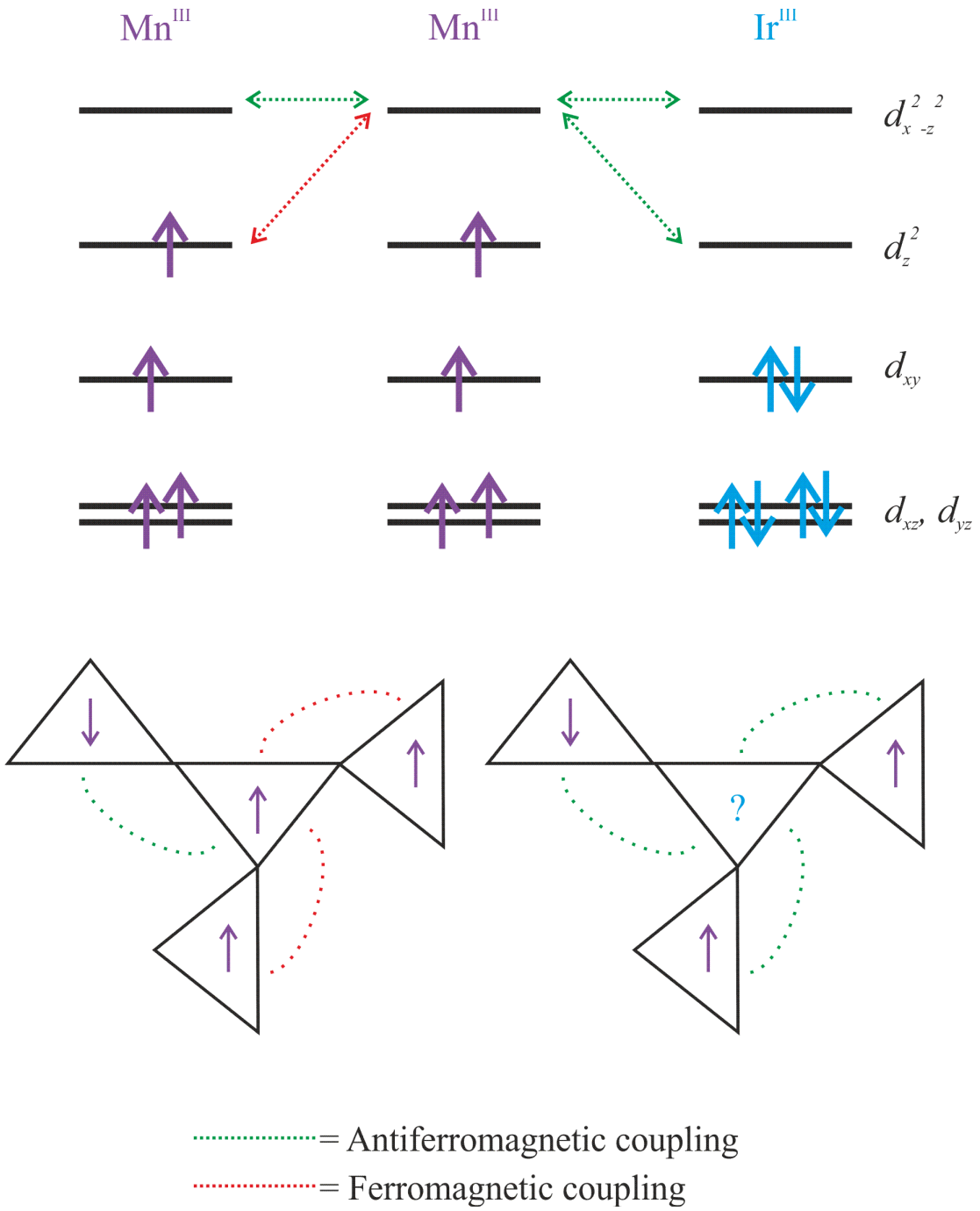

Figure 7.13: a) The electronic states on Mn^{III} and Ir^{III} in square pyramidal coordination geometries. b) The local couplings of a MnO_5 site that lead to an antiferromagnetic state. c) The local couplings of an Ir substituted site that lead to frustration.

7.5 Conclusions

The reaction of $CaMn_{0.5}Ir_{0.5}O_3$ with NaH via a getter style reaction results in the formation of an oxide-deficient phase. Compositional analysis suggests this phase is $CaMn_{0.5}Ir_{0.5}O_{2.5}$. Refinement of synchrotron X-ray diffraction data initially suggested that $CaMn_{0.5}Ir_{0.5}O_{2.5}$ had a structure with cubic symmetry however neutron powder diffraction data showed that it has orthorhombic symmetry. The structure of $CaMn_{0.5}Ir_{0.5}O_{2.5}$ is an oxide-deficient perovskite structure with B-site cation disorder in which the oxide vacancies are statistically distributed in the *ac*-plane. Comparison of $CaMn_{0.5}Ir_{0.5}O_{2.5}$ with other related compounds suggests that the oxidation states of Mn and Ir are both III, making this the first example of Ir^{III} in a topochemically reduced oxide phase. Further analysis of the structure of $CaMn_{0.5}Ir_{0.5}O_{2.5}$ suggests that its anion lattice can be regarded as a disordered arrangement of corner-sharing square pyramidal units as opposed to an ordered array of vertex-sharing 6-coordinate and 4-coordinate units. Magnetisation data collected from $CaMn_{0.5}Ir_{0.5}O_{2.5}$ suggest $CaMn_{0.5}Ir_{0.5}O_{2.5}$ undergoes a transition to a spin glass state at 110 K.

Chapter 8 – Synthesis and Characterisation of $La_xSr_{2-x}Co_{0.5}Ir_{0.5}O_4$ (x = 0, 0.5)

8.1 Introduction

In recent years oxides that adopt the Ruddlesden-Popper structures have been shown to be excellent parent phases from which reduced phases can be synthesised. The reduction of Ruddlesden-Popper phases have been highly successful resulting in a variety of metastable reduced phases that include Sr_2FeO_3[99], $Sr_2Fe_{0.5}Ru_{0.5}O_{3+\delta}$[46], $Sr_3FeRuO_{5+\delta}$[46], $LaSrCoO_3H_{0.7}$[58] and $LaSr_3NiRuO_4H_4$[59]. Furthermore, as outlined in Chapter 6 of this thesis, investigation into the topochemical reduction of iridium containing oxides has successfully been expanded to include the *n* = 1 Ruddlesden-Popper phase $Sr_2Fe_{0.5}Ir_{0.5}O_4$.

Building on these findings the work presented in this thesis was extended to include the cobalt and iridium containing Ruddlesden-Popper phases. To this end the *n* = 1 Ruddlesden-Popper phases $La_xSr_{2-x}Co_{0.5}Ir_{0.5}O_4$ (x = 0, 0.5) were synthesised and fully characterised. Synthesis of these phases was vital to expand the otherwise narrow pool of parent phases that contain iridium that are stable enough to reduce.

8.2 Synthesis

8.2.1 Synthesis of $La_xSr_{2-x}Co_{0.5}Ir_{0.5}O_4$ (x = 0, 0.5)

A sample of $La_xSr_{2-x}Co_{0.5}Ir_{0.5}O_4$ (x = 0, 0.5) was prepared using a citrate gel method. Appropriate quantities of $SrCO_3$ (99.994%), La_2O_3 (99.999%) and Co (99.996%) were dissolved in a minimal quantity of a 1:1 mixture of conc. nitric acid and distilled water, then the required amount of IrO_2 (99.99%, dried at 700 ^oC for 2 hours) was added. Citric acid and analar ethylene glycol were added and the solution was heated whilst being

stirred. The gel thus formed was allowed to dry and then combust in air. The subsequent product was ground into a fine powder, placed in an alumina crucible and heated at 1000 ^{o}C in air at a rate of 1 ^{o}C min^{-1} to remove the organic components of the sample. The resulting powder was pressed into a 13 mm diameter pellet. The pellet $Sr_2Co_{0.5}Ir_{0.5}O_4$ was heated at 1000 ^{o}C for 2 cycles of 2 days and the $La_{0.5}Sr_{1.5}Co_{1.5}Co_{0.5}Ir_{0.5}O_4$ pellet was heated at 1300 ^{o}C for two cycles of 2 days.

The resulting powders were observed to be phase-pure by laboratory X-ray powder diffraction which could be indexed using CMPR[78] using lattice parameters detailed in Table 8.1. No additional peaks associated with a supercell were detected indicating there is not a larger until cell that incorporates structural distortions or B-site cation order.

Compound	a (Å)	c (Å)
$Sr_2Co_{0.5}Ir_{0.5}O_4$	3.93	12.5
$La_{0.5}Co_{1.5}Co_{0.5}Ir_{0.5}O_4$	3.90	12.6

Table 8.1: Lattice parameters of $La_xSr_{2-x}Co_{0.5}Ir_{0.5}O_4$ (x = 0, 0.5) extracted from CMPR

8.3 Results

8.3.1 Structural characterisation of $La_xSr_{2-x}Co_{0.5}Ir_{0.5}O_4$ (x = 0, 0.5)

8.3.1.1 Synchrotron powder X-ray diffraction data

High resolution powder X-ray diffraction data were collected from samples of $La_xSr_{2-x}Co_{0.5}Ir_{0.5}O_4$ (x = 0, 0.5) using instrument I11 at the Diamond Light Source (Chapter 2, Section 2.7.1.2). Owing to the similarities in lattice parameters and composition of $Sr_2Fe_{0.5}Ru_{0.5}O_4$ and $La_xSr_{2-x}Co_{0.5}Ir_{0.5}O_4$ (x = 0, 0.5) structural models based on that of $Sr_2Fe_{0.5}Ru_{0.5}O_4$ with *I4/mmm* symmetry was constructed and refined against the synchrotron powder X-ray diffraction data. The unit cell of the model is shown in Figure 8.1. The refinements converged to give good statistical fits. The observed, calculated and difference plots for the refinements are shown in Figures 8.2 and 8.3.

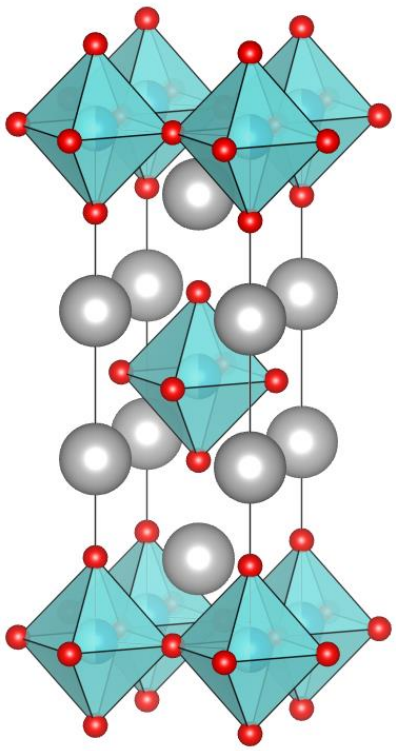

Figure 8.1: The structural unit cell of $La_xSr_{2-x}Co_{0.5}Ir_{0.5}O_4$ (x = 0, 0.5) with *I4/mmm* space symmetry. The light blue and dark blue spheres are cobalt and iridium respectively.

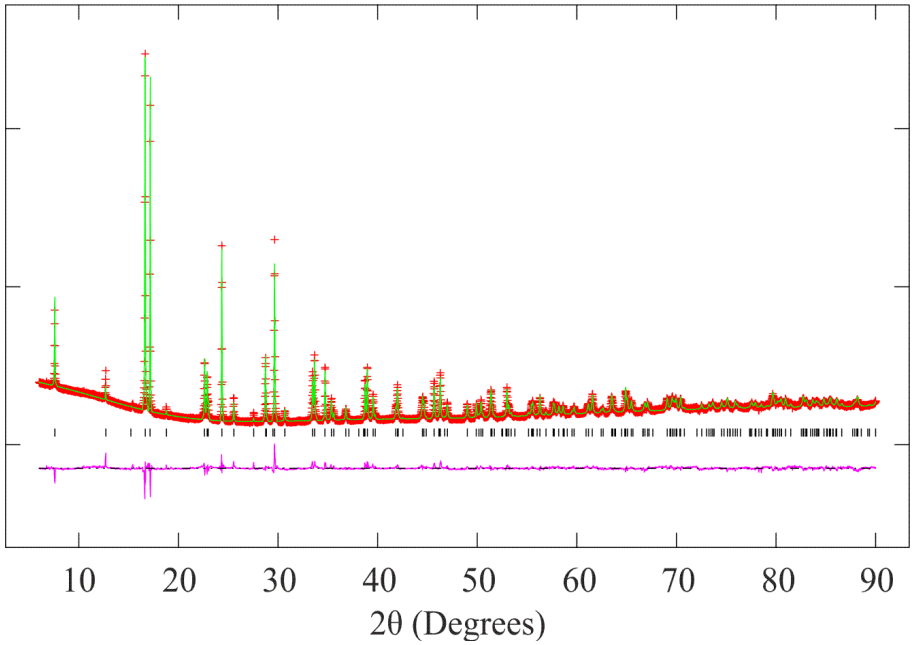

Figure 8.2: Observed, calculated and difference plots from the refinement of the *I4/mmm* structural model of $Sr_2Co_{0.5}Ir_{0.5}O_4$ against synchrotron powder diffraction data collected at room temperature using the I11 instrument.
χ^2 = 11.78, wR_p = 2.39% and R_p = 1.65%; *a* = *b* = 3.91987(2) Å, *c* = 12.4997(1) Å

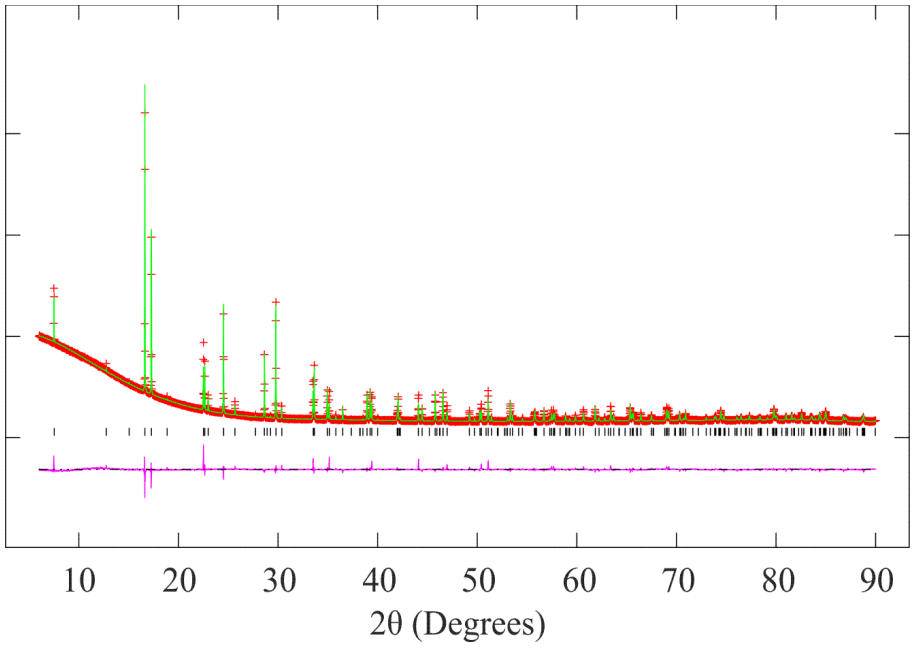

Figure 8.3: Observed, calculated and difference plots from the refinement of the *I4/mmm* structural model of $La_{0.5}Sr_{1.5}Co_{0.5}Ir_{0.5}O_4$ against synchrotron powder diffraction data collected at room temperature using the I11 instrument.
χ^2 = 19.20, wR_p = 4.43% and R_p = 2.79%; *a* = *b* = 3.88737(1) Å, *c* = 12.61233(4) Å

8.3.1.2 Neutron powder diffraction data

Neutron powder diffraction data were collected from samples of $La_xSr_{2-x}Co_{0.5}Ir_{0.5}O_4$ (x = 0, 0.5) using the D2B instrument at the ILL (Chapter 2, Section 2.7.1.2) at room temperature. The data collected at room temperature could be fully indexed using CMPR[78] using the same lattice parameters extracted from the refinement of the synchrotron powder diffraction data. The same *I*4/*mmm* model shown in Figure 8.1 were refined against the neutron powder diffraction data collected at room temperature to give an excellent statistical fit. The observed, calculated and difference plot for the refinements are shown in Figures 8.4 and 8.5 and full details of the structural parameters are given in Tables 8.2 and 8.3. Selected bond lengths extracted from the refinements of the room temperature data are given in Table 8.2. The results extracted from the refinement of $Sr_2Co_{0.5}Ir_{0.5}O_4$ are consistent with those reported in the literature[82].

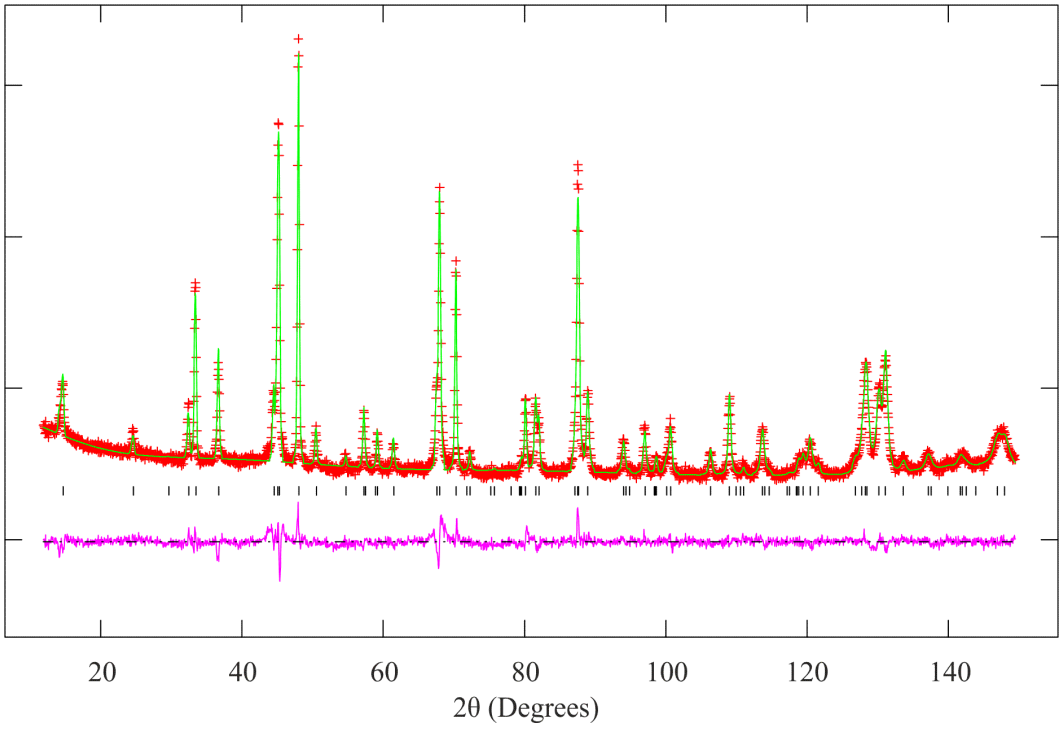

Figure 8.4: Observed, calculated and difference plots from the of the *I*4/*mmm* structural model of $Sr_2Co_{0.5}Ir_{0.5}O_4$ against the neutron powder diffraction data collected at room temperature using the D2B instrument.

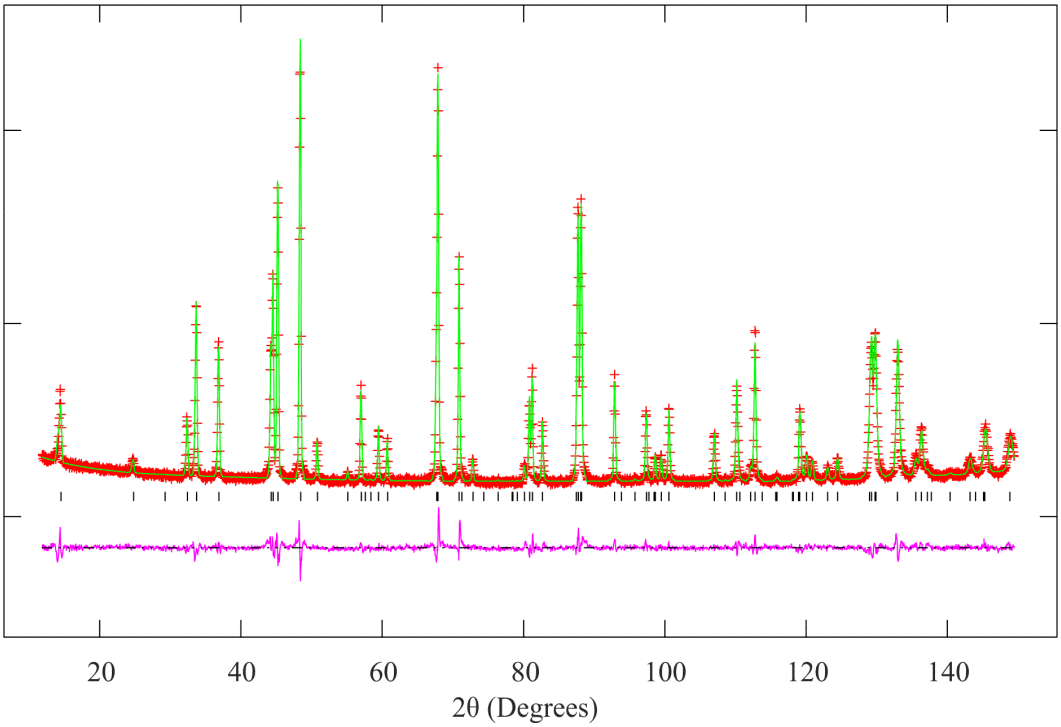

Figure 8.5: Observed, calculated and difference plots from the of the *I*4/*mmm* structural model of $La_{0.5}Sr_{1.5}Co_{0.5}Ir_{0.5}O_4$ against the neutron powder diffraction data collected at room temperature using the D2B instrument.

Atom	site	*x*	*y*	*z*	Fraction	U_{11} (Å^2)	U_{22} (Å^2)	U_{33} (Å^2)
Sr	4*e*	0	0	0.3562(1)	1	0.0028(6)	0.0028(6)	0.002(1)
Co/Ir	2*a*	0	0	0	0.5/0.5	0.0012(1)	0.0012(1)	0.011(1)
O(1)	4*e*	0	0	0.1604(2)	1	0.0095(6)	0.0095(6)	0.00052(1)
O(2)	4*c*	0	½	0	1	0.0095(6)	0.004(1)	0.00052(1)
$Sr_2Co_{0.5}Ir_{0.5}O_4$ - Space Group: *I*4/*mmm* (#139) Formula weight = 364.815 g mol^{-1} *a* = *b* =3.9173(1) Å, *c* = 12.4826(5) Å, volume = 191.55(1) Å^3								
Radiation source: Constant wavelength, λ = 1.54 Å Temperature: Room temperature χ^2 = 2.743; *wRp* = 4.62%; *Rp* = 3.51%.								

Table 8.2: Parameters from the structural refinement of $Sr_2Co_{0.5}Ir_{0.5}O_4$ against neutron powder diffraction data collected at room temperature.

Atom	site	*x*	*y*	*z*	Fraction	U_{11} (Å^2)	U_{22} (Å^2)	U_{33} (Å^2)
Sr/La	4*e*	0	0	0.35678(9)	0.75/0.25	0.0073(4)	0.0073(4)	0.00059(1)
Co/Ir	2*a*	0	0	0	0.5/0.5	0.0031(5)	0.0031(5)	0.0036(1)
O(1)	4*e*	0	0	0.1647(1)	1	0.0138(3)	0.0138(3)	0.0056(5)
O(2)	4*c*	0	½	0	1	0.0138(3)	0.0040(6)	0.0056(5)
$La_{0.5}Sr_{1.5}Co_{0.5}Ir_{0.5}O_4$ - Space Group: *I*4/*mmm* (#139) Formula weight = 390.46 g mol^{-1} *a* = *b* =3.88892(5) Å, *c* = 12.6166(2) Å, volume = 190.811(7) Å^3								
Radiation source: Constant wavelength, λ = 1.54 Å Temperature: Room temperature χ^2 = 3.233; *wRp* = 4.86%; *Rp* = 3.72%.								

Table 8.3: Parameters from the structural refinement of $La_{0.5}Sr_{1.5}Co_{0.5}Ir_{0.5}O_4$ against neutron powder diffraction data collected at room temperature.

		Bond lengths (Å)	
Compound	Temperature	M-O(1)	M-O(2)
$Sr_2Co_{0.5}Ir_{0.5}O_4$	Room Temperature	2.004(2)	1.95870(6)
$La_{0.5}Sr_{1.5}Co_{0.5}Ir_{0.5}O_4$	Room Temperature	2.078(1)	1.94446(3)
	5 K	2.068(1)	1.93897(3)

Table 8.4: Selected bonds length from the refined structures of $La_xSr_{2-x}Co_{0.5}Ir_{0.5}O_4$ (x = 0, 0.5) at room temperature and 5 K

8.3.2 Magnetic characterisation of $La_xSr_{2-x}Co_{0.5}Ir_{0.5}O_4$ (x =0, 0.5)

8.3.2.1 SQUID Magnetometry

Magnetisation data were collected from a samples of $La_xSr_{2-x}Co_{0.5}Ir_{0.5}O_4$ (x = 0, 0.5) in an applied field of 100 Oe in the temperature range $5 \leq T / K \leq 300$. The zero-field cooled (ZFC) and field cooled (FC) data and magnetisation-field isotherms collected at 300 K and 5 K are shown in Figure 8.6. For $La_{0.5}Sr_{1.5}Co_{0.5}Ir_{0.5}O_4$, at temperatures above 170 K the zero-field cooled and field cooled measurements are convergent however neither data set could fit to the Curie-Weiss law, even with a large temperature independent parameter. At temperatures below 170 K the zero-field cooled and field cooled measurements are divergent and the ZFC measurement reaches a local maximum at 15 K. For $Sr_2Co_{0.5}Ir_{0.5}O_4$, at temperatures above 45 K the zero-field-cooled and field-cooled

measurements are convergent however neither data set could fit to the Curie-Weiss law, even with a large temperature independent parameter. At temperatures below 170 K the zero-field cooled and field cooled measurements are divergent and the ZFC measurement reaches a local maximum at 45 K. The magnetisation isotherms collected at 300 K show no hysteresis clearly showing that divergence in the data collected from both samples is not due to the presence of a ferromagnetic impurity, such as elemental cobalt. The magnetisation isotherm collected from $La_{0.5}Sr_{1.5}Co_{0.5}Ir_{0.5}O_4$ at 5 K after field-cooling the sample shows a small amount of hysteresis, indicating that $La_{0.5}Sr_{1.5}Co_{0.5}Ir_{0.5}O_4$ undergoes a transition to a magnetically ordered state at 15 K. Similarly the magnetisation isotherm collected from $Sr_2Co_{0.5}Ir_{0.5}O_4$ at 5 K after field-cooling the sample shows a small amount of hysteresis, however it is also displaced indicating it adopts a spin glass state.

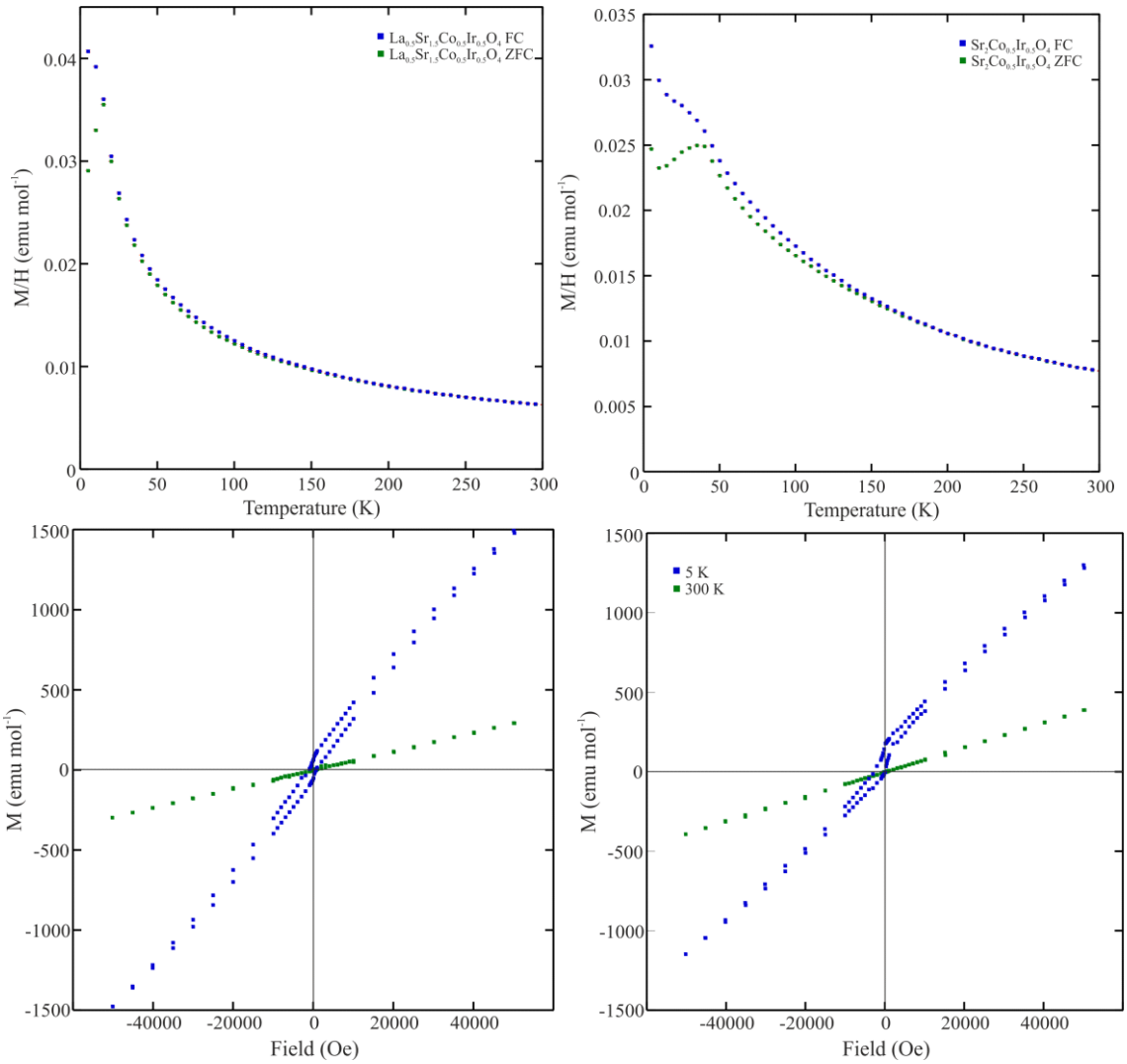

Figure 8.6: Zero-field cooled and field-cooled magnetisation data collected from $La_{0.5}Sr_{1.5}Co_{0.5}Ir_{0.5}O_4$ (Top left) and $Sr_2Co_{0.5}Ir_{0.5}O_4$ (Top right). Magnetisation-field isotherms collected from $La_{0.5}Sr_{1.5}Co_{0.5}Ir_{0.5}O_4$ (Bottom left) and $Sr_2Co_{0.5}Ir_{0.5}O_4$ (Bottom right)

8.3.2.2 Low temperature neutron diffraction data

Comparison of the neutron diffraction data collected from $La_{0.5}Sr_{1.5}Fe0_{.5}Ir_{0.5}O_4$ at room temperature and 5 K did not reveal the presence of additional diffraction peaks that could not be attributed to the closed-circuit refrigeration system in which the sample was cooled. Furthermore refinement of simple ferromagnetic unit cells against the data collected at 5 K did not converge. These results indicate $La_{0.5}Sr_{1.5}Fe_{0.5}Ir_{0.5}O_4$ does not have a magnetically ordered state that can be detected by diffraction. The observed,

calculated and difference plot for the refinement is shown in Figure 8.7 and full details of the structural parameters are given in Table 8.5.

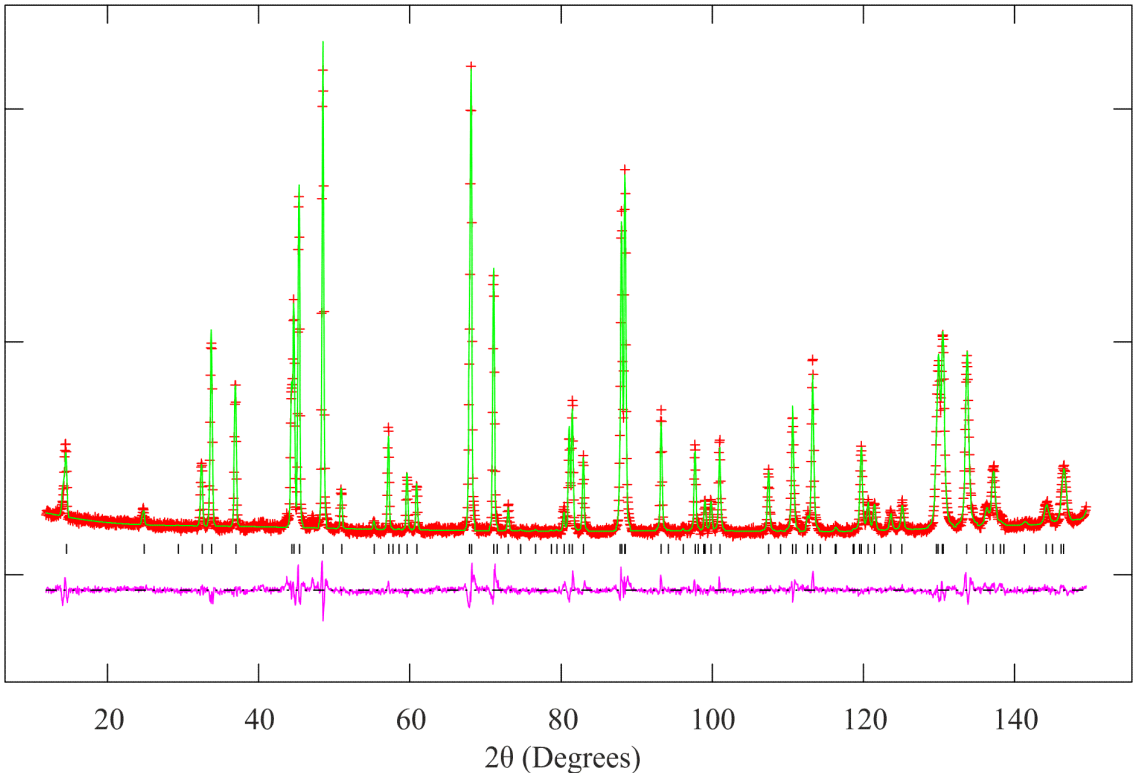

Figure 8.7: Observed, calculated and difference plots from the of the *I*4/*mmm* structural model of $La_{0.5}Sr_{1.5}Co_{0.5}Ir_{0.5}O_4$ against the neutron powder diffraction data collected at 5 K using the D2B instrument.

Atom	site	*x*	*y*	*z*	Fraction	U_{11} (Å^2)	U_{22} (Å^2)	U_{33} (Å^2)
Sr/La	4*e*	0	0	0.3573(1)	0.75/0.25	0.0017(4)	0.0017(4)	0.0015(1)
Co/Ir	2*a*	0	0	0	0.5/0.5	0.0026(5)	0.0026(5)	0.005(1)
O(1)	4*e*	0	0	0.1644(1)	1	0.0094(4)	0.0094(4)	0.0004(5)
O(2)	4*c*	0	½	0	1	0.0094(4)	0.0043(7)	0.0043(5)
$La_{0.5}Sr_{1.5}Co_{0.5}Ir_{0.5}O_4$ - Space Group: *I*4/*mmm* (#139) Formula weight = 390.46 g mol^{-1} *a* = *b* =3.87794(6) Å, *c* = 12.5766(2) Å, volume = 189.133(9) Å^3								
Radiation source: Constant wavelength, λ = 1.54 Å Temperature: 5K χ^2 = 3.544; *wRp* = 5.08%; *Rp* = 3.92%.								

Table 8.5: Parameters from the structural refinement of $La_{0.5}Sr_{1.5}Co_{0.5}Ir_{0.5}O_4$ against neutron powder diffraction data collected at 5 K.

8.4 Discussion

8.4.1 Structure of $La_xSr_{2-x}Co_{0.5}Ir_{0.5}O_4$ (x = 0, 0.5)

The refinement of synchrotron X-ray powder diffraction data and neutron powder diffraction collected from $La_xSr_{2-x}Co_{0.5}Ir_{0.5}O_4$ (x = 0, 0.5) (Section 8.3.1.2) show that both compounds adopt the archetypal *n* = 1 Ruddlesden-Popper structure with tetragonal *I4/mmm* space symmetry (Figure 8.1). This is consistent with the structure of $Sr_2Co_{0.5}Ir_{0.5}O_4$ reported by Mikhailova et al.[82], and the structure of $Sr_2Fe_{0.5}Ir_{0.5}O_4$ (Chapter 6). The bond lengths also show that the B-sites of $Sr_2Co_{0.5}Ir_{0.5}O_4$ and $La_{0.05}Sr_{1.5}Co_{0.5}Ir_{0.5}O_4$ have slightly different octahedral geometries. In $La_{0.5}Sr_{1.5}Co_{0.5}Ir_{0.5}O_4$ the apical bond is markedly longer than the apical bond in $Sr_2Co_{0.5}Ir_{0.5}O_4$. This can be attributed to the presence of La^{3+} in the rock salt layer. The result of this is that the charge of the B-site is reduced by one unit and, more importantly, the charge of the rock salt layer is increased. The increase in the overall charge of the rock salt layer means that the apical oxygen in $La_{0.5}Sr_{1.5}Co_{0.5}Ir_{0.5}O_4$ experiences stronger coulombic attraction towards the rock salt layer than the analogous oxygen in $Sr_2Co_{0.5}Ir_{0.5}O_4$, thus the bond is elongated. The secondary effect of this is that the planar bonds of $La_{0.5}Sr_{1.5}Co_{0.5}Ir_{0.5}O_4$ are slightly shorter than those of $Sr_2Co_{0.5}Ir_{0.5}O_4$. This occurs because as the apical oxygen is drawn away from the B-site the net charge of the site slightly increases, drawing in the planar oxide. The composition of the AO rock salt layer has previously been shown to have significant effects on the structure of Ruddlesden-Popper phases, a notable example being the structure of $La_2SrCr_2O_7$[135].

	Bond Length (Å)			*c/a* ratio
Compound	M-O(1)	M-O(2)	M-O(3)	
$SrFeO_3$[116]	1.913(14)	1.921(5)	-	1
Sr_2FeO_4[117]	1.950(9)	1.932(1)	-	3.21
Sr_2CoO_4[136]	1.898	1.994	-	3.29
$La_{0.5}Sr_{1.5}CoO_4$[136]	1.899(1)	2.005(8)	-	3.30
Sr_2FeIrO_6 (M = Fe)[22]	1.938(3)	1.950(7)	1.931(7)	1.41
Sr_2FeIrO_6 (M = Ir)[22]	2.054(3)	2.038(7)	2.067(7)	-
$Sr_2Fe_{0.5}Ir_{0.5}O_4$	2.013(1)	1.958(3)	-	3.21
Sr_2CoIrO_6 (M = Co)[80]	1.985(2)	1.971(3)	-	1.38
Sr_2CoIrO_6 (M = Ir)[80]	1.947(2)	1.948(3)	-	-
$Sr_2Co_{0.5}Ir_{0.5}O_4$	2.004(2)	1.95870(6)	-	3.19
$La_{0.5}Sr_{1.5}Co_{0.5}Ir_{0.5}O_4$	2.078(1)	1.94446(3)	-	3.24

Table 8.6: Selected bond lengths and c/a ratios from the refined structures of some Perovskite and Ruddlesden-Popper phases

8.4.2 B-site structure of $La_xSr_{2-x}Co_{0.5}Ir_{0.5}O_4$ (x = 0, 0.5)

To understand the structure and bulk properties of $La_xSr_{2-x}Co_{0.5}Ir_{0.5}O_4$ it is important to understand the structure of the B-site lattices. The conditions that lead to cation order have been discussed multiple times in this thesis as it is key to understanding the chemistry of iridium containing complex oxides. The most important factor is the difference in formal oxidation states of the B-site cations.

The B-site structure of $La_{0.5}Sr_{1.5}Co_{0.5}Ir_{0.5}O_4$ is the simplest to understand. For $La_{0.5}Sr_{1.5}Co_{0.5}Ir_{0.5}O_4$ the possible oxidation state combinations are Co^{III}/Ir^{IV} and Co^{II}/Ir^{V}. The perovskite analogue is reported to have a B-site cation structure that is ordered[81] with a cation pairing of Co^{II}/Ir^{V}. Although a perovskite and analogous Ruddlesden-Popper phase do not necessarily have to have the same cation ordering it is in indication that the Co^{II}/Ir^{V} pairing is the more likely combination. Furthermore magnetisation data, that will be discussed later suggest $La_{0.5}Sr_{1.5}Co_{0.5}Ir_{0.5}O_4$ adopts a long range magnetically ordered state, this would not be possible if the structure were disordered. Thus we can conclude

with some confidence that the B-site cations in $La_{0.5}Sr_{1.5}Co_{0.5}Ir_{0.5}O_4$ are ordered with oxidation states Co^{II}/Ir^{V}. This result suggests that $La_{0.5}Sr_{1.5}Co_{0.5}Ir_{0.5}O_4$ is paracrystalline.

$Sr_2Co_{0.5}Ir_{0.5}O_4$ appears to have a different B-site structure to that of $La_{0.5}Sr_{1.5}Co_{0.5}Ir_{0.5}O_4$. The possible oxidation states of Co and Ir in $Sr_2Co_{0.5}Ir_{0.5}O_4$ Co^{IV}/Ir^{IV} and Co^{III}/Ir^{V}. Given that the reported oxidation states for the analogous perovskite, Sr_2CoIrO_6[80], are Co^{III}/Ir^{V} and the oxidation states for $La_{0.5}Sr_{1.5}Co_{0.5}Ir_{0.5}O_4$ are most likely Co^{II}/Ir^{V} it reasonably follows that the oxidation states of $Sr_2Co_{0.5}Ir_{0.5}O_4$ are Co^{III}/Ir^{V}. The difference in charge between these cations is +2 which can be regarded as a borderline state. A difference in oxidation states of 2+ is enough to lead to cation disorder as exemplified by Sr_2RuCoO_6[137] however it does not cause disorder in Sr_2FeIrO_6 or Sr_2CoIrO_6. Given that Sr_2CoIrO_6 is B-site cation ordered we might expect $Sr_2Co_{0.5}Ir_{0.5}O_4$ to also be ordered. However as discussed in Section 6.4.1.1 the structure of a perovskite does not always transfer to its analogous Ruddlesden-Popper phase as exemplified by Sr_2FeMoO_6[119] and $Sr_2Fe_{0.5}Mo_{0.5}O_4$[120]. The key piece of evidence that breaks the tie is the magnetisation data (Figure 8.6). The magnetisation isotherm collected from $Sr_2Co_{0.5}Ir_{0.5}O_4$ at 5 K shows that at low temperatures it adopts a spin glass state. For a spin glass state to propagate there must be chemical disorder. Thus we can conclude that $Sr_2Co_{0.5}Ir_{0.5}O_4$ is a B-site disordered phase with a Co^{III}/Ir^{V} oxidation state pairing.

8.4.3 Magnetic properties of $La_xSr_{2-x}Co_{0.5}Ir_{0.5}O_4$ (x = 0, 0.5)

8.4.3.1 Magnitude of magnetic moments

The magnetisation data collected from $La_xSr_{2-x}Co_{0.5}Ir_{0.5}O_4$ (x = 0, 0.5) could not be fit to the Curie-Weiss law (Section 8.3.2.1) thus it is not possible to determine the size of the cobalt moments in both compounds. However we can qualitatively compare and contrast the moments using the magnetisation data.

We can see from the magnetisation data collected from $Sr_2Co_{0.5}Ir_{0.5}O_4$ that it is not diamagnetic. This tells us a lot about the electronic state of cobalt in this compound. The oxidation states of Co and Ir in $Sr_2Co_{0.5}Ir_{0.5}O_4$ are III and V respectively. We can be confident that Ir^V is $j_{eff} = 0$ in $Sr_2Co_{0.5}Ir_{0.5}O_4$ given that it has been observed to adopt such a state in $BaLaCoIrO_6$, yielding a type-II antiferromagnetic state[23]. This means the magnetic moment must come from the Co^{III} centres. Co^{III} is a d^6 cation and as such can adopt one of two electronic states: a low-spin S = 0 state; or a high spin S = 2 state. If it were to adopt a low spin state we would expect $Sr_2Co_{0.5}Ir_{0.5}O_4$ to be diamagnetic, which it is clearly not. Therefore it is clear that the Co^{III} in $Sr_2Co_{0.5}Ir_{0.5}O_4$ must be high spin.

Comparison of the magnetisation isotherms collected from $La_xSr_{2-x}Co_{0.5}Ir_{0.5}O_4$ (x = 0, 0.5) at 5 K shows that at 5 K both compounds have moments with very similar magnitudes, with that of $La_{0.5}Sr_{1.5}Co_{0.5}Ir_{0.5}O_4$ being larger. The magnetic cation in $Sr_2Co_{0.5}Ir_{0.5}O_4$ is high spin Co^{III} which has a S = 2 electronic state. In contrast the magnetic cation in $La_{0.5}Sr_{0.5}Co_{0.5}Ir_{0.5}O_4$ is Co^{II} which is most likely high spin and therefore has a S = 3/2 electronic state. From these states we would expect the moment of $Sr_2Co_{0.5}Ir_{0.5}O_4$ to be significantly larger than that of $La_{0.5}Sr_{1.5}Co_{0.5}Ir_{0.5}O_4$ which is clearly not the case. The reason the moments of $La_xSr_{x-2}Co_{0.5}Ir_{0.5}O_4$ (x = 0, 0.5) is because of the unquenched orbital angular momentum of the t_{2g} set in Co^{II}. The t_{2g} set of Co^{II} has a vacancy, thus the angular moment is not quenched and there is a significant orbital contribution to the magnetic moment. Co^{III} will also have an orbital component to it its moment but it is not as large, thus the ordered moments of $La_xSr_{2-x}Co_{0.5}Ir_{0.5}O_4$ (x = 0, 0.5) are similar.

8.4.3.2 Magnetic order vs spin-glass

Comparison of the magnetisation isotherms collected from $La_xSr_{2-x}Co_{0.5}Ir_{0.5}O_4$ (x = 0, 0.5) at 5 K shows that there is one significant difference. The magnetisation isotherm collected from $La_{0.5}Sr_{1.5}Co_{0.5}Ir_{0.5}O_4$ is symmetric about the origin however the magnetisation isotherm collected from $Sr_2Co_{0.5}Ir_{0.5}O_4$ is displaced from the origin (Figures 8.6). The isotherm collected from $La_{0.5}Sr_{15}Co_{0.5}Ir_{0.5}o_4$ is consistent with the onset of a canted antiferromagnetic state. In contrast the displacement of the $Sr_2Co_{0.5}Ir_{0.5}O_4$ isotherm suggests that there is a significant degree of magnetic frustration, leading to a spin-glass state. For a spin-glass to propagate two criteria must be met. Firstly there must be chemical disorder, and secondly there must be magnetic frustration. The discussion of B-site structures of $La_xSr_{2-x}Co_{0.5}Ir_{0.5}O_4$ (x = 0, 0.5) in Section 8.4.2 proves that $Sr_2Co_{0.5}Ir_{0.5}O_4$ has a B-site disordered structure. If we examine the superexchange interactions of an ordered array of Co^{III}/Ir^{V} and then introduce disorder we can if the magnetic interactions in $Sr_2Co_{0.5}Ir_{0.5}O_4$ are indeed frustrated.

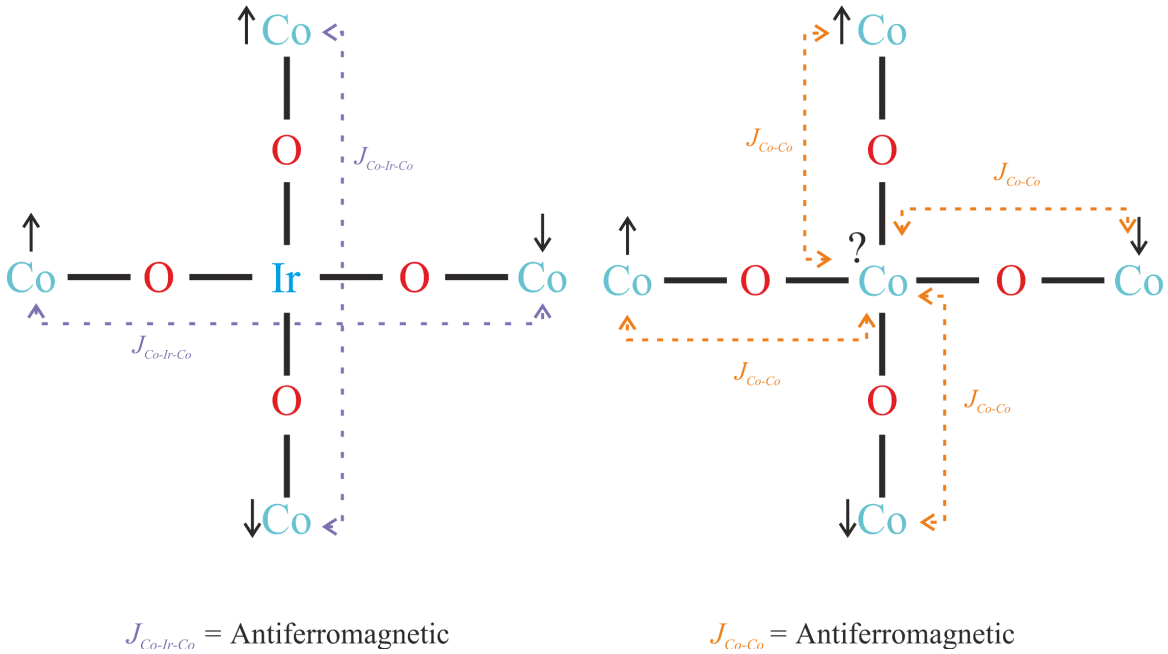

Figure 8.8: The coupling regime in $Sr_2Co_{0.5}Ir_{0.5}O_3$ and the magnetic frustration that leads to a spin glass state.

Figure 8.9 shows the superexchange interactions of an ordered array of Ir^{V} and Co^{III}. There is significant precedent to suggest Ir^{V} would adopt a $j_{eff} = 0$ state and mediate the propagation of a type-II antiferromagnetic state. Replacing the Ir^{V} centre with a Co^{III} centre changes the dominant exchange interaction from the $J_{Co\text{-}Ir\text{-}Co}$ supersuperexchange interaction to the $J_{Co\text{-}Co}$ superexchange interaction, both of which are antiferromagnetic. If we do not allow the surrounding Co spins to change we can clearly see in Figure 8.9 that the centre Co^{III} cannot satisfy all of the superexchange interactions and is thus frustrated. Given that $Sr_2Co_{0.5}Ir_{0.5}O_4$ has a disordered B-site lattice it can clearly be seen that it is magnetically frustrated, confirming the validity of its low temperature spin glass state.

8.5 Conclusions

The work presented in this chapter shows that we have successfully synthesised and reduced $La_xSr_{2-x}Co_{0.5}Ir_{0.5}O_4$ (x = 0, 0.5). Refinement of X-ray and neutron powder diffraction data show that $La_xSr_{2-x}Co_{0.5}Ir_{0.5}O_4$ (x = 0, 0.5) adopt the classic *I*4/*mmm n* = 1 Ruddlesden-Popper structure. Analysis of magnetisation data suggest the $La_{0.5}Sr_{1.5}Co_{0.5}Ir_{0.5}O_4$ adopts a canted antiferromagnetic state at low temperatures and is paracrystalline. In contrast magnetisation data collected from $Sr_2Co_{0.5}Ir_{0.5}o_4$ suggests the B-site lattice is disordered and at low temperatures it undergoes at transition to a spin glass state. Low temperature neutron diffraction data do not suggest either compound has a magnetic state detectable by diffraction.

Chapter 9 – Topochemical Reduction of $La_xSr_{2-x}Co_{0.5}Ir_{0.5}O_4$ (x = 0, 0.5)

9.1 Introduction

The work presented in previous chapters of this thesis shows that by coupling iridium with a 3*d* cation complex oxides of iridium can be reduced to form metastable phases. In Chapters 4 and 7 it has been shown that complex oxides with the perovskite structure can be reduced and in Chapter 6 it was shown that iridium oxides that adopt the $n = 1$ Ruddlesden-Popper structure can also be reduced.

Previous research has also shown that a number of cobalt containing complex oxides can be reduced to form metastable phases. The most notable examples of topochemically reduced cobalt containing oxides are $LaBaCo_2O_{4.25}$[48], $YBaCo_2O_{4.5}$[48], $LaSrCoO_3H_{0.7}$[58] and $Sr_3Co_2O_{4.33}H_{0.84}$[138].

In order to expand research into the reduction chemistry of iridium containing oxides, and that of topochemical manipulation more generally, the investigation was extended to include the reduction of the cobalt containing $n = 1$ Ruddlesden-Popper phases $La_xSr_{2-x}Co_{0.5}Ir_{0.5}O_4$ (x = 0, 0.5). The synthesis and characterisation of $La_xSr_{2-x}Co_{0.5}Ir_{0.5}O_4$ (x = 0, 0.5) is detailed in Chapter 8 of this thesis. Building on the precedent set by the work in this thesis and previous research it was possible to examine the properties of a new set of metastable phases that contain cobalt and iridium.

9.2 Synthesis

9.2.1 Synthesis of $La_xSr_{2-x}Co_{0.5}Ir_{0.5}O_{4-y}$ (x = 0, 0.5)

A full discussion pertaining to the reduction chemistry of iridium-containing oxides and the challenges this process presents, including that of $La_xSr_{2-x}Co_{0.5}Ir_{0.5}O_4$ (x = 0, 0.5), is given in Chapter 3. A sample of $La_{0.5}Sr_{1.5}Co_{0.5}Ir_{0.5}O_{4-y}$ for analysis by neutron powder diffraction was prepared by reacting approximately 1.25g of $La_{0.5}Sr_{1.5}Co_{0.5}Ir_{0.5}O_4$ with zirconium in a sealed ampule using the method described in Chapter 3, Section 3.2.5.3. The sample was heated for 10 periods of 7 days at temperatures between $450 \leq T / ^oC \leq 550$. A sample of $Sr_2Co_{1.5}Co_{0.5}Ir_{0.5}O_{4-y}$ for analysis by neutron powder diffraction was prepared by reacting approximately 1.25g of $Sr_2Co_{0.5}Ir_{0.5}O_4$ with zirconium using the method described in Chapter 3, Section 3.2.5.3. The sample was heated for 5 periods of 7 days at temperatures between $300 \leq T / ^oC \leq 320$. Between heating cycles the samples were taken into an Ar filled glovebox, without being exposed to air, and ground with an agate pestle and mortar.

9.3 Results

9.3.1 Structural characterisation of $La_xSr_{2-x}Co_{0.5}Ir_{0.5}O_{4-y}$ (x = 0, 0.5)

9.3.1.1 Thermogravimetric analysis

Oxidative thermogravimetric experiments were conducted to confirm the oxygen content of $La_xSr_{2-x}Co_{0.5}Ir_{0.5}O_{4-y}$ (x = 0, 0.5). A small quantity of each reduced sample was heated under a flow of oxygen to reform $La_xSr_{2-x}Co_{0.5}Ir_{0.5}O_4$ (x = 0, 0.5), as confirmed by X-ray powder diffraction. During this reaction the $La_{0.5}Sr_{1.5}Co_{0.5}Ir_{0.5}O_{4-y}$ sample gained 3.3875(5) % of its initial mass, an increase that is consistent with a composition of $La_{0.5}Sr_{1.5}Co_{0.5}Ir_{0.5}O_{3.17(1)}$ for the reduced phase (Figure 9.1). The $Sr_2Co_{0.5}Ir_{0.5}O_{4-y}$ sample

gained 3.60(3) % of its initial mass, an increase that is consistent with a composition of $Sr_2Co_{0.5}Ir_{0.5}O_{3.18(2)}$ for the reduced phase (Figure 9.1). From this point on the $La_xSr_{2-x}Co_{0.5}Ir_{0.5}O_{4-y}$ (x = 0, 0.5) phases will be referred to as $La_xSr_{2-x}Co_{0.5}Ir_{0.5}O_3$.

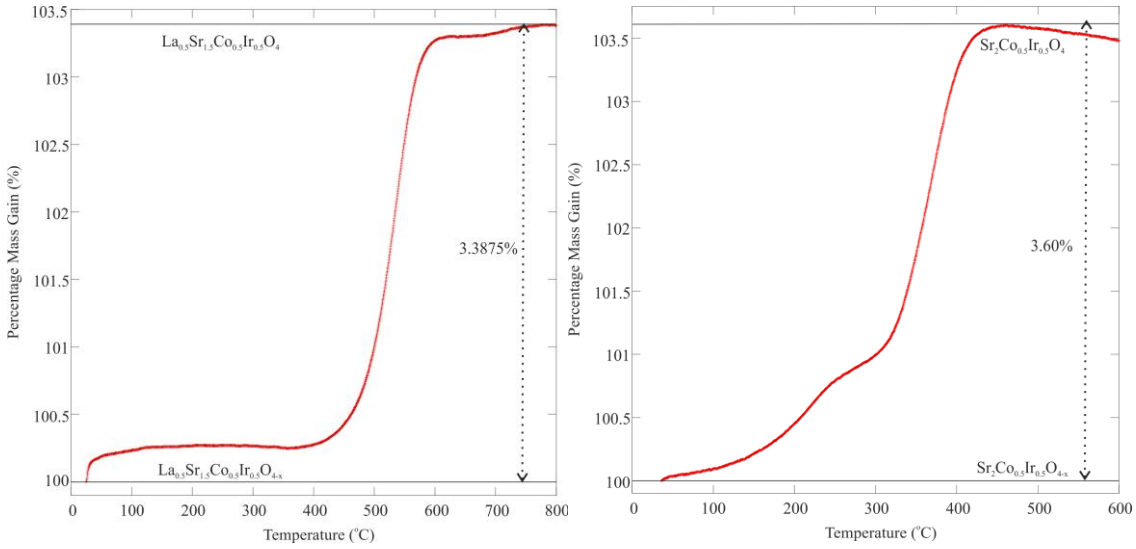

Figure 9.1: Thermogravimetric data collected during the oxidation of: Left) $La_{0.5}Sr_{1.5}Co_{0.5}Ir_{0.5}O_{4-y}$ to $La_{0.5}Sr_{1.5}Co_{0.5}Ir_{0.5}O_4$ Right) $Sr_2Co_{0.5}Ir_{0.5}O_{4-y}$ to $Sr_2Co_{0.5}Ir_{0.5}O_3$

9.3.1.2 Synchrotron X-ray powder diffraction data

High resolution powder X-ray diffraction data were collected from samples of $La_xSr_{2-x}Co_{0.5}Ir_{0.5}O_3$ (x = 0, 0.5) using instrument I11 at the Diamond Light Source (Chapter 2, Section 2.7.1.2). The diffraction patterns could be indexed to a body-centred orthorhombic unit cell. A structural model with *Immm* symmetry was constructed, based on those of Sr_2FeO_3 and $Sr_2Fe_{0.5}Ru_{0.5}O_3$, and refined against the synchrotron X-ray diffraction data. The unit cell of the model is shown in Figure 9.2 The refinement gave a good statistical fit. The observed, calculated and difference plots for the refinements are shown in Figures 9.3 and 9.4.

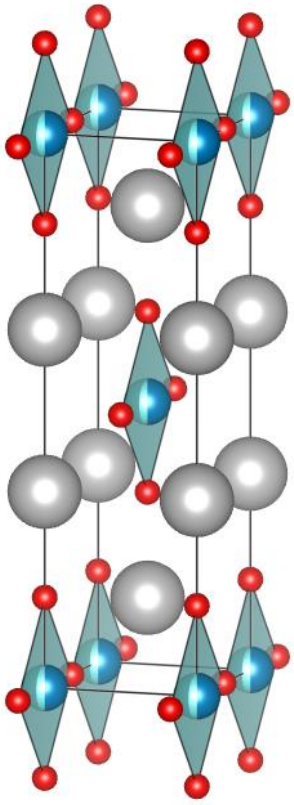

Figure 9.2: The structural unit cell of $La_xSr_{2-x}Co_{0.5}Ir_{0.5}O_3$ (x = 0, 0.5) with *Immm* space symmetry. The light blue and dark blue spheres are cobalt and iridium respectively.

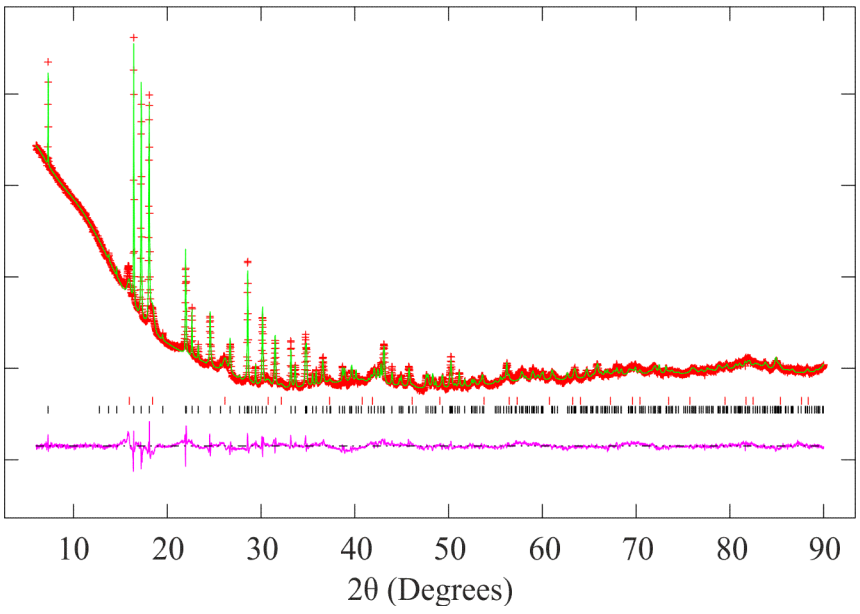

Figure 9.3: Observed, calculated and difference plots from the refinement of the *I4/mmm* structural model of $La_{0.5}Sr_{1.5}Co_{0.5}Ir_{0.5}O_3$ against synchrotron powder diffraction data collected at room temperature using the I11 instrument.
χ^2 = 12.53, wR_p = 2.28% and R_p = 1.60%; *a* = 3.87941(6) Å, b = 3.57603(6) Å, *c* = 13.0066(1) Å

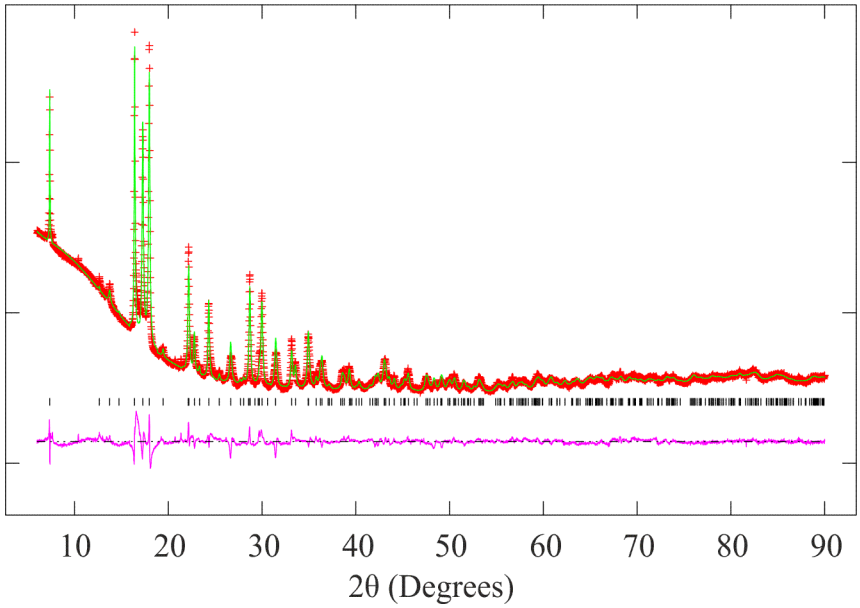

Figure 9.4: Observed, calculated and difference plots from the refinement of the *I4/mmm* structural model of $Sr_2Co_{0.5}Ir_{0.5}O_3$ against synchrotron powder diffraction data collected at room temperature using the I11 instrument.
χ^2 = 28.10, wR_p = 2.88% and R_p = 1.97%; *a* = 3.9180(1) Å, *b* = 3.5799(1) Å, *c* = 12.8656(4) Å

9.3.1.3 Neutron diffraction data

Neutron powder diffraction data were collected from samples of $La_xSr_{2-x}Co_{0.5}Ir_{0.5}O_3$ (x =, 0, 0.5) using the D2B instrument at the ILL (Chapter 2, Section 2.7.1.2) at room temperature and 5 K. The data collected from both samples at room temperature could be fully indexed using CMPR[78] to the same lattice parameters extracted from the refinement of their respective synchrotron X-ray powder diffraction data. The *Immm* model shown in Figure 9.2 was refined against the neutron powder diffraction data collected at room temperature to give good statistical fits. The observed, calculated and difference plots for the refinements are shown in Figures 9.5 and 9.6 and full details of the structural parameters are given in Tables 9.1 and 9.2. Selected bond lengths extracted from the refinements are given in Table 9.3.

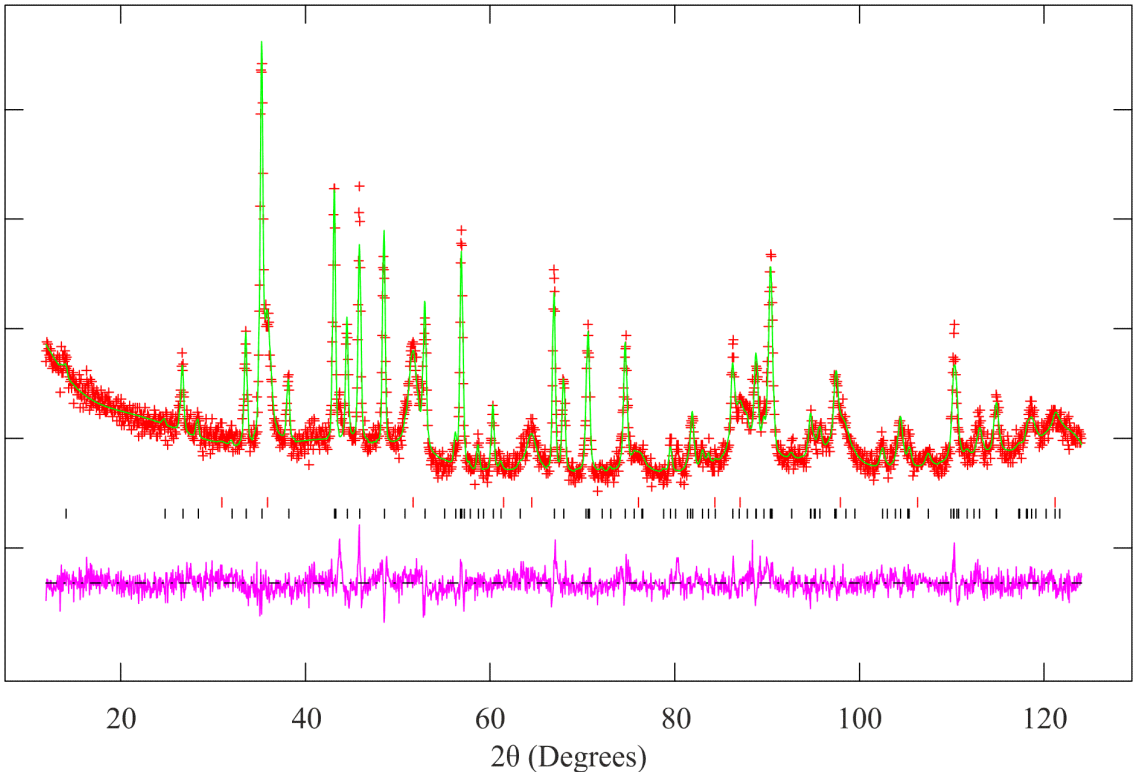

Figure 9.5: Observed, calculated and difference plots from the of the *I*4/*mmm* structural model of $La_{0.5}Sr_{1.5}Co_{0.5}Ir_{0.5}O_3$ against the neutron powder diffraction data collected at room temperature using the D2B instrument. Tick marks correspond to the following: Black = $La_{0.5}Sr_{1.5}Co_{0.5}Ir_{0.5}O_3$, Red = SrO

Atom	site	*x*	*y*	*z*	Fraction	U_{11} (Å^2)	U_{22} (Å^2)	U_{33} (Å^2)
Sr/La	4*i*	0	0	0.3542(3)	0.75/0.25	0.013(2)	0.007(1)	0.006(1)
Co/Ir	2*a*	0	0	0	0.5/0.5	0.024(5)	0.006(4)	0.001(1)
O(1)	4*i*	0	0	0.1645(4)	1	0.019(3)	0.009(3)	0.004(1)
O(2)	4*f*	½	0	0	1	0.012(4)	0.036(6)	0.003(4)
$La_{0.5}Sr_{1.5}Co_{0.5}Ir_{0.5}O_3$ - Space Group: *Immm* (#71) Formula weight = 347.275 g mol^{-1}, Weight Fraction = 76.2% *a* = 3.8799(3) Å, *b* = 3.5763(3) Å, *c* = 13.008(1) Å, volume = 180.50(4) Å^3								
Atom	site	*x*	*y*	*z*	Fraction	U_{iso} (Å^2)		
Sr	4*b*	½	½	½	1	0.002(1)		
O(1)	4*a*	0	0	0	1	0.002(1)		
SrO - Space Group: $Fm\bar{3}m$ (#225) Formula weight = 487.30 g mol^{-1}, Weight Fraction = 23.8% *a* = *b* = *c* = 5.176(1) Å, volume = 138.72(8) Å^3								
Radiation source: Constant wavelength, λ = 1.54 Å Temperature: Room Temperature χ^2 = 1.705; *wRp* = 3.86 %; *Rp* = 3.00 %								

Table 9.1: Parameters from the structural refinement of $La_{0.5}Sr_{1.5}Co_{0.5}Ir_{0.5}O_3$ against neutron powder diffraction data collected at room temperature.

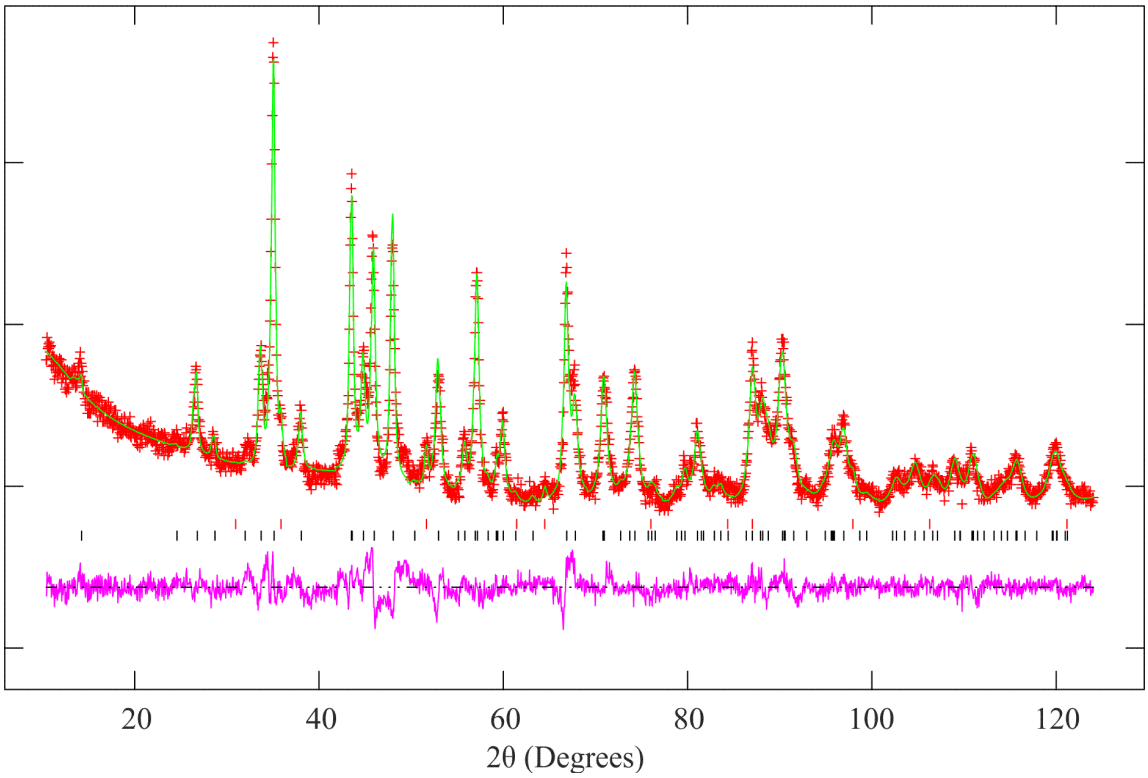

Figure 9.6: Observed, calculated and difference plots from the of the *I*4/*mmm* structural model of $Sr_2Co_{0.5}Ir_{0.5}O_3$ against the neutron powder diffraction data collected at room temperature using the D2B instrument. Tick marks correspond to the following: Black = $Sr_2Co_{0.5}Ir_{0.5}O_3$, Red = SrO

Atom	site	*x*	*y*	*z*	Fraction	U_{11} (Å^2)	U_{22} (Å^2)	U_{33} (Å^2)
Sr	4*i*	0	0	0.3531(2)	1	0.018(2)	0.027(3)	0.022(2)
Co/Ir	2*a*	0	0	0	0.5/0.5	0.015(3)	0.014 (4)	0.033(3)
O(1)	4*i*	0	0	0.1604(1)	1	0.018(2)	0.048(3)	0.036(1)
O(2)	4*f*	½	0	0	1	0.015(3)	0.070(5)	0.003(3)
$Sr_2Co_{0.5}Ir_{0.5}O_3$ - Space Group: *Immm* (#71) Formula weight = 348.815 g mol^{-1}, Weight Fraction = 98.04% *a* = 3.9170(4) Å, *b* = 3.5758(5) Å, *c* = 12.880(1) Å, volume = 180.41(5) Å^3								
Atom	site	*x*	*y*	*z*	Fraction	U_{iso}		
Sr	4*b*	½	½	½	1	0.017(7)		
O	4*a*	0	0	0	1	0.017(7)		
SrO - Space Group: $Fm\bar{3}m$ (#225) Formula weight = 487.30 g mol^{-1}, Weight Fraction = 1.96% *a* = *b* = *c* = 5.176(1) Å, volume = 138.72(8) Å^3								
Radiation source: Constant wavelength, λ = 1.54 Å Temperature: Room Temperature χ^2 = 2.615; *wRp* = 4.71 %; *Rp* = 3.64 %								

Table 9.2: Parameters from the structural refinement of $Sr_2Co_{0.5}Ir_{0.5}O_3$ against neutron powder diffraction data collected at room temperature.

Compound		Bond lengths (Å)	
	Temperature	M-O(1)	M-O(2)
$La_{0.5}Sr_{1.5}Co_{0.5}Ir_{0.5}O_3$	Room Temperature	2.141(5)	1.9399(1)
	5 K	2.141(5)	1.9363(1)
$Sr_2Co_{0.5}Ir_{0.5}O_3$	Room Temperature	2.070(5)	1.9585(2)
	5 K	2.064(4)	1.9537 (2)

Table 9.3: Selected bonds length from the refined structures of $La_xSr_{2-x}Co_{0.5}Ir_{0.5}O_3$ at room temperature and 5 K

9.3.1.3.1 Distorted structure of $La_xSr_{2-x}Co_{0.5}Ir_{0.5}O_3$ (x = 0, 0.5)

Examination of the bond lengths extracted from the refinements outlined in Section 9.3.1.3 shows they do not follow the trend one would expect. The planar bond of $Sr_2Co_{0.5}Ir_{0.5}O_3$ is roughly the same length as the same bond in $Sr_2Co_{0.5}Ir_{0.5}O_4$ and the planar bond of $La_{0.5}Sr_{1.5}Co_{0.5}Ir_{0.5}O_3$ is shorter than that of $La_{0.5}Sr_{1.5}Co_{0.5}Ir_{0.5}O_4$. Both of these results are contrary to the trends observed in the reduced products of other n = 1 Ruddlesden-Popper phases, as shown in Table 9.4. The bond lengths are calculated by measuring the distance between the B-site position and the planar oxide site. The smaller than expected bond lengths are an indication that the lattices of $La_xSr_{2-x}Co_{0.5}Ir_{0.5}O_4$ (x = 0, 0.5) are distorted.

	Bond Length (Å)	
Compound	M-O(1)	M-O(2)
$Sr_2Co_{0.5}Ir_{0.5}O_4$	2.004(2)	1.95870(6)
$Sr_2Co_{0.5}Ir_{0.5}O_3$	2.070(5)	1.9585(2)
$La_{0.5}Sr_{1.5}Co_{0.5}Ir_{0.5}O_4$	2.078(1)	1.94446(3)
$La_{0.5}Sr_{1.5}Co_{0.5}Ir_{0.5}O_3$	2.141(5)	1.9399(1)
$Sr_2Fe_{0.5}Ru_{0.5}O_4$[118]	2.009	1.951
$Sr_2Fe_{0.5}Ru_{0.5}O_{3+\delta}$[46]	1.951(1)/1.947(1)	2.038(13)/2.089(10)

A similar result is seen when comparing the lattice parameters extracted from the refinements. Table 9.5 outlines the lattice parameters of $La_xSr_{2-x}Co_{0.5}Ir_{0.5}O_4$ and $La_xSr_{2-x}Co_{0.5}Ir_{0.5}O_3$ (x = 0, 0.5) and other related oxides. It can clearly be seen that the reduction of $La_xSr_{2-x}Co_{0.5}Ir_{0.5}O_3$ (x = 0, 0.5) follows the well-established pattern of lattice parameter changes i.e. there is a significant contraction along the axis the oxide is removed. However for both $La_xSr_{2-x}Co_{0.5}Ir_{0.5}O_3$ (x = 0, 0.5) there is a slight contraction along the *a*-axis. This is unexpected. The examples given in Table 9.5 show that upon reduction the lattice parameters along which oxide ions have not been removed expand. This is because upon reduction the radii of the B-site cations increase. The contraction of the *a* lattice parameter is a further indication that $La_xSr_{2-x}Co_{0.5}Ir_{0.5}O_3$ (x = 0, 0.5) are likely distorted.

Compound	*a* (Å)	*b* (Å)	*c* (Å)
Sr_2FeO_4*	3.8642(1)	3.8642(1)	12.3968(2)
Sr_2FeO_3	3.5337(9)	3.9095(9)	12.9123(12)
$Sr_2Fe_2O_7$	3.8526(1)	3.8526(1)	20.1490(1)
$Sr_2Fe_2O_5$	3.514825(2)	3.95271(2)	20.9125(1)
$Sr_2Fe_{0.5}Ru_{0.5}O_4$$^+$	3.9025(1)	3.9025(1)	12.5943(3)
$Sr_2Fe_{0.5}Ru_{0.5}O_{3.25}$	3.6459(7)	3.9300(3)	12.898(2)
$Sr_2Fe_{0.5}Ru_{0.5}O_{3.44}$	3.7169(8)	3.9028(7)	12.856(2)
$Sr_2(Fe_{0.5}Ru_{0.5})_2O_7$$^+$	3.9187(1)	3.9187(1)	20.4146
$Sr_2(Fe_{0.5}Ru_{0.5})_2O_{5.50}$	3.6553(5)	3.9300(3)	20.815(2)
$Sr_2(Fe_{0.5}Ru_{0.5})_2O_{5.86}$	3.7164(5)	3.9208(4)	20.740(2)
$Sr_2Fe_{0.5}Ir_{0.5}O_4$	3.91663(6)	3.91663(6)	12.5781(2)
$Sr_2Fe_{0.5}Ir_{0.5}O_3$	3.9252(2)	3.5999(2)	12.8538(6)
$Sr_2Co_{0.5}Ir_{0.5}O_4$	3.9173(1)	3.9173(1)	12.4826(5)
$Sr_2Co_{0.5}Ir_{0.5}O_3$	3.9075(4)	3.5621(4)	12.861(1)
$La_{0.5}Sr_{1.5}Co_{0.5}Ir_{0.5}O_4$	3.88892(5)	3.88892(5)	12.6166(2)
$La_{0.5}Sr_{1.5}Co_{0.5}Ir_{0.5}O_3$	3.8726(3)	3.5660(3)	12.982(1)

Table 9.5: The reported lattice parameters of selected Ruddlesden-Popper structures and their reduced analogues. * Reported from X-ray powder diffraction data; $^+$ Reported from neutron powder diffraction data collected at 1.7 K.

There are two distortions in the oxide lattice that could result in the contraction of the *a* lattice parameter and smaller than expected planar B-O bond: either an MO_4 twist around

the *b*-axis or an MO_4 twist around the *c*-axis (Figure 9.7). The thermal parameters are used in refinements as a correction factor that account for atoms appearing larger than they are due to thermal vibrations. During a refinement thermal parameters can couple to the atomic position and refine to values that disguise the true position of the atom in the lattice. Due to the lack of connection along the *c* axis the layers in $La_xSr_{2-x}Co_{0.5}Ir_{0.5}O_3$ (x = 0, 0.5) can stack in a disordered arrangement, disguising any distortion. Consequently the position of O (2) extracted from refinement will be the average between all layers and as such we cannot determine if the structure is distorted by refining the oxide position. However we can use the thermal parameters and the shape of thermal ellipsoids as a proxy to see if there could be a distortion.

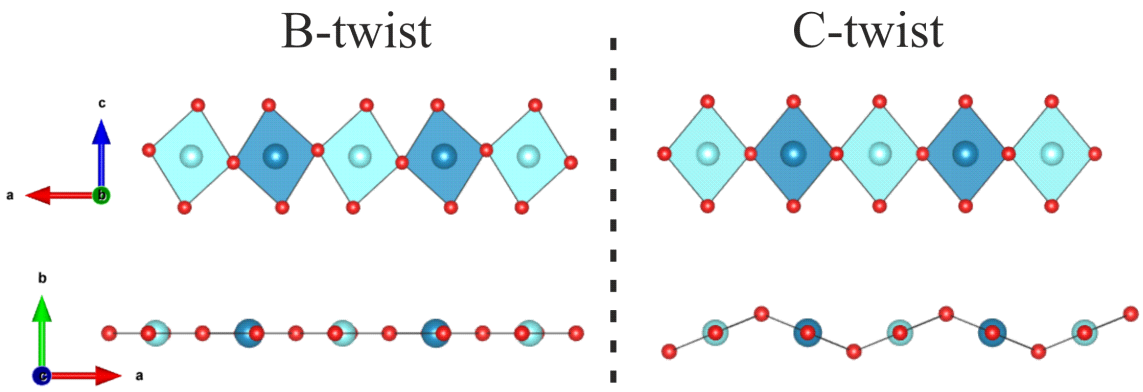

Figure 9.7: The potential twisting distortions present in $La_xSr_{2-x}Co_{0.5}Ir_{0.5}O_3$

Table 9.6 shows the thermal parameters of the O (2) anion extracted from the refinement of the neutron powder diffraction data collected from $La_xSr_{2-x}Co_{0.5}Ir_{0.5}O_4$ and $La_xSr_{2-x}Co_{0.5}Ir_{0.5}O_3$ (x = 0, 0.5) (Section 9.3.1.3.1). Comparing these parameters, we can see that there is an increase by one order of magnitude in U_{22} upon reduction whereas U_{11} and U_{33} have values that are of the same order of magnitude. The U_{22} parameter describes the shape of the thermal ellipsoid along the *b*-axis. Figure 9.8 shows the thermal ellipsoids of $La_xSr_{2-x}Co_{0.5}Ir_{0.5}O_3$ (x = 0. 0.5). The larger value of U_{22} suggests that O (2) may not sit at *y* = 0 but is in fact alternately sits at y = 0 $\pm$ δ, a result that is not inconsistent with an

MO_4 twist along the *c*-axis. A twist along the *c*-axis effectively concertinas the *a*-lattice direction resulting in a smaller *a* lattice parameter and the incorrect determination of the B-O bond lengths, as shown in Figure 9.9.

Compound	U_{11} (Å^2)	U_{22} (Å^2)	U_{33} (Å^2)
$Sr_2Co_{0.5}Ir_{0.5}O_4$	0.0095(6)	0.004(1)	0.00052(1)
$Sr_2Co_{0.5}Ir_{0.5}O_3$	0.015(3)	0.070(5)	0.003(3)
$La_{0.5}Sr_{1.5}Co_{0.5}Ir_{0.5}O_4$	0.0138(3)	0.0040(6)	0.0056(5)
$La_{0.5}Sr_{1.5}Co_{0.5}Ir_{0.5}O_3$	0.012(4)	0.036(6)	0.003(4)

Table 9.6: Values of U_{xx} extracted from refinements of neutron powder diffraction data collected from $La_xSr_{2-x}Co_{0.5}Ir_{0.5}O_4$ and $La_xSr_{2-x}Co_{0.5}Ir_{0.5}O_3$ (x = 0, 0.5)

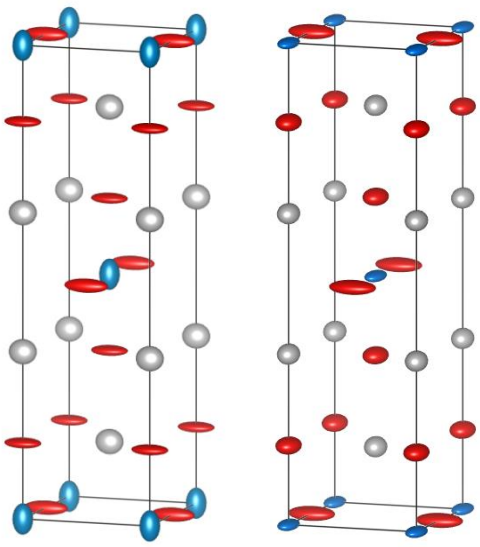

Figure 9.8: The thermal ellipsoids of $Sr_2Co_{0.5}Ir_{0.5}O_3$ (left) and $La_{0.5}Sr_{1.5}Co_{0.5}Ir_{0.5}O_3$ (right). The colours of the ellipsoids correspond to the following: Blue = Cobalt/Iridium; Red = Oxygen; Grey = Strontium/Lanthanum

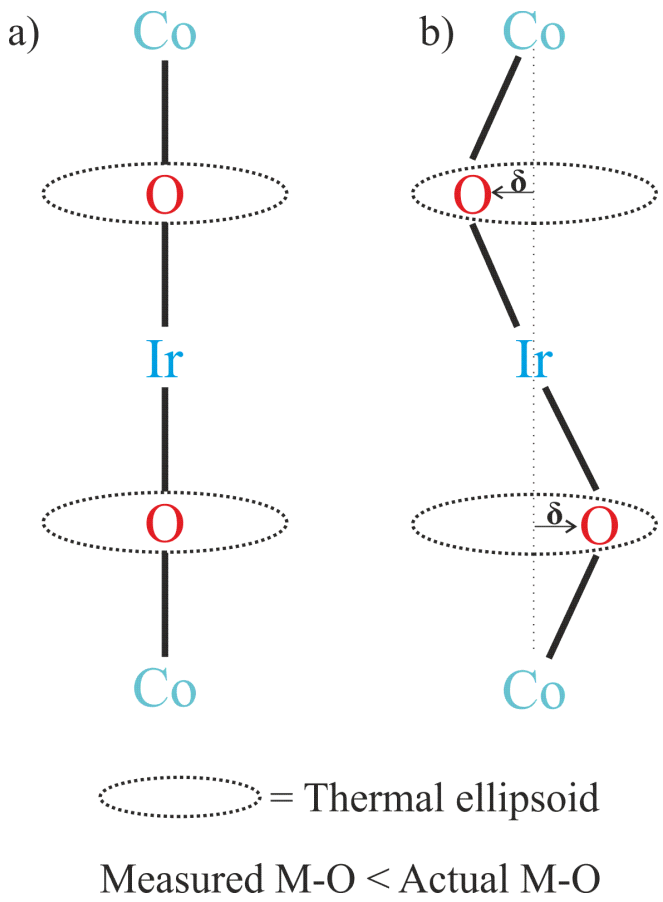

Figure 9.9: A cartoon representation of how an undetectable distortion alters the bond lengths extracted from refinement of neutron powder diffraction data. a) the bonds as "seen" by diffraction b) the true distorted structure.

The stacking disorder that is a structural feature of n = 1 Ruddlesden-popper is a barrier to accurately determining a distorted anion structure. However one tool we have at our disposal is the refinement of diffraction data. As discussed above the thermal ellipsoid can act as a proxy to determining the movement of oxide anions from there true positions. It is possible to decouple an anisotropic thermal factor and oxide position by setting the thermal factor to be isotropic and splitting the oxide site into two. Refinement of such a model will allow us to confirm if the distortion exists and potentially quantify it by more accurately extracting bond lengths and angles. To this end two further refinements of the neutron powder diffraction data collected at room temperature from samples of $La_xSr_{2-x}Co_{0.5}Ir_{0.5}O_3$ (x = 0, 0.5). During these refinements the only parameters that were allowed

to refine were the O(2) site position and the isotropic thermal parameter of this site. The refinements converged to give very good statistical fits. The observed, calculated and difference plots for the refinements are shown in Figure 9.11 and 9.12 and full details of the structural parameters are given in Tables 9.8 and 9.9. Selected bond lengths extracted from the refinements are given in Table 9.7 and the unit cells extracted from the refinements are shown in Figure 9.10.

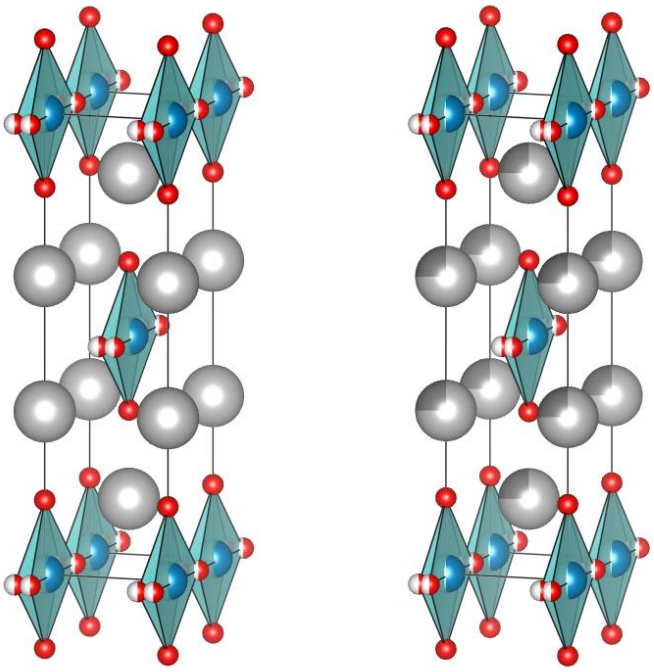

Figure 9.10: The unit cells of $Sr_2Co_{0.5}Ir_{0.5}O_3$ (Left) and $La_{0.5}Sr_{1.5}Co_{0.5}Ir_{0.5}O_3$ (Right) extracted from the split-site refinements of the neutron powder diffraction data collected at room temperature. The light blue and dark blue spheres are cobalt and iridium respectively.

	M-O(1) (Å)	M-O(2) (Å)	M-O(2)-M (°)
$Sr_2Co_{0.5}Ir_{0.5}O_3$	2.0702(2)	1.972(1)	166.8(5)
$L_{0.5}Sr_{1.5}Co_{0.5}O_3$	2.1406(1)	1.946(1)	170.7(11)

Table 9.7: Bond lengths and angles extracted from the split-site refinements of $La_xSr_{2-x}Co_{0.5}Ir_{0.5}O_3$.

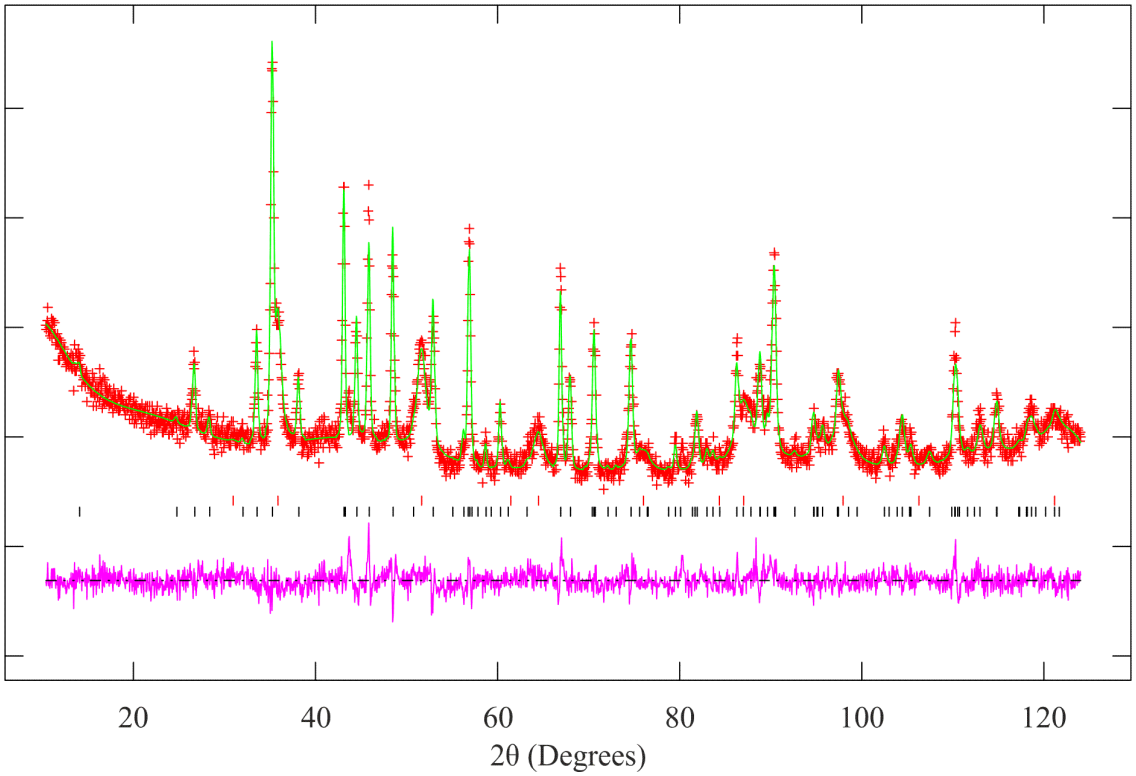

Figure 9.11: Observed, calculated and difference plots from the of the "split site" *I*4/*mmm* structural model of $La_{0.5}Sr_{1.5}Co_{0.5}Ir_{0.5}O_3$ against the neutron powder diffraction data collected at room temperature using the D2B instrument. Tick marks correspond to the following: Black = $La_{0.5}Sr_{1.5}Co_{0.5}Ir_{0.5}O_3$, Red = SrO

Atom	site	*x*	*y*	*z*	Fraction	U_{11} (Å^2)	U_{22} (Å^2)	U_{33} (Å^2)
Sr/La	4*i*	0	0	0.3542(3)	0.75/0.25	0.013(2)	0.007(1)	0.006(1)
Co/Ir	2*a*	0	0	0	0.5/0.5	0.024(5)	0.006(4)	0.001(1)
O(1)	4*i*	0	0	0.1645(4)	1	0.019(3)	0.009(3)	0.004(1)
Atom	site	*x*	*y*	*z*	Fraction	U_{iso} (Å^2)		
O(2)	4*f*	½	0.956(5)	0	0.5	0.007(2)		
$La_{0.5}Sr_{1.5}Co_{0.5}Ir_{0.5}O_3$ - Space Group: *Immm* (#71) Formula weight = 347.275 g mol^{-1}, Weight Fraction = 76.2% *a* = 3.8799(3) Å, *b* = 3.5763(3) Å, *c* = 13.008(1) Å, volume = 180.50(4) Å^3								
Atom	site	*x*	*y*	*z*	Fraction	U_{iso} (Å^2)		
Sr	4*b*	½	½	½	1	0.002(1)		
O(1)	4*a*	0	0	0	1	0.002(1)		
SrO - Space Group: $Fm\bar{3}m$ (#225) Formula weight = 487.30 g mol^{-1}, Weight Fraction = 23.8% *a* = *b* = *c* = 5.176(1) Å, volume = 138.72(8) Å^3								
Radiation source: Constant wavelength, λ = 1.54 Å Temperature: Room Temperature χ^2 = 1.688; *wRp* = 3.86 %; *Rp* = 3.00 %								

Table 9.8: Parameters from the structural refinement of the "split-site" model of $La_{0.5}Sr_{1.5}Co_{0.5}Ir_{0.5}O_3$ against neutron powder diffraction data collected at room temperature.

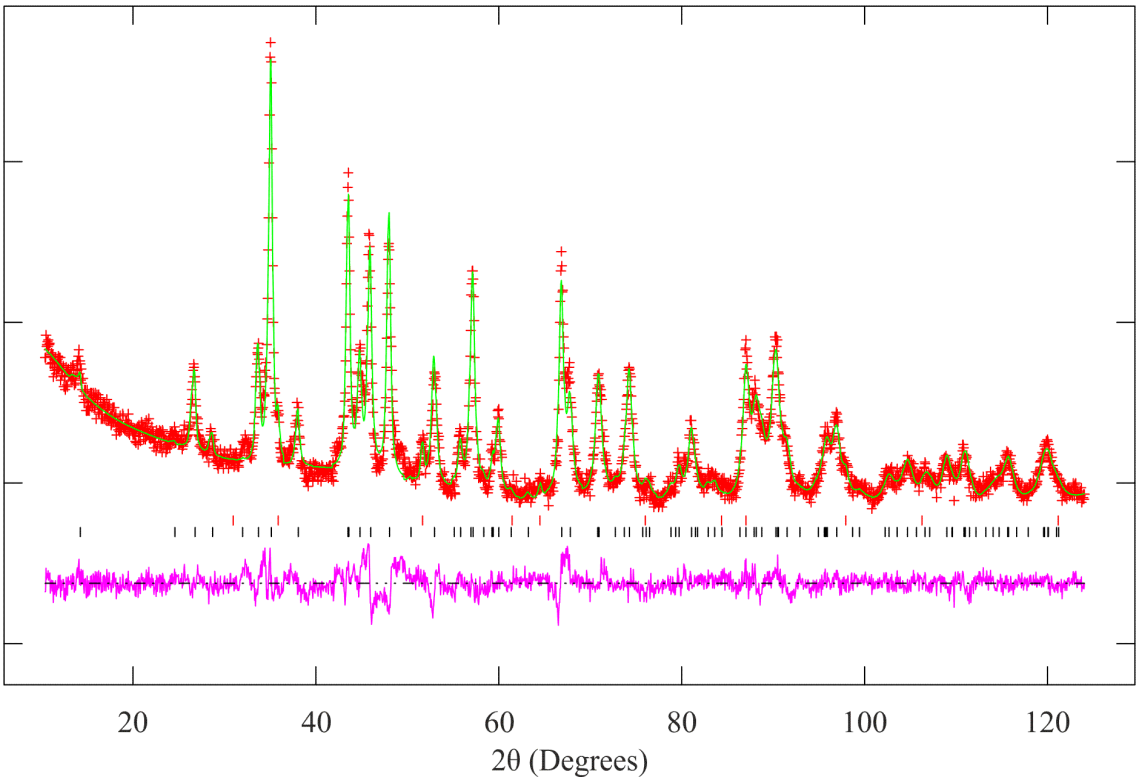

Figure 9.12: Observed, calculated and difference plots from the of the "split site" *I*4/*mmm* structural model of $Sr_2Co_{0.5}Ir_{0.5}O_3$ against the neutron powder diffraction data collected at room temperature using the D2B instrument. Tick marks correspond to the following: Black = $La_{0.5}Sr_{1.5}Co_{0.5}Ir_{0.5}O_3$, Red = SrO

Atom	site	*x*	*y*	*z*	Fraction	U_{11} (Å^2)	U_{22} (Å^2)	U_{33} (Å^2)
Sr	4*i*	0	0	0.3531(2)	1	0.018(2)	0.027(3)	0.022(2)
Co/Ir	2*a*	0	0	0	0.5/0.5	0.015(3)	0.014 (4)	0.033(3)
O(1)	4*i*	0	0	0.1604(1)	1	0.018(2)	0.048(3)	0.036(1)
Atom	site	*x*	*y*	*z*	Fraction	U_{iso} (Å^2)		
O(2)	4*f*	½	0.063(5)	0	0.5	0.009(1)		
$Sr_2Co_{0.5}Ir_{0.5}O_3$ - Space Group: *Immm* (#71) Formula weight = 348.815 g mol^{-1}, Weight Fraction = 98.04% *a* = 3.9170(4) Å, *b* = 3.5758(5) Å, *c* = 12.880(1) Å, volume = 180.41(5) Å^3								
Atom	site	*x*	*y*	*z*	Fraction	U_{iso}		
Sr	4*b*	½	½	½	1	0.017(7)		
O	4*a*	0	0	0	1	0.017(7)		
SrO - Space Group: $Fm\bar{3}m$ (#225) Formula weight = 487.30 g mol^{-1}, Weight Fraction = 1.96% *a* = *b* = *c* = 5.176(1) Å, volume = 138.72(8) Å^3								
Radiation source: Constant wavelength, λ = 1.54 Å Temperature: Room Temperature								

Table 9.9: Parameters from the structural refinement of the "split-site" model of $Sr_2Co_{0.5}Ir_{0.5}O_3$ against neutron powder diffraction data collected at room temperature.

9.3.2 Magnetic characterisation of $La_xSr_{2-x}Co_{0.5}Ir_{0.5}O_3$ (x = 0, 0.5)

9.3.2.1 Magnetisation data

Magnetisation isotherms collected from small samples of $La_xSr_{2-x}Co_{0.5}Ir_{0.5}O_3$ (x = 0, 0.5) at 300 K exhibited hysteresis suggesting the presence of a small amount of a ferromagnetic impurity, most likely elemental cobalt. To determine the bulk magnetic behaviours of $La_xSr_{2-x}Co_{0.5}Ir_{0.5}O_3$ (x = 0, 0.5) ferrosubtraction measurements were conducted (Chapter 2, Section 2.11.1). The paramagnetic susceptibility and saturated ferromagnetic moment plots are shown in Figure 9.13. The paramagnetic susceptibility of $Sr_2Co_{0.5}Ir_{0.5}O_3$ increases non-linearly in the temperature range $25 \leq T / K \leq 300$ until it reaches a maximum at 25 K. The data in this temperature range cannot be fit to the Curie-Weiss law, even with a large temperature independent parameter. The saturated ferromagnetic moment increases at a roughly linear rate in the temperature range $50 \leq T / K \leq 300$, after which there is a dramatic increase. These results suggest $Sr_2Co_{0.5}Ir_{0.2}O_3$ undergoes a magnetic ordering event at around 50 K to a canted antiferromagnetic state. The paramagnetic susceptibility plot shows that the paramagnetic susceptibility of $La_{0.5}Sr_{1.5}Co_{0.5}Ir_{0.5}O_3$ increases linearly until around 100 K where it begins to curve and reaches a maximum at 10 K. The susceptibility data cannot be fit to the Curie-Weiss law, suggesting the spins are interacting strongly and are possibly frustrated. The rate of increase of the saturated ferromagnetic moment gets larger at around 30 K, suggesting $La_{0.5}Sr_{1.5}Co_{0.5}Ir_{0.5}O_3$ adopts a canted antiferromagnetic state.

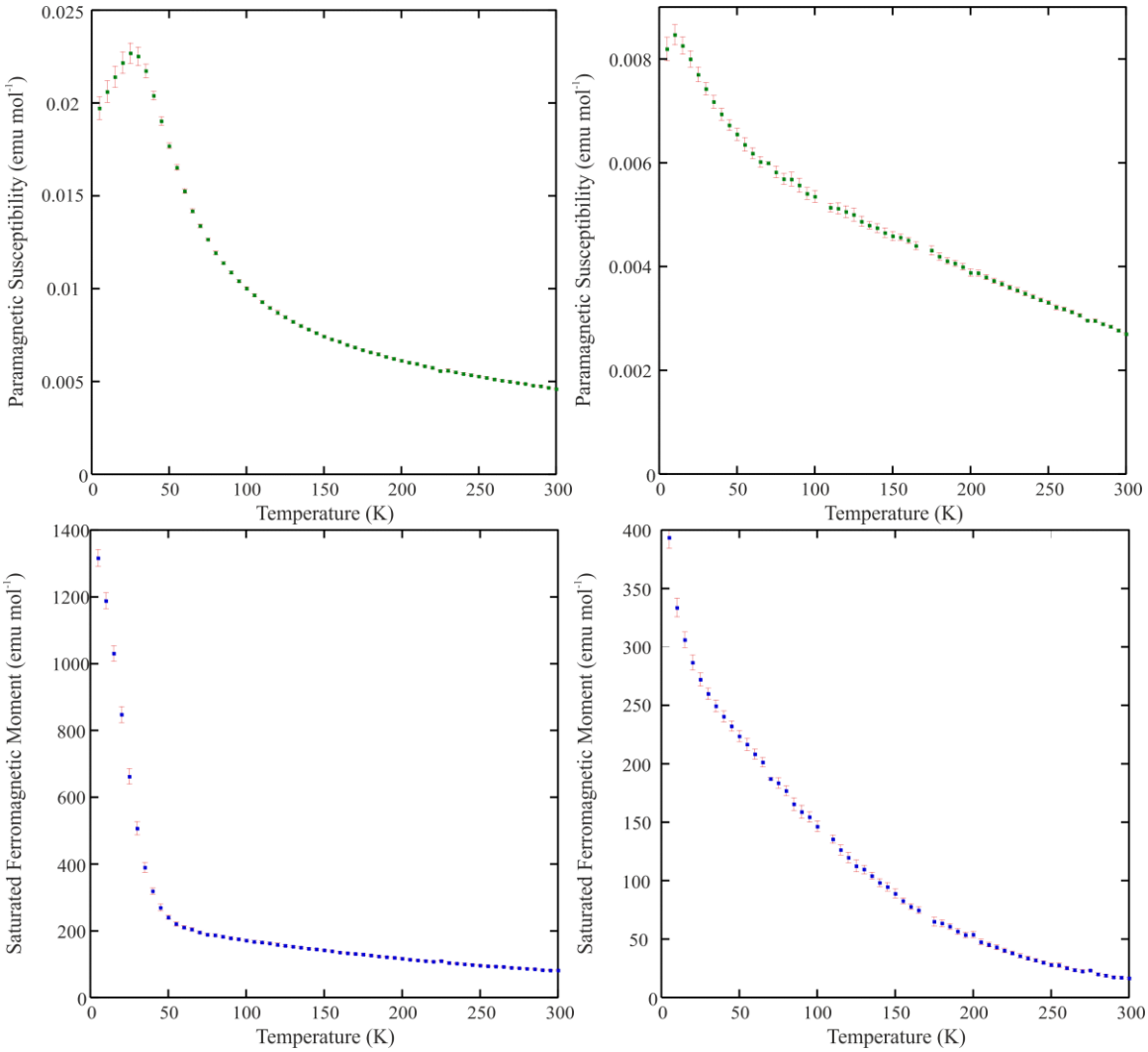

Figure 9.13: Top left) Paramagnetic susceptibility of $Sr_2Co_{0.5}Ir_{0.5}O_4$. Bottom left) Saturated ferromagnetic moment of $Sr_2Co_{0.5}Ir_{0.5}O_4$. Top right) Paramagnetic susceptibility of $La_{0.5}Sr_{1.5}Co_{0.5}Ir_{0.5}O_4$. Bottom right) Saturated ferromagnetic moment of $La_{0.5}Sr_{1.5}Co_{0.5}Ir_{0.5}O_4$

The magnetisation isotherms collected from $La_xSr_{2-x}Co_{0.5}Ir_{0.5}O_4$ (x = 0, 0.5) after field cooling at 5 K are shown in Figure 9.14. Both magnetisation isotherms exhibit hysteresis which is to be expected as both samples contain elemental cobalt . The isotherms for both samples are symmetric about the origin, clearly indicating that there is no component of frustration in either compounds low temperature magnetic state. This would suggest that both compounds adopted ordered, canted antiferromagnetic states.

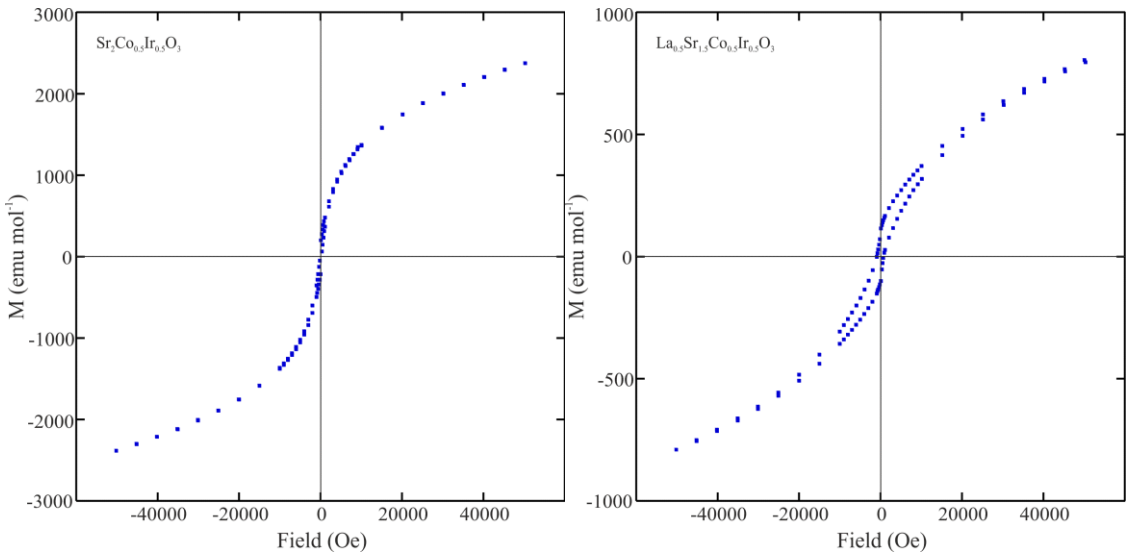

Figure 9.14: Magnetisation isotherms collected at 5 K from: Left) $Sr_2Co_{0.5}Ir_{0.5}O_3$ and Right) $La_{0.5}Sr_{1.5}Co_{0.5}Ir_{0.5}O_3$

9.3.2.2 Neutron diffraction data

Comparison of the neutron diffraction data collected from $La_xSr_{x-2}Co_{0.5}Ir_{0.5}O_3$ (x = 0, 0.5) at room temperature and 5 K did not reveal additional diffraction peaks that could not be attributed to the closed-circuit refrigeration system in which the samples were cooled. A series of ferromagnetic unit cells were constructed and refined against the data collected at 5 K. None of these refinements converged indicating $La_xSr_{x-2}Co_{0.5}Ir_{0.5}O_3$ (x = 0, 0.5) do not have magnetically ordered states that are observable by neutron diffraction. The observed, calculated and difference plots for the refinement is shown in Figures 9.10 and 9.11. Full details of the structural parameters are given in Tables 9.10 and 9.11.

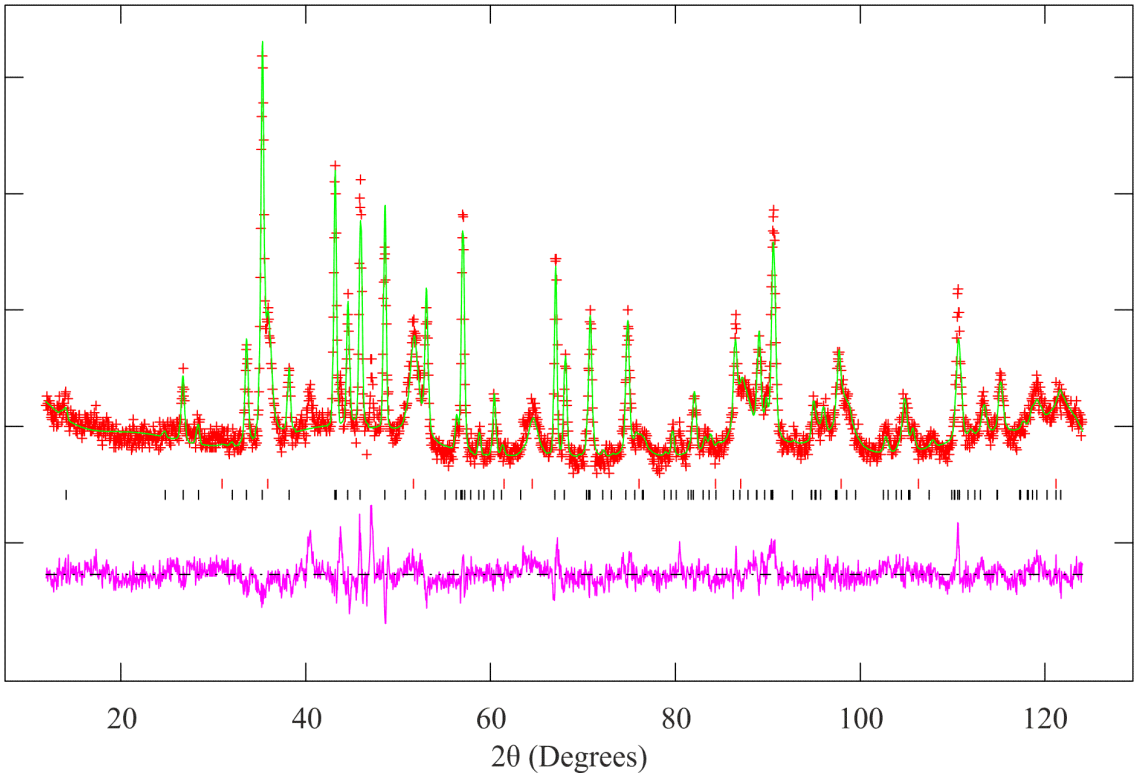

Figure 9.15: Observed, calculated and difference plots from the of the *I*4/*mmm* structural model of $La_{0.5}Sr_{1.5}Co_{0.5}Ir_{0.5}O_3$ against the neutron powder diffraction data collected at 5 K using the D2B instrument. Tick marks correspond to the following: Black = $La_{0.5}Sr_{1.5}Co_{0.5}Ir_{0.5}O_3$, Red = SrO

Atom	site	*x*	*y*	*z*	Fraction	U_{11} (Å^2)	U_{22} (Å^2)	U_{33} (Å^2)
Sr/La	4*i*	0	0	0.3547(3)	0.75/0.25	0.017(3)	0.010(3)	0.009(1)
Co/Ir	2*a*	0	0	0	0.5/0.5	0.023(5)	0.017(5)	0.013(1)
O(1)	4*i*	0	0	0.1648(4)	1	0.017(3)	0.003(3)	0.003(1)
O(2)	4*f*	½	0	0	1	0.006(4)	0.037(6)	0.015(1)
$La_{0.5}Sr_{1.5}Co_{0.5}Ir_{0.5}O_3$ - Space Group: *Immm* (#71) Formula weight = 347.275 g mol^{-1}, Weight Fraction = 76.2% *a* = 3.8726(3) Å, *b* = 3.5660(3) Å, *c* = 12.982(1) Å, volume = 179.28(4) Å^3								
Atom	site	*x*	*y*	*z*	Fraction	U_{iso} (Å^2)		
Sr	4*b*	½	½	½	1	0.006(1)		
O(1)	4*a*	0	0	0	1	0.006(1)		
SrO - Space Group: $Fm\bar{3}m$ (#225) Formula weight = 487.30 g mol^{-1}, Weight Fraction = 23.8% *a* = *b* = *c* = 5.176(1) Å, volume = 138.72(8) Å^3								
Radiation source: Constant wavelength, λ = 1.54 Å Temperature: 5K χ^2 = 2.193; *wRp* = 4.30 %; *Rp* = 3.27 %								

Table 9.10: Parameters from the structural refinement of $La_{0.5}Sr_{1.5}Co_{0.5}Ir_{0.5}O_3$ against neutron powder diffraction data collected at 5 K.

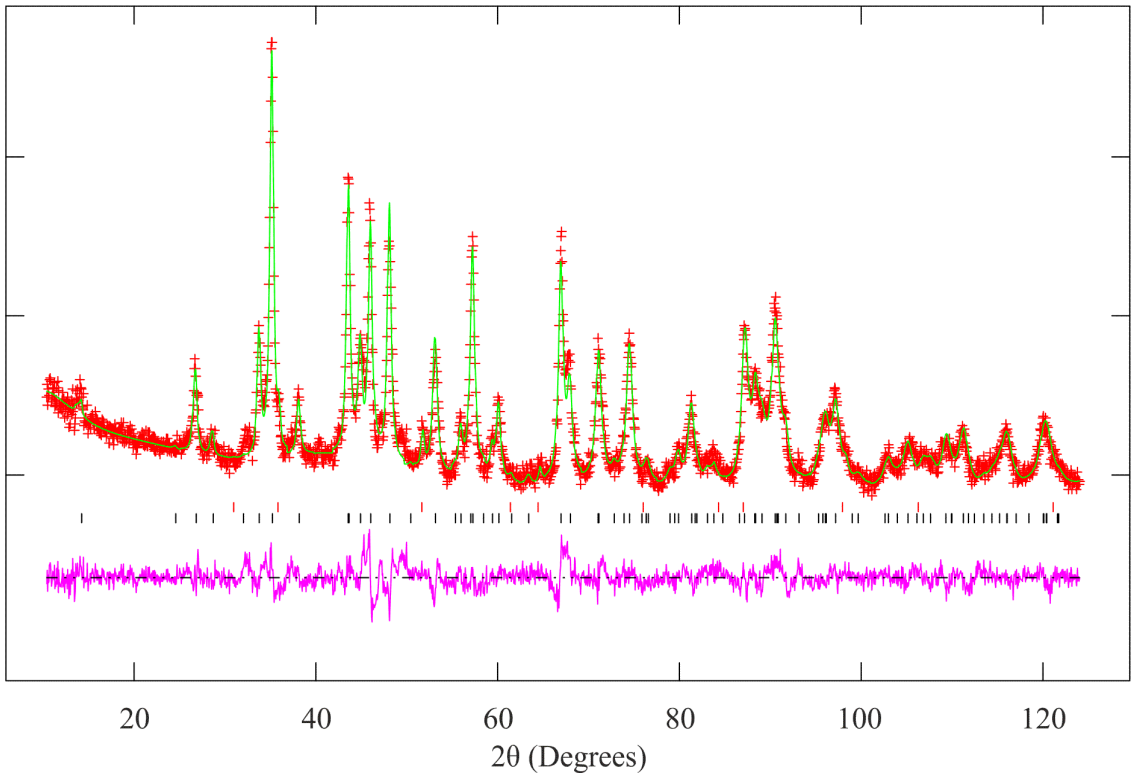

Figure 9.16: Observed, calculated and difference plots from the of the *I*4/*mmm* structural model of $Sr_2Co_{0.5}Ir_{0.5}O_3$ against the neutron powder diffraction data collected at 5 K using the D2B instrument. Tick marks correspond to the following: Black = $La_{0.5}Sr_{1.5}Co_{0.5}Ir_{0.5}O_3$, Red = SrO

Atom	site	*x*	*y*	*z*	Fraction	U_{11} (Å^2)	U_{22} (Å^2)	U_{33} (Å^2)
Sr	4*i*	0	0	0.3531(2)	1	0.016(2)	0.027(2)	0.015(1)
Fe/Ir	2*a*	0	0	0	0.5/0.5	0.015(3)	0.010(4)	0.036(2)
O(1)	4*i*	0	0	0.1604(1)	1	0.014(1)	0.054(2)	0.036(2)
O(2)	4*f*	½	0	0	1	0.010(3)	0.068(5)	0.009(3)
$Sr_2Co_{0.5}Ir_{0.5}O_3$ - Space Group: *Immm* (#71) Formula weight = 348.815 g mol^{-1} *a* = 3.9075(4) Å, *b* = 3.5621(4) Å, *c* = 12.861(1) Å, volume = 180.50(4) Å^3								
Atom	site	*x*	*y*	*z*	Fraction	U_{iso}		
Sr	4*b*	½	½	½	1	0.022(5)		
O	4*a*	0	0	0	1	0.022(5)		
SrO - Space Group: *Fm*$\bar{3}$*m* (#225) Formula weight = 487.30 g mol^{-1}, Weight Fraction = 1.96% *a* = *b* = *c* = 5.161(1) Å, volume = 138.72(8) Å^3								
Radiation source: Constant wavelength, λ = 1.54 Å								

Table 9.11: Parameters from the structural refinement of $Sr_2Co_{0.5}Ir_{0.5}O_3$ against neutron powder diffraction data collected at 5 K.

9.4 Discussion

9.4.1 The structural distortion of $La_xSr_{2-x}Co_{0.5}Ir_{0.5}O_3$ (x = 0, 0.5)

The refinements conducted in Sections 9.3.1.3 and 9.3.1.3.1 show that the structures of $La_xSr_{2-x}Co_{0.5}Ir_{0.5}O_3$ (x = 0, 0.5) are distorted. Examining the data extracted from the refinements outlined in Section 9.3.1.3 we can see that the distortions of $La_xSr_{2-x}Co_{0.5}Ir_{0.5}O_3$ (x = 0, 0.5) have different magnitudes. Comparing the lattice parameters of $La_xSr_{2-x}Co_{0.5}Ir_{0.5}O_3$ (x = 0, 0.5) we can see that upon reduction the largest decrease in *a* is observed for $Sr_2Co_{0.5}Ir_{0.5}O_3$. Furthermore U_{22} of O(2) is greater for $Sr_2Co_{0.5}Ir_{0.5}O_3$ than it is for $La_{0.5}Sr_{1.5}Co_{0.5}Ir_{0.5}O_3$, these results suggest if there is a distortion it is larger in $Sr_2Co_{0.5}Ir_{0.5}O_3$ than it is in $La_{0.5}Sr_{1.5}Co_{0.5}Ir_{0.5}O_3$. This is confirmed by the refinements outlined in Section 9.3.1.3.1 in which we can see the M-O(2)-M bond angle is smaller for $Sr_2Co_{0.5}Ir_{0.5}O_3$ than it is for $La_{0.5}Sr_{1.5}Co_{0.5}Ir_{0.5}O_3$ (Table 9.7) Distortions in oxide structures most often arise as a result of mismatches in the size of cations, as explained in Chapter 1, Section 1.4.1, thus the distortions in $La_xSr_{2-x}Co_{0.5}Ir_{0.5}O_3$ (x = 0, 0.5) could come from the differences in cation sizes. There are two differences between $Sr_2Co_{0.5}Ir_{0.5}O_3$ and $La_{0.5}Sr_{1.5}Co_{0.5}Ir_{0.5}O_3$: firstly they have different A-site species and secondly the oxidation states of the B-site differ by one charge unit. To understand why $Sr_2Co_{0.5}Ir_{0.5}O_3$ and $La_{0.5}Sr_{1.5}Co_{0.5}Ir_{0.5}O_3$ might have different size distortions we can use the Goldschmidt Tolerance factor (Chapter 1, Section 1.4.1, Equation 1.5). First let us consider the A-site cations. The radii of Ca^{II} and La^{III} in a 12-coordinate environment are 1.34 nm and 1.36 nm respectively[121]. This is a very small difference and as such is not likely to be the cause of the distortions or the reason the distortion of $Sr_2Co_{0.5}Ir_{0.5}O_3$ is

Thus the most chemically reasonable oxidation state combination for $Sr_2Co_{0.5}Ir_{0.5}O_3$ is Co^{II}/Ir^{II} and for $La_{0.5}Sr_{1.5}Co_{0.5}Ir_{0.5}O_3$ it is Co^{I}/Ir^{II}. There is no data published for the ionic radii of $Co^{I/II}$ and Ir^{II} but it has generally been observed that cations with higher oxidation states have smaller ionic radii[121], thus it is reasonable to assume the radius of Co^{I} is greater than that of Co^{II}. Following this logic we would expect the tolerance factor of $La_{0.5}Sr_{1.5}Co_{0.5}Ir_{0.5}O_3$ to be smaller than that of $Sr_2Co_{0.5}Ir_{0.5}O_3$ and therefore more distorted. This is not the case, therefore there must be another factor driving the larger distortion of $Sr_2Co_{0.5}Ir_{0.5}O_3$. Figure 9.17 shows the electronic structures of Co^{I} and Co^{II} in a square planar coordination environment. The difference between these two electronic states lies in the degenerate $d_{yz/xz}$ orbital set. For Co^{I} these orbitals are fully occupied but for Co^{II} they are partially occupied. This partial occupation is unstable, an instability that could be relieved by a Jahn-Teller distortion. If the $Co^{II}O_4$ units were to distort this would create tension with the $Ir^{II}O_4$ which strongly favours rigorous square planar geometry, as demonstrated in Chapter 4. This tension could be relieved by a structural distortion, resulting in $Sr_2Co_{0.5}Ir_{0.5}O_3$ having a greater structural distortion than $La_{0.5}Sr_{1.5}Co_{0.5}Ir_{0.5}O_3$. The explanation is not inconsistent with the results extracted from the refinements of $La_xSr_{2-x}Co_{0.5}Ir_{0.5}O_3$ (x = 0, 0.5). Further investigation into the structures of $La_xSr_{2-x}Co_{0.5}Ir_{0.5}O_3$ (x = 0, 0.5) using local probes and density functional theory calculations are necessary to confirm if a Jahn-Teller distortion is indeed the cause of the larger distortion of $Sr_2Co_{0.5}Ir_{0.5}O_3$.

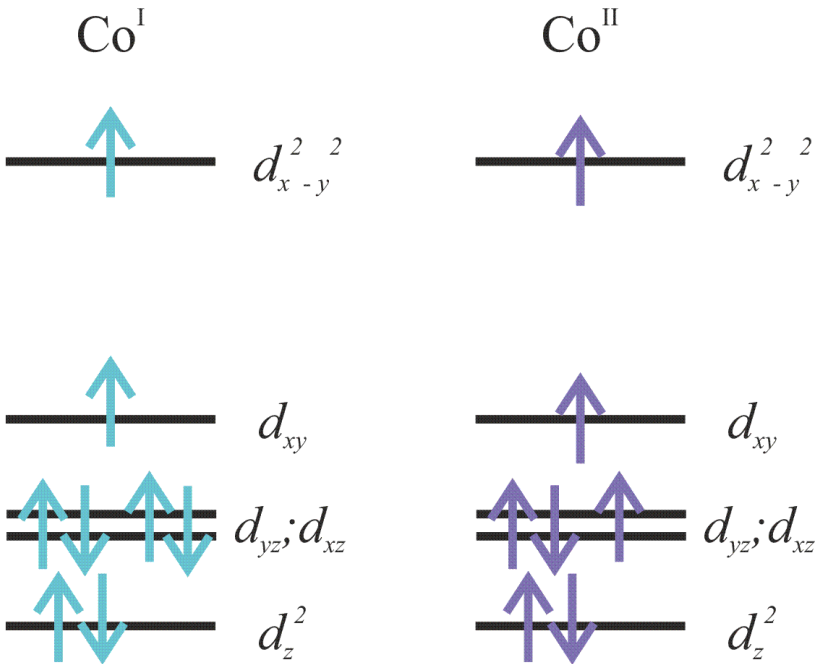

Figure 9.17: The electronic states of square planar Co^{I} and Co^{II}

9.4.2 Magnetism of $La_xSr_{2-x}Co_{0.5}Ir_{0.5}O_3$ (x = 0, 0.5)

The reduction of $La_xSr_{2-x}Co_{0.5}Ir_{0.5}O_4$ to $La_xSr_{2-x}Co_{0.5}Ir_{0.5}O_3$ (x = 0, 0.5) results in the extrusion of a small amount of elemental cobalt. Cobalt is a ferromagnetic metal and masks the true magnetic behaviour of $La_xSr_{2-x}Co_{0.5}Ir_{0.5}O_4$ (x = 0, 0.5). To counter this ferrosubtraction measurements were conducted, allowing us to observe some of the magnetic properties of $La_xSr_{2-x}Co_{0.5}Ir_{0.5}O_3$ (x = 0, 0.5). The data collected from $La_{0.5}Sr_{1.5}Co_{0.5}O_3$ and $Sr_2Co_{0.5}Ir_{0.5}O_3$ show that both compounds order at low temperatures to adopt canted antiferromagnetic states. This is most clearly illustrated for $Sr_2Co_{0.5}Ir_{0.5}O_3$. The saturated ferromagnetic moment extracted from the data collected from $Sr_2Co_{0.5}Ir_{0.5}O_3$ rapidly increases at around 50 K and is coincident with the onset of a maxima in the paramagnetic susceptibility (Figure 9.13), indicative of a canted antiferromagnetic state. The magnetisation data collected from $La_{0.5}Sr_{1.5}Co_{0.5}O_3$ are less clear. At temperatures above 100 K the paramagnetic susceptibility of $La_{0.5}Sr_{1.5}Co_{0.5}O_3$ is roughly linear (Figure 9.13). This is highly unusual and suggests the spins in $La_{0.5}Sr_{1.5}Co_{0.5}O_3$ are strongly interacting and potentially frustrated as they are observed to

be in Sr_2FeIrO_4 (Chapter 4). At around 100 K the paramagnetic susceptibility begins to increase non-linearly and the saturated ferromagnetic moment begins to increase at a different rate. The increase in the saturated ferromagnetic moment is significantly less than that of $Sr_2Co_{0.5}O_3$ which would indicate that the canting may not be as large. The magnetisation isotherms collected from $La_xSr_{2-x}Co_{0.5}Ir_{0.5}O_3$ (x = 0, 0.5) (Figure 9.14) are symmetric about the origin. This is a clear indication that neither compound is adopts a spin glass state at low temperature. This is not particularly surprising for $La_{0.5}Sr_{1.5}Co_{0.5}Ir_{0.5}O_3$ given that it retains the paracrystalline B-site structure of its parent $La_{0.5}Sr_{1.5}Co_{0.5}Ir_{0.5}O_4$ (Chapter 8). However, for $Sr_2Co_{0.5}Ir_{0.5}O_3$ it is somewhat surprising. $Sr_2Co_{0.5}Ir_{0.5}O_3$ retains the B-site disorder of its parent (Chapter 8) and as such satisfies the first requirement for the adoption of a spin glass state. The symmetry of the magnetisation isotherm collected from $Sr_2Co_{0.5}Ir_{0.5}O_3$ would therefore suggest that there is no magnetic frustration that could lead to a spin glass state.

The neutron powder diffraction data collected from $La_xSr_{2-x}Co_{0.5}Ir_{0.5}O_3$ (x = 0, 0.5) at 5 K do not have any addition magnetic Bragg peaks thus it is not possible to determine the structures of the canted antiferromagnetic states. Consequently we are unable to ascertain the spin coupling regimes present in $La_xSr_{2-x}Co_{0.5}Ir_{0.5}O_3$ (x = 0, 0.5). To fully understand the magnetic structure and properties of $La_xSr_{2-x}Co_{0.5}Ir_{0.5}O_3$ (x = 0, 0.5) further investigation is required using density functional theory calculations

9.5 Conclusions

Reaction of $La_xSr_{2-x}Co_{0.5}Ir_{0.5}O_4$ (x = 0, 0.5) with zirconium using the getter method resulted in the formation of oxide deficient phases. Compositional analysis prove that these phases are $La_xSr_{2-x}Co_{0.5}Ir_{0.5}O_3$ (x = 0, 0.5). The refinement of X-ray and neutron powder diffraction data shows these phases adopt an *Immm* structure. Interrogation of the

lattice parameters, thermal parameters and bond lengths extracted from these phases suggest the phases may have a distorted anion structure that is masked by the paracrystallinity of the structure. Refinement of the neutron diffraction data collected from both samples in which the oxide site was split proved both have a *c*-twist in their structures. The refinement also showed that the distortion is bigger for $Sr_2Co_{0.5}Ir_{0.5}O_3$ than it is for $La_{0.5}Sr_{1.5}Co_{0.5}Ir_{0.5}O_3$. The larger distortion present in $Sr_2Co_{0.5}Ir_{0.5}O_3$ cannot be rationalised by using tolerance factor arguments. Inspection of the electronic states of square planar Co^{II} and Ir^{II} in $Sr_2Co_{0.5}Ir_{0.5}O_3$ suggest that the larger distortion could be due to a Jahn-Teller distortion of the CoO_4 sites which relieves the degeneracy of the d_{yz}, d_{xz} orbital set. The magnetisation data collected from $La_xSr_{2-x}Co_{0.5}Ir_{0.5}O_3$ (x = 0, 0.5) show that both compounds adopt canted antiferromagnetic states ate low temperatures, however the lack of magnetic peaks in neutron diffraction data mean the structure of these states cannot be determined.

Chapter 10 – Conclusions

In this thesis a wide range of work has been presented that explores several aspects of the chemistry of complex iridium oxides. One of the key findings is that the principles of topochemical reduction can be, and have been, applied to oxide phases that contain iridium. This extension has led to the isolation of Ir^{II} and Ir^{III} in extended oxide frameworks. However, the reduced metastable phases presented in this work are far less stable than those that have previously been reported. This is most clearly evidenced by the inability to isolate a pure reduced phase of an iridium reduced oxide using the well-established method of reduction using group I/II hydrides. The instability of these oxides is most likely due to two factors. The first factor is the relative weakness of the Ir-O bond and by extension, the Ir-O lattice. As discussed in Chapter 3 the Ir-O bond is weaker than the Ru-O bond due to poorer energy match between the iridium and oxygen orbitals than ruthenium. This weaker bond results in a weaker lattice that will decompose more easily. The second factor is the low oxidation states of iridium. Secondly. the oxidation states of iridium in the metastable phases presented in this work are low. These states are not thermodynamically stable and thus will disproportionate in order to maximise free energy. These factors are not unique to iridium and are shared by other late 5*d* elements, suggesting that while it may be possible to extend this work to other late 5*d* element containing oxides the number of reduced metastable phases that can be isolated will be lower than the number of 3*d* and 4*d* containing phases.

The topochemically reduced phases presented in this thesis all have unprecedented oxidation states, most notably Ir^{II}. The low oxidation states of iridium cannot be accessed by traditional thermodynamic synthesis routes and are thus coupled to the unusual structures of which they are constituent. The existence of these topochemically reduced

phases proves the principle that structure is linked to the bulk properties of a material. This is exemplified by Sr_2FeIrO_4 (Chapter 4). The unique magnetic properties of Sr_2FeIrO_4 are intrinsically linked to Ir^{II} in a square-planar geometry, both features that could only be achieved by topochemical reduction. As such this work further vindicates and supports the efficacy of topochemical manipulation as an avenue via which new materials with unprecedented and potentially useful properties can be found.

The phases presented in this thesis have a variety of structures, properties and oxidation states however there is one group of metastable compounds that are not represented: the oxyhydrides. In many ways the absence of oxyhydride is not surprising. The reduced cobalt phases $La_xSr_{2-x}Co_{0.5}Ir_{0.5}O_3$ (x = 0, 0.5) were synthesised using a zirconium getter in which no hydrogen was present and there have been no iron-containing oxyhydride phases reported, thus it was never reasonable to assume we could make oxyhydride phases from reduction of Sr_2FeIrO_6 or $Sr_2Fe_{0.5}Ir_{0.5}O_4$. However the limited scope of this work leaves a significant question surrounding the reduction chemistry of complex iridium oxides: Can an iridium-containing oxyhydride phase be isolated? There are a number of factors that suggest it is possible. There are a large number of iridium complexes that have been reported that have Ir-H bonds, a classic example being the hydrogenated version of Vaska's complex. The existence of these complexes shows that Ir-H bonds are stable and that it more likely than not that they can be found in the solid state. Furthermore in recent years there has been significant growth in the number of oxyhydride phases discovered, with a particular emphasis on the oxyhydride phases of 4*d* containing oxides. The relative abundance of oxyhydrides phases that contain ruthenium and rhodium suggests that oxides containing heavier *d*-block elements are more likely to reduce to form oxyhydride phases than their lighter counterparts. Given the factors that appear to favour the existence of an iridium oxyhydride phase the lack an oxyhydride in

this work should not be taken as proof against the possibility of synthesising such a phase. Instead the extensive synthetic work presented should be used as a base to expand the synthetic methods available to researchers and expanded such that more targeted investigation can be facilitated.

A second avenue of research that has been pursued in this thesis is the doping of Sr_2FeIrO_6. The evidence presented in Chapter 5 shows that doping Sr_2FeIrO_6 leads two significant, related phenomena. Firstly doping leads to phase separation in which doped parts of the sample are extruded from the $I\bar{1}$ phase of the sample and form a structurally similar $P2_1/n$ phase. The second effect of doping is that an additional, higher temperature magnetic transition is observed in the magnetisation data collected from the doped samples. ^{57}Fe Mössbauer data show that the additional magnetic transition does not originate from the iron lattice. The data show no evidence of impurities, implying the source of the magnetic moment is the iridium lattice. These results are highly unusual and fly in the face of conventional wisdom regarding the magnetic properties of Ir^V containing compounds. Due to spin orbit coupling we expect Ir^V to adopt a diamagnetic $j_{eff} = 0$ state. The results of this careful work suggest this may not always be the case. There is also evidence to suggest that the related $n = 1$ Ruddlesden-Popper phase $Sr_2Fe_{0.5}Ir_{0.5}O_4$ may have similar magnetic properties. In recent years the functional materials community has begun to focus more on the oxides of iridium due to its strong spin orbit coupling and unusual magnetic properties. The reasons for why and how Ir^V adopts a $j_{eff} \neq 0$ state are beyond the scope of this thesis but the results presented in this work highlights that aspects of iridium physics that have previously been thought to simple and understood need to be revisited and fully investigated.

Overall the work presented in this thesis shows that complex iridium oxides have a rich reduction chemistry that has allowed for the isolation of some unique compounds. The

properties of these compounds are intimately linked to their structure and as such reinforce the integral link between the structure of a compound and the properties it exhibits. This thesis represents a vast amount of work but is by no means exhaustive. The general direction of related areas of research suggest that there are still many avenues down which research pertaining to the bulk properties and topochemical manipulation of complex iridium oxides can be taken. The two clearest directions that can build upon this work are the pursuit of an iridium containing oxyhydride and a deeper investigation into the magnetic properties of the Ir^{V} oxides.

Appendix 1 – Index of Figures

Figure 1.1: The orbital energies of a) an atom, b) a small molecule c) a large molecule d) a solid.....2

Figure 1.2: Hubbard sub-bands as a function of bandwidth, *W*.....4

Figure 1.3: The orbital arrangements of a) an iridium free ion, b) iridium in octahedral co-ordination c) iridium in octahedral co-ordination with spin-orbit coupling.....7

Figure 1.4: The simple cubic Perovskite structure (left), the double Perovskite structure (right).....11

Figure 1.5: The simple Perovskite structure (left), the n=1 Ruddlesden-Popper structure (centre), the n=2 Ruddlesden-Popper structure (right).....12

Figure 1.6: The topochemical reduction of $LaNiO_3$ to $LaNiO_2$.....13

Figure 1.7: The topochemical reduction of $SrFe_{0.5}Ru_{0.5}O_3$ to $SrFe_{0.5}Ru_{0.5}O_2$ 14

Figure 1.8: The structures of the topochemically reduced phases $LaBaCo_2O_{4.25}$ and $YBaCo_2O_{4.5}$.....15

Figure 1.9: The structures of $Sr_3M_2O_7$ (M = Mn, Fe) and their topochemically reduced analogues.....16

Figure 1.10: The structure of iron-based *n*=2 Ruddlesden-Popper phases and their topochemically reduced analogues.....17

Figure 1.11: The structures of some oxyhydride phases: a) $BaTiO_{2.51}H_{0.49}$ b) $SrCrO_2H$ c) $SrVO_2H$ d) $LaSrCoO_3H_{0.7}$ and e) $LaSr_3NiRuO_4H_4$.....18

Figure 1.12: The structures of Sr_2RuO_4, Ca_2RuO_4, Sr_2IrO_4 and their structures as observed down the crystallographic *c*-axis.....20

Figure 2.1: Air sensitive X-Ray Holder.....24

Figure 2.2: Venting System Set Up.....26

Figure 2.3: a) “Horizontal” set-up for the hydrogen gas reduction reaction b) “Vertical set-up for the hydrogen gas reduction reaction.....27

Figure 2.4: Getter reaction vessel.....28

Figure 2.5 Cartoon depiction of Braggs’s Model of diffraction.....29

Figure 2.6: D2B instrument at the Insitut Laue-Laugevin.....35

Figure 2.7: A magnetisation-field isotherm indicating the susceptibility of a bulk paramagnetic phase and a ferromagnetic impurity phase.....38

Figure 2.8: A schematic of M-O-M 180 ^{o} and 90 ^{o} superexchange interactions.....41

Figure 2.9: Quadrupole splitting from a 1/2 to 3/2 transition. The magnitude of the quadrupole splitting is Δ.....43

Figure 2.10: Magnetic splitting of nuclear energy levels.....44

Figure 3.1: Additional broad diffraction feature attributed to elemental iridium nanoparticles.....48

Figure 3.2: Schematic of the topochemical reduction of Sr_2FeIrO_6.....50

Figure 3.3: Powder X-ray diffraction data collected from the reactions of $Sr_2Fe_{0.5}Ir_{0.5}O_4$ with 95%/5% N_2/H_2. * = Impurity peaks.....53

Figure 3.4: Schematic of the topochemical reduction of $Sr_2Fe_{0.5}Ir_{0.5}O_4$.....54

Figure 3.5: Schematic of the topochemical reduction of $La_xSr_{2-x}Co_{0.5}Ir_{0.5}O_4$ (x = 0, 0.5).57

Figure 3.6: Schematic of the topochemical reduction of $CaMn_{0.5}Ir_{0.5}O_3$.....59

Figure 3.7: The electronic configurations of Ru^{II} and Ir^{II} in a square-planar co-ordination geometry.....63

Figure 3.8: a) "Horizontal" set-up for the hydrogen gas reduction reaction b) "Vertical set-up for the hydrogen gas reduction reaction.....65

Figure 3.9: The unit cells of $LaSrCoIrO_6$ and $La_{0.5}Sr_{1.5}Co_{0.5}Ir_{0.5}O_4$.....68

Figure 4.1: Thermogravimetric data collected during the oxidation of Sr_2FeIrO_{6-x} to Sr_2FeIrO_6.....74

Figure 4.2: Observed, calculated and difference plots from the refinement of the *I4/mmm* structural model of Sr_2FeIrO_4 against synchrotron powder diffraction data collected at room temperature using the I11 instrument.....75

Figure 4.4: Structural models of the four possible structures of Sr_2FeIrO_4. Blue and gold spheres are iridium and iron respectively. The difference between the $P2_1$ and *I2/m* models are the opposing rotations. In $P2_1$ the rotation is in-phase and in *I2/m* the rotation is out of phase.....77

Figure 4.4: Observed, calculated and difference plots from the of the *I4/mmm* structural model of Sr_2FeIrO_4 against neutron powder diffraction data collected at 150 K using the WISH instrument. Tick marks correspond to the following: Green= $Sr_2Fe_2O_5$; Blue= SrO; Red= Ir and Black= Sr_2FeIrO_4.....80

Figure 4.5: Observed, calculated and difference plots from the refinement of the *I2/m* structural model of Sr_2FeIrO_4 against neutron powder diffraction data collected at 1.5 K using the WISH instrument. Tick marks correspond to the following: Orange= Magnetic Unit Cell Green= $Sr_2Fe_2O_5$; Blue= SrO; Red= Ir and Black= Sr_2FeIrO_4.....82

Figure 4.6: a) Zero-field cooled and field-cooled magnetisation data collected from Sr_2FeIrO_4. b) Magnetisation-field isotherms collected from Sr_2FeIrO_4.....85

Figure 4.7: a) Paramagnetic susceptibility extracted from a ferrosubtraction measurement carried out on Sr_2FeIrO_4 b) Saturated ferromagnetic moment extracted from a ferrosubtraction measurement carried out on Sr_2FeIrO_4.....86

Figure 4.8 The refined magnetic unit cell of Sr_2FeIrO_4. The blue and gold spheres are iridium and iron respectively.....88

Figure 4.9: Observed, calculated and difference plots from the 58 º bank for refinement of the *I2/m* structural model of Sr_2FeIrO_4 against neutron powder diffraction data collected at 1.5 K using the WISH instrument. Tick marks correspond to the following: Orange= Magnetic Unit Cell Green= $Sr_2Fe_2O_5$; Blue= SrO; Red= Ir and Black= Sr_2FeIrO_4.....88

Figure 4.10: The ordered magnetic moment on Fe and Ir centres and bond distortion index defined as [[M-O(1)]-[M-O(2)]]/[0.5x[[M-O(1)+[M-O(2)]]] extracted from fits to neutron diffraction data.....89

Figure 4.11: The proposed electronic states of square planar Ir^{II}, square planar Ir^{I} and octahedral Ir^{III} in an oxide ligand field.....91

Figure 4.12: The magnetic coupling scheme of Sr_2FeIrO_4. Blue and gold spheres are iridium and iron respectively.....95

Figure 4.13: The iron and iridium magnetic sublattices of Sr_2FeIrO_4. Blue and gold spheres are iridium and iron respectively.....95

Figure 4.14: The three key magnetic couplings in the *ab*-plane of Sr_2FeIrO_4. Blue and gold spheres are iridium and iron respectively.....96

Figure 4.15: The three key magnetic ground states that arise from different magnitudes of the coupling constants shown in Figure 4.13. I) Is if $J_\alpha > J_\beta, J_\gamma$ II) Is if $J_\gamma > J_\beta > J_\alpha$ and III) Is if $J_\beta \approx J_\gamma > J_\alpha$.....98

Figure 4.16: The three key magnetic couplings in the *ab*-plane of Sr_2FeIrO_4. Blue and gold spheres are iridium and iron respectively.....100

Figure 5.1: The orbital arrangements of a) an iridium free ion, b) iridium in octahedral co-ordination c) iridium in octahedral co-ordination with spin-orbit coupling.....104

Figure 5.2: Structural models of the three possible structures of Sr_2FeIrO_6. Blue and brown spheres are iridium and iron respectively.....107

Figure 5.3: Observed, calculated and difference plots from the refinement of the $I\bar{1}$, *I2/m* and $P2_1/n$ structural models of Sr_2FeIrO_6 against synchrotron powder diffraction data collected at room temperature using the I11 instrument.....108

Figure 5.4: Observed, calculated and difference plots from the refinement of the $I\bar{1}$, *I2/m* and $P2_1/n$ structural models of $La_{0.05}Sr_{1.95}FeIrO_6$ against synchrotron powder diffraction data collected at room temperature using the I11 instrument.....110

Figure 5.5: Observed, calculated and difference plots from the refinement of the $I\bar{1}$ + $P2_1/n$ and *I2/m* + $P2_1/n$ two-phase structural models of $La_{0.05}Sr_{1.95}FeIrO_6$ against synchrotron powder diffraction data collected at room temperature using the I11 instrument.....112

Figure 5.6: The lattice parameters extracted from the refinement of synchrotron X-ray diffraction data collected from $La_{0.5}Sr_{1.95}FeIrO_6$ in the temperature range $100 \leq T / K \leq 300$. Left) $I\bar{1}$ phase Right) $P2_1/n$ phase.....113

Figure 5.7: Observed, calculated and difference plots from the 152.91 º bank for refinement of the $I\bar{1}$ + $P2_1/n$ structural model of $La_{0.05}Sr_{1.95}FeIrO_6$ against neutron powder diffraction data collected at 1.5 K using the WISH instrument. The arrows highlight weak primitive peaks.....115

Figure 5.8: Observed, calculated and difference plots from the 152.91 º bank for refinement of the $I2/m$ structural model of Sr_2FeIrO_4 against neutron powder diffraction data collected at 1.5 K using the WISH instrument. Tick marks correspond to the following: Black= $I\bar{1}$ Red= $P2_1/n$.....116

Figure 5.9: a) Zero-field cooled and field-cooled magnetisation data collected from $La_{0.05}Sr_{1.95}FeIrO_6$. b) Magnetisation-field isotherms collected from $La_{0.05}Sr_{1.95}FeIrO_6$..119

Figure 5.10: Zero-field cooled and field-cooled magnetisation data collected from Sr_2FeIrO_6.....120

Figure 5.11 The refined magnetic unit cell of $La_{0.05}Sr_{1.95}FeIrO_6$. The blue and brown spheres are iridium and iron respectively.....121

Figure 5.12: Observed, calculated and difference plots from the 152.91 º bank for refinement of the $I\bar{1}$ + $P2_1/n$ structural model of $La_{0.05}Sr_{1.95}FeIrO_6$ against neutron powder diffraction data collected at 1.5 K using the WISH instrument. Tick marks correspond to the following: Black= $I\bar{1}$ Red= $P2_1/n$ Blue= Magnetic model.....122

Figure 5.13: The zero-field cooled and field-cooled magnetisation data of $La_{0.05}Sr_{1.95}FeIrO_6$ and the refined ordered moments extracted from refinements of neutron diffraction data.....123

Figure 5.14: ^{57}Fe Mössbauer spectra collected at 293 K, 200 K and 10 K.....124

Figure 5.15: Observed, calculated and difference plots from the refinement of the $I\bar{1}$, $I2/m$ and $P2_1/n$ structural models of $La_{0.025}Sr_{1.975}FeIrO_6$ against synchrotron powder diffraction data collected at room temperature using the I11 instrument.....127

Figure 5.16: Observed, calculated and difference plots from the refinement of the $I\bar{1}$, $I2/m$ and $P2_1/n$ structural models of $Ca_{0.05}Sr_{1.95}FeIrO_6$ against synchrotron powder diffraction data collected at room temperature using the I11 instrument.....128

Figure 5.17: Observed, calculated and difference plots from the refinement of the $I\bar{1}$, $I2/m$ and $P2_1/n$ structural models of $Ba_{0.0185}Ca_{0.315}Sr_{1.95}FeIrO_6$ against synchrotron powder diffraction data collected at room temperature using the I11 instrument.....129

Figure 5.18: Observed, calculated and difference plots from the refinement of the $I\bar{1}$, $I2/m$ and $P2_1/n$ structural models of $Sr_2Ga_{0.05}Fe_{0.95}IrO_6$ against synchrotron powder diffraction data collected at room temperature using the I11 instrument.....130

Figure 5.19: Observed, calculated and difference plots from the refinement of the $I\bar{1}$ + $P2_1/n$ and $I2/m$ + $P2_1/n$ two-phase structural models of $La_{0.025}Sr_{1.975}FeIrO_6$ against

synchrotron powder diffraction data collected at room temperature using the I11 instrument.....132

Figure 5.20: Observed, calculated and difference plots from the refinement of the $I\bar{1}$ + $P2_1/n$ and $I2/m$ + $P2_1/n$ two-phase structural models of $Ca_{0.05}Sr_{1.95}FeIrO_6$ against synchrotron powder diffraction data collected at room temperature using the I11 instrument.....133

Figure 5.21: Observed, calculated and difference plots from the refinement of the $I\bar{1}$ + $P2_1/n$ and $I2/m$ + $P2_1/n$ two-phase structural models of $Ba_{0.0185}Ca_{0.315}Sr_{1.95}FeIrO_6$ against synchrotron powder diffraction data collected at room temperature using the I11 instrument.....134

Figure 5.22: Observed, calculated and difference plots from the refinement of the $I\bar{1}$ + $P2_1/n$ and $I2/m$ + $P2_1/n$ two-phase structural models of $Sr_2Ga_{0.05}Fe_{0.95}IrO_6$ against synchrotron powder diffraction data collected at room temperature using the I11 instrument.....135

Figure 5.23: Zero-field cooled and field-cooled magnetisation data collected from Sr_2FeIrO_6 and all other doped samples.....137

Figure 5.24: Magnetisation-field isotherms collected from a) $La_{0.025}Sr_{1.95}FeIrO_6$ b) $Ca_{0.05}Sr_{1.95}FeIrO_6$ c) $Ba_{0.0185}Ca_{0.0315}FeIrO_6$ d) $Sr_2Ga_{0.05}Fe_{0.95}IrO_6$.....138

Figure 5.25: MO_6 bond lengths extracted from refinement of neutron diffraction data collected from the WISH instrument at 250 K. The Blue and brown spheres are iron and iridium respectively.....144

Figure 5.26: The electronic states of Ir^{V} and Fe^{III} in Sr_2FeIrO_6.....146

Figure 5.27: Observed, calculated and difference plots from the refinement of the $I\bar{1}$ + $P2_1/n$ and $I2/m$ + $P2_1/n$ two-phase structural models of $La_{0.05}Sr_{1.95}FeIrO_6$ against synchrotron powder diffraction data collected at room temperature using the I11 instrument with 0.03% weight fraction of Sr_2IrO_4. Tick marks correspond to the following: Black= $I\bar{1}$ Red= $P2_1/n$ Blue= Sr_2IrO_4.....147

Figure 5.28: Left) The magnetic unit cell of Sr_2FeIrO_6 Right) The refined magnetic unit cell of $La_{0.05}Sr_{1.95}FeIrO_6$.....148

Figure 5.29: The lattice parameters extracted from the refinement of the $P2_1/n$ model against synchrotron X-ray diffraction data collected from $La_{0.5}Sr_{1.95}FeIrO_6$ in the temperature range $100 \leq T / K \leq 300$ compared to the magnetisation data of $La_{0.05}Sr_{1.95}FeIrO_6$.....150

Figure 6.1: The structural unit cell of $Sr_2Fe_{0.5}Ir_{0.5}O_4$ with $I4/mmm$ space symmetry. The blue and gold spheres are iridium and iron respectively.....157

Figure 6.2: Observed, calculated and difference plots from the refinement of the $I4/mmm$ structural model of $Sr_2Fe_{0.5}Ir_{0.5}O_4$ against synchrotron powder diffraction data collected at room temperature using the I11 instrument. $\chi^2 = 155.9$, $wR_p = 5.43\%$ and $R_p = 3.23\%$; $a = b = 3.91762(4)$ Å, $c = 12.5845(1)$ Å.....158

Figure 6.3: Observed, calculated and difference plots from the of the *I*4/*mmm* structural model of $Sr_2Fe_{0.5}Ir_{0.5}O_4$ against the neutron powder diffraction data collected at room temperature using the D2B instrument.....159

Figure 6.4: a) Zero-field cooled and field-cooled magnetisation data collected from $Sr_2Fe_{0.5}Ir_{0.5}O_4$. b) Magnetisation-field isotherms collected from $Sr_2Fe_{0.5}Ir_{0.5}O_4$.....161

Figure 6.5: Observed, calculated and difference plots from the of the *I*4*mmm* structural model of $Sr_2Fe_{0.5}Ir_{0.5}O_4$ against the neutron powder diffraction data collected at 5 K using the D2B instrument.....162

Figure 6.6: Thermogravimetric data collected during the oxidation of $Sr_2Fe_{0.5}Ir_{0.5}O_{4-x}$ to $Sr_2Fe_{0.5}Ir_{0.5}O_4$.....164

Figure 6.7: Observed, calculated and difference plots from the refinement of the *Immm* structural model of $Sr_2Fe_{0.5}Ir_{0.5}O_3$ against synchrotron powder diffraction data collected at room temperature using the I11 instrument. $\chi^2 = 39.98$, $wR_p = 3.37\%$ and $R_p = 2.24\%$; a = 3.9232(1) Å, b = 3.6426 (1) Å, c = 12.8486(4) Å.....165

Figure 6.8: The structural unit cell of $Sr_2Fe_{0.5}Ir_{0.5}O_3$ with *Immm* space symmetry. The blue and gold spheres are iridium and iron respectively.....165

Figure 6.9: Observed, calculated and difference plots from the of the *Immm* structural model of $Sr_2Fe_{0.5}Ir_{0.5}O_3$ against the neutron powder diffraction data collected at room temperature using the D2B instrument. The tick marks correspond to the following: Black = $Sr_2Fe_{0.5}Ir_{0.5}O_3$; Red = SrO.....166

Figure 6.10: a) Zero-field cooled and field-cooled magnetisation data collected from $Sr_2Fe_{0.5}Ir_{0.5}O_3$. b) Magnetisation-field isotherms collected from $Sr_2Fe_{0.5}Ir_{0.5}O_3$.....168

Figure 6.11: Observed, calculated and difference plots from the of the *Immm* structural model of $Sr_2Fe_{0.5}Ir_{0.5}O_3$ against the neutron powder diffraction data collected at 5 K using the D2B instrument. The tick marks correspond to the following: Black = $Sr_2Fe_{0.5}Ir_{0.5}O_3$; Red = SrO.....169

Figure 6.12: The unit cells of Sr_2FeIrO_6 (left) and $Sr_2Fe_{0.5}Ir_{0.5}O_4$ (right). The blue and gold spheres are iridium and iron respectively.....171

Figure 6.13: A cartoon representation of paracrystallinity: a) a disordered arrangement of ordered layers, b) the disordered structure "seen" by diffraction.....173

Figure 6.14: The ZFC-FC plots of $La_{0.05}Sr_{1.95}FeIrO_6$ (Top) and $Sr_2Fe_{0.5}Ir_{0.5}O_4$ (Bottom).....178

Figure 6.15: The unit cells of Sr_2FeIrO_4 (left) and $Sr_2Fe_{0.5}Ir_{0.5}O_3$ (right).....182

Figure 6.16: The magnetisation isotherms collected from Sr_2FeIrO_4 and $Sr_2Fe_{0.5}Ir_{0.5}O_3$ at 5 K.....184

Figure 6.17: The coupling regime in Sr_2FeIrO_4 and the frustration present due to the 7% antisite disorder.....185

Figure 6.18: The coupling regime in $Sr_2Fe_{0.5}Ir_{0.5}O_3$ and the frustration present due to antisite disorder.....186

Figure 7.1: The crystal structures of $CaMnO_{2.5}$, $La_{0.5}Ba_{0.5}MnO_{2.5}$ and $Sr_3Mn_2O_{6+\delta}$.....190

Figure 7.2: Thermogravimetric data collected during the oxidation of $CaMn_{0.5}Ir_{0.5}O_{2.5}$ to $CaMn_{0.5}Ir_{0.5}O_3$.....192

Figure 7.3: The $40 \leq 2\theta / ^{o} \leq 50$ portion of the refinement of a cubic model against the synchrotron X-ray powder diffraction data collected from $CaMn_{0.5}Ir_{0.5}O_{2.5}$.....193

Figure 7.4: The structural unit cell of $CaMn_{0.5}Ir_{0.5}O_{2.5}$ with *Pnma* space symmetry. The blue and purple spheres are iridium and manganese respectively.....194

Figure 7.5: Observed, calculated and difference plots from the refinement of the *Pnma* structural model of $CaMn_{0.5}Ir_{0.5}O_{2.5}$ against synchrotron powder diffraction data collected at room temperature using the I11 instrument. χ^2 = 8.499, wRp = 2.08% Rp= 1.49%; a = 5.4087(1) Å, b = 7.6243(1) Å, c = 5.3953 (1) Å, V = 222.497(7) $Å^3$.....194

Figure 7.6: The structural unit cell of $CaMn_{0.5}Ir_{0.5}O_{2.5}$ with *Pnma* space symmetry extracted from the refinement shown in Figure 7.9. The blue and purple spheres are iridium and manganese respectively.....196

Figure 7.7: Observed, calculated and difference plots from the refinement of the *Pnma* structural model of $CaMn_{0.5}Ir_{0.5}O_{2.5}$ against neutron powder diffraction data collected at room temperature using the I11 instrument.....196

Figure 7.8: a) Zero-field cooled and field-cooled magnetisation data collected from $CaMn_{0.5}Ir_{0.5}O_{2.5}$. b) Magnetisation-field isotherms collected from $CaMn_{0.5}Ir_{0.5}O_{2.5}$...199

Figure 7.9: Observed, calculated and difference plots from the refinement of the *Pnma* structural model of $CaMn_{0.5}Ir_{0.5}O_{2.5}$ against neutron powder diffraction data collected at 5 K using the I11 instrument.....200

Figure 7.10: The crystal structures of $CaMnO_{2.5}$, $La_2Co_2O_5$, $La_2Cu_2O_5$, $La_2Ni_2O_5$ and $YBaCo_2O_5$.....205

Figure 7.11: The electronic structures of tetrahedral and square pyramidal coordinated Mn^{III}.....206

Figure 7.12: The proposed microstructure of $CaMn_{0.5}Ir_{0.5}O_{2.5}$ and the observed structure of $CaMn_{0.5}Ir_{0.5}O_{2.5}$.....210

Figure 7.13: a) The electronic states on Mn^{III} and Ir^{III} in square pyramidal coordination geometries. b) The local couplings of a MnO_5 site that lead to an antiferromagnetic state. c) The local couplings of an Ir substituted site that lead to frustration.....212

Figure 8.1: The structural unit cell of $La_xSr_{2-x}Co_{0.5}Ir_{0.5}O_4$ (x = 0, 0.5) with *I*4/*mmm* space symmetry. The light blue and dark blue spheres are cobalt and iridium respectively.....216

Figure 8.2: Observed, calculated and difference plots from the refinement of the *I*4/*mmm* structural model of $Sr_2Co_{0.5}Ir_{0.5}O_4$ against synchrotron powder diffraction data collected

at room temperature using the I11 instrument. χ^2 = 11.78, wR_p = 2.39% and R_p = 1.65%; *a* = *b* = 3.91987(2) Å, *c* = 12.4997(1) Å.....217

Figure 8.3: Observed, calculated and difference plots from the refinement of the *I*4/*mmm* structural model of $La_{0.5}Sr_{1.5}Co_{0.5}Ir_{0.5}O_4$ against synchrotron powder diffraction data collected at room temperature using the I11 instrument. χ^2 = 19.20, wR_p = 4.43% and R_p = 2.79%; *a* = *b* = 3.88737(1) Å, *c* = 12.61233(4) Å.....217

Figure 8.4: Observed, calculated and difference plots from the of the *I*4/*mmm* structural model of $Sr_2Co_{0.5}Ir_{0.5}O_4$ against the neutron powder diffraction data collected at room temperature using the D2B instrument.....218

Figure 8.5: Observed, calculated and difference plots from the of the *I*4/*mmm* structural model of $La_{0.5}Sr_{1.5}Co_{0.5}Ir_{0.5}O_4$ against the neutron powder diffraction data collected at room temperature using the D2B instrument.....219

Figure 8.6: Zero-field cooled and field-cooled magnetisation data collected from $La_{0.5}Sr_{1.5}Co_{0.5}Ir_{0.5}O_4$ (Top left) and $Sr_2Co_{0.5}Ir_{0.5}O_4$ (Top right). Magnetisation-field isotherms collected from $La_{0.5}Sr_{1.5}Co_{0.5}Ir_{0.5}O_4$ (Bottom left) and $Sr_2Co_{0.5}Ir_{0.5}O_4$ (Bottom right).....222

Figure 8.7: Observed, calculated and difference plots from the of the *I*4/*mmm* structural model of $La_{0.5}Sr_{1.5}Co_{0.5}Ir_{0.5}O_4$ against the neutron powder diffraction data collected at 5 K using the D2B instrument.....223

Figure 8.8: The coupling regime in $Sr_2Co_{0.5}Ir_{0.5}O_4$ that could lead to a spin glass state.....228

Figure 9.1: Thermogravimetric data collected during the oxidation of: Left) $La_{0.5}Sr_{1.5}Co_{0.5}Ir_{0.5}O_{4-y}$ to $La_{0.5}Sr_{1.5}Co_{0.5}Ir_{0.5}O_4$ Right) $Sr_2Co_{0.5}Ir_{0.5}O_{4-y}$ to $Sr_2Co_{0.5}Ir_{0.5}O_3$.....232

Figure 9.2: The structural unit cell of $La_xSr_{2-x}Co_{0.5}Ir_{0.5}O_3$ (x = 0, 0.5) with *Immm* space symmetry. The light blue and dark blue spheres are cobalt and iridium respectively....233

Figure 9.3: Observed, calculated and difference plots from the refinement of the *I*4/*mmm* structural model of $La_{0.5}Sr_{1.5}Co_{0.5}Ir_{0.5}O_3$ against synchrotron powder diffraction data collected at room temperature using the I11 instrument. χ^2 = 12.53, wR_p = 2.28% and R_p = 1.60%; *a* = 3.87941(6) Å, b = 3.57603(6) Å, *c* = 13.0066(1) Å.....233

Figure 9.4: Observed, calculated and difference plots from the refinement of the *I*4/*mmm* structural model of $Sr_2Co_{0.5}Ir_{0.5}O_3$ against synchrotron powder diffraction data collected at room temperature using the I11 instrument. χ^2 = 28.10, wR_p = 2.88% and R_p = 1.97%; *a* = 3.9180(1) Å, *b* = 3.5799(1) Å, *c* = 12.8656(4) Å.....234

Figure 9.5: Observed, calculated and difference plots from the of the *I*4/*mmm* structural model of $La_{0.5}Sr_{1.5}Co_{0.5}Ir_{0.5}O_3$ against the neutron powder diffraction data collected at room temperature using the D2B instrument. Tick marks correspond to the following: Black = $La_{0.5}Sr_{1.5}Co_{0.5}Ir_{0.5}O_3$, Red = SrO.....235

Figure 9.6: Observed, calculated and difference plots from the of the *I*4/*mmm* structural model of $Sr_2Co_{0.5}Ir_{0.5}O_3$ against the neutron powder diffraction data collected at room

temperature using the D2B instrument. Tick marks correspond to the following: Black = $Sr_2Co_{0.5}Ir_{0.5}O_3$, Red = SrO.....236

Figure 9.7: The potential twisting distortions present in $La_xSr_{2-x}Co_{0.5}Ir_{0.5}O_3$.....239

Figure 9.8: The thermal ellipsoids of $Sr_2Co_{0.5}Ir_{0.5}O_3$ (left) and $La_{0.5}Sr_{1.5}Co_{0.5}Ir_{0.5}O_3$ (right). The colours of the ellipsoids correspond to the following: Blue = Cobalt/Iridium; Red = Oxygen; Grey = Strontium/Lanthanum.....240

Figure 9.9: A cartoon representation of how an undetectable distortion alters the bond lengths extracted from refinement of neutron powder diffraction data. a) the bonds as "seen" by diffraction b) the true distorted structure.....241

Figure 9.10: The unit cells of $Sr_2Co_{0.5}Ir_{0.5}O_3$ (Left) and $La_{0.5}Sr_{1.5}Co_{0.5}Ir_{0.5}O_3$ (Right) extracted from the split-site refinements of the neutron powder diffraction data collected at room temperature. The light blue and dark blue spheres are cobalt and iridium respectively.....242

Figure 9.11: Observed, calculated and difference plots from the of the "split site" *I*4/*mmm* structural model of $La_{0.5}Sr_{1.5}Co_{0.5}Ir_{0.5}O_3$ against the neutron powder diffraction data collected at room temperature using the D2B instrument. Tick marks correspond to the following: Black = $La_{0.5}Sr_{1.5}Co_{0.5}Ir_{0.5}O_3$, Red = SrO.....243

Figure 9.12: Observed, calculated and difference plots from the of the "split site" *I*4/*mmm* structural model of $Sr_2Co_{0.5}Ir_{0.5}O_3$ against the neutron powder diffraction data collected at room temperature using the D2B instrument. Tick marks correspond to the following: Black = $La_{0.5}Sr_{1.5}Co_{0.5}Ir_{0.5}O_3$, Red = SrO.....244

Figure 9.13: Top left) Paramagnetic susceptibility of $Sr_2Co_{0.5}Ir_{0.5}O_4$. Bottom left) Saturated ferromagnetic moment of $Sr_2Co_{0.5}Ir_{0.5}O_4$. Top right) Paramagnetic susceptibility of $La_{0.5}Sr_{1.5}Co_{0.5}Ir_{0.5}O_4$. Bottom right) Saturated ferromagnetic moment of $La_{0.5}Sr_{1.5}Co_{0.5}Ir_{0.5}O_4$.....246

Figure 9.14: Magnetisation isotherms collected at 5 K from: Left) $Sr_2Co_{0.5}Ir_{0.5}O_3$ and Right) $La_{0.5}Sr_{1.5}Co_{0.5}Ir_{0.5}O_3$.....247

Figure 9.15: Observed, calculated and difference plots from the of the *I*4/*mmm* structural model of $La_{0.5}Sr_{1.5}Co_{0.5}Ir_{0.5}O_3$ against the neutron powder diffraction data collected at 5 K using the D2B instrument. Tick marks correspond to the following: Black = $La_{0.5}Sr_{1.5}Co_{0.5}Ir_{0.5}O_3$, Red = SrO.....248

Figure 9.16: Observed, calculated and difference plots from the of the *I*4/*mmm* structural model of $Sr_2Co_{0.5}Ir_{0.5}O_3$ against the neutron powder diffraction data collected at 5 K using the D2B instrument. Tick marks correspond to the following: Black = $La_{0.5}Sr_{1.5}Co_{0.5}Ir_{0.5}O_3$, Red = SrO.....249

Figure 9.17: The electronic states of square planar Co^{I} and Co^{II}.....252

Bibliography

1. https://www.ill.eu/users/instruments/instruments-list/d2b/how-it-works/simulated-experiment/.
2. Poeppelmeier, K. R.; Leonowicz, M. E.; Longo, J. M., CaMnO2.5 and Ca2MnO3.5: New oxygen-defect perovskite-type oxides. *Journal of Solid State Chemistry* **1982,** *44* (1), 89-98.
3. Cox, P. A., *Transition Metal Oxides: An Introduction to Their Electronic Structure and Properties*. OUP: Oxford, 2010.
4. Rao, C. N. R. R., B., *Transition Metal Oxides: Structure, Properties and Synthesis of Ceramic Oxides*. Wiley: 1998.
5. Norman, M. R.; Pépin, C., The electronic nature of high temperature cuprate superconductors. *Reports on Progress in Physics* **2003,** *66* (10), 1547.
6. Bednorz, J. G.; Müller, K. A., Possible highT c superconductivity in the Ba−La−Cu−O system. *Z. Physik B - Condensed Matter* **1986,** *64* (2), 189-193.
7. Coey, J. M. D.; Chien, C. L., Half-Metallic Ferromagnetic Oxides. *MRS Bulletin* **2003,** *28* (10), 720-724.
8. Kobayashi, K. I.; Kimura, T.; Tomioka, Y.; Sawada, H.; Terakura, K.; Tokura, Y., *Intergrain Tunneling Magnetoresistance in Polycrystals of the Ordered Double Perovskite Sr2FeReO6*. 1999; Vol. 591, p 69977-11162.
9. Eerenstein, W.; Mathur, N. D.; Scott, J. F., Multiferroic and magnetoelectric materials. *Nature* **2006,** *442* (7104), 759-765.
10. Moreau, J. M. M., C.; Gerson, R.; James, W. J., Ferroelectric bismuth ferrite [BiFeO3] x-ray and neutron diffraction study. *Journal of Physics and Chemistry of Solids* **1971,** *32* (4), 1315-20.
11. Spaldin, N. A., *Magnetic Materials: Fundamentals and Applications*. Cambridge University Press: Cambridge, 2010.
12. Peña, M. A.; Fierro, J. L. G., Chemical Structures and Performance of Perovskite Oxides. *Chemical Reviews* **2001,** *101* (7), 1981-2018.
13. Dawber, M.; Rabe, K. M.; Scott, J. F., Physics of thin-film ferroelectric oxides. *Reviews of Modern Physics* **2005,** *77* (4), 1083-1130.
14. *Perovskite Oxide for Solid Oxide Fuel Cells*. Springer US: 2009.
15. Cox, P. A., *The Electronic Structure and Chemistry of Solids*. OUP: Oxford, 1987.
16. Electron correlations in narrow energy bands. *Proceedings of the Royal Society of London. Series A. Mathematical and Physical Sciences* **1963,** *276* (1365), 238-257.
17. Moruzzi, V. L. M., P. M.; Schwarz, K.; Mohn, P., Ferromagnetic phases of bcc, and fcc. iron, cobalt, and nickel. *Physical Review B: Condensed Matter and Materials Physics* **1986,** *34* (3), 1784-91.
18. Blundell, S., *Magnetism in Condensed Matter*. OUP: United States, 2001.
19. Orchard, A. F., *Magnetochemistry*. OUP: Oxford, 2003; Vol. 75.
20. Ge, M.; Tan, S.; Huang, Y.; Zhang, L.; Tong, W.; Pi, L.; Zhang, Y., Magnetism of insulator Sr2IrO4 with strong spin–orbit coupling. *Journal of Magnetism and Magnetic Materials* **2013,** *345* (0), 13-17.
21. Choi, S. K.; Coldea, R.; Kolmogorov, A. N.; Lancaster, T.; Mazin, I. I.; Blundell, S. J.; Radaelli, P. G.; Singh, Y.; Gegenwart, P.; Choi, K. R.; Cheong, S. W.; Baker, P. J.; Stock, C.; Taylor, J., Spin Waves and Revised Crystal Structure of Honeycomb Iridate ${\mathrm{Na}}_{2}{\mathrm{IrO}}_{3}$. *Physical Review Letters* **2012,** *108* (12), 127204.

22. Battle, P. D.; Blake, G. R.; Gibb, T. C.; Vente, J. F., Structural Chemistry and Electronic Properties of Sr2FeIrO6. *Journal of Solid State Chemistry* **1999,** *145* (2), 541-548.
23. Battle, P. D.; Gore, J. G.; Hollyman, R. C.; Powell, A. V., The magnetic properties of BaLaCoIrO6 and Ba3CoIrxRu2−xO9. *Journal of Alloys and Compounds* **1995,** *218* (1), 110-116.
24. Bremholm, M.; Dutton, S. E.; Stephens, P. W.; Cava, R. J., NaIrO3—A pentavalent post-perovskite. *Journal of Solid State Chemistry* **2011,** *184* (3), 601-607.
25. K., W. K.; Stefano, A.; Arata, T.; Martin, J.; Hao, T. L., Comparative Study of Potentially Jeff = 0 Ground State Iridium(V) in SrLaNiIrO6, SrLaMgIrO6, and SrLaZnIrO6. *Zeitschrift für anorganische und allgemeine Chemie* **2017,** *643* (23), 2095-2101.
26. Mugavero Iii, S. J.; Smith, M. D.; zur Loye, H.-C., The crystal growth and magnetic properties of Ln2LiIrO6 (Ln=La, Pr, Nd, Sm, Eu). *Journal of Solid State Chemistry* **2005,** *178* (1), 200-206.
27. Davis, M. J.; Mugavero, S. J.; Glab, K. I.; Smith, M. D.; zur Loye, H.-C., The crystal growth and characterization of the lanthanide-containing double perovskites Ln2NaIrO6 (Ln=La, Pr, Nd). *Solid State Sciences* **2004,** *6* (5), 413-417.
28. Kayser, P.; Kennedy, B. J.; Ranjbar, B.; Kimpton, J. A.; Avdeev, M., Spin–Orbit Coupling Controlled Ground State in the Ir(V) Perovskites A2ScIrO6 (A = Ba or Sr). *Inorganic Chemistry* **2017,** *56* (4), 2204-2209.
29. Ranjbar, B.; Reynolds, E.; Kayser, P.; Kennedy, B. J.; Hester, J. R.; Kimpton, J. A., Structural and Magnetic Properties of the Iridium Double Perovskites Ba2–xSrxYIrO6. *Inorganic Chemistry* **2015,** *54* (21), 10468-10476.
30. Dey, T.; Maljuk, A.; Efremov, D. V.; Kataeva, O.; Gass, S.; Blum, C. G. F.; Steckel, F.; Gruner, D.; Ritschel, T.; Wolter, A. U. B.; Geck, J.; Hess, C.; Koepernik, K.; van den Brink, J.; Wurmehl, S.; Büchner, B., ${\text{Ba}}_{2}{\text{YIrO}}_{6}$: A cubic double perovskite material with ${\text{Ir}}^{5+}$ ions. *Physical Review B* **2016,** *93* (1), 014434.
31. Wakeshima, M.; Harada, D.; Hinatsu, Y., Crystal structures and magnetic properties of ordered perovskites A2R3+Ir5+O6 (A=Sr, Ba; R=Sc, Y, La, Lu). *Journal of Alloys and Compounds* **1999,** *287* (1), 130-136.
32. Tilley, R. J. D., *Perovskites: Structure-Property Relationships*. Wiley: United Kingdom, 2016.
33. Goldschmidt, V. M., *Naturwissenschaften* **1926,** *14*.
34. King, G.; Woodward, P., Cation Order in perovskites. *Journal of Materials Chemistry* **2010,** *20*, 5785-5796.
35. Woodward, P., Octahedral Tilting in Perovskites. I. Geometrical Considerations. *Acta Crystallographica Section B* **1997,** *53* (1), 32-43.
36. Jia, T.; Zeng, Z.; Li, X. G.; Lin, H. Q., The magnetic origin of multiferroic Y2CoMnO6. *Journal of Applied Physics* **2015,** *117* (17), 17E119.
37. Yáñez-Vilar, S.; Mun, E. D.; Zapf, V. S.; Ueland, B. G.; Gardner, J. S.; Thompson, J. D.; Singleton, J.; Sánchez-Andújar, M.; Mira, J.; Biskup, N.; Señarís-Rodríguez, M. A.; Batista, C. D., Multiferroic behavior in the double-perovskite Lu${}_{2}$MnCoO${}_{6}$. *Physical Review B* **2011,** *84* (13), 134427.
38. Dass, R. I.; Yan, J. Q.; Goodenough, J. B., Oxygen stoichiometry, ferromagnetism, and transport properties of ${\mathrm{La}}_{2\ensuremath{-}x}{\mathrm{NiMnO}}_{6+\ensuremath{\delta}}$. *Physical Review B* **2003,** *68* (6), 064415.

39. Azuma, M.; Takata, K.; Saito, T.; Ishiwata, S.; Shimakawa, Y.; Takano, M., Designed Ferromagnetic, Ferroelectric Bi2NiMnO6. *Journal of the American Chemical Society* **2005,** *127* (24), 8889-8892.
40. Bull, C. L.; Gleeson, D.; Knight, K. S., Determination of B-site ordering and structural transformations in the mixed transition metal perovskites La 2 CoMnO 6 and La 2 NiMnO 6. *Journal of Physics: Condensed Matter* **2003,** *15* (29), 4927.
41. Burley, J. C.; Battle, P. D.; Gallon, D. J.; Sloan, J.; Grey, C. P.; Rosseinsky, M. J., Magnetism and Structural Chemistry of the n = 1 Ruddlesden−Popper Phases La4LiMnO8 and La3SrLiMnO8. *Journal of the American Chemical Society* **2002,** *124* (4), 620-628.
42. Hayward, M. A.; Green, M. A.; Rosseinsky, M. J.; Sloan, J., Sodium Hydride as a Powerful Reducing Agent for Topotactic Oxide Deintercalation: Synthesis and Characterization of the Nickel(I) Oxide LaNiO2. *Journal of the American Chemical Society* **1999,** *121* (38), 8843-8854.
43. Hayward, M. A., Topochemical reactions of layered transition-metal oxides. *Semiconductor Science and Technology* **2014,** *29* (6), 064010.
44. Denis Romero, F.; Burr, S. J.; McGrady, J. E.; Gianolio, D.; Cibin, G.; Hayward, M. A., SrFe0.5Ru0.5O2: Square-Planar Ru2+ in an Extended Oxide. *Journal of the American Chemical Society* **2013,** *135* (5), 1838-1844.
45. Amano Patino, M.; Smith, T.; Zhang, W.; Halasyamani, P. S.; Hayward, M. A., Cation Exchange in a 3D Perovskite—Synthesis of Ni0.5TaO3. *Inorganic Chemistry* **2014,** *53* (15), 8020-8024.
46. Denis Romero, F.; Gianolio, D.; Cibin, G.; Bingham, P. A.; d'Hollander, J.-C.; Forder, S. D.; Hayward, M. A., Topochemical Reduction of the Ruddlesden–Popper Phases Sr2Fe0.5Ru0.5O4 and Sr3(Fe0.5Ru0.5)2O7. *Inorganic Chemistry* **2013,** *52* (19), 10920-10928.
47. Tsujimoto, Y.; Tassel, C.; Hayashi, N.; Watanabe, T.; Kageyama, H.; Yoshimura, K.; Takano, M.; Ceretti, M.; Ritter, C.; Paulus, W., Infinite-layer iron oxide with a square-planar coordination. *Nature* **2007,** *450* (7172), 1062-1065.
48. Seddon, J.; Suard, E.; Hayward, M. A., Topotactic Reduction of YBaCo2O5 and LaBaCo2O5: Square-Planar Co(I) in an Extended Oxide. *Journal of the American Chemical Society* **2010,** *132* (8), 2802-2810.
49. Hayward, M. A.; Rosseinsky, M. J., Anion Vacancy Distribution and Magnetism in the New Reduced Layered Co(II)/Co(I) Phase LaSrCoO3.5-x. *Chemistry of Materials* **2000,** *12* (8), 2182-2195.
50. Dixon, E.; Hadermann, J.; Ramos, S.; Goodwin, A. L.; Hayward, M. A., Mn(I) in an Extended Oxide: The Synthesis and Characterization of La1−xCaxMnO2+δ ($0.6 \leq x \leq 1$). *Journal of the American Chemical Society* **2011,** *133* (45), 18397-18405.
51. Dann, S. E.; Weller, M. T.; Currie, D. B., Structure and oxygen stoichiometry in Sr3Fe2O7−y, $0 \leq y \leq 1.0$. *Journal of Solid State Chemistry* **1992,** *97* (1), 179-185.
52. Gillie, L. J.; Wright, A. J.; Hadermann, J.; Van Tendeloo, G.; Greaves, C., Synthesis and characterization of the reduced double-layer manganite Sr3Mn2O6+x. *Journal of Solid State Chemistry* **2003,** *175* (2), 188-196.
53. Kageyama, H.; Watanabe, T.; Tsujimoto, Y.; Kitada, A.; Sumida, Y.; Kanamori, K.; Yoshimura, K.; Hayashi, N.; Muranaka, S.; Takano, M.; Ceretti, M.; Paulus, W.; Ritter, C.; André, G., Spin-Ladder Iron Oxide: Sr3Fe2O5. *Angewandte Chemie International Edition* **2008,** *47* (31), 5740-5745.
54. Dixon, E.; Hayward, M. A., The Topotactic Reduction of Sr3Fe2O5Cl2—Square Planar Fe(II) in an Extended Oxyhalide. *Inorganic Chemistry* **2010,** *49* (20), 9649-9654.

55. Denis Romero, F.; Leach, A.; Möller, J. S.; Foronda, F.; Blundell, S. J.; Hayward, M. A., Strontium Vanadium Oxide–Hydrides: "Square-Planar" Two-Electron Phases. *Angewandte Chemie International Edition* **2014,** *53* (29), 7556-7559.
56. Sakaguchi, T.; Kobayashi, Y.; Yajima, T.; Ohkura, M.; Tassel, C.; Takeiri, F.; Mitsuoka, S.; Ohkubo, H.; Yamamoto, T.; Kim, J. e.; Tsuji, N.; Fujihara, A.; Matsushita, Y.; Hester, J.; Avdeev, M.; Ohoyama, K.; Kageyama, H., Oxyhydrides of (Ca,Sr,Ba)TiO3 Perovskite Solid Solutions. *Inorganic Chemistry* **2012,** *51* (21), 11371-11376.
57. Tassel, C.; Goto, Y.; Kuno, Y.; Hester, J.; Green, M.; Kobayashi, Y.; Kageyama, H., Direct Synthesis of Chromium Perovskite Oxyhydride with a High Magnetic-Transition Temperature. *Angewandte Chemie International Edition* **2014,** *53* (39), 10377-10380.
58. Hayward, M. A.; Cussen, E. J.; Claridge, J. B.; Bieringer, M.; Rosseinsky, M. J.; Kiely, C. J.; Blundell, S. J.; Marshall, I. M.; Pratt, F. L., The Hydride Anion in an Extended Transition Metal Oxide Array: LaSrCoO3H0.7. *Science* **2002,** *295* (5561), 1882-1884.
59. Lun, J.; Michael, L.; Dihao, Z.; K., K. F. K.; Franz, L.; Pascal, M.; J., B. S.; E., M. J.; A., H. M., LaSr3NiRuO4H4: A 4d Transition-Metal Oxide–Hydride Containing Metal Hydride Sheets. *Angewandte Chemie International Edition* **2018,** *57* (18), 5025-5028.
60. Wollan, E. O.; Koehler, W. C., Neutron Diffraction Study of the Magnetic Properties of the Series of Perovskite-Type Compounds $[(1\ensuremath{-}x)\mathrm{La}, x\mathrm{Ca}]\mathrm{Mn}{\mathrm{O}}_{3}$. *Physical Review* **1955,** *100* (2), 545-563.
61. Tokura, Y., *Colossal Magnetoresistive Oxides*. Gordan and Breach Science Publishers: 2000.
62. Goodenough, J. B., Metallic oxides. *Progress in Solid State Chemistry* **1971,** *5*, 145-399.
63. Wang, X. L.; Takayama-Muromachi, E., Magnetic and transport properties of the layered perovskite system ${\mathrm{Sr}}_{2\ensuremath{-}y}{\mathrm{Y}}_{y}\mathrm{Co}{\mathrm{O}}_{4}$ $(0\ensuremath{\leqslant}y\ensuremath{\leqslant}1)$. *Physical Review B* **2005,** *72* (6), 064401.
64. Allen, P. B.; Berger, H.; Chauvet, O.; Forro, L.; Jarlborg, T.; Junod, A.; Revaz, B.; Santi, G., Transport properties, thermodynamic properties, and electronic structure of ${\mathrm{SrRuO}}_{3}$. *Physical Review B* **1996,** *53* (8), 4393-4398.
65. Itoh, M.; Shimura, T.; Inaguma, Y.; Morii, Y., Structure of Two-Dimensional Conductor of Sr2RhO4. *Journal of Solid State Chemistry* **1995,** *118* (1), 206-209.
66. Huang, Q.; Soubeyroux, J. L.; Chmaissem, O.; Sora, I. N.; Santoro, A.; Cava, R. J.; Krajewski, J. J.; Peck Jr, W. F., Neutron Powder Diffraction Study of the Crystal Structures of Sr2RuO4 and Sr2IrO4 at Room Temperature and at 10 K. *Journal of Solid State Chemistry* **1994,** *112* (2), 355-361.
67. Maeno, Y.; Rice, T. M.; Sigrist, M., The Intriguing Superconductivity of Strontium Ruthenate. *Physics Today* **2001,** *54* (1), 42-47.
68. Nakatsuji, S.; Maeno, Y., Quasi-Two-Dimensional Mott Transition System ${\mathrm{Ca}}_{2\ensuremath{-}\mathit{x}}{\mathrm{Sr}}_{\mathit{x}}{\mathrm{RuO}}_{4}$. *Physical Review Letters* **2000,** *84* (12), 2666-2669.
69. Randall, J. J.; Katz, L.; Ward, R., The Preparation of a Strontium-Iridium Oxide Sr2iro4. *Journal of the American Chemical Society* **1957,** *79* (2), 266-267.
70. Cava, R. J., Schizophrenic electrons in ruthenium-based oxides. *Dalton Transactions* **2004,** (19), 2979-2987.

71. Thompson, S. P.; Parker, J. E.; Potter, J.; Hill, T. P.; Birt, A.; Cobb, T. M.; Yuan, F.; Tang, C. C., Beamline I11 at Diamond: A new instrument for high resolution powder diffraction. *Review of Scientific Instruments* **2009,** *80* (7), 075107.
72. Sears, V. F., Appendix. Neutron Scattering Lengths and Cross Sections. In *Methods in Experimental Physics*, Kurt, S.; David, L. P., Eds. Academic Press: 1986; Vol. Volume 23, Part A, pp 521-550.
73. C. Chapon, L.; Manuel, P.; G. Radaelli, P.; Benson, C.; Perrott, L.; Ansell, S.; J. Rhodes, N.; Raspino, D.; Duxbury, D. M.; Spill, E.; Norris, J., *Wish: The New Powder and Single Crystal Magnetic Diffractometer on the Second Target Station*. 2011; Vol. 22, p 22-25.
74. Rietveld, H., A profile refinement method for nuclear and magnetic structures. *Journal of Applied Crystallography* **1969,** *2* (2), 65-71.
75. Clarke, J., SQUIDs. *Scientfic American* **1994**, 46-53.
76. Bearden, A. J., Mössbauer Effect: Principles and Applications. Gunther K. Wertheim. Academic Press, New York, 1964. viii + 116 pp. Illus. Paper, $2.45; cloth, $5.50. *Science* **1965,** *147* (3662), 1139-1139.
77. Cranshaw, T. E.; Dale, B. W.; Longworth, G. O.; Johnson, C. E., *Mössbauer Spectroscopy and Its Applications*. Cambridge University Press: 1985.
78. Toby, B. *CMPR*.
79. Mizusaki, S.; Sato, J.; Taniguchi, T.; Nagata, Y.; Lai, S. H.; Lan, M. D.; Ozawa, T. C.; Noro, Y.; Samata, H., Ferromagnetism in CaMn 1− x Ir x O 3. *Journal of Physics: Condensed Matter* **2008,** *20* (23), 235242.
80. Mikhailova, D.; Narayanan, N.; Gruner, W.; Voss, A.; Senyshyn, A.; Trots, D. M.; Fuess, H.; Ehrenberg, H., The Role of Oxygen Stoichiometry on Phase Stability, Structure, and Magnetic Properties of Sr2CoIrO6−δ. *Inorganic Chemistry* **2010,** *49* (22), 10348-10356.
81. Narayanan, N.; Mikhailova, D.; Senyshyn, A.; Trots, D. M.; Laskowski, R.; Blaha, P.; Schwarz, K.; Fuess, H.; Ehrenberg, H., Temperature and composition dependence of crystal structures and magnetic and electronic properties of the double perovskites ${\text{La}}_{2\ensuremath{-}x}{\text{Sr}}_{x}{\text{CoIrO}}_{6}$ $(0\ensuremath{\le}x\ensuremath{\le}2)$. *Physical Review B* **2010,** *82* (2), 024403.
82. Daria, M.; Zhiwei, H.; Chang-Yang, K.; Steffen, O.; M., M. K.; Stefano, A.; Jyh-Fu, L.; Chin-Wen, P.; Shin-An, C.; Jenn-Min, L.; Shu-Chih, H.; Jin-Ming, C.; Yen-Fa, L.; Hirofumi, I.; Ku-Ding, T.; Anatoliy, S.; Helmut, E., Charge Transfer and Structural Anomaly in Stoichiometric Layered Perovskite Sr2Co0.5Ir0.5O4. *European Journal of Inorganic Chemistry* **2017,** *2017* (3), 587-595.
83. Romero, F. D.; Coyle, L.; Hayward, M. A., Structure and Magnetism of Sr3Co2O4Cl2—An Electronically Driven Lattice Distortion in an Oxychloride Containing Square Planar CoII Centers. *Journal of the American Chemical Society* **2012,** *134* (38), 15946-15952.
84. Wheeler, T. S., A note on the interaction of glycerol with calcium oxide and calcium hydroxide. *Chem. News* **1931,** *142* (241).
85. Fujii, K.; Kondo, W., Calcium glyceroxides formed in the System of calcium oxide-glycerol. With 4 figures. *Zeitschrift für anorganische und allgemeine Chemie* **1968,** *359* (5-6), 296-304.
86. Bower, R. Topochemical Reduction of Ruthenium-containing Mixed Perovskites. University of Oxford, Oxford, 2014.
87. Patino, M. A.; Zeng, D.; Bower, R.; McGrady, J. E.; Hayward, M. A., Coupled Electronic and Magnetic Phase Transition in the Infinite-Layer Phase LaSrNiRuO4. *Inorganic Chemistry* **2016,** *55* (17), 9012-9016.

88. Linus, P., *The nature of the chemical bond and the structure of molecules and crystals: an introduction to modern structural chemistry*. 3rd ed.; Cornell University Press; Oxford University Press: Ithaca; London, 1960; p 644.
89. Luo, Y., *Comprehensive Handbook of Chemical Bond Energies*. CRC Press: Boca Raton, 2007.
90. Pratt, J. A.; Shepherd, A. M.; Hayward, M. A., Diamagnetic Ru2+ in Na2La2Ti2RuO10–x (0 < x < 2): A Series of Complex Oxides Prepared by Topochemical Reduction. *Inorganic Chemistry* **2015,** *54* (22), 10993-10997.
91. Battle, P. D.; Blake, G. R.; Sloan, J.; Vente, J. F., Commensurate and Incommensurate Phases in the SystemA4A′Ir2O9(A=Sr, Ba;A′=Cu, Zn). *Journal of Solid State Chemistry* **1998,** *136* (1), 103-114.
92. Powell, A. V.; Gore, J. G.; Battle, P. D., The magnetic properties of iridium in mixed-metal oxides. *Journal of Alloys and Compounds* **1993,** *201* (1), 73-84.
93. Takayama, T.; Yaresko, A.; Matsumoto, A.; Nuss, J.; Ishii, K.; Yoshida, M.; Mizuki, J.; Takagi, H., Spin-orbit coupling induced semi-metallic state in the 1/3 hole-doped hyper-kagome Na3Ir3O8. *Scientific Reports* **2014,** *4*, 6818.
94. Siegrist, T.; Chamberland, B. L., The crystal structure of BaIrO3. *Journal of the Less Common Metals* **1991,** *170* (1), 93-99.
95. Fuchigami, K.; Rath, N. P.; Mirica, L. M., Mononuclear Rhodium(II) and Iridium(II) Complexes Supported by Tetradentate Pyridinophane Ligands. *Inorganic Chemistry* **2017,** *56* (16), 9404-9408.
96. Garcia, M. P.; Jiménez, M. V.; Oro, L. A.; Lahoz, F. J.; Alonso, P. J., Ein paramagnetischer, einkerniger metallorganischer Iridium(II)-Komplex: [Ir(C6Cl5)2(cod)]. *Angewandte Chemie* **1992,** *104* (11), 1512-1514.
97. Meiners, J.; Scheibel, M. G.; Lemée-Cailleau, M.-H.; Mason, S. A.; Boeddinghaus, M. B.; Fässler, T. F.; Herdtweck, E.; Khusniyarov, M. M.; Schneider, S., Square-Planar Iridium(II) and Iridium(III) Amido Complexes Stabilized by a PNP Pincer Ligand. *Angewandte Chemie International Edition* **2011,** *50* (35), 8184-8187.
98. Greenwood, N. N.; Earnshaw, A., *Chemistry of the Elements*. Butterworth-Heinemann: Boston, Mass, 1997; Vol. 2nd ed.
99. Tassel, C.; Seinberg, L.; Hayashi, N.; Ganesanpotti, S.; Ajiro, Y.; Kobayashi, Y.; Kageyama, H., Sr2FeO3 with Stacked Infinite Chains of FeO4 Square Planes. *Inorganic Chemistry* **2013,** *52* (10), 6096-6102.
100. Seinberg, L.; Yamamoto, T.; Tassel, C.; Kobayashi, Y.; Hayashi, N.; Kitada, A.; Sumida, Y.; Watanabe, T.; Nishi, M.; Ohoyama, K.; Yoshimura, K.; Takano, M.; Paulus, W.; Kageyama, H., Fe-Site Substitution Effect on the Structural and Magnetic Properties in SrFeO2. *Inorganic Chemistry* **2011,** *50* (9), 3988-3995.
101. Kanungo, S.; Yan, B.; Merz, P.; Felser, C.; Jansen, M., Na4IrO4: Square-Planar Coordination of a Transition Metal in d5 Configuration due to Weak On-Site Coulomb Interactions. *Angewandte Chemie International Edition* **2015,** *54* (18), 5417-5420.
102. Morrow, R.; Freeland, J. W.; Woodward, P. M., Probing the Links between Structure and Magnetism in Sr2–xCaxFeOsO6 Double Perovskites. *Inorganic Chemistry* **2014,** *53* (15), 7983-7992.
103. Morrow, R.; Mishra, R.; Restrepo, O. D.; Ball, M. R.; Windl, W.; Wurmehl, S.; Stockert, U.; Büchner, B.; Woodward, P. M., Independent Ordering of Two Interpenetrating Magnetic Sublattices in the Double Perovskite Sr2CoOsO6. *Journal of the American Chemical Society* **2013,** *135* (50), 18824-18830.
104. Ling, C. D.; Kennedy, B. J.; Zhou, Q.; Spencer, J. R.; Avdeev, M., Synthesis, structures, and phase transitions of barium bismuth iridium oxide perovskites Ba2BiIrO6 and Ba3BiIr2O9. *Journal of Solid State Chemistry* **2010,** *183* (3), 727-735.

105. Kharkwal, K. C.; Pramanik, A. K., Structure, magnetism and electronic properties in 3 d –5 d based double perovskite (##IMG## [http://ej.iop.org/images/0953-8984/29/49/495801/toc_cmaa941aieqn001.gif] {${{\rm Sr}_{1-x}}$} Y x) 2 FeIrO 6. *Journal of Physics: Condensed Matter* **2017,** *29* (49), 495801.
106. Bufaiçal, L.; Adriano, C.; Lora-Serrano, R.; Duque, J. G. S.; Mendonça-Ferreira, L.; Rojas-Ayala, C.; Baggio-Saitovitch, E.; Bittar, E. M.; Pagliuso, P. G., Structural, electronic and magnetic properties of the series of double perovskites (Ca,Sr)2−xLaxFeIrO6. *Journal of Solid State Chemistry* **2014,** *212*, 23-29.
107. Bufaiçal, L.; Coutrim, L. T.; Santos, T. O.; Terashita, H.; Jesus, C. B. R.; Pagliuso, P. G.; Bittar, E. M., Physical properties of Sr2FeIrO6 and Sr1.2La0.8FeIrO6 double perovskites obtained by a new synthesis route. *Materials Chemistry and Physics* **2016,** *182*, 459-465.
108. Qasim, I.; Blanchard, P. E. R.; Liu, S.; Tang, C.; Kennedy, B. J.; Avdeev, M.; Kimpton, J. A., Ordered vs. disordered perovskites; structural studies of Fe-doped SrIrO3 and SrRuO3. *Journal of Solid State Chemistry* **2013,** *206*, 242-250.
109. Paula, K.; A., A. J.; J., M. F.; Maria, R.; Mark, C.; Alexander, I.; T., F. D. M., Crystal and Magnetic Structure of Sr2BIrO6 (B = Sc, Ti, Fe, Co, In) in the Framework of Multivalent Iridium Double Perovskites. *European Journal of Inorganic Chemistry* **2015,** *2015* (30), 5027-5038.
110. Zhou, Q.; Kennedy, B. J.; Avdeev, M.; Giachini, L.; Kimpton, J. A., Structural studies of the phases in Ba2LaIrO6—New light on an old problem. *Journal of Solid State Chemistry* **2009,** *182* (11), 3195-3200.
111. Cao, G.; Qi, T. F.; Li, L.; Terzic, J.; Yuan, S. J.; DeLong, L. E.; Murthy, G.; Kaul, R. K., Novel Magnetism of ${\mathrm{Ir}}^{5+}(5{d}^{4})$ Ions in the Double Perovskite ${\mathrm{Sr}}_{2}{\mathrm{YIrO}}_{6}$. *Physical Review Letters* **2014,** *112* (5), 056402.
112. Bhowal, S.; Baidya, S.; Dasgupta, I.; Saha-Dasgupta, T., Breakdown of $J=0$ nonmagnetic state in ${d}^{4}$ iridate double perovskites: A first-principles study. *Physical Review B* **2015,** *92* (12), 121113.
113. Phelan, B. F.; Seibel, E. M.; Badoe, D.; Xie, W.; Cava, R. J., Influence of structural distortions on the Ir magnetism in Ba2−xSrxYIrO6 double perovskites. *Solid State Communications* **2016,** *236*, 37-40.
114. T. Corredor, L.; Aslan-Cansever, G.; Sturza, M.; Manna, K.; Maljuk, A.; Gass, S.; Zimmermann, A.; Dey, T.; G. F. Blum, C.; Geyer, M.; Wolter, A.; Wurmehl, S.; Büchner, B., *The iridium double perovskite Sr2YIrO6 revisited: A combined structural and specific heat study*. 2016.
115. Pajskr, K.; Novák, P.; Pokorný, V.; Kolorenč, J.; Arita, R.; Kuneš, J., On the possibility of excitonic magnetism in Ir double perovskites. *Physical Review B* **2016,** *93* (3), 035129.
116. Takeda, T.; Kanno, R.; Kawamoto, Y.; Takano, M.; Kawasaki, S.; Kamiyama, T.; Izumi, F., Metal–semiconductor transition, charge disproportionation, and low-temperature structure of Ca1–xSrxFeO3 synthesized under high-oxygen pressure. *Solid State Sciences* **2000,** *2* (7), 673-687.
117. Dann, S. E.; Weller, M. T.; Currie, D. B.; Thomas, M. F.; Al-Rawwas, A. D., Structure and magnetic properties of Sr2FeO4 and Sr3Fe2O7 studied by powder neutron diffraction and Mossbauer spectroscopy. *Journal of Materials Chemistry* **1993,** *3* (12), 1231-1237.
118. Battle, P. D.; Bollen, S. K.; Powell, A. V., Spin glass behavior in Sr3FeRuO7 and Sr4FeRuO8. *Journal of Solid State Chemistry* **1992,** *99* (2), 267-275.

119. Nakamura, S.; Oikawa, K., Precise Structure Analysis Consistent with Mössbauer Quadrupole Effect: A Case of the Ordered Double Perovskites Sr2FeMO6 (M = Mo and Re). *Journal of the Physical Society of Japan* **2003,** *72* (12), 3123-3127.
120. Sher, F.; Williams, A. J.; Venimadhev, A.; Blamire, M. G.; Attfield, J. P., Synthesis, Structure, and Properties of Two New Ruddlesden−Popper Phase Analogues of SFMO (Sr2FeMoO6). *Chemistry of Materials* **2005,** *17* (7), 1792-1796.
121. Shannon, R., Revised effective ionic radii and systematic studies of interatomic distances in halides and chalcogenides. *Acta Crystallographica Section A* **1976,** *32* (5), 751-767.
122. Parsons, T. G.; D'Hondt, H.; Hadermann, J.; Hayward, M. A., Synthesis and Structural Characterization of La1−xAxMnO2.5 (A = Ba, Sr, Ca) Phases: Mapping the Variants of the Brownmillerite Structure. *Chemistry of Materials* **2009,** *21* (22), 5527-5538.
123. King, G.; Thompson, C. M.; Luo, K.; Greedan, J. E.; Hayward, M. A., Identifying the local structural units in La0.5Ba0.5MnO2.5 and BaY0.25Fe0.75O2.5 through the neutron pair distribution function. *Dalton Transactions* **2017,** *46* (4), 1145-1152.
124. Mitchell, J. F.; Millburn, J. E.; Medarde, M.; Short, S.; Jorgensen, J. D.; Fernández-Díaz, M. T., Sr3Mn2O7: Mn4+Parent Compound of then=2 Layered CMR Manganites. *Journal of Solid State Chemistry* **1998,** *141* (2), 599-603.
125. Neetika; Das, A.; Dhiman, I.; Nigam, A. K.; Yadav, A. K.; Bhattacharyya, D.; Meena, S. S., Transport and magnetic properties of Fe doped CaMnO3. *Journal of Applied Physics* **2012,** *112* (12), 123913.
126. Kun, R.; Populoh, S.; Karvonen, L.; Gumbert, J.; Weidenkaff, A.; Busse, M., Structural and thermoelectric characterization of Ba substituted LaCoO3 perovskite-type materials obtained by polymerized gel combustion method. *Journal of Alloys and Compounds* **2013,** *579*, 147-155.
127. Hansteen, O. H.; Fjellvåg, H.; Hauback, B. C., Crystal Structure and Magnetic Properties of La2Co2O5. *Journal of Solid State Chemistry* **1998,** *141* (2), 411-417.
128. Garcia-Munoz, J. L. R.-C., J.; Lacorre, P.; Torrance, J. B, Neutron-diffraction study of RNiO3 (R = La, Pr, Nd, Sm): electronically induced structural changes across the metal-insulator transition. *Physical Review B: Condensed Matter and Materials Physics* **1992,** *46* (8), 4414-25.
129. Alonso, J. A.; Martínez-Lope, M. J., Resolution of the Crystal Structure of the Deficient Perovskite LaNiO2.5 from Neutron Powder Diffraction Data. *Materials Science Forum* **1996,** *228-231*, 747-752.
130. Battle, P. D.; Gibb, T. C.; Jones, C. W.; Studer, F., Spin-glass behavior in Sr2FeRuO6 and BaLaNiRuO6: A comparison with antiferromagnetic BaLaZnRuO6. *Journal of Solid State Chemistry* **1989,** *78* (2), 281-293.
131. La Placa, S. J.; Bringley, J. F.; Scott, B. A.; Cox, D. E., Structure of La2Cu2O5 by high-resolution synchrotron X-ray powder diffraction. *Acta Crystallographica Section C* **1993,** *49* (8), 1415-1417.
132. Vogt, T.; Woodward, P. M.; Karen, P.; Hunter, B. A.; Henning, P.; Moodenbaugh, A. R., Low to High Spin-State Transition Induced by Charge Ordering in Antiferromagnetic ${\mathrm{YBaCo}}_{2}{O}_{5}$. *Physical Review Letters* **2000,** *84* (13), 2969-2972.
133. James, M.; Morales, L.; Wallwork, K.; Avdeev, M.; Withers, R.; Goossens, D., Structure and magnetism in rare earth strontium-doped cobaltates. *Physica B: Condensed Matter* **2006,** *385-386*, 199-201.
134. Weber, D.; Schoop, L. M.; Wurmbrand, D.; Nuss, J.; Seibel, E. M.; Tafti, F. F.; Ji, H.; Cava, R. J.; Dinnebier, R. E.; Lotsch, B. V., Trivalent Iridium Oxides: Layered

Triangular Lattice Iridate K0.75Na0.25IrO2 and Oxyhydroxide IrOOH. *Chemistry of Materials* **2017,** *29* (19), 8338-8345.
135. Zhang, R.; Read, G.; Lang, F.; Lancaster, T.; Blundell, S. J.; Hayward, M. A., La2SrCr2O7F2: A Ruddlesden–Popper Oxyfluoride Containing Octahedrally Coordinated Cr4+ Centers. *Inorganic Chemistry* **2016,** *55* (6), 3169-3174.
136. James, M.; Tedesco, A.; Cassidy, D.; Colella, M.; Smythe, P. J., The phase diagram and crystal chemistry of strontium-doped rare earth cobaltates: Ln2−xSrxCoO4+δ (Ln=La–Dy). *Journal of Alloys and Compounds* **2006,** *419* (1), 201-207.
137. Kim, S. H.; Battle, P. D., Structural and Electronic Properties of the Mixed Co/Ru Perovskites AA′CoRuO6 (A, A′ = Sr, Ba, La). *Journal of Solid State Chemistry* **1995,** *114* (1), 174-183.
138. Helps, R. M.; Rees, N. H.; Hayward, M. A., Sr3Co2O4.33H0.84: An Extended Transition Metal Oxide-Hydride. *Inorganic Chemistry* **2010,** *49* (23), 11062-11068.
139. Vasala, S.; Karppinen, M., $A_2B'BO_6$ perovskites: A review. *Progress in Solid State Chemistry* **2015**, *43* (1-2), 1-36.